Physics from Time Variability of the VHE Blazar PKS 2155-304

BARRES-DE-ALMEIDA, ULISSES

Physics from Time Variability of the VHE Blazar PKS 2155-304

Ulisses Barres de Almeida

A Thesis presented for the degree of
Doctor of Philosophy

The H.E.S.S. Collaboration
Department of Physics
University of Durham
England

October 2010

A meus pais, José e Sônia, pertence este trabalho.

Physics from Time Variability of the VHE Blazar PKS 2155-304

Ulisses Barres de Almeida

Submitted for the degree of Doctor of Philosophy
October 2010

Abstract

Blazars are the principal extragalactic sources of very high energy gamma-ray emission in the Universe. These objects constitute a sub-class of Active Galactic Nuclei whose emission is dominated by Doppler boosted non-thermal radiation from plasma outflowing at relativistic speeds from the central engine. This plasma outflow happens in the form of large-scale collimated structures called jets, which can extend for Mpc in length and transport energy from the central engine of the galaxy to the larger scale intergalactic medium. Over thirty such sources have been discovered to date by ground-based gamma-ray telescopes such as H.E.S.S., and PKS 2155-304 is the prototypical southern-hemisphere representative of this population of objects.

In this thesis we have studied in detail some aspects of the temporal variability of the jet emission from PKS 2155-304, combining coordinated observations across the electromagnetic spectrum, from optical polarimetric measurements to X-ray and ground-based gamma-ray data. The temporal properties of the dataset allowed us to derive important physical information about the structure and emission mechanisms of the source and put constraints to the location of the sites of VHE emission and particle acceleration within the jet. We have also derived a sensitive statistical measure, called Kolmogorov distance, which we applied to the large outburst observed from PKS 2155-304 in July 2006, to derive the most stringent constraints to date on limits for the violation of Lorentz invariance induced by quantum-gravity effects from AGN measurements.

Declaration

The work in this thesis is based on research carried out at the Gamma-ray Astronomy Group of the Department of Physics, the University of Durham, England, and is partly associated to the activities of the H.E.S.S. Collaboration. None of this thesis has been submitted elsewhere for any other degree or qualification and it is all my own work unless referenced to the contrary in the text.

Acknowledgements

As the list of people that I *necessarily* need to mention here keeps on growing in my head, it becomes clear to me how much of a gift anything we have is and how much everyday is a “watershed” of gratuity bestowed upon us, so large is the gap which stands between what one is given and what one deserves. Therefore, I cannot but think that gratitude is the right measure of degree to which an individual is conscious of his own condition and his place and cinrcumstance in the world.

I would like to start by thanking the academic colleagues with whom I worked in this thesis. First of all, Dr. Paula M. Chadwick, who invited me to pursue this Ph.D. at Durham under her supervision. Throughout these years she has gone much beyond her duties to encourage and support me on the pursuit of this large task. Her faithfulness, honesty and thoughful care won in me a respect that goes much beyond the academic sphere and working environment, and I am therefore grateful for having worked under her responsibility these years. I wonder that, had I had someone else in whom to rely, my lack of academic qualities and the many difficulties through which I went during the initial years of my stay in England could have been a real impediment to the succesfull completion of this work.

I would also like to mention a few other names without whom I am certain I would not have been able to conclude this project. First among them is Prof. Martin J. Ward, who helped me with many aspects of this work, creatively encouraging me to go ahead with it. From the few instances in which I had the pleasure of enjoying his company in a non-strictly academic context, and specially during the few weeks when we were co-observers at the H.E.S.S. telescopes in Namibia, I nurtured a great admiration not only for his academic qualities but also his person. Dr. Michael K. Daniel is another person to whom I am greatly indebted and to whom I own at least half of this work. He was a

friend inside and outside the office and I am sure he knows I consider him a “gift” to my thesis. I also want to mention Dr. Catherine Boisson, who greatly helped me, specially while hosting me during a research stay in Paris in 2009 and during the work of one of the papers which compose this work.

I wish to express my heartfelt thanks to my other colleagues of the gamma-ray group at Durham, specially Dr. Christos Hadjichristidis, whose friendship I take with me as an indelible mark, Dr. Sam J. Nolan, Dave Allan, Dr. John Osborne, Dr. Steve Rayner, Dr. Lowry McComb as well as my fellow students: Dominic Keogh, Hugh Dickinson, Cameron Ruelten and Nikki Pekeur. Other colleagues of the University of Durham which I wish to thank are Dr. Matt Middleton (along with the whole of the X-ray group), my brazilian friend Thiago S. Fleury, and Prof. Sir Arnold Wolfendale, whom I had the good luck to know better in this past year. I also would like to thank Dr. Peter Craig, who thought me Bayesian statistics.

During the last two years, my participation in the activities of the Institute of Advanced Studies, where I was welcomed with great consideration as a postgraduate representative and editor of the Kaleidoscope Journal, was fundamental for my academic formation. I wish I could have devoted more work and time to the IAS activities than I managed to do. I take many friendships from my two years at the IAS, above all with Chris Gollon and David Tregunna, and two other fellows from the 2008/09 group: Prof. Frances Bartkowski and Prof. Eduardo Mendieta. I also wish to thank explicitly the directors of the IAS which welcomed me there, in particular Prof. Michael O’Neill. It is also a pleasure for me to remember the colleagues from the editorial board of Kaleidoscope, with whom I worked while there.

To have worked for fours years as part of such a successful and high-profile experiment as H.E.S.S. is truly a privilege. It is indeed necessary for me to thank, indistinctively, all the colleagues from the Collaboration from whom I learned much of the Astrophysics I know. I wish nevertheless to invoke some particular names, starting from those people with whom I shared observation periodes in Namibia: Dr. Matthieu Vivier, Dr. Armand Fiasson, Dr. Dirk Gerbig, Dr. Jens Ruppel, Prof. Wlodek Kluziniak and Mr. Albert Jahnke. It will suffice to say that I had a wonderful time all the three months I spent with them in the Namibian Desert, and I am thankful for the time we spent together and the

chance I had to get to know each of them more personally. My great consideration for them and friendship will be lasting. Other friends from H.E.S.S. which I want to mention very warmly are: Aldée Charbonnier, Matthias Füssling, Dr. Lukasz Stawarz, Prof. Jim Hinton and Dr. Jean-Philippe Lenain. An all-special thanks go for Joanna Skilton, for whom I carry a special affection.

There exists an almost uncountable number of other colleagues which I met around the world in my trips during these four years, from Alaska to Armenia, and whom I worked with and befriended, but which are very hard to list here. I would like therefore to remember only one of these friends in special, Dr. Eleonora Troja, who became a companion of many conferences. Although I seldom visited my home country during these four years, I wish to recall some academic colleagues from Brazil with whom I actually worked: Dr. Zulema Abraham, Dr. Tania Dominici. I also want to remember Prof. Gustavo Medina-Tanco and Dr. Vitor de Souza, who thought me Cosmic-Ray physics at University, as well as some friends from USP who were present to me in a particular way during these years, namely Alberto Krone-Martins, Rubens Garcia-Machado and Laura Paulucci.

I wish now to move on to thank all my non-academic colleagues of the University of Durham, specially the friends from the Catholic Society. Among them, I must mention my very beloved friend Emily Blackmore whose goodness, purity of heart and love for Christ I am honoured to have witnessed, and Fr. Anthony Currer to whom my debt of gratitude is immense and unpayable. To these two people I can assure they will be in my prayers forever.

None of these acknowledgements give me more joy than to remember my friends of the Fraternity of Communion and Liberation. I must start from those who were with me here in the North, and to whom I belong more than to any of the others, because in them it was more evident to me than in any other instance that reality is a gift and an invitation from Another for us to reach our destiny. These people are: Simone Oliva and Marta Farneti, Matteo de Tina, Marco Berci, Rachel Soemedi, Phillip Wherry, Carmino Massarella and Monica Massarella, Dominic Barnes, Pier Aldo Scozin, Veronica Cestari among many others. I reserve a special place for thanking Lucia Sbragia, whose friendship was a constant support for me when it would otherwise have been too difficult to remain here. She knows that I welcomed her and belong to her as if to Christ himself.

Saint-Exupèry once said that a man becomes eternally responsible for that which he captivates, and thus I consider myself before them.

Together with the names above, the other friends from CL that I mention here constantly offered me that Suppreme Treasure for which any reasonable man would sell all he has in order to buy it: Gianluca Marcato and all his family from London, Maria Ubiali and Giacomo Mazzi, Sandro Tubertini and Mariana Lucato, Francesco Fabrinni, Marco Sinisi, Francesca Macchioro, Giuditta Cirnigliaro, Fr. Christopher Hamilton-Gray and Fr. Julián Carrón, who educated me to become a truer man during these past four years. I wish also to thank a few friends of CL from Brazil, whose presence that knows no distance or time is a sign of the Eternal for which life is made: Alexandre Ferrari, Carlos Otavio, Fr. Vando Valentini and Bruno Tolentino, who truly accompanied me through his poetry, some of which I came to know by heart. The only way in which I can thank people of such human stature is to assure them I will do my best to remain faithful and to serve with love that which we met together.

I want also to remember here Werner Luckow and Marilene who welcomed me so many times in their house in London. I also remember here, with a profound gratituted, Debora. The only way to properly acknowledge what her company meant is to affirm every morning, and regardless of all my limits, that “all is Mystery”, and from that note start off the work of every day, since “the part that is reserved for each individual, that is, what God wants for you, must be done by you.”

I want to conclude by thanking my family, specially my parents, to whom I dedicate this work, my sister Carolina, and my late uncle, Gê. With them, more than through anyone else, I understand ever more that all of life is a gift, and the gratitude for this gift is the source of a growing charity without which nothing I did could claim any real value. With this awareness, I entrust them to the safe hands of Our Lady, asking her to guide and to guard their Destiny. As much as I am thankful for all of those mentioned here, I remain conscious of the One who gave me them all, and thus reserve my ultimate gratitude to Him alone.

I also thank the CAPES Foundation, Ministry of Education of Brazil, for funding this work.

“*In interiore homini habitat veritas.*”

St. Augustine - De Vera Religione.

“*It is the glory of God to conceal things, and that of the kings to investigate them.*”

Proverbs 25:2

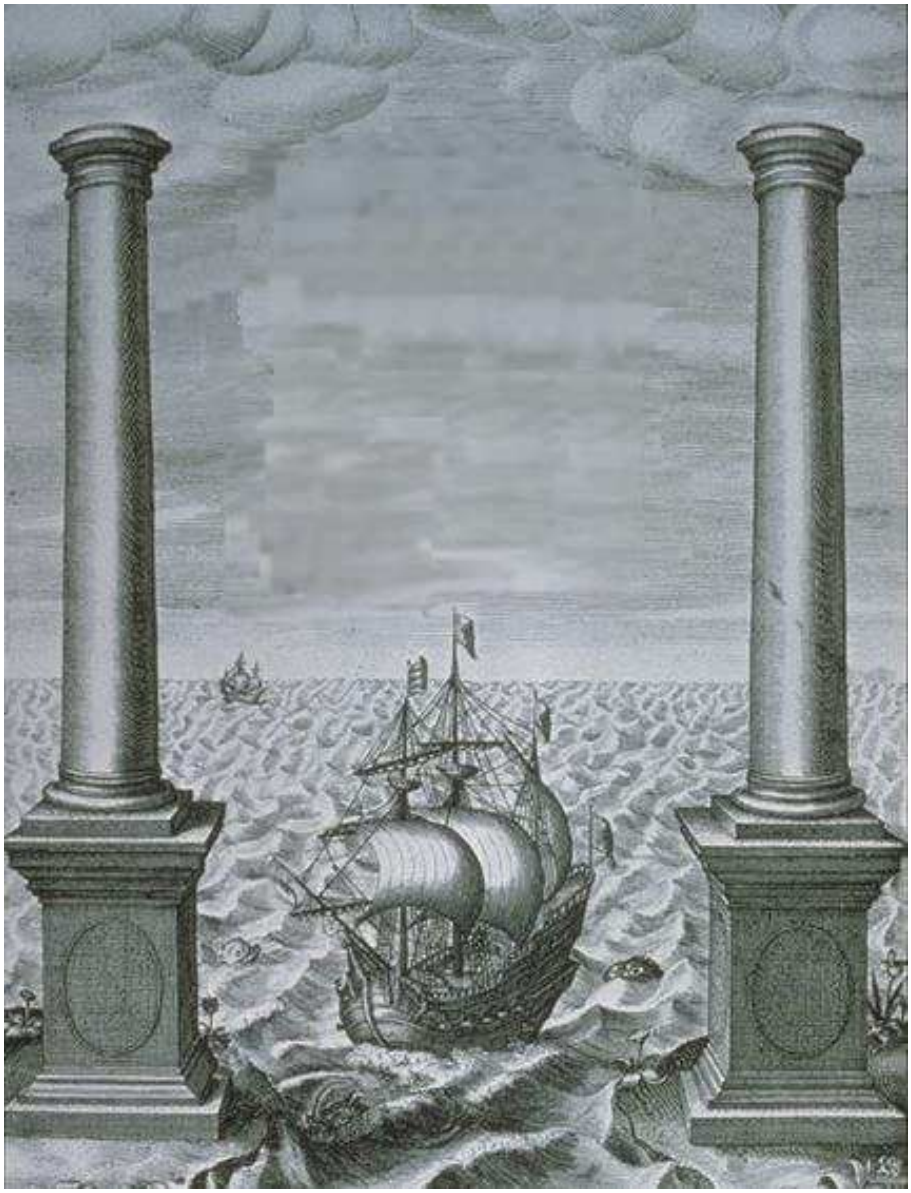

Figure 1: The crossing of the Pillars of Hercules. From F. Bacon's *Instauratio Magna*, 1620.

Contents

Abstract **iii**

Declaration **iv**

Acknowledgements **v**

1 The VHE γ-Ray Universe **1**

1.1 Introduction 1

1.2 Cosmic Radiation 3

1.2.1 Observations of Cosmic Rays 4

1.2.2 Cosmic-ray Electron Spectrum 8

1.2.3 The Environment of the Cosmic-Ray Sources 9

1.2.4 Diffuse Gamma-ray Emission 10

1.3 Sources of VHE gamma-rays 11

2 Observational Techniques **17**

2.1 Observational Techniques I: VHE Gamma-ray Astronomy 17

2.1.1 Electromagnetic Showers and Cherenkov Radiation in the Atmosphere 19

2.1.2 Imaging Atmospheric Cherenkov Telescopes 26

2.1.3 Imaging Atmospheric Cherenkov Technique 32

2.1.4 H.E.S.S. Data Analysis 41

2.2 Observational Techniques II: Optical Polarimetry 47

2.2.1 A Primer on Optical Polarimetry 48

2.2.2 Measurement Techniques: the IAGPOL 54
2.2.3 Principles of Reduction of Polarimetric Data 58

3 Radiation Processes in Blazars **61**
3.1 Particle Acceleration 61
3.1.1 Fermi Processes 62
3.1.2 Acceleration timescale and particle energies 66
3.1.3 Shocks in Jets 67
3.1.4 Interlude: The Bulk Flow 68
3.2 Radiation Mechanisms in Blazars 69
3.2.1 Synchrotron Emission 69
3.2.2 Inverse-Compton Emission 79

4 Blazars & Extragalactic Jets **86**
4.1 Active Galactic Nuclei 87
4.1.1 AGN Classification and Unification 91
4.2 Emission Models for Blazars 98
4.2.1 Synchrotron Self-Compton Models 99
4.2.2 External Compton Models 101
4.2.3 Hadronic Models 102
4.3 Blazars and TeV Emission 105
4.3.1 The blazar sequence rationale 108
4.3.2 The gamma-ray view of blazars 109
4.4 Gamma-ray Opacity: Pair Production 111
4.4.1 Emission Site Constraints from Internal Source Opacity 112
4.4.2 Propagation Through the EBL 114
4.5 Extragalactic Jets 115
4.5.1 Geometrical Structure and Superluminal Motion 115
4.5.2 Relativistic Boosting 117
4.6 The VHE Blazar PKS 2155-304 118

5 Time Variability and Spectral Dispersion in Blazars 120

5.1 Bayesian Studies of Time Variability: Unbinned Statistical Methods . . . 121

5.1.1 Fundamentals of Bayesian statistics . . . 121

5.1.2 Change-point detection of gamma-ray flares . . . 123

5.1.3 Dynamical Algorithm . . . 131

5.1.4 Application to PKS 2155-304 . . . 134

5.2 Energy-dependent dispersion in blazars . . . 136

5.2.1 Unbinned Methods: Motivation . . . 136

5.2.2 Dispersion Cancellation Algorithm . . . 137

5.2.3 The Kolmogorov distance method . . . 139

5.2.4 Monte Carlo Studies . . . 143

5.3 Application to PKS 2155-304 . . . 150

5.4 Application I: Quantum Gravity . . . 157

5.4.1 Energy-dependent propagation: time-of-flight experiments . . . 161

5.4.2 Results from the Kolmogorov distance method . . . 166

5.5 Application II: *in situ* acceleration . . . 168

5.5.1 Size and physical nature of the emitting region . . . 168

5.5.2 Energy dependent time-delays: . . . 169

6 Multiwavelength Polarimetric Campaign on PKS 2155-304 174

6.1 Description of the Campaign . . . 175

6.2 The Polarimetric view of PKS 2155-304 . . . 177

6.2.1 Optical Polarisation Properties . . . 178

6.2.2 Radio Jet Observations . . . 180

6.2.3 Implications for the source structure . . . 181

6.3 Multiwavelength Campaign: analyses and results . . . 184

6.4 Polarimetric Observations of PKS 2155-304 in 2008 . . . 188

6.4.1 Modelling of the Polarised Emission . . . 194

6.4.2 Origin of the Flux Variability . . . 203

6.4.3 Magnetic Field Structure . . . 206

6.4.4 Frequency Dependent Polarisation . . . 210

6.4.5 Timescales of Magnetic Field Evolution . . . 213

6.5 Conclusion: The Quiescent State of PKS 2155-304 215
6.5.1 Analysis of the quiescent state SED 215
6.5.2 Source structure and emitting regions 218
6.6 Epilogue: Do geometric effects play a role in the polarimetric variability? 220

7 Conclusions & Future Perspectives **226**

Bibliography **230**

Appendix **263**

A R Numerical Codes **263**
A.1 Bayesian Blocks 263
A.1.1 Routine InputEventSequence 263
A.1.2 Routine DataCell 264
A.1.3 Routine InspectEventSequence 265
A.1.4 Routine LikelihoodFunction 266
A.1.5 Routine BlockPartition 267
A.1.6 Routine PartitionModel 269
A.2 Kolmogorov Distance 271

Appendix **276**

B Complete Journal of PKS 2155-304 Multi-wavelenght Campaign **277**
B.1 LNA Optical Polarimetry Data 277

List of Figures

1 The crossing of the Pillars of Hercules. x

1.1 A photograph of Victor F. Hess. 4
1.2 The energy spectrum of cosmic rays. 5
1.3 Fermi-LAT one-year all sky map. 10
1.4 The VHE gamma-ray sky as of 2009. 11
1.5 Kifune's plot. 13
1.6 The H.E.S.S. Galactic plane scan. 15

2.1 Schematic design of the Fermi gamma-ray satellite. 19
2.2 Schematic development of an electromagnetic shower in the atmosphere. . 20
2.3 Illustration of the effects of a charged particle moving through a dielectric medium. 21
2.4 Propagation of wavefronts and development of a shock wave. 23
2.5 Differential cherenkov photon spectrum. 24
2.6 Illustration of the focusing effect of the varying Cherenkov angle $\theta(n)$ with altitude and formation of the Chrenkov light pool. 25
2.7 The H.E.S.S. telescopes. 28
2.8 Structure of one of the individual H.E.S.S. telescopes. 29
2.9 The shapes of Cherenkov images of true air-shower events as observed with the H.E.S.S. camera. 30
2.10 Schematic illustration of the development of a cosmic-ray initiated air-shower. 33
2.11 Comparison of a pure electromagnetic shower from a 300 GeV gamma-ray and a hadronic shower initiated by a 1 TeV proton. 35

2.12 Model of the geometry of the gamma-ray initiated shower ellipse as mapped by the detector for different relative positions of the shower axis. 36
2.13 The Hillas parameters. 37
2.14 Reconstruction of the shower parameters from stereoscopic observations. 39
2.15 Example of simulated MRSW and MRSL distributions used for gamma-hadron discrimination in the H.E.S.S. telescopes. 40
2.16 Geometric construction showing the meaning and mode of calculation of the angular parameter θ for image discrimination in the stereoscopic technique. 42
2.17 Scheme of the different methods of background estimation for H.E.S.S. analysis. 44
2.18 The polarisation ellipse 50
2.19 The Poincaré Sphere. 52
2.20 The "Pico dos dias" observatory of the National Astrophysics Laboratory (LNA/Brazil). 53
2.21 Scheme of a modulator for linear polarisation of halfwave rotator plate. . 57

3.1 Schematic representation of the first and second order Fermi particle acceleration mechanisms. 62
3.2 Geometry for the calculation of synchrotron emission 69
3.3 Pulse synchrotron emission from an electron gyrating about an uniform magnetic field line. 72
3.4 Wide-band power-law spectrum of a synchrotron source shown as the superposition of a sequence of mono-energetic synchrotron spectra. 75
3.5 Spectrum of a compact synchrotron source showing the effect of synchrotron self-absorption. 76
3.6 Diagramatic representation of inverse-Compton scattering. 80

4.1 Unification scheme of AGN. 90
4.2 Simple taxonomic diagram for AGN. 92
4.3 The blazar sequence: average SEDs for a complete blazar sample combined according to luminosity. 99

4.4 Spectral energy distribution (SED) of the TeV blazars PKS 0548-322. . . 106
4.5 Superluminal motion in the jet of the quasar 3C 345. 115
4.6 Geometry of superluminal motion. 116

5.1 Light curve of PKS 2155-304 big flare event of MJD 53944. 135
5.2 Cartoon of the effect of the energy-dependent dispersion on the shape of the low (L) and high (H) energy profiles. 140
5.3 Choice of the light-curve representation for the Kolmogorov distance method 142
5.4 Sensitivity of the Kolmogorov distance algorithm in relation to the ratio lag/burst width for different energy resolutions of the observations. 145
5.5 Sensitivity of the method in relation to the width of the burst and the number of events in it. 146
5.6 Sensitivity of the Kolmogorov distance method in relation to the size of the “transparent” window used to contruct the CDFs from the burst profile. 148
5.7 Sensitivity of the Kolmogorov distance in relation to the size of the “opaque” window used to construct the CDFs from the burst profile. 149
5.8 Comparison of the sensitivity for detecting a lag between the minimum distance Kolmogorov method and the maximum sharpness methods. . . . 150
5.9 Modeled light curve of the PKS 2155-304 big flare event of MJD 53944, for photons above 170 GeV. 151
5.10 Effect of the choice of the energy cut for the high energy band on the accuracy of the determined dispersion based on Monte Carlo simulations of the burst profiles BF1-5. 153
5.11 Simulation of 10,000 events for the profile of BF2, with no dispersion introduced. 155
5.12 The accuracy to which the method can recover a fixed dispersion parameter introduced into the light-curves representing the PKS 2155-304 flares. 156
5.13 Kolmogorov distance profiles for the search of energy-dependent dispersion in the bursts BF1-5 of PKS 2155-304. 156
5.14 Pictorial model for the inner jet structure of blazars. 172

6.1 VLA image of PKS 2155-304 at 15.4 GHz. 180

6.2 Runwise light curves for the entire timespan of the campaign on PKS 2155-304, presenting H.E.S.S. and RXTE data. 185
6.3 Light curves for the entire multiwavelength campaign dataset. 186
6.4 R-band optical light-curve for PKS 2155-304 from 01 September 2008. . 189
6.5 The intranight polarimetric variability of PKS 2155-304 in the Stokes $Q-U$ plane for each individual night of the LNA optical campaign. 192
6.6 Multiband light-curves for PKS 2155-304 in optical. 193
6.7 Polarised versus total flux relation for the six nights of the optical campaign. 195
6.8 Results of the two-component synchrotron model fitted to the optical polarimetric observations of PKS 2155-304. 199
6.9 Optical spectra of PKS 2155-304 for the 5 days of the optical campaign with V, R and I multiband information. 202
6.10 Schematic picture of AGN jet model and shock-heating radiation emission. 209
6.11 Frequency dependence of polaristaion degree and polarisation angle. . . . 210
6.12 Scenario for production of variable frequency-dependent polarisation based on a shock-in-jet model. 213
6.13 Plot of the V-band poalrisation degree versus V-I spectral index. 214
6.14 Spectral energy distribution of PKS 2155-304 during the MWL campaign. 216
6.15 Geometrical model for the changes in the polarisation degree of PKS 2155-304 due to relativistic aberration of a shock with changing angle to the line-of-sight. 220
6.16 Reconstruction of the optical photo-polarimetric parameters and light curve behaviour from the geometrical model. 223

7.1 Simulated sensitivity curve for CTA, in relation to other gamma-ray observatories. 228
7.2 229

List of Tables

1.1 Complete census of VHE sources as of September 2010. 12

2.1 Properties of current-generation air-Cherenkov telescopes. 27
2.2 Optimised gamma-ray selection cuts for a point source analysis 41

5.1 Parameters used for the generalised Gaussin fit to the PKS 2155-304 flare simulations. 152
5.2 Temporal window and low- and high-energy boundaries used for the construction of the CDFs for each burst from PKS 2155-304. 154
5.3 Quantum gravity energy scale limits derived using the five bursts from the PKS 2155-304 large flare. 166

6.1 Summary of 2008 observations of PKS 2155-304. 176
6.2 Host galaxy contribution for PKS 2155-304. 189
6.3 Optical and polarimetric micro-variability analysis results. 191
6.4 Polarisation parameters of the variable component. 197
6.5 SSC model parameters for the SED of PKs 2155-304. 217

B.1 Journal of LNA Polarimetric Observations 277

Chapter 1

The VHE γ-Ray Universe

1.1 Introduction

This chapter introduces the high-energy sky, concentrating on its GeV-TeV gamma-ray aspects and its fundamental link with the most extreme astrophysical sources known. The high-energy Universe is dominated by non-thermal sources of radiation which act as efficient particle accelerators. Very-high energy (VHE; $E > 100$ GeV) gamma-ray sources are therefore the primary candidates for cosmic ray generation. In fact, one of the principal goals of, and perhaps the original motivation for, gamma-ray astronomy was the quest for understanding the origin of the cosmic rays. Because the acceleration mechanisms in these sources are closely linked with the presence of magnetic fields in the systems, VHE gamma-rays are among the most interesting ways to probe astrophysical magnetic fields and relativistic dynamics such as shocks in high energy plasmas. Furthermore, unlike with cosmic rays, which are deflected from a straight path by magnetic field lines as they travel towards the Earth, the celestial sources of gamma-rays can be directly traced from the observations. As will be shown later, with observations of TeV gamma-rays, and assuming the standard synchrotron and inverse-Compton emission mechanisms, electron populations of energies up to 10^{14} eV – and in principle proton populations of up to 10^{20} eV (see Chapter 3) – or so can be probed.

Recent developments in the field of gamma-ray astronomy have revealed a Universe that is rich in high-energy nonthermal processes and in which gamma-ray production is a common phenomenon to many different objects. In this work we are concerned with a

very specific class of TeV emitters of extragalactic nature, namely the blazars, a sub-class of active galactic nuclei (AGN) whose radiative output at VHE energies is favoured by the relativistic expansion and outflow of particles within a magnetised plasma. These sources constitute the most extreme[1] among the VHE emitters and some of the recent discoveries of the field (as revealing as they were) have come as a challenge to understanding their inner workings and the details of their nature. The role played by gamma-ray observations in the study of these sources is far from secondary, given that their radiative output above 1 GeV is comparable and can sometimes (during extreme emission states) dominate over the power emitted in the rest of the EM spectrum. The extended radio structures of active galaxies (which can extend for several Mpc) have also been hypothesised in the past as potential reservoirs of high-energy particles and as the possible (and most likely) sites of ultra-high energy cosmic rays, with energies of up to 10^{18} eV and beyond, but their role as extreme accelerators is still inconclusive (Auger Collaboration 2007 [287] and Gorbunov et al. 2008 [179]).

This work is concerned with a particular branch on the astrophysics of blazars, viz. the study of their time variability. In fact, the VHE emission from blazars has revealed itself to be the most variable of all their spectrum, which extends from the metre radio waves to TeV gamma-rays, with episodic variations as short as O(100s) being registered from two of the prototypical TeV blazars, PKS 2155-304 [26] and Mkn 501 [39]. Part of this work will focus on timing studies of the extremely rapid variability from PKS 2155-304, which was also the most energetic, short duration AGN outburst ever observed at any wavelength, with a peak luminosity above 200 GeV of ≈ 15 Crab, or $\sim 10^5$ erg s^{-1}, and a total VHE luminosity of the order of 10^8 ergs, spread over a time of little over an hour.

Such extreme variability episodes have the potential to provide the most stringent constraints that can be put on the radiation mechanisms and physical processes in relativistic jets, being also excellent tracers of *in situ* particle acceleration. In this work, they will also be used to test predictions of new physics such as searching for quantum gravity effects and Lorentz invariance violation in the free propagation of γ-ray photons in vacuum (see Chapter 4). The preoccupation with the use of and the search for efficient

[1] With typical radiative luminosities of $\gtrsim 10^{46}$ erg s^{-1}, or $\sim 10^{11} L_{\odot}$ and a total lifetime output $> 10^{60}$ ergs.

statistical methods for time series analysis was central in this work, and the variability studies are centered on the application and development of two new methods: namely, the Bayesian blocks algorithm to search for change points in unbinned high-energy light curves (Scargle 1998 [311]), and the Kolmogorov distance measure for the detection of spectral-dependent delays in unbinned high-energy time series (Barres de Almeida & Daniel 2010 [66] – see Chapter 5).

Further to that, the fundamental role played by magnetic fields in particle acceleration within extragalactic relativistic jets led us to start a project focused on the study of correlated optical polarimetric/ TeV emission. This project is the first systematic attempt to study the two types of emission together and some of its first results will be presented here, also in relation to the VHE blazar PKS 2155-304 (Barres de Almeida et al. [65] – see Chapter 6). This multiwavelength approach will allow us to put better constraints on the source structure and consequently better locate the sites of VHE emission and particle acceleration within the blazar jets.

1.2 Cosmic Radiation

Very-high energy γ-ray photons are produced by very energetic charged particles when they undergo some sort of interaction with the ambient medium; therefore, cosmic ray sources are also bound to be γ-ray emitters at some level. Typically, the maximum energy fraction that can be converted from these particles into EM radiation via the canonical astrophysical channels is around 10%. If the relativistic particles in question are electrons, the available mechanisms rely on the interaction with magnetic (e.g. synchrotron radiation) or lower energy photon fields (e.g. inverse-Compton radiation); in the case of hadrons, the most efficient way to generate high-energy photons will be via interaction with interestellar target material (i.e. meson-production), although proton-synchrotron and inverse-Compton processes can also play a relevant role at more extreme conditions (i.e. higher particle energies and stronger magnetic fields). All these processes are discussed in more detail in Chapter 3. This being said, it is clear that the astrophysical VHE sources are to be multi-TeV particle accelerators, or conversely, environments capable of acting as reservoirs of relativistic particles. In both cases, a relatively powerful source of

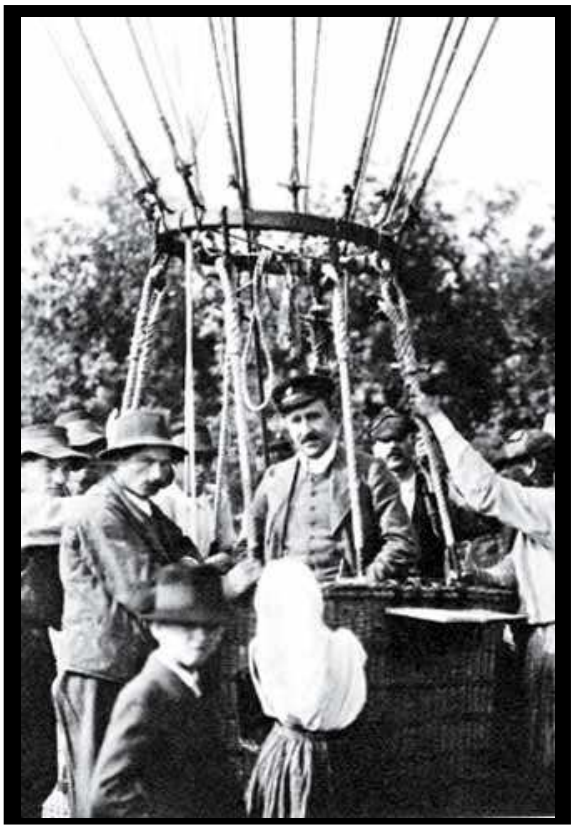

Figure 1.1: A photograph of Victor F. Hess before one of the balloon flights which led to the discovery of the cosmic rays. Credits: A. Weber, Fordham University Archives.

charged particles and/or more or less intense ambient magnetic fields will constitute the fundamental ingredients necessary to produce γ-rays.

1.2.1 Observations of Cosmic Rays

Cosmic rays are energetic charged particles (electrons, protons, α-particles and other nuclear fragments) that reach the Earth from extraterrestrial sources. Their discovery happened essentially simultaneously to the unveiling of the atomic structure and its elementary constituents, and came as an answer to the question of the origin of the natural radiation responsible for the ionisation of gas-chambers and passive charging of electroscopes as observed in experiments by Rutherford and others at the turn of the XX$^{\text{th}}$ century. Initially, the discovery of the radioactive properties of the periodic elements suggested that the free charges had a terrestrial origin, and in fact this hypothesis was in accord with preliminary measurements of a decrease of the rate of ionisation with altitude. Nevertheless, in 1912, Victor Hess performed high altitude balloon flights (see Figure 1.1)

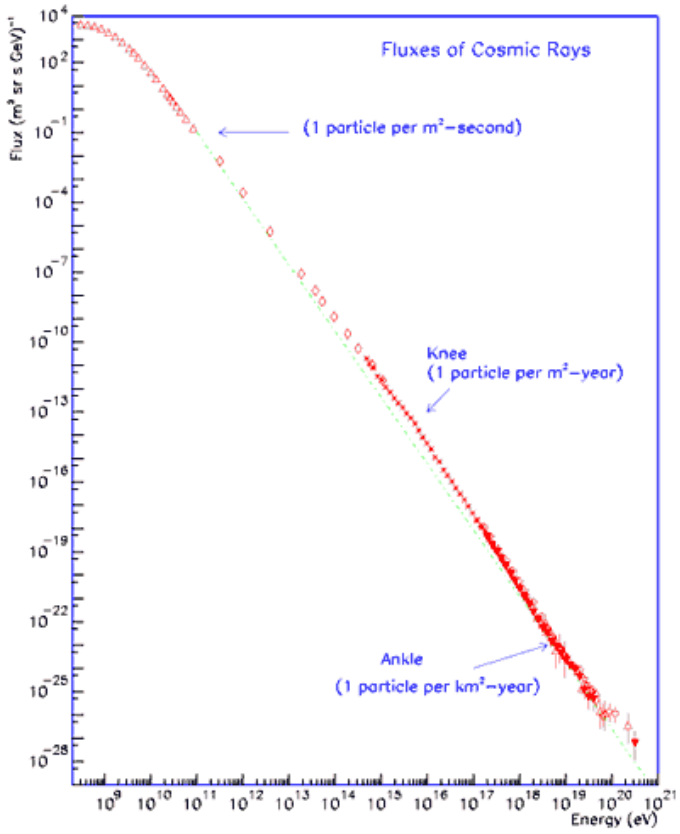

Figure 1.2: The energy spectrum of cosmic rays. From a compilation by S. Swordy.

which showed that this trend was reversed and that the flux of free ionising charges in the atmosphere increased above $\sim$ 1.5 km [192]. After that, the study of cosmic radiation progressed at great pace, delving into questions such as the energy, composition and nature of the progenitor sources of the radiation.

Cosmic rays are a fundamental constituent of the Galaxy, with an energy density that is comparable to that of the photon and magnetic fields, suggesting that these three constitutents live in a situation of quasi-equilibrium. In the interstellar gas clouds, near-equipartition is also frequently verified between the energy density of cosmic rays and the kinetic energy of the turbulent gas motions, an indication that interstellar material is efficiently heated by the isotropic cosmic ray flux.

As for their composition, cosmic rays are mostly made up of protons (about 90% – of which 70% are believed to be of an elemental origin and the rest the product of spallation of higher nuclei). Seen from Earth they appear to come as an isotropic flux, and this has to do with their “irregular” trajectories along the Galactic magnetic field lines

(which have an average intensity of $B_G \sim 10^{-6}$ G). The spectrum of cosmic rays consists of a power law in energy with index in the range -2.5 to -2.7 at sub-TeV energies and extends through 20 decades (Figure 1.2). Except for energies below 10^{12-14} eV (those whose parent sources can often be probed indirectly via γ-ray measurements), the flux of particles is so low (< 1 particle m^{-2} yr^{-1}) that large, several-km^2 ground-based arrays are necessary to obtain the required statistics for study. Such arrays benefit from the fact that these highly energetic cosmic rays interact with the air upon entering the atmosphere to give origin to the so-called extensive cosmic-ray showers, a phenomenon discovered by Auger et al. in 1939 [55], and which is also exploited in ground-based gamma-ray astronomy.

Despite its remarkably smooth power law character, which attests to the universality of the acceleration mechanism that produces these particles, the cosmic ray spectrum presents certain features that may be associated with a change in the origin of the particles [140]. The "knee", at about 10^{16} eV, where the spectrum suffers a kink and softens to an index of ≈ -3, is believed to be the region where the transition happens between a Galactic to an extraglactic origin for the cosmic-rays. This is because at these energies the particles are already too energetic to be confined within the Galaxy during their acceleration process (i.e. their Larmor radius is larger than the thickness of the Galactic disc) and they are therefore expected to diffuse away into the inter-galactic magnetic field. In fact, according to the celebrated Hillas formula [194], the condition for acceleration of cosmic ray particles of charge Ze to a given energy E can be related to the confinement capacity of the acceleration site $E \leq ZecBR$, and so scale with the magnetic field intensity B and the linear size R of the accelerator, meaning that large structures such as radio galaxy lobes are expected to be necessary for very- and ultra-high energy cosmic ray production.

Below the "knee", cosmic rays are believed to originate in supernovae remnants, where Fermi acceleration processes are at work in shocked gas between supersonically expanding winds [197]. Gamma-ray observations are key to testing some of the models proposed for the origin of the cosmic-ray particles in Galactic systems, as revealed by a series of recent observations by the H.E.S.S. Collaboration (e.g., [14]).

At still higher energies ($E \sim 10^{19}$ eV) another break, the so-called "ankle", is present in the energy spectrum of CR particles. At these ultra-high energies (UHE), cosmic-

ray protons, which must be extragalactic in origin due to the confinement considerations mentioned before, are expected to suffer little deflection by the intergalactic magnetic field and attempts have been made to trace back their origin to locate directly their acceleration sites. Until now, the low statistics of UHE particles (as many as 81 events above 10^{18} eV [289] as of 2008) allows little correlation with particular sources, and although it can be argued (at the 99% confidence level) that the spatial distribution of UHECR is anisotropic, more integration time seems necessary to identify particular objects with which to associate their production [348].

The high expectations towards some correlation being detected between nearby astrophysical sources and UHECR is strengthened by the recent detection by the Pierre Auger observatory of the Greisen-Zatsepin-Kuz'min cut-off [288][2]. In any case, the difficulty of pin-pointing these sources of extreme particle acceleration continue to strengthen the relations with ground-based gamma-ray astronomy, which is a fundamental tool in the search for the sites of generation of cosmic radiation.

Conversely, cosmic-ray physics can also provide crucial information for studies of the astrophysical sources of gamma-rays. The detection of protons of extreme energies proves that cosmic accelerators can efficiently produce highly energetic hadrons. If the extragalactic sources of VHE and UHE cosmic-rays are indeed active galaxies as expected from energetic considerations [297], then the role hadronic radiation processes play in these sources and to what extent they contribute to the gamma-ray emission from AGN is still to be understood. Comprehensive, recent reviews about the status of the highest energy cosmic ray physics can be found in Torres & Anchordoqui 2004 [334] and Beatty & Westerhoff 2009 [68].

[2]The so-called GZK cut-off is a suppression on the arriving flux of UHECR resulting from their interaction with cosmic microwave background photons as propagating on intergalactic space. The existence of the effect was independently suggest by Greisen [182] and Zatsepin & Kuz'min in 1966 [356], soon after the discoveries of Penzias & Wilson in 1965 [284] concerning the CMB. It anticipates a sharp (due to the steepness of the high-frequency tail of the Planck distribution) and catastrophic (a suppression factor of several hundreds in the observed flux) cut-off in the energy spectrum characterising the UHECR proton flux around 6×10^{19} eV due to photo-pion production on the CMB photons. The peak of the interaction cross section is achieved for CR of $\sim 10^{20}$ eV and photons at the peak of the CMB energy distribution, and the resulting mean-free-path of interaction is of ~ 6 Mpc [163]. The energy loss per interaction is $\Delta E/E \sim 0.22$ at its peak resonance value and the characteristic time for energy losses by the proton is much less than the Hubble time (of the order of 10^{15} s), and so the process was expected to reflect in observations.

1.2.2 Cosmic-ray Electron Spectrum

Since the most favoured models for production of γ-rays in many cosmic environments are of leptonic nature, gamma-ray astronomy is in a particularly favourable position to study the electronic ($e^{\pm}$) component of the cosmic-ray spectrum. In addition to the indirect probes mentioned above, both the satellite and ground-based gamma-ray experiments can be used as *direct* and efficient electron detectors, with large collecting areas. The interest in studying the electron spectrum of cosmic rays comes from the fact that, due to strong energy losses via synchrotron and inverse-Compton emission during propagation, their lifetime is considerably shorter than that of the hadronic component (see Chapter 3), and so sources of cosmic-ray electrons must be local in nature ($<$ 1 kpc distance). In 2008, the ATIC collaboration reported the measurement of an excess in the electron spectrum between 300-800 GeV [103] (present as a deviation from the typical e^{-} energy power law trend of $E^{-3.3}$ with a sharp cut-off at 620 GeV) which could be either interpreted as a dark matter signature or the indication for a nearby source of cosmic-ray electrons.

Following this result, H.E.S.S. performed measurements of the energy spectrum of the cosmic ray electrons above 300 GeV and found a steepening of the spectrum above 600 GeV (as expected from energy losses), followed by a cutoff in the power law distribution at $\sim$ 2 TeV. This result was argued to be compatible with the existence of a local source of cosmic rays within the $\sim$ 1 kpc local Galaxy environment [29]. Nevertheless, a pronounced excess at $\sim$ 600 GeV such as suggested by ATIC is excluded by the H.E.S.S. measurements. These results favour the origin of the peak in the specturm as due to a nearby astrophysical source of electrons which is contributing to the electron flux at high-energies, rather than it being a dark matter decay signal, which would result in a sharper excess peak [36]. The H.E.S.S. results have been recently confirmed by the *Fermi* collaboration (see [144] and [152]), which recorded a smooth spectrum with $E^{-3.08\pm0.05}$, presenting only a slight hardening around 100 GeV, followed by a softening above 500 GeV, compatible with energy propagation losses. The combined data seems to agree with the scenario where a local component of cosmic ray electrons explains the spectral excess, but as discussed by Grasso et al. 2009 [180], a definitive choice of this hypothesis over dark matter decay signature needs a measure of electron anisotropy, specially in view of PAMELA's detection of anomalous positron abundances in CR between 1.5-100 GeV [8].

1.2.3 The Environment of the Cosmic-Ray Sources

VHE γ-rays are produced in the interactions of accelerated charged particles – either leptons or hadrons – with ambient matter or radiation fields, and regardless of the process, the flux of γ-rays reflects the densities of particles in the production sites: high-energy gamma-rays are therefore direct tracers of the populations of high energy particles in astrophysical sources and of their dynamical evolution. Because of their close association with the CR particles, γ-ray sources will share the morphological and spectral properties of the sites of cosmic ray production or of the target materials with which CR interact (such as gases in Molecular Clouds or the ISM), as well as extended magnetised regions (e.g., the lobes of FR-II radio galaxies [297]) which act as reservoirs of charged particles. Therefore, despite the fact that many of the astrophysical objects that can dissipate gravitational energy in order to accelerate particles efficiently are compact objects, extended regions of γ-ray emission will be produced when cosmic rays diffuse away from their production zones.

In the absence of bulk motions, such as strong winds or the environment of a relativistic jet, the transport of cosmic-rays is governed by diffusion in the ambient magnetic field [199]. For typical interstellar magnetic field intensities $O(\mu\mathrm{G})$, the mean-free path ($\sim$ gyro-radius) of a TeV CR particle of mass m and energy E_{TeV} is $R_g \sim 10^{-3}(m/m_p)E_{\mathrm{TeV}}$ pc, where m_p is the proton mass. Recalling that the diffusive propagation is described by $\langle r^2 \rangle = 2Dt$, where $D \propto (\delta B/B)^{-2} R_g c$, and t is the diffusion time ($\sim$ source's age) and $(\delta B/B)$ is the relative degree of turbulence in the local magnetic field, we can write the typical size of a gamma-ray source as $\langle r^2 \rangle \sim E_{TeV}^{0.3-0.6} t_{yr}$; the exponent on the energy reflects the particular magnetic field structure and diffusion regime (this case the Bohm regime) adopted for the CR propagation model [199]. An interesting image of this evolving and extended character of cosmic ray sources was provided by H.E.S.S. in a spatially and spectrally resolved image of the pulsar-wind nebula RX J1825-137 [25]. Radiation losses are another important way in which the morphology of the sources will be influenced, but this will be discussed in Chapter 3.

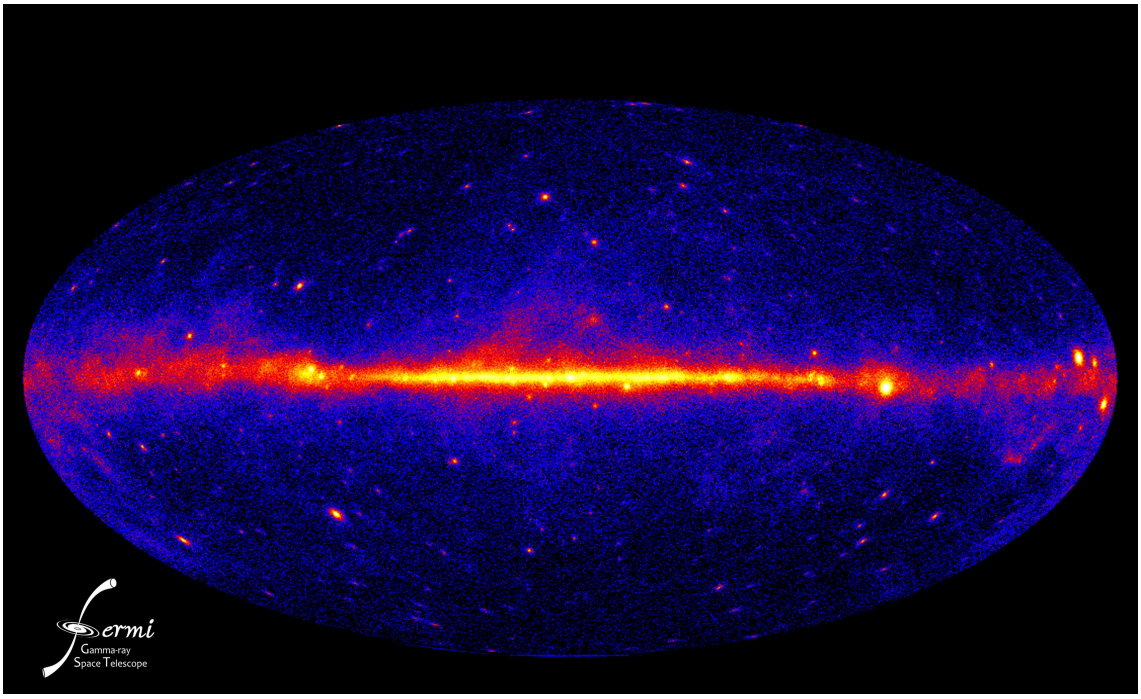

Figure 1.3: Fermi-LAT one-year all sky map showing the dominance of diffuse gamma-ray emission in the Galaxy. Credits: Fermi/LAT Collaboration.

1.2.4 Diffuse Gamma-ray Emission

As is apparent from Figure 1.3, the most prominent feature in the gamma-ray sky at GeV energies is the diffuse emission fom the Milky Way. The diffuse gamma-ray flux reflects the diffusive nature of the cosmic ray distribution and propagation in the Galaxy, which will interact with the molecular clouds present in the Galactic plane and produce gamma-rays by proton-nucleon interactions (see Section 3.3). In fact, the detailed study of this extended emission component is important to constrain the cosmic ray spectrum in distant parts of the Galaxy and near the sources, since the spectrum observed at Earth suffers from propagation and diffusion-related energy losses, which are believed to explain (at least in part) the difference between the predicted energy spectrum from shock acceleration theory (energy index ~ -2 – see Chapter 3) and the observed spectrum, with index ~ -2.7.

Before *Fermi*, the *EGRET* instrument onboard the *Compton Gamma-ray Observatory* (CGRO) had measured an excess gamma-ray flux at 1 GeV, for which likely explanations included a non-uniform cosmic-ray spectrum in the Galaxy or contribution from nearby high-energy electrons [27]. At TeV energies, the gamma-ray sky is dominated by individual sources, except for the Cygnus region in the galactic disc, between $l = 30^\circ - 90^\circ$,

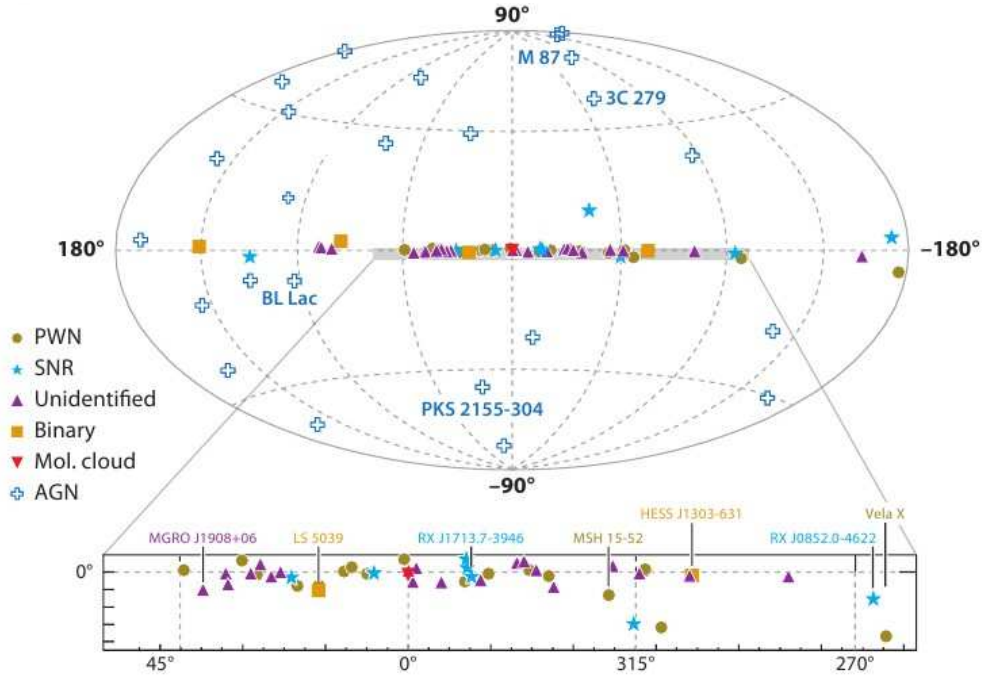

Figure 1.4: The VHE gamma-ray sky as of 2009, indicating some of the most important Galactic and extragalactic sources and with coded information on the source categories (see Table 1.1 for a complete census of VHE source cathegories. From [199]

where the *Milagro* experiment [268] has measured the presence of some diffuse emission at a level $(6.8 \pm 1.5 \pm 2.2) \times 10^{-11}\text{cm}^{-2}\text{s}^{-1}\text{sr}^{-1}$, shown to be compatible with a differential spectral index from GeV-TeV of 2.61 ± 0.03 in energy. The H.E.S.S. Galactic plane survey has also detected point source emission near the position of the Galactic centre source Sagittarius A* [23], accompanied by a diffuse extension, which seems correlated with that of the molecular clouds (MC) in the region, corroborating the hypothesis made earlier of the interaction of relativistic particles with the interstellar medium as the origin of the diffuse VHE γ-rays.

1.3 Sources of VHE gamma-rays

In the last decade, thanks to the activities of the new generation of imaging Cherenkov experiments, astronomy in VHE gamma-rays has greatly expanded in its breadth and scientific impact, solidly establishing itself as a branch of observational astrophysics and revealing a universe which is abundant in environments capable of accelerating particles to extreme energies. The study of the sky at VHE energies is now recognised to be funda-

Category	Number	First Exemplar	Year of first discovery	Discoverer
Blazars	31	Mkn 421	1992	Whipple
PWN	28	Crab	1989	Whipple
SNR	13	SN 1006	1998	CANGAROO
X-ray bin.	04	LS 5039	2005	H.E.S.S.
Quasars	03	3C279	2008	MAGIC
Wolf-Rayets	03	Westerlund 2	2007	H.E.S.S.
Radio Galaxy	02	M87	2003	HEGRA
Starburst	02	NGC 253	2009	H.E.S.S.
Dark sources	01	J1503-582	2008	H.E.S.S.
Unidentified	35	–	–	–

Table 1.1: Complete census of VHE sources as of September 2010. Data collected from TeVCat (tevcat.uchicago.edu).

mental for the understanding of a wealth of sources, members of a wide cross section of different classes of astrophysical objects. Greater typological diversity is found amongst the Galactic population, where compact objects, binary systems and massive stars at late evolutionary stages figure as the primary sites of VHE emission. However, the current (c. Sept. 2010 – see Table 1.1 and Figure 1.4) source list extends to over 30 extragalactic objects, almost all AGNs, of which the majority are blazars. Two recent additions to this list are the starburst galaxies (NGC 253 [3] and M 82 [342]), the emission from which is believed to originate from the combined activity of a large number of supernovae which give rise to a large density of CR particles in their central regions ($\sim 10^3\times$ the average Milky Way density), making this an important result in connection with the origin of cosmic rays.

Relativistic outflows are the environment of extreme physics *par excellence*, being the locus of the observed multi-TeV particle acceleration in a number of the detected objects. The rapidly populating TeV sky today (see an updated version of Kifune's plot in Figure 1.5) numbers over 100 detected sources[3]. In contrast to the picture of the sky at GeV energies, the TeV sky is dominated by individual sources, rather than diffuse emission, and this fact is most clearly seen by comparing the images of the Galactic plane taken at both these energies by *Fermi* and H.E.S.S. (Figures 1.3 and 1.6).

[3]A regularly updated and comprehensive catalogue of VHE sources maintained by S. Wakely And D. Horan of the University of Chicago can be found at http://tevcat.uchicago.edu/. Website last accessed in September 10, 2010.

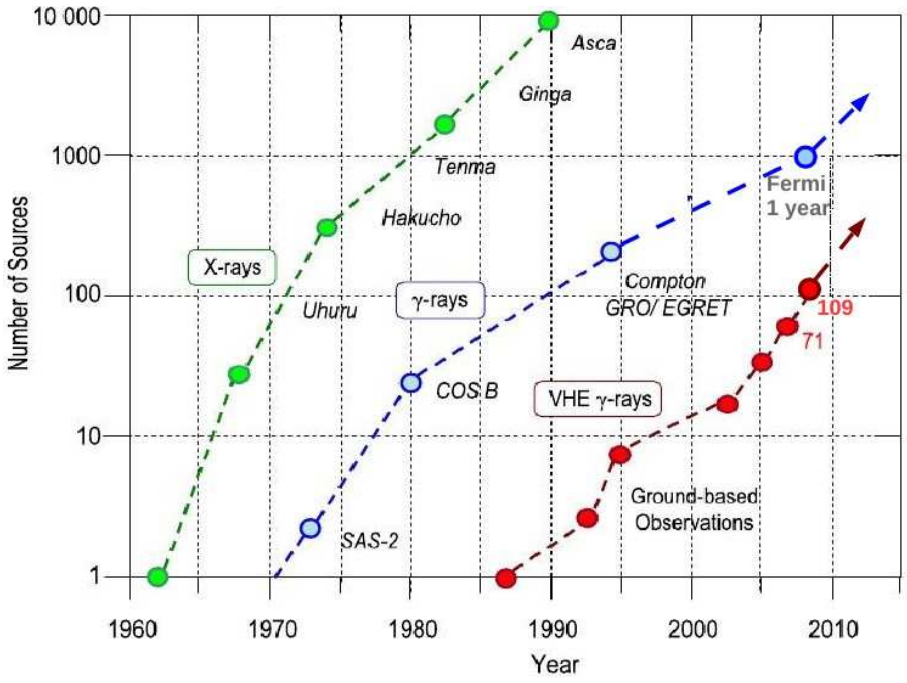

Figure 1.5: Kifune's plot: evolution of the number of sources detected in different domains of high-energy astrophysics showing the progress brought by the different instruments in history. Adapted from a plot by J. Hinton, 2007.

In fact, the Galactic plane scan performed by the H.E.S.S. collaboration (Aharonian et al. 2005 [16] and Aharonian et al. 2006 [22]) stands as one of the most important results of the field, revealing a number of Galactic sources among which almost half of the total of c. 60 objects have no clearly identified counterpart in other energy domains. In several cases, dedicated follow-ups at radio and X-ray energies were performed with no successful identification of lower-energy counterparts, earning such objects the name of "dark accelerators". The lack of synchrotron counterparts to these unidentified sources is a challenge for leptonic scenarios and suggests that the γ-ray emission might be produced by hadrons. This poses a further question on the nature of these objects, since other Galactic sources with known counterparts all have their low-energy emission attributed to leptonic synchrotron processes rather than protons. Of course, some of these "dark sources" have in time had their counterparts identified, and most of these were shown to belong to the classes of pulsar-wind-nebulae (PWN) or supernova remnants (SNR), and it is possible that some of the remaining unidentified systems will still be assigned to these categories of objects. In fact, aged nebulae are still able to emit γ-rays via inverse-Compton scattering of the background radiation but have a very weak synchrotron flux

due to their expanded character. Source confusion can also play an important role in obscuring the immediate detection of counterparts.

Supernovae remnants, the favoured sources of Galactic cosmic rays of energies up to the knee of the CR spectrum and maybe beyond (10^{15-17} GeV) are one of the most abundant amongst the VHE Galactic sources, and part of the task of gamma-ray observations (and one that has not yet been achieved) is to try to decide between the leptonic/hadronic origin of its emission. Given their kinetic energy (K.E.) output of 10^{51} erg s^{-1} per explosion and the estimated rate of 2-3 SN per 100 years, a conversion rate of 10% of K.E. is enough to supply the energetics of the observed local cosmic ray spectrum. The detection by H.E.S.S. of the SNR RXJ 1713.7-3946 [21] allowed for the first spatial and energy resolved map of any source in VHEs. In some of these sources (such as W28 [30]), interaction of the radiation from the SNR with the surrounding molecular gas produces TeV emission further away from the particle acceleration sites by pair-cascading. VHE gamma-ray emission from extragalactic SNRs is believed to have been detected in the starburst galaxies M82 and NGC 253, as mentioned before.

Pulsar-wind nebulae (PWN) are the most numerous amongst the celestial emitters of VHE gamma-rays. The intensity of emission of some of these sources is attested by the first detected VHE source in history, the Crab Nebula, which is also used as a standard candle throughout the gamma-ray energy range (see [19] and [146]) due to its high and steady flux[4]. The emission mechanism in the case of PWN is the interaction of the pulsar wind with the surrounding material, which creates shock waves capable of accelerating particles to high energies, with a nonthermal power law spectrum. One of the most interesting recent results on the study of these objects is the discovery by the MAGIC telescope of the first pulsed emission above 25 GeV (from the Crab pulsar [43]), showing that the pulsar itself is able to generate emission, and helping to distinguish between

[4]Note that a significant (at the 9σ confidence level) enhancement on the MeV-GeV gamma-ray flux from the Crab Nebula of about 2.5 × was registered by the *AGILE* and *Fermi* satellites between 18-22 September, 2010 (Atels 2855 and 2856). Phase-resolved analysis of the *Fermi* signal showed the enhanced emission to have no pulsed component (Atel 2893) and no indication of an increase in flux was registered on any other wavebands. The Fermi flux was seen to return to its previous level on the 23 September (Atel 2861). Follow-up imaging by Chandra (Atel 2882) and HST (Atel 2903) both noticed an increased emission about 3" East of the pulsar, with bright features seen present also at the wisps north-west of the pulsar. Given that this event happened contemporaneously to the epoch of submission of this work, no detailed information or interpretation of the flaring emission was yet available.

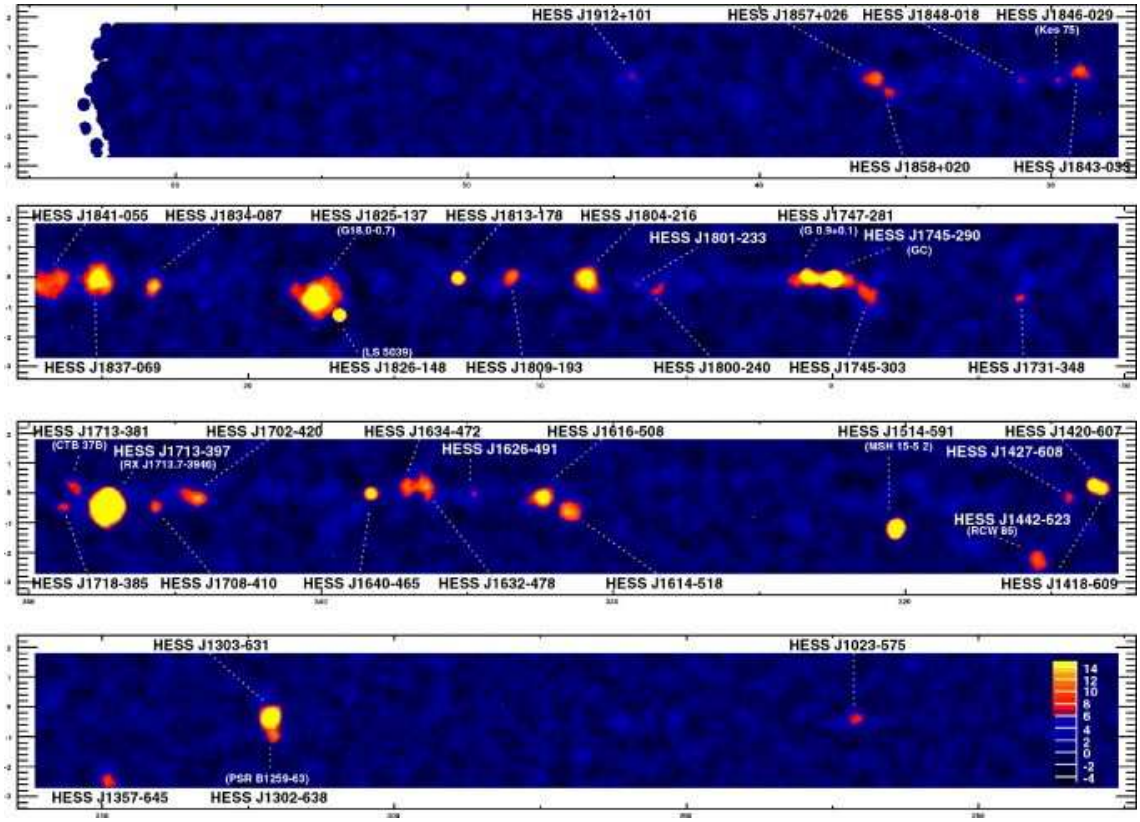

Figure 1.6: The H.E.S.S. Galactic plane scan. Credits: The H.E.S.S. collaboration [16] and [22].

competing models of γ-ray production from the pulsar's magnetosphere. Signals from distant pulsars are also expected to be detectable at VHE gamma-rays: in the same way that starburst galaxies represent a good environment for intense SN explosions, the large demography of pulsars within (old) globular clusters makes then a potential and interesting source of VHE gamma-rays, as shown by H.E.S.S. [34] and *Fermi* observations of 47 Tucanae [143].

LS 5039 [17] and PSR B1259-63 [18] are the only two variable galactic TeV sources detected by H.E.S.S. unambiguously associated with compact binary systems. Another such source, LSI +61° 303, was also detected by the MAGIC telescope [38], and the three systems might differ in the nature of the compact object [64]. Whereas PSR B1259-63 is known to be a "binary plerion", LSI +61° 303 is the first example of a γ-ray emitting microquasar. The case of LS 5039 is interesting, since it is debatable if here it is a spinning neutron star or a black hole that is orbiting the massive companion. These two possibilities leave the interpretation open as to whether the TeV emission results from pulsar wind interaction as in PSR B1259-63 or if it is the product of accretion, and we are again seeing

observational evidence of TeV emission from microquasars, as for LSI +61° 303. In the latter scenario, emission would come from relativistic jets of particles emanating from the BH-accretion disc system in an analagous (albeit scaled-down) way to what happens in active galaxies, making the study of these objects a very interesting parallel to the main subject of this thesis [270].

In addition to Galactic sources, H.E.S.S. and other contemporaneous VHE instruments have produced a wealth of important results on extragalactic sources, which will be the main subject of this work and whose detailed discussion will be therefore postponed to Chapter 4. The application of VHE observations to the study of new physical theories such as violation of Lorentz invariance, quantum-gravity and dark matter models is another active line of investigation in the field. Lorentz invariance violation (LIV) and tests of quantum-gravity (QG) theories will be discussed in Chapter 5.

Chapter 2

Observational Techniques

In this Chapter we will discuss the observational techniques relevant to this work. The Chapter is divided into two main sections: the first dealing with observational techniques in ground-based gamma-ray astronomy, and the second with general aspects related to polarisation of radiation and the analysis of polarimetric observations in optical astronomy. In both parts all the principles necessary for the understanding of the data analysis steps used in this work are discussed in detail, so that the reader can grasp the significance and meaning of the results obtained. We will nevertheless exclude from the discussion any software-related reduction technicalities as well as extensive presentation of the intermediary steps of the process of data analysis, the presentation of which, when necessary, will be deferred to later chapters

2.1 Observational Techniques I: VHE Gamma-ray Astronomy

The first measurements of Cherenkov radiation from cosmic-ray muons were made in the early 1950's using a distilled water-detector at the Harwell Atomic Energy Research Establishment, in Berkshire, UK, by J.V. Jelley [212]. Concurrently, observational activities had recently started at the Jodrell Bank observatory, where one of the main scientific goals was the detection of radio signals from fast air-shower particles [349], sowing the first seeds of a ground-based cosmic-ray and gamma-ray astronomy.

The development of high-energy astrophysics as an observational science first progressed, nevertheless, with a few rocket experiments in the 1960's, which continued into the 1970's with the High Energy Astronomical Observatory (HEAO) and in particular HEAO-2 (a.k.a. *Einstein Observatory*), which performed the first all-sky surveys in X-rays. High-energy astronomy found a greater pace of advancements in the 1990's with the first major gamma-ray all-sky survey instrument, the *Compton Gamma-Ray Observatory* (CGRO), launched in 1990 and operational for 10 years. The CGRO was the first to explore the gamma-ray sky at such high-energies, having had four instruments which covered six orders of magnitude in energy: from 30 keV to 30 GeV in total. In addition to the *Burst and Transient Source Experiment* (BATSE), mainly oriented to the all-sky monitoring for the search of gamma-ray bursts (GRBs), and which proved their extragalactic origin, a work to which the Italian instrument BeppoSAX also greatly contributed, the Compton Observatory had other two "low energy" instruments (OSSE and COMPTEL), and one high energy detector, operating between 30 MeV and 30 GeV. The latter, named *Energetic Gamma-ray Experiment Telescope* (EGRET), was extremely important for the development of high-energy extragalactic astrophysics, with the discovery of the powerful γ-ray luminosity of blazars, having catalogued over 60 such sources plus detecting GeV emission from the radio galaxy Centaurus A [97].

The *Fermi* satellite (Figure 2.1), launched in June 2008, is the successor GeV and GRB gamma-ray mission to CGRO; operational in the band from 10 MeV to 300 GeV, it gives continuity and further expansion into higher energies of the activities of EGRET and BATSE. Its high-energy capability well into the GeV-range also has the advantage of allowing some spectral overlap with the ground-based observations. The *Large Area Telescope* (LAT) operates between 20 MeV and 300 GeV, with a peak effective detector area of $\sim$ 8000 cm^2 at an energy of $\sim$ 1 GeV, and a FOV $\sim$ 2 sr. The detector is made of segmented 20-cm CsI bars which work as calorimeters and are arranged to give both longitudinal and transverse information about the energy deposition of a γ-ray penetrating the scintillator detector.

After its first year, *Fermi* has produced an all-sky LAT catalogue [149] and a dedicated catalogue of bright AGNs [150]. Dedicated variability [151] and spectral [148] studies of LAT blazars have also been published, with a special view of mis-aligned AGNs [147].

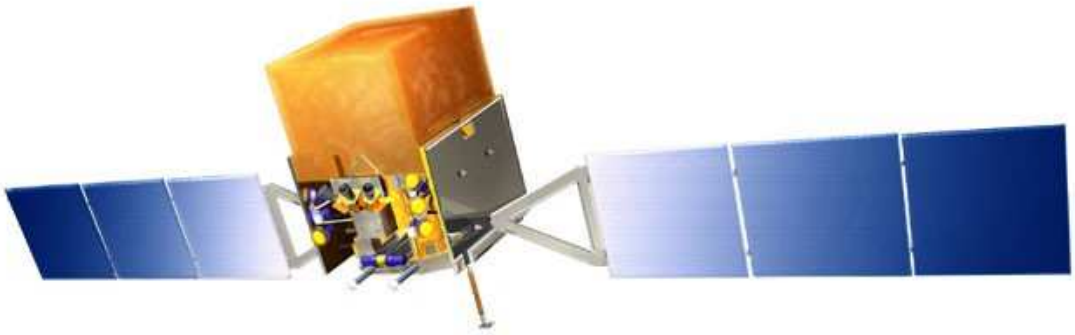

Figure 2.1: Schematic design of the Fermi gamma-ray satellite. Credits: NASA Goddard Space Flight Centre.

2.1.1 Electromagnetic Showers and Cherenkov Radiation in the Atmosphere

When we move further in energy scale, from the GeV to the TeV domain, satellite-based experiments such as *Fermi* are of no more use, due to the extremely low photon fluxes at these energies, i.e. $O(10^{-11})$ photons per cm^2 per sec, which require large collection areas – in contrast to the very limited detector sizes of satellites, in practice limited to ~ 1 m^2. This difficulty is circumvented by the advent of ground-based instruments, which use the Earth's atmosphere as a detection medium[1] and therefore can enjoy a very large effective collection area of hundreds of m^2. The ground-based detection of gamma-ray photons is actually an indirect process, given that these highly energetic photons cannot penetrate the atmosphere, but get absorbed by it. Fortuitiously, due to their extreme energies, the

[1] In ground-based gamma-ray astronomy the atmosphere works essentially as a calorimeter, where the incident gamma-ray (or equivalently, a charged cosmic ray particle) deposits its energy through the interaction with molecules of the air.

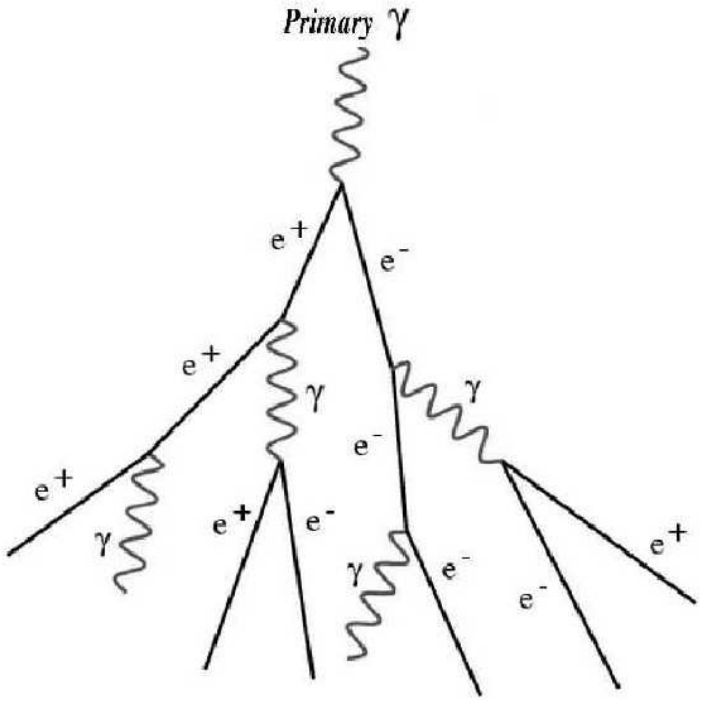

Figure 2.2: Schematic development of an electromagentic shower in the atmosphere. From [278].

gamma-ray's interaction with the atmosphere produces a cascade of secondary particles and radiation that can be detected from the ground and used to infer (not without much ingenuity) the primary photon's properties.

Upon entrance in the atmosphere, gamma-ray photons ($E > 2m_e c^2$) will interact in the electric field of an atom to create an $e^{\pm}$-pair, which will in turn lose energy radiatively via bremsstrahlung emission of secondary gamma-rays. The characteristic distance scale for these interactions is called the radiation length X_0 (dependent on the composition of the medium, and for the atmosphere equal to ~ 37.1 g/cm^2) and is defined as the distance over which the secondary electron's energy falls to $1/e$ of its initial kinetic energy. The altitude of first interaction in the atmosphere is governed by this parameter, and varies statistically. For a 0.1 TeV photon, the altitude of first interaction is typically $\sim$ 20 km a.s.l. (see Figure 5 in [27]). The radiation length is very similar (to $\sim$ 8 parts in 10) to the mean free path for pair creation in the same medium, so X_0 can be thought of as the "fundamental" interaction scale for the electromagnetic shower development. The term "electromagnetic shower" arises because approximately after each X_0 crossed by either the electron or the photon one of the two processes happen:

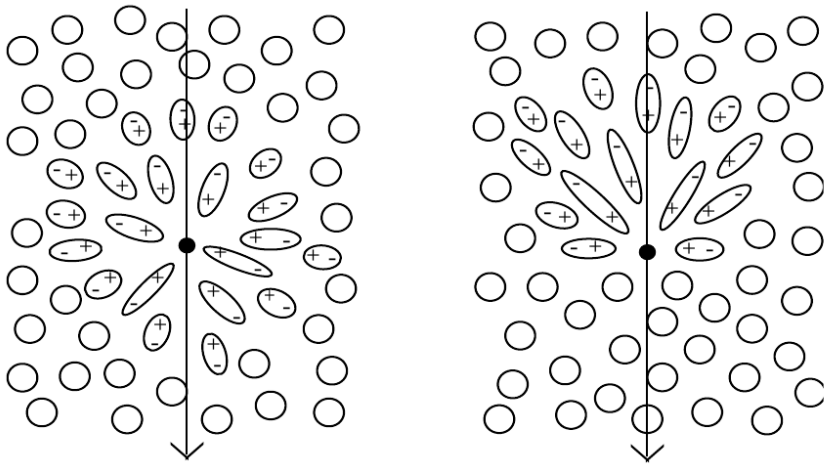

Figure 2.3: Illustration of the effects of charged particles moving through a dielectric medium, first with a velocity v slower than the phase velocity of light c/n (*left panel*) and then with $v > c/n$ (*right panel*). Credits: [278].

$$\begin{cases} \gamma \xrightarrow{\frac{7}{9}X_0} e^- + e^+ \\ e^- \xrightarrow{X_0} e^- + \gamma \end{cases} \tag{2.1}$$

generating a cascade of energetic leptons and electromagnetic radiation which will propagate and grow in multiplicity (see Figure 2.2) until energy losses are such that new pairs can no longer be created [163]. The precise point when this happens is when the cross section for the ionization losses (which now becomes the dominant interaction process) exceeds that for bremsstrahlung ($\propto ln(E)/E$, where $E = \gamma m_e c^2$), which in the atmosphere happens for an energy of O(GeV).

The secondary electrons and positrons composing the cascade will be very energetic and will therefore propagate through the atmosphere at relativistic speeds. If this speed v is superior to the phase velocity of light in the medium c/n, it will create an electromagnetic perturbation akin to a shock wave in the case of supersonic motion in a material medium [153] (see Figure 2.4), which will propagate away from the shower and can be detected at the ground. This radiation phenomenon is called Cherenkov radiation, after the physicist who explained the effect [104], and will be emitted as long as the Lorentz factor of the particle is $\gamma > \gamma_0 = n/\sqrt{n^2 - 1}$.

The mechanism by which the electromagnetic shock wave develops due to the superluminal propagation of a particle in matter can be described in terms of the dielectric

properties of the medium, and is illustrated in Figure 2.3 [350]. When a charged particle traverses a dielectric medium of refractive index n, it disturbs the EM field of its constitutent atoms, causing polarisation of the material about the particle's trajectory. After the particle's passage, the medium relaxes by emission of photons, whose geometry is described by the left panel of Figure 2.4. If the particle is moving very rapidly, the geometrical arrangement of the wavefronts of the EM perturbation will have a conical shape characteristic of shock fronts, where constructive interference of the waves happens. The emission formula of Cherenkov radiation is, according to Frank & Tamm 1937 [157],

$$\frac{dE}{dt} = \frac{e^2}{c^2} \int \sin^2 \theta d\theta \, \omega d\omega, \tag{2.2}$$

where the analogy with the medium radiating as a dipole is clear both from the e^2-dependency of the intensity and the angular distribution of the power as $\sin^2 \theta d\theta$. The final term $\omega d\omega$ gives the spectral dependency of the radiation and results from the δ-distribution (in the time domain) of the radiation as seen by the observer, which in the frequency domain has a uniform function as its Fourier transformation. It is important to note that the Cherenkov radiation is emitted by the *medium* during its relaxation, and that the energy of an optical Cherenkov photon, compared with the $\sim$ MeV energies of the particle is negligible, and therefore does not contribute as a significant energy-loss channel during the shower's development.

The dependence of the Cherenkov emitted power (Equation 2.2) on the refractive index of the medium, n, means that there is a particular threshold of energy below which no radiation is emitted by the medium; for the air, $n \simeq 1.0003$ and the limit on the Lorentz factor for Cherenkov emission $\gamma_{min} = 1/\sqrt{1-\beta^2}$ is:

$$\gamma_{min} \sim \frac{1}{\sqrt{2(n-1)}} \sim 50, \tag{2.3}$$

which corresponds to the condition $\beta_{min} = 1/n$ and has a geometrical interpretation according to Figure 2.4 in the expression for the half-angle of the Chrenkov cone $\theta = \cos^{-1}(1/\beta n)$. In energy terms, this threshold corresponds to $E_{min} = \gamma_{min} m_e c^2 \approx 44$ MeV for an electron at 10 km above sea level [27], since n is a function of the altitude in the atmosphere, and increases with depth. The spectrum of Cherenkov radiation is given by

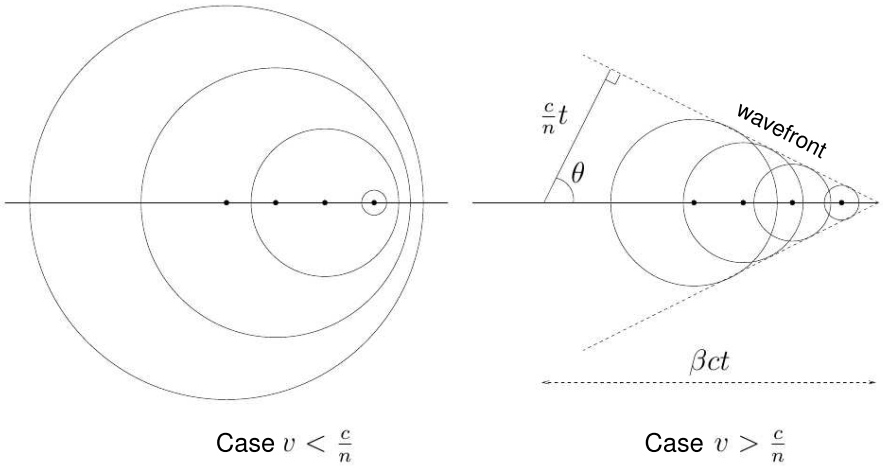

Figure 2.4: Propagation of wavefronts generated by a particle of velocity v in a material medium. For $v > c/n$, a shock wave will develop due to constructive interference of the perturbations in the medium, which will form a cone with apex at the source and half-angle $\theta = \cos^{-1} 1/\beta n$. Figure adapted from [239].

the Frank-Tamm relation [157] and is strongly peaked at short wavelengths (UV-blue):

$$\frac{d^2N}{dx\,d\lambda} = \frac{2\pi\alpha}{\lambda^2}\sin^2\theta, \tag{2.4}$$

where $\alpha = 1/137$ is the fine structure constant. Figure 2.5 shows the Cherenkov spectrum given by Equation 2.4 for a single particle. Although it extends with ever lower intensity towards longer-wavelengths, in the high energy side the spectrum abruptly cuts-off at the UV range because beyond it Frank-Tamm's formula cannot be satisfied, *viz.* the refractive index for the X-rays becomes less than unity and no radiation is emitted.

Because the UV light is absorbed during its propagation in the atmosphere (atmospheric attenuation follows the Rayleigh relation and is $\propto 1/\lambda^4$), Cherenkov light peaks at the blue range of the visible spectrum, and can therefore be ideally detected with ordinary optics. Frank-Tamm's equation also gives the number of Cherenkov photons per unit path-length dx. For small Cherenkov angles, $\sin\theta \approx \theta$, and integrating $\lambda^{-2}d\lambda$ about the peak emission (280nm to 640 nm), we arrive at $dN/dx \sim 780\,(n-1)$, which corresponds to ≈ 30 photons/m [350]. Multiplying this number by the *total path length* of the shower particles, which is of the order of $\sim 10^5$ cm, we estimate that the total number of Cherenkov photons detected at ground level over the entire area of the shower of $\sim 10^{4-5}$ m^2 will be $\sim 10^7$.

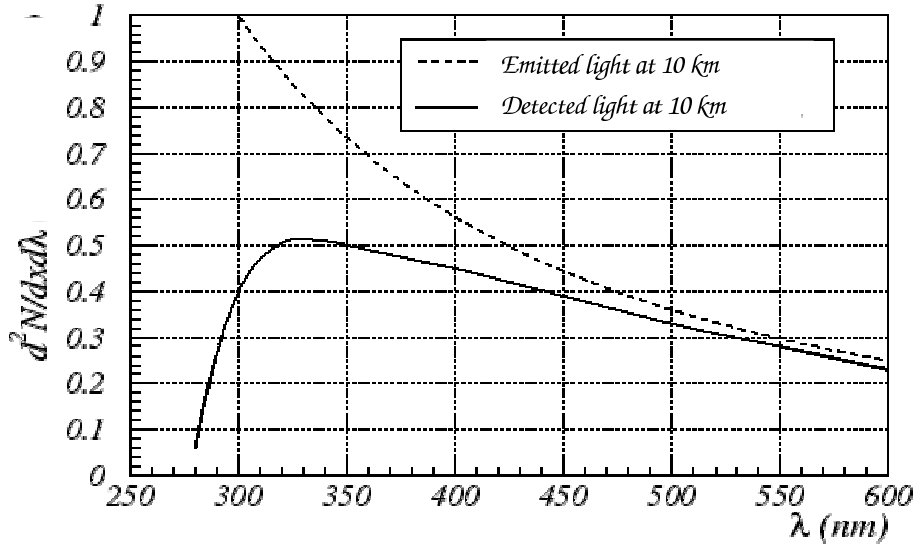

Figure 2.5: Differential Cherenkov photon spectrum. Credits: E.O. Whilhelmi (adapted).

.

Cherenkov image of extensive air-showers

As for the Cherenkov images of extensive air-showers (EAS), we have first to consider their *duration*. This is a simple estimate to derive, and the main thing to observe is that due to the low refractive index of air, the speed of the emitted photons will not differ much from that of the energetic particles, and so all (non-absorbed) photons emitted by a shower during its development will arrive at ground level within a short pulse, of width:

$$\Delta t = \frac{d}{c}\left(\frac{n-1}{n}\right) \sim \text{ns}, \tag{2.5}$$

where d is the total path-length over which photons are emitted, $\sim 8 - 10$ km [278]. It is important to notice that the shape of the pulse front along the lightpool's extent is not plane parallel, but curved: in the centre, near the position of the shower's core, it is of the order of ns, whereas at the borders it can spread up to $\sim$ 100 ns, a difference which is relevant to the triggering conditions used in the observations. This is due to the lateral spread and Cherenkov emission from particles distant from the shower axis. The lateral spread of the shower is determined by the multiple Coulomb scatterings suffered by the particles, which was described by Molière. The lateral distribution for EM showers is inversely proportional to the particle's energy and scales with a quantity known as the Molière radius, which at its maximum is $\approx$ 200 m and corresponds to the radius around

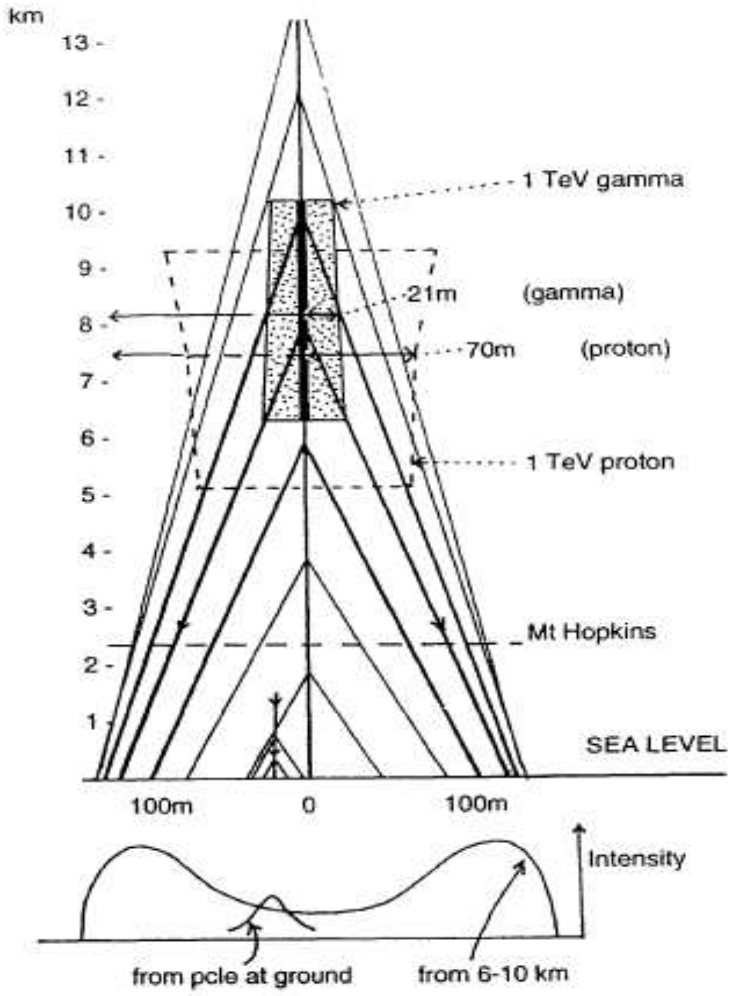

Figure 2.6: Illustration of the focusing effect of the varying Cherenkov angle $\theta(n)$ with altitude on the lateral light pool density distribution. Credits: M. Hillas [196].

.

the shower axis within which 90% of the secondary particles are concentrated.

Now, this lateral spread of the Cherenkov light pool can be characterised by the Cherenkov angle θ, which for a 0.3 TeV gamma-ray primary (or rather its secondary pairs from first interaction, each with approximately half the primary's energy content), is $\approx 1^\circ$ [27]. Light generated at a given height h, with angle $\theta = \sqrt{2(n-1)}$, will propagate away from the shower axis where most particles are concentrated. Noticing that the index of refraction of the atmosphere is a function of the height according to an exponential density profile [27], $n = n_o \exp(-h/h_o)$, we have that the distance r from the axis at which photons reach the ground is [213]:

$$r = h\sqrt{(n-1)}\exp(-h/h_o). \tag{2.6}$$

Here h_0 is the height at which the emission will contribute to the maximum radius of the Cherenkov lightpool at ground level (see Figure 2.6), also roughly coincident with the height of maximum of the shower development (i.e. where we have the greatest multiplicity of secondary particles in the shower[2]) and is of the order of $6-8$ km. The corresponding radius of the Cherenkov light pool at the ground for maximum development height (and $\theta \sim 1^\circ$) is thus ~ 120 m [278], and the shape of the light pool is shown in Figure 2.6. Observe the presence of a ring of maximum flux near the outside border of the pool, which is formed by a "fortuitious" focusing effect due to the gradual increase of n towards lower altitudes in the atmosphere, as mentioned previously; this focusing effect for the emitted Cherenkov light is described according to Equation 2.6 [27].

The plateau emission closer to the shower axis is generated by the particles nearer to the ground, when the shower is already dying out. Beyond the ring, the radial distribution of light falls as $1/r^2$, and is due to the few secondary electrons that suffer large (multiple) Coulomb deflections during their path, according to Molière's theory. It is this relatively large size of the Cherenkov pool of a few 100 m that will determine the typical spacing of the arrays of Cherenkov telescopes used in stereoscopic experiments, such as H.E.S.S.

2.1.2 Imaging Atmospheric Cherenkov Telescopes

Brief history of Cherenkov observatories

Although the first search for Cherenkov radiation from the atmosphere was made in 1954 with a prototype telescope developed by Jelley & Galbraith [214], the first serious theoretical proposal for the existence of *astrophysical sources* of TeV gamma-rays came with Cocconi in 1959 [105], following P. Morrison's suggestion of high-energy cosmic-ray production in the Crab Nebula [274]. In fact, the first operating TeV gamma-ray experiment shortly followed, built in the Crimea by Chudakov and collaborators at the Lebedev

[2]Maximum shower development is reached at about $\sim$ 6-8 km a.s.l. for the range 0.1-10 TeV photon energy (see Figure 4 and Equation 11 of [27]). The maximum number of secondary particles eventually reached by the shower at its maximum development is $\sim 10^5$, before decaying away due to energy losses.

Instrument	Lat. [°]	Long. [°]	Altitude [m]	Tels.	Area [m^2]	Pixels	FOV [°]	Thresh. [TeV]	Sens. [% Crab]
HESS	-23	16	1800	4	428	960	5	0.1	0.7
MAGIC-II	29	18	2225	2	468	574	3.5	0.04	1
VERITAS	32	-111	1275	4	424	499	3.5	0.1	1

Table 2.1: Properties of current-generation air-Cherenkov telescopes. Adapted from [199]. Information on MAGIC-II is from [96] and sensitivity information is for 50 hrs integration times.

Institute. The first successful purpose-built instrument for gamma-ray astronomy was the Whipple observatory [98], consisting of a 10-m Cherenkov telescope, fitted originally with a camera of only 7 photomultiplier tubes (now upgraded to 337) constructed in 1968, and still in operation. The Whipple observatory was responsible for the first detection of VHE gamma-rays from the Crab Nebula in 1989 [351]. The first extragalactic object discovered at VHE was the blazar Mkn 421, also using the Whipple telescope, in 1992 [294].

The second generation of instruments followed in the 90's with telescopes responsible for pioneering the technical developments which would eventually allow the field to reach its maturity. The University of Durham Mark 6 telescope [53], located in Narrabri, Australia, could provide with three independent image samples of the Cherenkov light, thus allowing for a lower energy threshold to be attained. The French collaboration *Cherenkov Array at Themis* (CAT) operated a small, $\sim$ 20 m^2 reflector, but with a 558-pixel camera, thus providing the first high-resolution image of the atmospheric showers; the French group was also responsible for pioneering the fast-electronics cameras that are used today in the field. At the same time, the collaboration *High Energy Gamma-ray Astronomy* (HEGRA) took the stereoscopic technique (then recently developed) to its full potential, by combining multiple telescopes at the Canary Islands.

The third and current generation of Cherenkov instruments combine the advances obtained with high-speed cameras, multiple pixels, large mirror areas and stereoscopy, and is represented by three major experiments, the main characteristics of which are given in Table 2.1:

- **High Energy Stereoscopic System** (H.E.S.S.): constituted of four 13-m diameter imaging atmospheric Cherenkov telescopes (IACTs) and which is described in detail in the next section;

Figure 2.7: The H.E.S.S. telescopes. Credit: H.E.S.S. Collaboration.

.

- **Major Atmospheric Gamma-ray Imaging Cherenkov** (MAGIC): located in the Canary Islands, operating two 17-m diameter telescopes, whose large sizes allow for a very low energy threshold, < 100 GeV;
- **Very Energetic Radiation Imaging Telescope Array System** (VERITAS): located in the desert of Arizona, is a successor to the Whipple Telescope, consisting of four telescopes of similar diameter and properties to H.E.S.S.

H.E.S.S.

Most modern IACTs use multiple telescopes. This is so that the Cherenkov images of the air shower can be made from different viewing angles so as to improve the reconstruction of γ-ray direction and rejection of the CR background (see Section 2.1.3). The properties of the IACT array are dictated by the properties of the Cherenkov light development and shape of the pool at ground, which will provide the constraints not only for the choice of site (the optimal altitude a.s.l. $\sim$ 2000 m for energies around 1 TeV) but also for the separation and arrangement of the array's instruments.

The High Energy Stereoscopic System (H.E.S.S.) consists of four 13 m diameter telescopes which work together for simultaneous imaging of the showers (i.e. stereoscopically). It is located in the Khomas Highlands of Namibia, by the Gamsberg plateau, at

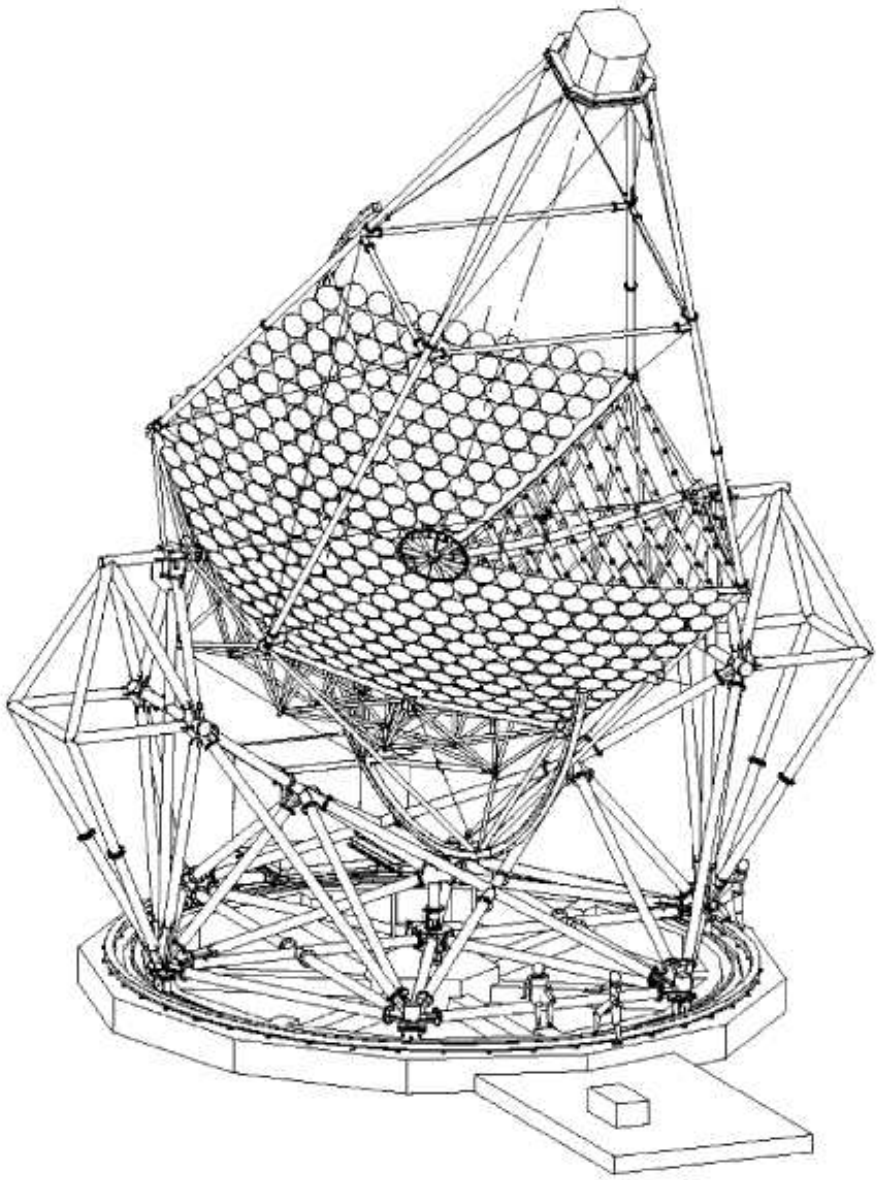

Figure 2.8: Structure of one of the individual H.E.S.S. telescopes [80].

.

an altitude of 1800 m a.s.l. and geographical coordinates 23°16′18″ S and 16°30′00″ E (Figure 2.7). The four telescopes which make up the array are positioned at the vertices of a square with sides of 120 m and diagonals aligned with the North-South/East-West axes. The dimensions of the array are such as to optimise the detectors' response at an energy threshold of 100 GeV.

Each individual telescope is built according to a Davies-Cotton design [120], so as to optimise the off-axis performance at the same time as maximising the field of view

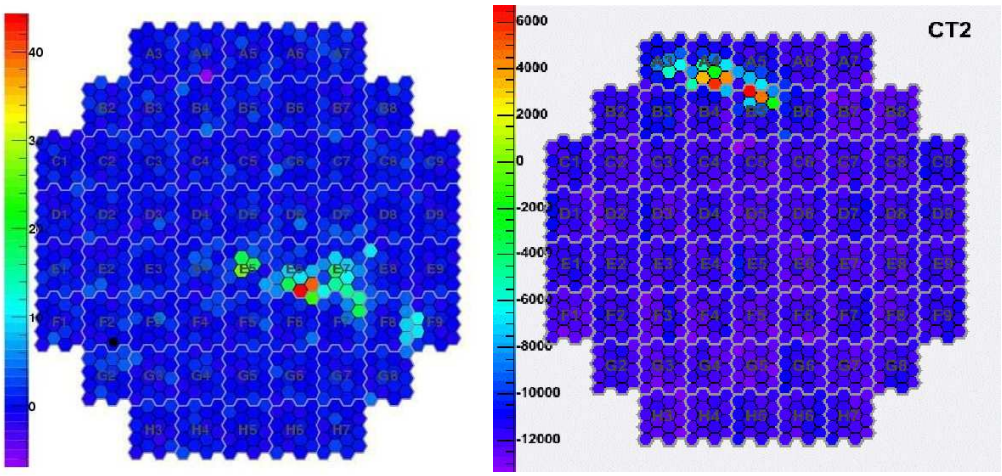

Figure 2.9: The shapes of Cherenkov images of true air-shower events as observed with the H.E.S.S. camera. Notice the marked disparity between the form of the event on the left, characteristic of a hadron-initiated shower and the elliptical image on the right, of a candidate γ-initiated event. Credits: H.E.S.S. Collaboration.

.

(FOV), which is of $\sim 5^\circ$ [80] (see Figure 2.8). The reflecting component is formed by a 13-m tesselated mirror arrangement, consisting of 380 round facets of 60 cm diameter each, mounted onto a spherical dish structure with radius of curvature of 30 m. The focal length of each individual mirror element is 15 m. The typical angular extent of a Cherenkov shower image is $\sim 2-3^\circ$ length and can be easily encompassed by each individual camera; in terms of source size, the 5° FOV is enough to grasp in their entirety most nearby extended sources such as supernova remnants.

The telescopes are equipped with ultra-fast cameras, each composed of 960 photomultiplier tubes (PMTs); each pixel of the camera subtends therefore $\sim 0.16^\circ$ in the sky plane, allowing for good image quality for the observation of the Cherenkov images (see Figure 2.9). The photomultiplier tubes are fitted with hexagonal *Winston Cones* [355], which are reflective elements that focus light onto the PMTs. The deadtime of the electronics readout is of 446 μs for a γ-like event which succesfully triggers the entire array[3], which requires positive detection by at least two individual telescopes over an integration window of 80 ns.

The first level trigger of the system is the *pixel trigger*, which requires a minimum

[3]This time is short compared to the times between events for typical, sub-Crab gamma-ray fluxes, with photon rates under 1 Hz

signal of typically 5-6 photoelectrons (p.e.) within a window of 1.3 ns, and is followed by the second level trigger (the *camera trigger*). Individual camera trigger conditions require that at least 3 out of a 64-adjacent pixel region register a minimum p.e. signal before the central trigger of the telescope system is activated. This is done by requiring coincidence signals of at least two telescopes in a window of about $\sim$ 80 ns to account for the different paths of the shower front to reach different telescopes of the array. The details of the trigger system are given by Funk et al. 2004 [161].

The effective collecting area of the H.E.S.S. array varies as a function of energy, and knowledge of A_{eff} is necessary in order to convert the observed rate of γ-like events into fiducial source flux units. A_{eff} can be calculated by simulating the detection of N_γ γ-ray events randomly distributed within a large area A_0 about the array (e.g., a circle of diameter > 500 m). We then have [118]:

$$A_{eff}(E) = A_0 \frac{N_{det}(E)}{N_\gamma(E)}, \tag{2.7}$$

where N_{det} is the total number of events passing the selection cuts and triggering the system. The energy dependence on the effective area results from the influence of the primary gamma-ray energy on the properties of the Cherenkov light pool, as pointed out before. The operational energy domain of the H.E.S.S. telescopes is from 100 GeV to 10+ TeV, and depends on the zenith angle of the observations, which will affect the deposition of Cherenkov light at the ground due to varying atmospheric absorption with airmass. This means that the weakest, low-energy showers, with the smallest footprints at the ground, can only be seen at small zenith angles, and the energy threshold of the observations will increase as a function of zenith angle. At zenith, A_{eff}(100GeV) $\sim$ 10^4 m^2. Conversely, at higher $Z \sim 60^\circ$, A_{eff}(1TeV) will increase to $\sim 10^6$ m^2, because the projection of the light pool on the ground will spread over large areas [198].

The H.E.S.S. instrument is now under expansion. H.E.S.S. phase-II is likely to start operation in 2012 with addition of a larger, 20-m diameter telescope at the centre of the present array, which will allow a decrease of the system's threshold to $\sim$ 25 GeV, and further improve its sensitivity by a factor of 1.5-2 at high-energies [121].

2.1.3 Imaging Atmospheric Cherenkov Technique

The relatively high degree of collimation of the electromagnetic air showers means that the Cherenkov light pool will be compact. When viewed by the camera of an Atmospheric Cherenkov Telescope (ACT), the shape of the light pool will be elliptical, because the shower is usually seen off-axis. This geometrical property of the image is at the heart of the Imaging Atmopsheric Cherenkov Technique (IACT), which we now describe.

The flux brightness of the Cherenkov light (about 10^6 photons per shower, in a window of a few 10 ns) is relatively strong when compared to the dark night sky background (NSB; $\Phi_{NSB} \sim 10^{12}$ cm^{-2} s^{-1} sr^{-1} – or $\sim 10^4$ cm^{-2} sr^{-1} in the $\sim$ ns integration times of IACTs) though the ratio can be worse for pixels where starlight enters the field of view directly. For this reason, to use the fact that the pulse of Cherenkov light is very short (Equation 2.5) is the first ingredient in separating the Cherenkov signal from the background. This is achieved by applying very short integration windows comparable with the Cherenkov pulse width of the shower (in the case of H.E.S.S. $\sim$ few ns [161]), inside which the brightness of the Cherenkov pulse dominates. Trigger conditions of > 5 p.e./pixel inside this window are usually enough to discriminate the Cherenkov pulse against the dark NSB [161], but as mentioned before, additional, multi-pixel and multi-telescope conditions are also used.

From this minimum threshold condition necessary to detect the event as an air-shower against NSB fluctuations comes the energy threshold of the instrument, since the amount of Cherenkov light produced is directly proportional to the energy of the incident γ-ray. The amount of NSB noise is formally given by:

$$N_{NSB} \propto \sqrt{\Omega A^* \Delta\tau \epsilon \Phi_{NSB}}, \tag{2.8}$$

where Ω is the solid angle subtended by the detector, A^* is the mirror collecting area, $\Delta\tau$ is the integration time and ϵ is the quantum efficiency of the detector. Writing the number of Cherenkov photons detected as $N_{Ch} \propto \epsilon A^*$, and noting that this number is $\propto E_\gamma$, we have the following signal-to-noise (SNR) relation:

$$E_{\gamma;\,min} \propto \left(\frac{N_{Ch}}{N_{NSB}}\right)^{-1} \propto \sqrt{\frac{\Omega \Delta\tau \Phi_{NSB}}{\epsilon A^*}}, \tag{2.9}$$

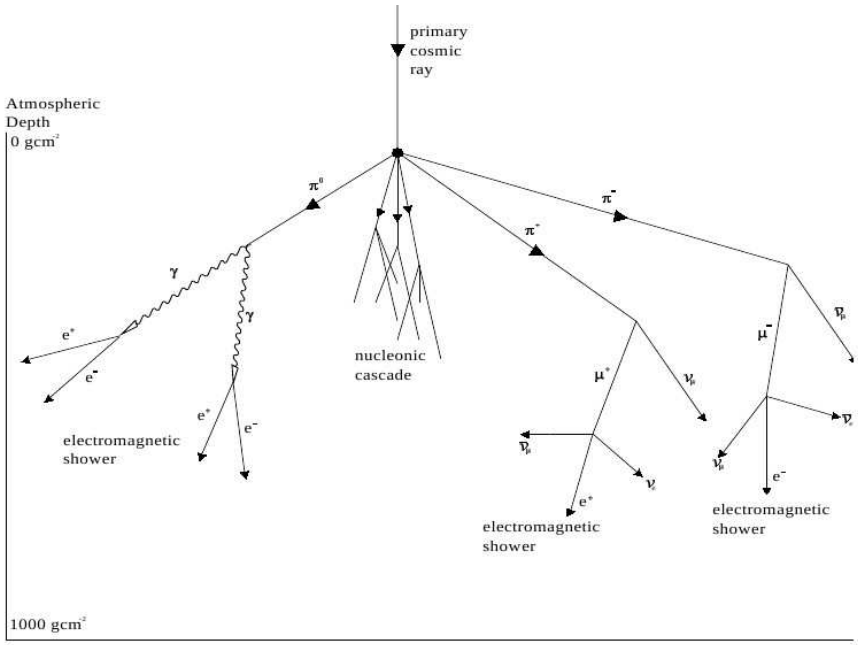

Figure 2.10: Schematic illustration of the development of a cosmic-ray inititated air-shower [247]
.

which can be improved by increasing the mirror area of the telescopes. The threshold energy is then formally defined as the one which maximises the relation $E_{thr}^{-\alpha} A_{eff}(E)$, where $\alpha \approx 2.2$ is approximately the differential spectral slope of gamma-rays for Galactic synchrotron sources [272].

The hadronic background

Cosmic-ray initiated air-showers constitute the most important source of background for the IACT. Charged cosmic-ray particles (mostly protons and alpha particles) also give rise to atmospheric showers which outnumber the γ-ray initiated ones by a factor of 1000. Upon its entrance in the atmosphere, an energetic nucleon will interact with the other nuclei present in the atmosphere by means of the strong force, generating a number of secondary pions, as well as a smaller quantity of kaons and fragmented nuclei (see Figure 2.10). Because the interaction path length for CR is larger than that of γ-rays (about 80 g cm^{-2}), the hadronic showers will be initiated further down in the atmosphere than their electromagnetic counterparts.

In the first interaction, the CR loses approximately half its energy which is chanelled in roughly equal amounts between π^0 and $\pi^{\pm}$, which will then proceed to generate fur-

ther secondary hadrons, until the energy per nucleon has gone below 1 GeV, which is the threshold energy for multiple pion production. The π^0's decay very rapidly ($\tau_{\pi^0} = 8 \times 10^{-17}$s), producing two gamma-rays which proceed to develop electromagnetic sub-showers. The charged pions survive for a longer time ($\tau_{\pi^\pm} = 1.2 \times 10^{-8}$s) before decaying into muons, in which time they can also interact again to initiate new hadronic sub-showers of their own. Muons have longer lifetime and possess low interaction cross sections, which means they will mostly proceed unabated to the ground. Direct detection of the muon content of the air-shower is therefore an unequivocal indicator of a hadronic-initiated shower. Otherwise (especially at lower-energies) they can decay into electrons and positrons which will also generate EM sub-showers.

The fact that hadronic interactions generate multiple subparticles means that these can have a relatively large lateral momentum, which will in turn mean that the shower will spread sideways much more (and do so in a random way) than its electromagnetic counterpart. In fact one could think of a hadronic shower as made up of a collection of scattered mini EM showers. As expected, the image of the Cherenkov lightpool of the hadronic showers will be very different from that of showers produced by gamma-rays and this will provide the means of differentiating between them (see Figure 2.11).

Gamma-Hadron separation

Given the small lateral extent of the electromagnetic shower, the Cherenkov image of a gamma-ray initiated air shower formed in the camera is best described by an ellipse. The general appearance of this ellipse will depend on the relative core location and the energy of the shower. The width of the ellipse is related to the lateral development of the shower, whereas its length is also a function of the core position with respect to the detector as testified in Figure 2.12.

The major axis of the ellipse points towards the origin of the shower and thus allows the location of the source in the sky. When multiple images of the same shower are available (as for stereoscopy; see Figure 2.14) the precision of the source's location in the sky can be improved (see [200]). Today, the best source location sensitivity achieved is of the order of $\lesssim 0.1^\circ$, much superior to that possible for satellite-based experiments at

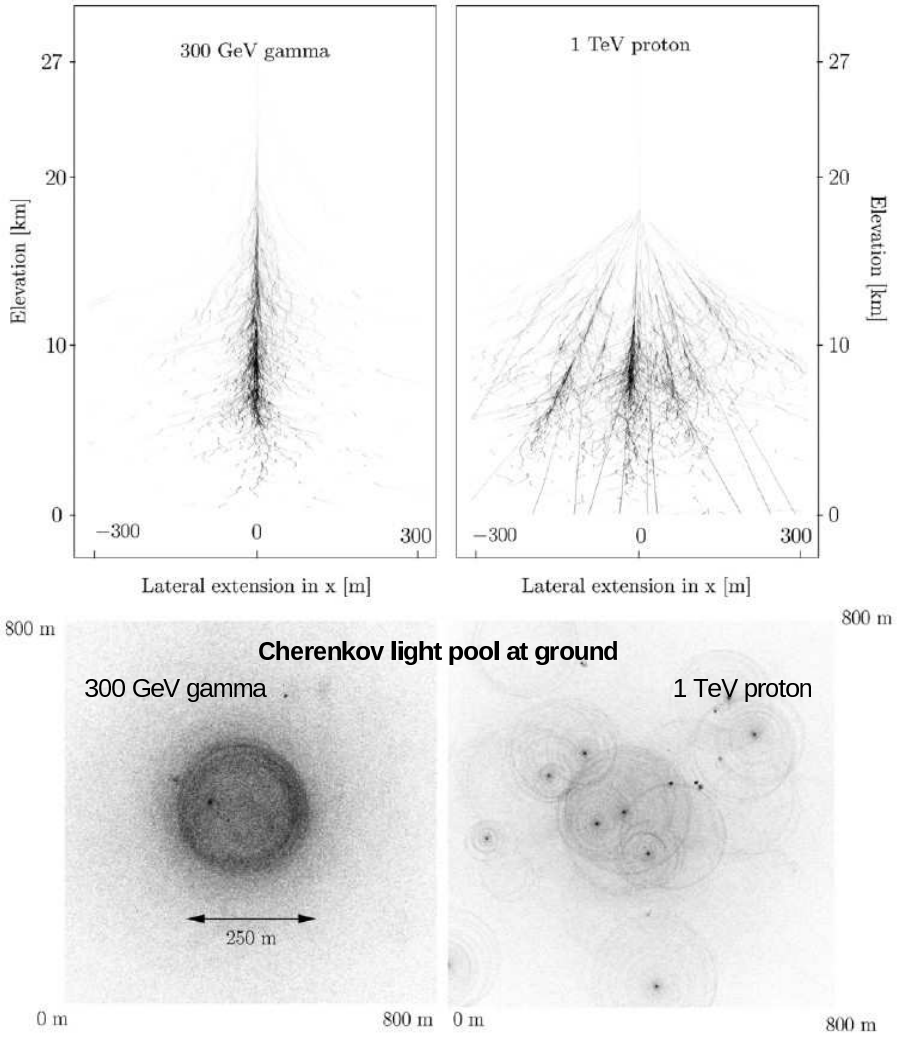

Figure 2.11: Comparison of a pure electromagnetic shower from a 300 GeV gamma-ray and a hadronic shower inititated by a 1 TeV proton. The bottom panel shows the distribution of Cherenkov light on the ground corresponding to these showers. Results are from Monte Carlo simulations by S. Funk [27]

.

the GeVs[4]. Apart from that, a thorough analysis of the ellipses' geometrical properties allow to distinguish each individual EM shower image from its hadron-initiated counterpart. This technique of gamma-hadron separation by means of the analysis of the shower image was developed by M. Hillas in 1985 [195] and nowadays allows discrimination between the two kinds of atmospheric showers with a precision of 99%, effectively solving the problem of background dominance and allowing for high-sensitivity gamma-ray

[4]In fact, for point sources the accuracy in the source location can be much better, and for example the Galactic Centre emission was located down to a precision of 13" – see Acero et al. 2010 [5].

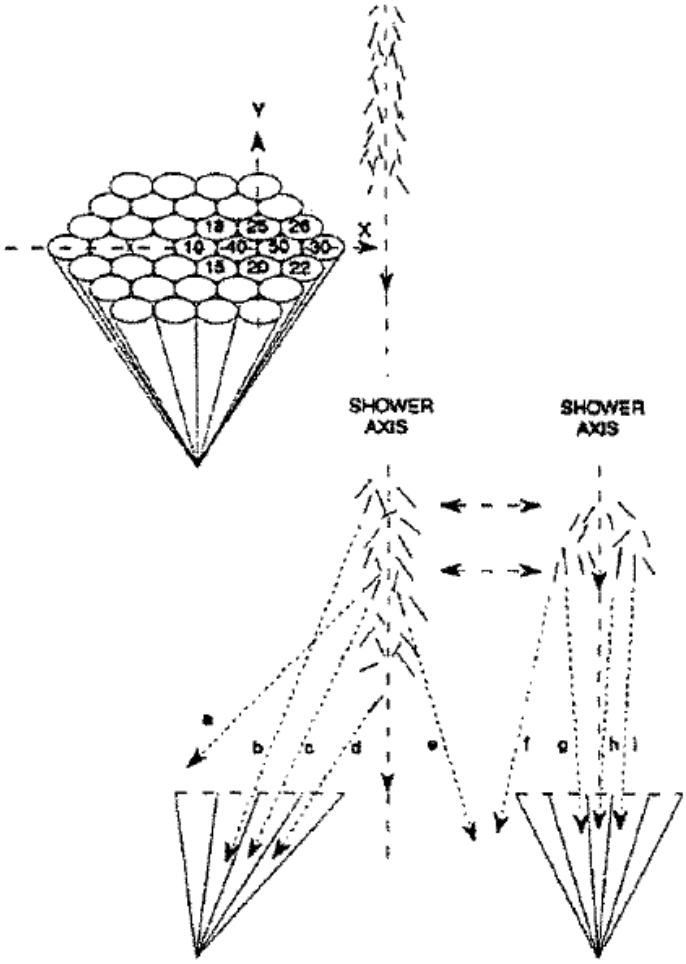

Figure 2.12: Model of the geometry of the gamma-ray shower ellipse as mapped by the detector for different relative positions of the shower axis. In the top figure it is schematically shown the elliptical distribution of counts from a shower observed off-axis, for the different pixels of the camera. The bottom figure shows the geometry by which the elliptical shape is formed as we move the shower-axis from the centre of the detector to an off-axis position. Credits: Fegan [138].

.

astronomy to be performed.

A complete geometrical characterisation of the shower image can be given by specifying the moments ω of the count distribution. These are statistical parameters of the image given by the quantity

$$\omega_l = \frac{1}{N} \sum_i \rho_i x_i^l, \tag{2.10}$$

constructed from the spatial distribution (in terms of pixel elements i relative to the centre of the camera) x_i (or y_i) to the power l; N is a normalising factor corresponding to the total number of pixel elements in the image. The term ρ_i gives the density (or number of

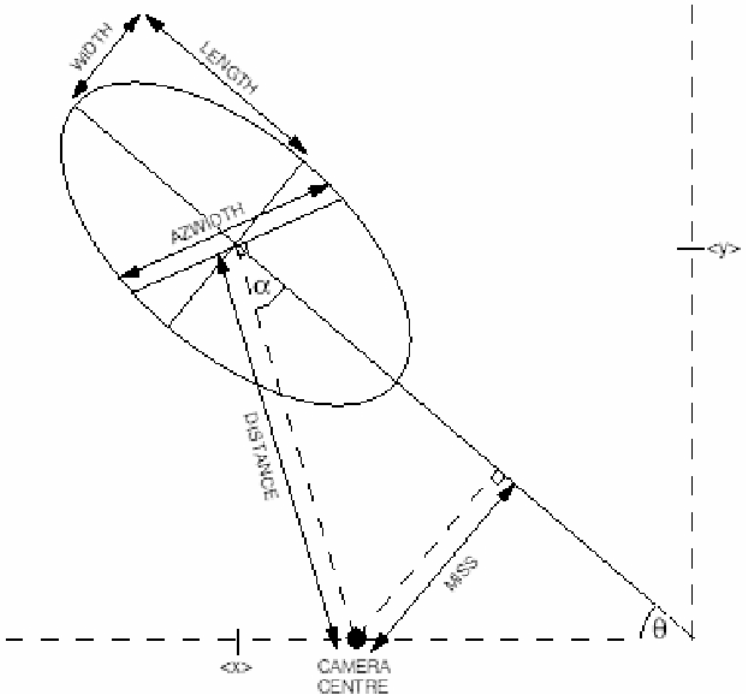

Figure 2.13: The Hillas parameters [278].

.

counts) of each pixel, and to each order l of the moments there will correspond a property of the image (we thus speak of the l-th moment ω_l), be it the mean ($l = 1$, $\langle x \rangle$ and $\langle y \rangle$), the standard deviation ($l = 2$; σ_x^2 and σ_y^2), the skewness ($l = 3$), &c.

The Hillas parameters are functions of the image moments up to the second order only (see Figure 2.13) and are listed below:

$$\text{Distance} = \sqrt{\langle x \rangle^2 + \langle y \rangle^2}, \tag{2.11}$$

$$\text{Length} = \sqrt{\frac{\sigma_X^2 + \sigma_y^2 + z}{2}}, \tag{2.12}$$

$$\text{Width} = \sqrt{\frac{\sigma_X^2 + \sigma_y^2 - z}{2}}, \tag{2.13}$$

$$\text{Miss} = \sqrt{\frac{1}{2}(u\langle x \rangle^2 + v\langle x \rangle^2) - \left(\frac{2\sigma_{xy}\langle x \rangle\langle y \rangle}{z}\right)}, \tag{2.14}$$

$$\text{Alpha} = \sin^{-1}\left(\frac{\text{Miss}}{\text{Distance}}\right), \tag{2.15}$$

where the auxiliary quantities are $d = \sigma_x^2 - \sigma_y^2$, $z = \sqrt{d^2 + 4\sigma_{xy}^2}$, $u = 1 + d/z$ and $v = 2 - u$. A detailed account of these parameters and the discrimination between gamma and hadron-initated air showers is given in Fegan 1997 [138]. The angle α between the long axis of the ellipse and the source position in the camera is the crucial parameter in removing the cosmic-ray background for a point source. Unlike a gamma-ray-initiated air shower, which has its origin at a particular source position in the sky, the cosmic-ray background is isotropically distributed, and thus has a random distribution in α. The gamma-rays from a point source can therefore be identified on the basis that they will concentrate at small angles from the source position in the camera.

Further discrimination between gammas and hadrons is done by imposing *image cuts* on the different parameters of the image, which consist of lower and upper boundaries to their magnitudes. The values of the cuts can be determined via Monte Carlo simulations to create *lookup tables* of parameters for different source properties and observational conditions, such as spectrum, zenith angle of observations, energy range, &c.

Stereoscopy and shower reconstruction

Stereoscopy is a variation of the imaging technique by which multiple telescopes are used to image an atmospheric shower simultaneously [9] (Figure 2.14). The first advantage of the technique is that local muons, which reach the ground from the shower and are an important source of background (and the signatures of which are hard to separate from the gamma-rays on an image basis alone), are eliminated by trigger coincidence. Also, viewing the shower by more than one telescope with such a coincidence trigger (see Funk et al. 2004 [161]) improves the NSB background rejection and thus allows for a reduction of the energy threshold of the observations. Furthermore, the stereo image allows for the three dimensional reconstruction of the air-shower, which permits a more accurate calculation of the image parameters, in particular the shower incidence angle, and from it the core location and the altitude of the shower maximum in the atmosphere (see for example [231] and [281]).

For analysis of stereoscopic data, the original approach of the Hillas parameters can be extended to derive weighted combinations of the width and length parameters. These are called mean-scale-parameters, such as mean-reduced-scale-width (MRSW) and mean-

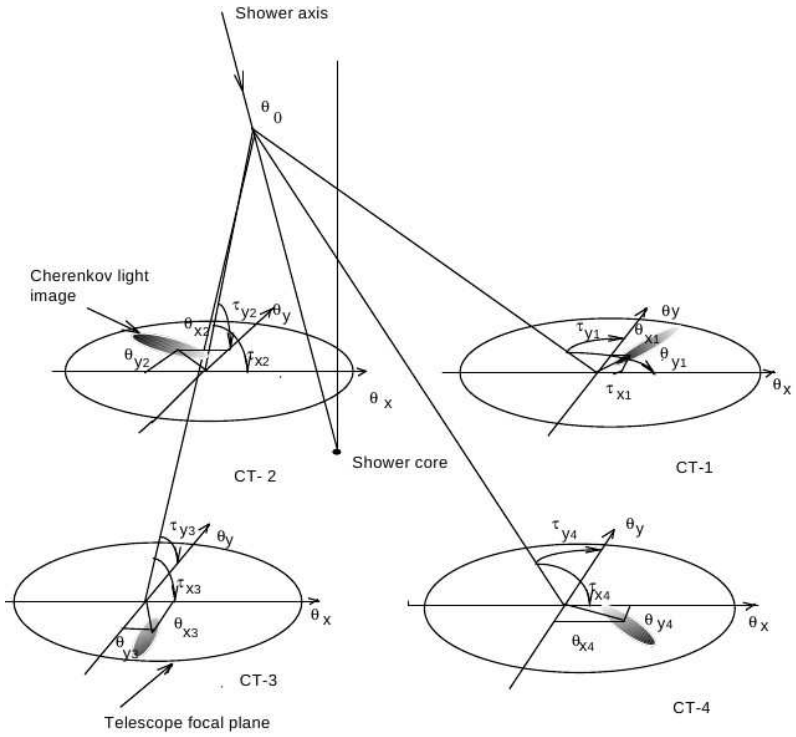

Figure 2.14: Reconstruction of the shower parameters from stereoscopic observations of 4 IACTs. Credits: Aharonian & Konopelko [9].

.

reduced-scale-length (MRSL), and are defined as [27]:

$$\mathrm{MRSP} = \frac{1}{\mathrm{N_{tel}}} \sum_{\mathrm{i=1}}^{\mathrm{N_{tel}}} \frac{\mathrm{p_i} - \langle \mathrm{p_i} \rangle}{\mathrm{sd}(\mathrm{p_i^{sim}}(\mathrm{Z, size, r}))}, \tag{2.16}$$

where p_i is a given parameter (width or length) for telescope i,$\langle p_i \rangle$ its mean value and $\mathrm{sd}(\mathrm{p_i^{sim}}(\mathrm{Z, size, r}))$ the parameter's standard deviation, both obtained from simulations for a given zenith angle Z, image size, and impact distance r.

Data collected by multiple telescopes in this way have the triggered images later selected as gamma-ray candidates based not only on MRSW and MRSL, according to image cuts, but also in function of the square of the angular parameter θ, defined in Figure 2.16. For one-telescope data, the angle cuts were done in the basis of low α, but with stereoscopic data, the position of the shower can be better reconstructed with the multi-telescope information on the parameter θ^2, *viz.* the square of the angular distance between the reconstructed shower position and the source position (not necessarily at the camera centre). This will be a more appropriate variable for background separation in stereoscopic data than α (see Figure 2.16).

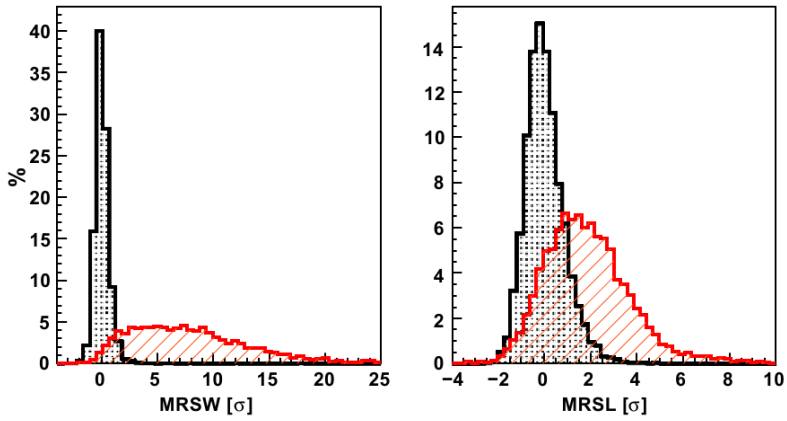

Figure 2.15: Example of simulated MRSW and MRSL distributions used for gamma-hadron discrimination in the H.E.S.S. telescopes. The training variables are for energies between 0.5-1 TeV and a zenith angle range of $15-25^{\circ}$. Black curves are for gammas and red for hadrons. From Ohm et al. 2009 [281].

.

Figure 2.15 gives an idea of how the cuts are produced based on simulations that give the expected parameter distribution for gammas and hadrons and how they are distinguished from each other. The background rejection power is measured by the *quality* of the cuts, termed Q and defined as the ratio of the gamma-ray acceptance efficiency over the square root of cosmic-ray background post-cuts acceptance efficiency. Typically, $Q_{MRSW} \approx 3$, corresponding to a factor of 10 in CR background rejection and a gamma-acceptance efficiency of about 80%.

Finally, an extra cut can be put on the image selection thanks to the improved angular resolution that is obtained with stereoscopy. If the arrival direction of the gamma-rays is restricted to lie within a certain solid angle Ω_{source}, then the sensitivity of rejection is improved by selecting the arrival direction of the events accordingly by a factor $Q_{\text{ang}} \approx \sqrt{\Omega_{FOV}/\Omega_{\text{source}}}$. In the case of a point source (and a typical PSF of $\approx 0.1^{\circ}$) one gets a Q-factor of $\sim 10^3$ when all shape cuts are included.

In fact, the H.E.S.S. collaboration has developed a particular set of cuts for its use which are optimised *a priori* with Monte Carlo γ-ray simulations to yield the maximum expected significance. The main parameters on which the choice of cuts depends are the source spectrum and brightness. A set of *standard cuts* exists however to be applied when searching for new sources whose properties are unknown and therefore avoiding having to correct for statistical trials resulting from analysis with different sets of cuts.

Configuration	MRSL min.	MRSL max.	MRSW min.	MRSW max.	θ^2 [degree^2]	Image Amp. [p.e.]	Distance [°]
Standard	-2.0	2.0	-2.0	0.9	0.0125	80	2.0
Hard	-2.0	2.0	-2.0	0.7	0.01	200	2.0
Loose	-2.0	2.0	-2.0	1.2	0.04	40	2.0
Extended	-2.0	2.0	-2.0	0.9	0.16	80	2.0

Table 2.2: Optmised gamma-ray selection cuts for a point source analysis. For a definition of the main cut parameters MRSL, MRSW and θ^2 see text. For acceptance of the event a minimum of two successfully triggered telescopes must pass the image cuts. From Aharonian et al. 2006 [19].

The *standard cuts* are optimised for a source with flux of 0.1 Crab and power-law photon index $\Gamma \sim -2.6$. The other two types of cuts are the *hard cuts*, optimised for a harder spectrum with $\Gamma \sim 2.$ and flux ~ 0.01 Crab, and the *soft cuts*, appropriate for a source with flux comparable to the Crab and of index $\Gamma \sim -3.2$. [19] and [78]. A summary of these different types of image cuts according to the *standard H.E.S.S. analysis* procedures is given in Aharonian et al. 2006 [19] and presented in Table 2.2.

As discussed by Benbow 2005 [78], the use of *hard cuts* has the effect of increasing the energy threshold of the observations, but the events which pass cuts tend to have a better ($\sim 20\%$) angular resolution, with fewer systematics issues on estimating the background. The *loose cuts*, on the other hand, are recomended for the spectral study of bright sources, such as the case of the blazar PKS 2155-304 in this work, where a higher acceptance of background events is not an issue for the analysis. In fact, for the data on PKS 2155-304 presented in this thesis, a set of loose cuts was used, the angle cut of which was $\theta^2_{\rm cut} = 0.2°$, corresponding to a relatively low energy threshold of 170 GeV in the case of the large flare of MJD 53944 presented in Chapter 4.

2.1.4 H.E.S.S. Data Analysis

Details of the standard H.E.S.S. analysis technique are given in Aharonian et al. 2006 [19]; a brief account of some advanced analysis methods is given by de Naurois 2006 [122]. H.E.S.S. data are taken as a series of *runs*, corresponding to a period of 28-min continuous observation of the source. The first step in the data analysis process is therefore the selection of good runs, when for example bad weather sequences are discarded

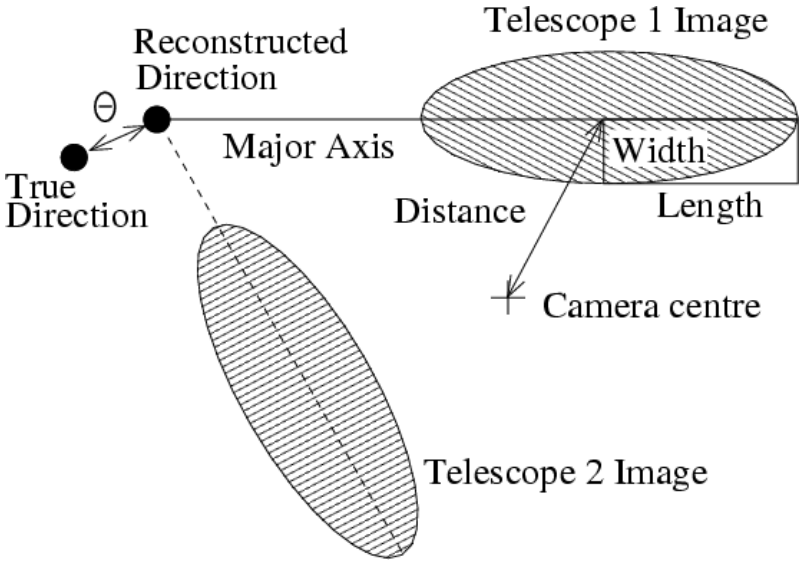

Figure 2.16: Geometric construction showing the meaning and mode of calculation of the parameter θ for image discrimination in the stereoscopic technique. From Aharonian et al. 2006 [19].

.

from the analysis. This choice is undertaken at the raw-data processing stage, when runs are classified according to their quality.

Event reconstruction, which allows the selection of the candidate gamma-ray events, is done as described in Section 2.1.3, where the arrival direction of the shower is recovered to produce a sky-map. In the process of event reconstruction, the energy of the primary particle is also estimated by comparison to Monte Carlo-generated energy *lookup tables*. The energy reconstruction is the most uncertain aspect of data processing due to intrinsic statistical uncertainties on the nature of the shower development, and each reconstructed event carries an energy uncertainty on average of 15%.

The typical triggering frequency of the H.E.S.S. telescopes for observations near the zenith is of $\sim$ 200 Hz of which the majority of events are hadron-initated. Typical strong sources, such as the Crab Nebula, which is used to calibrate the system, have in comparison a γ-ray trigger rate of $\sim$ 0.8 Hz at zenith. Hadronic background rejection is performed in the post-data-processing analysis, for which three independent analysis environments exist within the H.E.S.S. collaboration: *wobble chain*, *ParisAnalysis* and the *HESS Analysis Package* (HAP), an integrated analysis system jointly developed in France and Germany and supplied in England with a light-curve maker routine, the *Durham-LightcurveMaker* [123]. The analysis in this work was done using HAP and its associated

Durham extension.

Today there exist many different methods for event reconstruction, but in this work, where we will analyse exclusively data from the bright source PKS 2155-304 with abundant counts (the peak-gamma rate for the large flare of MJD 53944 was of $\sim$ 1 Hz and more than 10,000 events were registered in total during three runs), there is no need to go beyond the traditional Hillas method described in Section 2.1.3, given that the use of such advanced methods is very computationally expensive.

The first step in the Hillas method consists of image cleaning, in order to reduce the sky background. This is done by choosing the threshold level of charge in each pixel – in units of photo-electrons (p.e.) – which will dictate those pixels whose information will be retained for image analysis. After image cleaning, the moments of the Cherenkov images can be taken and analysed for performing background rejection, following the description for treatment of steresoscopic data given in the preceding section.

Signal determination

Once hadronic background rejection is done, it is necessary to evaluate the level of residual background signal of the sky, which is basically made up of gamma-like cosmic ray events which were accepted through the image cuts. The background estimation is done in a way pretty much similar to that of CCD astronomy, by estimating the flux levels outside the source region. In ground-based gamma-ray astronomy one must nevertheless be very attentive to two factors which will bear great influence on the result of this procedure. First, there are variations in the camera acceptance accross the field of view (FOV); secondly, the fact that the background cosmic ray flux is dependent on the zenithal distance, will imply that across the field of view and during the timespan of an observation run, energy-dependent variations on the background trigger rate will happen that may be significant.

Ground-based gamma-ray observations are usually conducted in what is called *wobble mode*, that is, the source is moved around the FOV and relative to the centre of the camera during the observations, by an angle of typically 0.5°. This is done so that part of the FOV containing the source can be used to *simultaneously* estimate the hadronic background, without the necessity of intercalating dedicated off-source observations for calibration

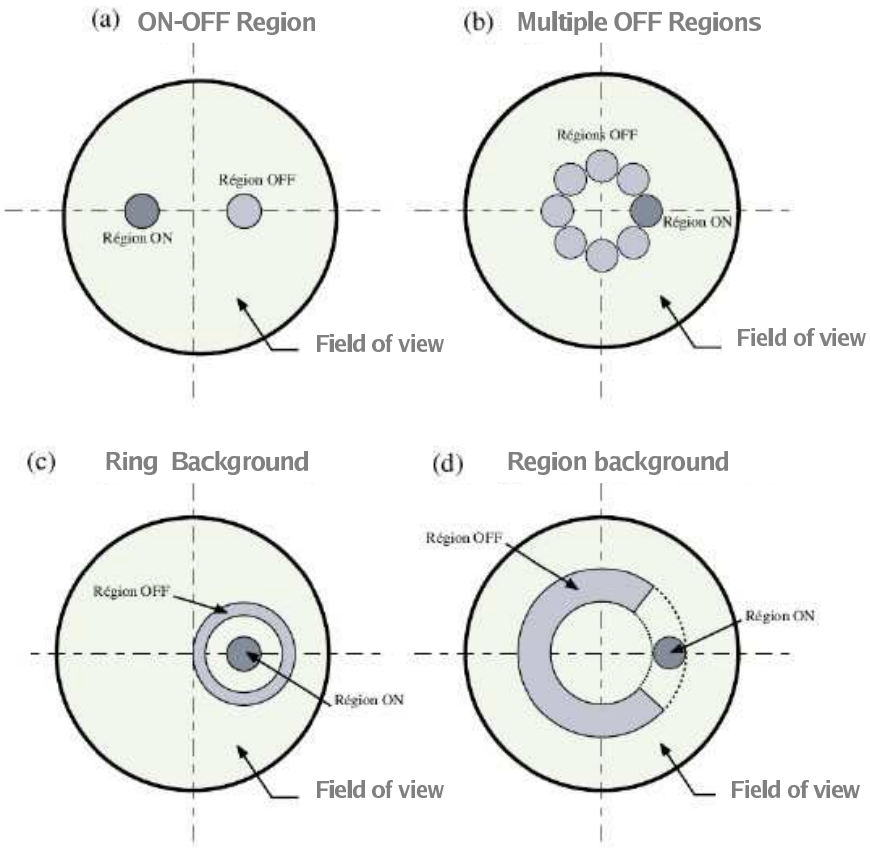

Figure 2.17: Scheme of the different methods of background estimation for H.E.S.S. analysis. Adapted from [239].

.

purposes. The *wobble mode* guarantees that the issues raised in the preceding paragraph are automatically accounted for during the observation procedures [79].

The situation is illustrated on panel (a) of Figure 2.17. During observations, the source is located at one side of the FOV (ON region), whereas a diametrically opposed region of same size (OFF region) is used for background estimation. In doing so, one assumes that the radial acceptance of the camera is isotropic, and the small $\sim 1^\circ$ difference in zenithal distance between the two regions should not affect the accuracy of the background determination.

The number of excess events N_{excess} which will in turn define the magnitude of the source signal are then estimated by the expression:

$$N_{\text{excess}} = N_{\text{ON}} - \alpha N_{\text{OFF}} \tag{2.17}$$

where $N_{\rm ON}$ and $N_{\rm OFF}$ are the number of counts in the ON and OFF regions respectively and α is a normalisation factor between the two regions. This depends on the integration times for the two regions and on the angular sizes of each one, and is necessary to correct for any imbalance between them.

To determine the significance level of the detection, we must know the statistical distribution which governs the background, so that the signal's deviation relative to the background, S, can be estimated. In ground-based gamma-ray astronomy, this is given by the so-called Li & Ma statistics, after the astronomers who first made this estimation in 1983 [242], during a research stay at the University of Durham. The Li & Ma estimator converges to a Gaussian distribution for large numbers, according to a χ^2 distribution, and is given by [242]:

$$S = \sqrt{2}\left\{N_{\rm ON}\ln\left[\frac{1+\alpha}{\alpha}\left(\frac{N_{\rm ON}}{N_{\rm ON}+N_{\rm OFF}}\right)\right] + N_{\rm OFF}\ln\left[(1+\alpha)\left(\frac{N_{\rm OFF}}{N_{\rm ON}+N_{\rm OFF}}\right)\right]\right\}^{1/2}. \quad (2.18)$$

It is conventional in ground-based gamma-ray astromy, and above all good statistical practice, to require that the significance of a signal be worth consideration only if it is above the threshold level of 5σ (i.e. false-alarm probability = $\lesssim 5\times10^{-7}$), below which the hypothesis of it originating in background fluctuations should not be dismissed.

Figure 2.17 shows a number of possible configurations for background estimation, which are discussed in detail in [19] and [79]. In this analysis of PKS 2155-304 the so-called *reflected-region* background model is used (panel b in figure 2.17), developed specially for application with *wobble mode* observations. Here, for a given source position, a ring of multiple OFF regions with equal shapes and sizes to the ON region, and positioned at an equal offset to the centre of the camera is used. Other background estimation methods include: *ring background* (panel c), which is centered at the ON-source position and is good for performing surveys and for the observation of extended sources, and the *template background* which uses background events displaced in image shape parameter space rather than angular (camera view) space [79]. The *region background* is a "free" variant of the methods (b) and (c), to account for particularities of the FOV, like the presence of other nearby sources and/or extended emission.

It is worth noticing that in all of the background configurations but the *region background*, the symmetry (either about the centre of the camera or the position of the source) on the choice of the OFF regions is carefully maintained, to avoid the issues with varying radial acceptance already discussed. In the presence of other sources in the FOV one should take care that the OFF regions are well clear from any contamination, sometimes at the expense of the ideal symmetry choice. For observations of point sources, such as PKS 2155-304, the employment of a ring background (panel (c) in the figure) is also usual [79].

Spectral analysis: forward folding

The method of spectral reconstruction usually used in ground-based gamma-ray astronomy and applyed within H.E.S.S. is the so-called *forward folding* principle (as opposed to the "unfolding principle", which uses Monte Carlo information to deconvolve the data from the "instrumental matrix"), common also to other fields of high-energy astronomy such as X-rays and in GeV gamma-rays. In this approach the initial spectral shape of the source is unknown *a priori*, and the method aims at finding the "true" spectral distribution by maximising the posterior probability of the data given the Monte Carlo expectation $p(\text{data}|\text{MC}, \text{I})$. Here, the data carry the convolved information of the true spectrum + the detector's response function. The method is described in some detail by for example Aharonian et al. 1999 [10].

A range of reasonble prior forms on the distribution of the spectrum are then tested and selected according to a best-fit criteria; a power-law function is one of such best-guesses:

$$\Phi(E) = \Phi_0 \left(\frac{E}{E_0} \right)^{-\Gamma}, \tag{2.19}$$

where E_0 is a reference point in the energy scale, Γ is the photon index and Φ_0 a normalisation factor for the flux, in units of $\text{cm}^{-2}\ \text{s}^{-1}\ \text{TeV}^{-1}$.

Other functional forms, such as a broken power law, are also possible and have physical basis for being chosen – such as the expected faster cooling of the highest energy particles:

$$\Phi(E) = \Phi_0 \left(\frac{E}{E_B}\right)^{-\Gamma_1} \left(1 + \left(\frac{E}{E_B}\right)^{1/0.3}\right)^{0.3(\Gamma_1-\Gamma_2)}, \tag{2.20}$$

where E_B is the break energy and Γ_1 and Γ_2 photons indexes above and below the break energy, respectively. A power-law with exponential cut-off is also commonly used:

$$\Phi(E) = \Phi_0 \left(\frac{E}{E_0}\right)^{-\Gamma} \exp(-\beta E), \tag{2.21}$$

where the cut-off energy is given by $1/\beta$.

The instrumental response function enters the process when the modelling has to be performed. The effective area or acceptance of the camera $A_{eff}(E, Z, d)$ must be known for every relevant energy range and observation parameter, usually via Monte Carlo simulation of *lookup tables*. It is also necessary to create *lookup tables* for the energy resolution function of the instrument $R(E, E', Z, d)$, which takes into consideration the error in the measured energy E' in relation to the true energy E of the reconstructed event. With these functions known, the model(s) can be tested for the different range of parameters Φ_0, Γ, E_B, &c. aiming at minimising the χ^2 distance between the data and the Monte Carlo predictions.

Flux estimates for a given energy range $[E'_i, E'_{i+1}]$ are derived as follows:

$$\frac{dN_{\text{excess}}(E'_i, Z, d)}{dE'\, dE\, dt} = U(E'_i)\left(\Phi(E) * A_{eff}(E, Z, d) * R(E, E', Z, d)\right), \tag{2.22}$$

where $U(E'_i)$ is a correction function that allows the differential flux of photons at energy E to be computed from the number of excess events registered in the range $[E'_i, E'_{i+1}]$. A comprehensive description of the process of energy estimation and spectral measurements with the Cherenkov imaging technique is given by Mohanty et al. 1998 [272].

2.2 Observational Techniques II: Optical Polarimetry

This section provides a brief description of the formalism and basic physical concepts necessary for understanding the phenomenon of astronomical polarisation. We will also discuss, in brief, the fundamental techniques involved in the analysis of optical polarisation data. More specialised information can be obtained in the references [224], [238], [332]

and [106]. An introduction to polarimetric techniques by Hildebrand et al. 2000 [193] also offers a good view on the subject.

2.2.1 A Primer on Optical Polarimetry

The polarised nature of light derives directly from the form of the wave equation in electromagnetism:

$$\nabla^2 \mathbf{E}(\mathbf{r}, t) = \frac{1}{c^2} \frac{\partial^2 \mathbf{E}(\mathbf{r}, r)}{\partial t^2}, \tag{2.23}$$

where $\mathbf{E}(\mathbf{r}, t) = E\hat{x} + E\hat{y}$ is the electric-field vector at position $\mathbf{r}$ and time t, decomposable in two orthogonal components in the plane perpendicular to the direction of the propagation $\hat{n}$. The plane-wave solution to these equations can be written as:

$$\mathbf{E}(\mathbf{r}, t) = \hat{x} E_x \cos(\omega t - k_0 r + \phi_x) + \hat{y} E_y \cos(\omega t - k_0 r + \phi_y), \tag{2.24}$$

where ω is the angular frequency of the wave, $k_0 = 2\pi/\lambda$ is the wavenumber and $\phi_{x,y}$ indicate the absolute phases of both components. There can exist a difference in phase between the two orthogonal components of the wave $\delta = \phi_x - \phi_y$. Depending on the relative intensity of the amplitudes E_x and E_y, and on δ, the light will be said to be of different polarisations.

To have a graphical visualisation of this, we can proceed to eliminate the propagator term $\omega t - k_0 r$ from the previous equation, to obtain the equation of an ellipse in the instantaneous $x - y$ plane:

$$\frac{E_x^2(r,t)}{E_{0x}} + \frac{E_y^2(r,t)}{E_{0y}} - \frac{2E_x(r,t)E_y(r,t)}{E_{0x}E_{0y}} \cos\delta = \sin^2\delta, \tag{2.25}$$

which is represented in Figure 2.18. From the figure one can see that the light will appear to be *linearly polarised* if, as it propagates, the resultant field direction $\hat{e}$ is constant in the plane (I, I×n). If this direction changes in time, but E_x and E_y have equal amplitudes, then the light will be *circularly polarised*, and for $E_x \neq E_y$ we will fall in the generic case of *elliptically polarised light*. Notice that a monochromatic wave can *never* be unpolarised, since superposition of two coherent beams of elliptically polarised light will give another

elliptically polarised beam. Unpolarised light is the result of incoherent polychromatic waves (that is, the propagator $\omega t - k_0 r$ cannot be simplified out of the wave-equation) with different relative E_x and E_y magnitudes and phase δ.

The fundamental parameters of the polarisation ellipse can be written as a function of the wave quantities χ and β:

$$\tan 2\chi = \frac{2E_{0x}E_{0y}}{E_{0x}^2 - E_{0y}^2} \cos\delta, \quad 0 \leq \chi \leq \pi \tag{2.26}$$

$$\sin 2\beta = \frac{2E_{0x}E_{0y}\sin\delta}{E_{0x}^2 + E_{0y}^2}, \qquad |\beta| \leq \pi/4 \tag{2.27}$$

From Figure 2.18 it is clear that the polarisation direction is given (least to an ambiguity of π) by the *polarisation angle* χ. Now, the other quantity of direct astrophysical interest, the *polarisation degree* p of the radiation, is defined as a function of the minimum and maximum intensities in orthogonal directions $E_{max} = E_0^2 \cos^2\beta$ and $E_{min} = E_0^2 \sin^2\beta$, where in the figure $E_0 \equiv a$. Thus:

$$p = \frac{E_{max} - E_{min}}{E_{max} + E_{min}} = \cos 2\beta. \tag{2.28}$$

Stokes parameters

In general, light can be assumed to be partially elliptically polarised. The quantities discussed until now, though of physical interest, are not practical in experimentation because they are not easily directly measurable. A very general and directly measurable quantity that completely describes mathematically the polarisation of light (and is also free from the angle ambiguities of the polarisation ellipse) is the Stokes 4-vector $\mathbf{S}$, introduced for astronomical use by Chandrasekhar in 1946 [102]. The components of the Stokes vector I, U, Q, V are four quantities derived by Sir George Stokes in 1852 [328] to completely describe the state of polarised light by decomposing the radiant energy into its different components.[5] They are therefore measures of spectral energy flux density, and are all

[5]It is important to keep in mind that the Stokes 4-vector is not a real vector and it does not form an orthogonal basis of independent components, with some implications for its algebra.

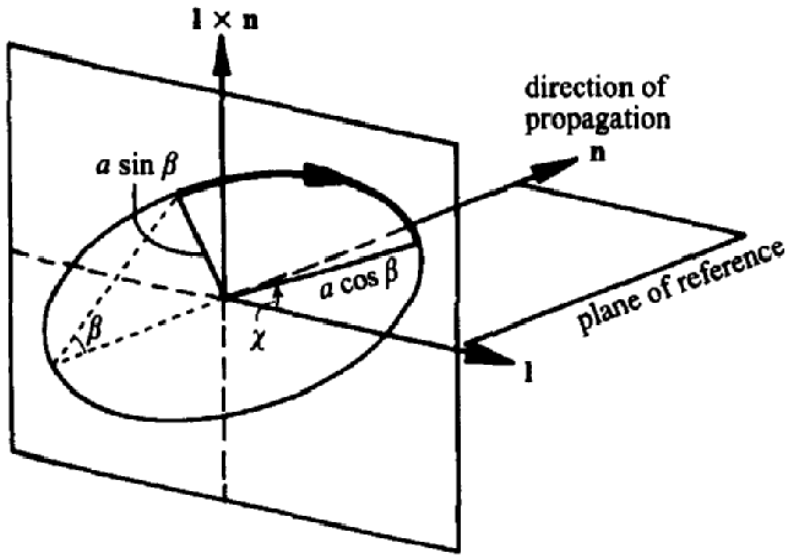

Figure 2.18: The polarisation ellipse. From [332].

.

quoted in the same units of erg s^{-1} Hz^{-1} cm^{-2}

To derive the Stokes parameters, let us consider that radiation is integrated for a certain time T over which the polarisation vectors arriving at the detector will have rotated, and consequently information of the *instantaneous* polarisation state of the light would have been lost (smeared out or averaged over). If we make the measurement time very small, then we recover this instantaneous information and can write:

$$\langle E_x(r,t)E_y(r,t)\rangle = \lim_{T\to 0}\frac{1}{T}\int_0^T E_x(r,t)E_y(r,t)\,dt. \tag{2.29}$$

Evaluating this time average over the equation of the polarisation ellipse 2.25 gives us the following decomposition: $I^2 = Q^2 + U^2 + V^2$, where the terms define the matrix of the Stokes vector:

$$\mathbf{S} = \begin{pmatrix} I \\ Q \\ U \\ V \end{pmatrix} = \begin{pmatrix} E_{0x}^2 + E_{0y}^2 \\ E_{0x}^2 - E_{0y}^2 \\ 2E_{0x}E_{0y}\cos\delta \\ 2E_{0x}E_{0y}\sin\delta \end{pmatrix}. \tag{2.30}$$

In terms of the polarisation ellipse parameters:

$$\mathbf{S} = \begin{pmatrix} a^2 \\ a^2 \cos 2\beta \cos 2\chi \\ a^2 \cos 2\beta \sin 2\chi \\ a^2 \sin 2\beta \end{pmatrix} \tag{2.31}$$

All quantities are as before: $a^2 = E_0^2$ is concerned with the intensity of the radiation, the angle χ, also called the "polarisation angle", indicates the orientation of the polarisation ellipse in the plane of the sky or of the detector (always measured from the North Celestial Pole, towards the Celestial East; see Figure 2.18), and β is a quantity related to the axial ratio of the ellipse, with $\beta = 0$ indicating the case of linearly polarised radiation, whereas $\tan\beta = 1$ is for light completely circularly polarised. The individual Stokes parameters describe therefore the total intensity $I \geqslant 0$ of the radiation, as well as its components for the linearly polarised (Q and U) and circularly polarised parts of the wave (V). Note that Q, U and V can assume both positive and negative values, and the sign carries information on the orientation of the polarisation. The components of the four-vector therefore obey the following relation $I^2 \geqslant Q^2 + U^2 + V^2$, where equality in the previous expression means that the light is 100% polarised.

The polarisation quantities of astrophysical interest, p and χ, can then be directly derived from the Stokes parameters as:

$$p = \frac{\sqrt{Q^2 + U^2}}{I} \tag{2.32}$$

$$\chi = \frac{1}{2} \arctan\left(\frac{U}{Q}\right) \tag{2.33}$$

Alternatively, one can use the so-called *relative* Stokes parameters, defined as $q = Q/I = p\cos 2\chi$ and $u = U/I = p\sin 2\chi$ without any change of meaning or requirement to alter the definitions above. The quantities Q and U are very useful for the representation of polarimetric data, since they represent the Cartesian components of the *true* vector $(a^2, 2\chi)$. The Q-U plane, or Stokes plane, is the equatorial disc of the Poincaré sphere defined in Figure 2.19, and provides a direct means of visualisation of all the polarisation information from an astrophysical source. The true vector diagram in this plane is called

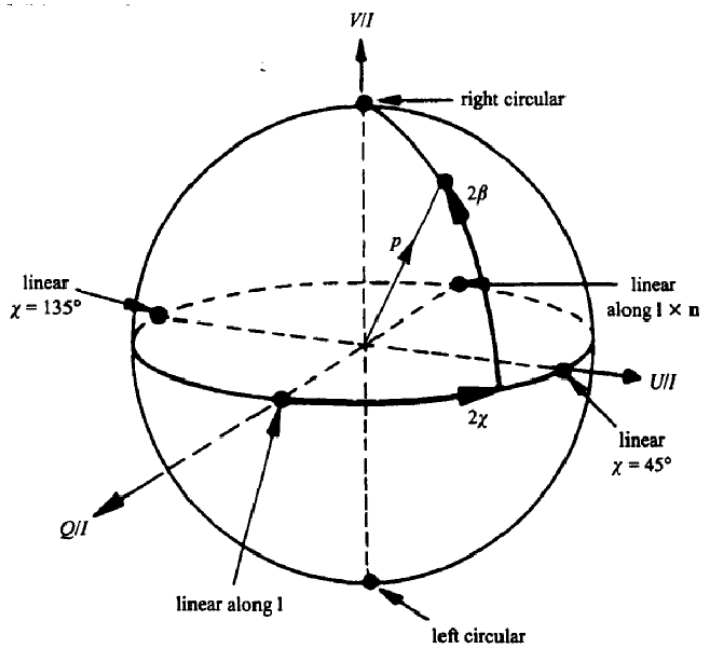

Figure 2.19: The Poincarè sphere. The equatorial plane has axis Q/I, and U/I is the area of partial linear polarisation. A vector diagram in this plane is called a "Stokes plot". From [332].

.

a "Stokes plot" and provides a convenient representation of the temporal evolution of the source's polarisation. In this plane, the length of the vector from the data point to the origin represents p, and the angle between the vector and the Q axis represents the χ; contours of constant polarisation are circles in the $Q-U$ plane, while contours of constant position angle are radii (see discussions in Impey et al. 1982 [204] and 1984 [205] and Moore et al. 1982 [273]).

Mueller algebra

The great advantage of the Stokes parameters is that they completely characterise the radiation's polarisation state and they are additive. This means that the effect of any polarising media through which the radiation happens to pass (including instrumental polarisation effects) can be taken into account by means of direct algebraic treatment of the Stokes parameters. This is called *Mueller algebra* [275] and it describes the set of linear transformations obeyed by the Stokes parameters[6]. The 4×4 transformation

[6] An extensive discussion of Mueller calculus is given in Tinbergen 2005 [332]

Figure 2.20: The “Pico dos Dias” observatory of the National Astrophysics Laboratory of Brazil, where the optical polarimetric data for this thesis was obtained. Credits: LNA

.

matrix which encodes the effect of the medium in the polarisation of radiation is called the *Mueller matrix*, $\mathcal{M}$. So, the effect of the passage of polarised radiation through a polarised medium can be mathematically expressed as the linear transformation:

$$\mathbb{S}' = \mathcal{M} \cdot \mathbb{S}, \tag{2.34}$$

where $m_{ij} \in \mathbb{R}$ and $m_{11} > 0$, because it transforms the Stokes-I parameter, which is always positive.

We shall not enter into much detail on the discussion of Mueller algebra, but the key to it is to know the correct form of the Mueller matrix for each particular operation one wants to perform in the light. These are given for example on Table 4.1 of [332]. Whenever necessary in the next section, the use of the calculus will be made explicitly.

2.2.2 Measurement Techniques: the IAGPOL

The optical polarimetric observations presented here were performed with IAGPOL[7], the high-precision CCD imaging polarimeter of the University of São Paulo [250], mounted on the 1.6 m Perkin-Elmer telescope at Pico dos Dias Observatory and operated by the National Astrophysics Laboratory (LNA) of Brazil[8].

The design of a polarimeter consists of the addition of certain optical elements in the telescope converging beam to the CCD camera which are capable of resolving the polarisation parameters of the incident radiation, before it is measured by the imaging detector. Depending on the effect they have on the polarisation, the optical elements have particular names. The simplest of them is the *rotator*, whose function is simply to rotate the polarisation ellipse without changing its ellipticity. Its Mueller matrix form is thus:

$$\mathcal{M}_{\rm ROT} = \begin{pmatrix} 1 & 0 & 0 & 0 \\ 0 & \cos 2\theta & \sin 2\theta & 0 \\ 0 & -\sin 2\theta & \cos 2\theta & 0 \\ 0 & 0 & 0 & 0 \end{pmatrix}. \tag{2.35}$$

The *polariser* is another important element and its function is to change the relative amplitudes of polarisation components of the radiation. In terms of Mueller matrices, the ideal linear polariser $\mathcal{M}_{\rm LIN}$ can be expressed as:

$$\begin{array}{cc} \text{Linear } \pm\text{Q Polariser} & \text{Linear } \pm\text{U Polariser} \\ \begin{pmatrix} 1 & \pm 1 & 0 & 0 \\ \pm 1 & 1 & 0 & 0 \\ 0 & 0 & 0 & 0 \\ 0 & 0 & 0 & 0 \end{pmatrix} & \begin{pmatrix} 1 & 0 & \pm 1 & 0 \\ 0 & 0 & 0 & 0 \\ \pm 1 & 0 & 1 & 0 \\ 0 & 0 & 0 & 0 \end{pmatrix} \end{array}, \tag{2.36}$$

[7] For the reader more acquainted with the techniques of optical polarimetry it might be of some use to know that this instrument is very similar in design to the Vatican Polarimeter (VATPOL), described in detail in Magalhães et al. 1984 [249], one of the main differences between them being the incorporation of CCD photometry which significantly improves the sensitivity of the equipment.

[8] A detailed description of IAGPOL and its operation and data reduction procedures can be found in Pereyra et al. 2000 [285] and http://www.astro.iag.usp.br/ antonio/gaveta/default.htm – Date of Access Sept 6, 2010.

for a $\pm Q$ and a $\pm U$ polariser, respectively.

The *polarimetric drawer* of the IAGPOL consists of a modulator, a fixed analyser and a filter, which are inserted in the optical axis of the system and are capable of dealing with both linear and circular polarisation, depending on the particular configuration chosen for the instrument. The IAG polarimetric drawer has a very high efficiency, being capable of measuring the linear polarisation parameters of a point source with photometry-limited accuracy.

The first optical element of the polarimeter is the *modulator*. The use of a modulator is fundamental because it circumvents many sources of error which would otherwise hinder an accurate measurement of the degree of polarisation. The presence of a modulator means that differential measurements of the polarised flux are made, and this is achieved by changing between two orthogonal states of polarisation and measuring the ratio of the signals. This ratio is directly proportional to the normalized Stokes parameters, Q/I and U/I, and by doing so one is able to measure small signals against a strong, irrelevant background of unpolarised light. Also, because we are measuring relative quantities, any sources of photometric error are automatically compensated for. In the linear mode, the modulator of the IAGPOL consists of a half-wave achromatic retarder plate. The effect of the retarder is to introduce a phase difference ϕ between the ordinary and extra-ordinary rays. For the half-wave plate, $\phi = \pi$. In the most general case, the Mueller matrix $\mathcal{M}_{\rm WP}$ for the retarder is:

$$\mathcal{M}_{\rm WP} = \begin{pmatrix} 1 & 0 & 0 & 0 \\ 0 & 1 & 0 & 0 \\ 0 & 0 & \cos\phi & -\sin\phi \\ 0 & 0 & \sin\phi & \cos\phi \end{pmatrix}. \tag{2.37}$$

A *half-wave retarder* is described as a diagonal matrix $\mathcal{M}_{\rm HWP}$ of $\det(\mathcal{M}_{\rm HWP}) = 1$ representing a reversion in the ellipticity and orientation angles of the polarisation ellipse (that is, a sign inversion of the U or V components):

$$\begin{pmatrix} 1 & 0 & 0 & 0 \\ 0 & 1 & 0 & 0 \\ 0 & 0 & -1 & 0 \\ 0 & 0 & 0 & -1 \end{pmatrix} \quad \text{or} \quad \begin{pmatrix} 1 & 0 & 0 & 0 \\ 0 & -1 & 0 & 0 \\ 0 & 0 & 1 & 0 \\ 0 & 0 & 0 & -1 \end{pmatrix} \tag{2.38}$$

for component orientations $\eta = 0^\circ$ or 90° and $\eta = \pm 45^\circ$ respectively, 0° denoting the principal component of the modulator. In the case of IAGPOL, the retarder consists of a plane-parallel plate with the optical axis parallel to its sides, which is rotated to modulate the polarisation of the light which will be registered by the detector. The half-wave retarder modulates the incoming polarisation with a frequency four times that of its physical rotation, meaning that a minimum of four positions of the retarder plate (and higher multiples of this fraction) are required to cover an entire modulation cycle. Since the Stokes *pseudo*-vectors have an intrinsic directional ambiguity, positions 90° apart are equivalent.

Figure 2.21 describes graphically the workings of a modulator for linear polarisation. In our observations we took images at eight different positions of the retarder, since the measurement errors scale with $1/\sqrt{n}$, where n is the number of positions of the plate. The different positions of the retarder lead to a sine wave in the analyser output, the phase of which corresponds to the polarisation angle of the incoming radiation. Its degree of polarisation results from the ratio of the intensity of the ordinary and extra-ordinary rays to the total intensity I incident on the detector and measured at each different position. Again, the greatest benefit of the technique of modulation is that it makes the measurement of the normalised Stokes parameters (Q/I and U/I) insensitive to most sources of error. These ratios are insensitive to any external effects – such as gain-variations or atmospheric scintillation – which equally affect the two orthogonal states of polarisation and the average signal. Thus the fractional error in the degree of polarisation is in practice limited by that of the total intensity I (called photometric error).

Due to the finite (and relatively large) integration times required by the CCD detector at each position of the retarder – for PKS 2155-304 typical integration times of $\sim$ 150 s per position of the modulator were necessary – extra noise will be introduced in the measurement process which can be eliminated by the use of a *two-beam analyser*,

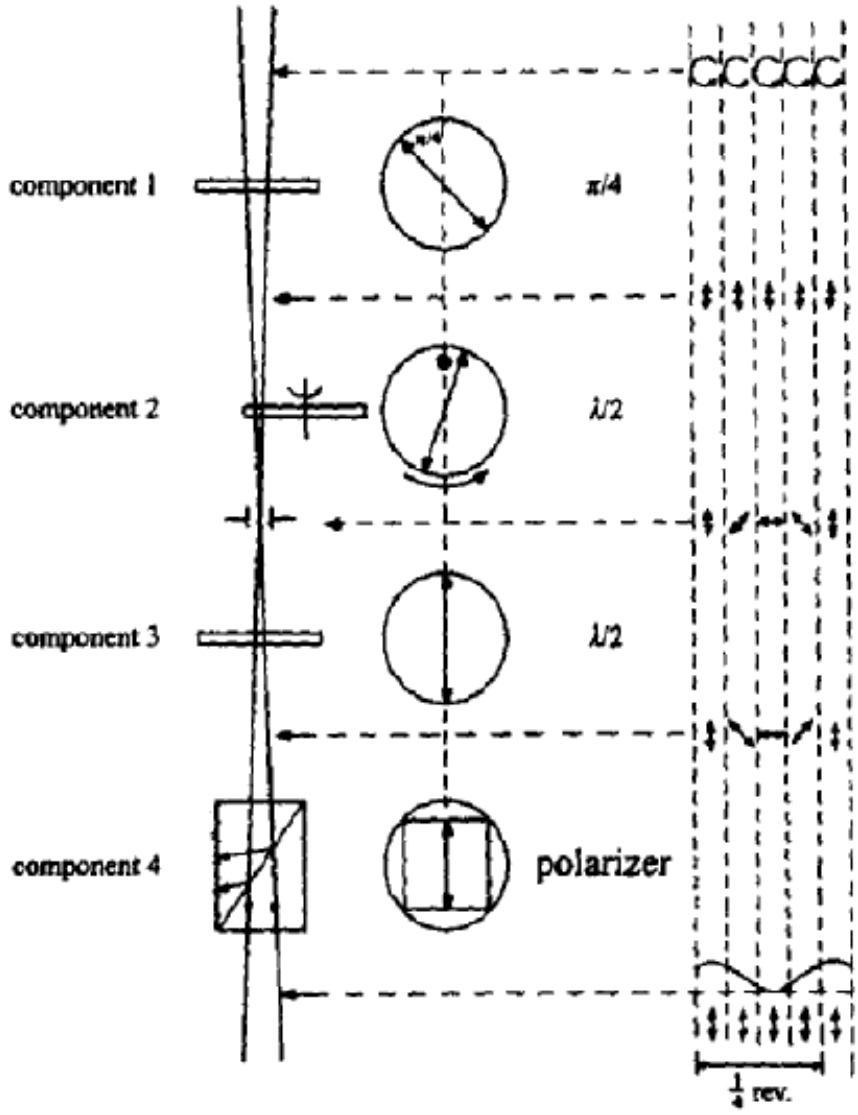

Figure 2.21: Scheme of a modulator for linear polarisation of halfwave rotator plate. The fundamental element of the modular is component 2, which is the retarder plate. Component 4 is called the analyser and consists of a polariser that splits the wave in two orthogonal rays for simultaneous measurement in the CCD. Component 4 can be for example a Savart-prism or a polaroid. Component 1 is not relevant for linear polarisation and component 3 has simply the function of correcting the phase of the modulated output signal. Figure from [332].

such as a calcite Savart prism [332], which splits the output of the modulator into two orthogonally-polarised images that are simultaneously imaged in the field of the CCD. In this way, observation under non-photometric conditions is possible and sky polarisation is automatically compensated for without the need for flatfielding. The effect of the *fixed analyser* is to single out a specific polarisation of the incident light (or to split it into its orthogonal components, in the case of a two-beam system); its effect can therefore be

described by the Mueller matrices for a linear polariser, $\mathcal{M}_{\pm Q}$ or $\mathcal{M}_{\pm U}$, such as given by Equations 2.36.

To conclude, a full description of the observational procedure can be given in a compact form using Mueller calculus. If $\mathcal{S}_{in}$ is the Stokes-vector representation of the incoming radiation and $\mathcal{S}_{out}$ represents the final measured quantities, we have, for example:

$$\mathcal{S}^{-}_{out} = \frac{1}{2}\,\mathcal{M}_{-Q} \cdot \mathcal{M}_{\theta} \cdot \mathcal{S}_{in} \tag{2.39}$$

$$\mathcal{S}^{+}_{out} = \frac{1}{2}\,\mathcal{M}_{+Q} \cdot \mathcal{M}_{\theta} \cdot \mathcal{S}_{in} \tag{2.40}$$

for an arrangement with two sequential half-wave retarder plate positions at 0° and 45° and an analyser with optical axis $\eta = 0°$ giving ordinary and extra-ordinary rays at the ±Q positions, respectively. The factor $1/2$ indicates that only half of the total intensity I of the partially polarised light goes to each orthogonal image of the ideal polariser. For the specific case of interest to us of a rotated half-wave plate, we have:

$$\mathcal{M}_{HWP}(\theta) = \begin{pmatrix} 1 & 0 & 0 & 0 \\ 0 & \pm\cos 4\theta & \sin 4\theta & 0 \\ 0 & \sin 4\theta & \mp\cos 4\theta & 0 \\ 0 & 0 & 0 & -1 \end{pmatrix}, \tag{2.41}$$

where the first sign in ± or ∓ is for component orientations $\eta = 0°$ or 90° and the second sign for $\eta = \pm 45°$. To get the final form of $\mathcal{S}_{out}$ for the two orthogonal beams, we just multiply by the specific polariser matrices of interest (Equation 2.36).

2.2.3 Principles of Reduction of Polarimetric Data

An in-depth description of the IAG polarimeter (IAGPOL), beyond what has been given in the previous sections, can be found in Pereyra 2000 [285]. The IRAF-based software (PCCDPACK) and data analysis procedures are described in that same document and

are also available on the web[9]. We now summarise the main steps of the data reduction procedure. Details of the observations in this thesis are presented in Chapter 6.

First of all, a sequence of eight images are taken for the object of interest (in our case the blazar PKS 2155-304), each one for a different position of the retarder plate, which differ therefore by $\pi/8$ on the optical angle; each of these images is a double image of the object due to the Savart prism, which splits the ray into its orthogonal polarisations. To each of these images corrections for *bias, flatfielding* and *overscan* are made, after which coordinates are assigned to the objects of the field so that the images can be combined *a posteriori*: these procedures are all done using standard IRAF reduction routines. Background subtraction is done within this process in the standard way as for any optical photometric measurement, and are carried out individually for each field.

This being done, the photometric reduction package PCCDPACK [285] is used to calculate the magnitude of the object of interest in the different fields. With the sequence of photometric information, a fit to the "sinusoidal" modulation of the intensity is done to derive the object's polarisation, such as schematically illustrated in the bottom diagram of Figure 2.21. Thus, measuring the level and angle of polarisation is equivalent to determining the amplitude and phase of a sinusoidal signal in the presence of noise. Comparison stars are used to calibrate these photometric measurements and the fits to the intensity modulation. Since we have two orthogonal images for each field with a given position of the retarder plate, the only component of the sky noise that will contribute to the measurements and needs to be accounted for in the reduction process is the *photometric* one, since errors in the polarimetric measurement due to sky variations are automatically compensated for (i.e. they affect both in the same way) when the orthogonal images are combined.

At this point of the analysis we have a sequence of reduced photometric data for each position of the half-wave retarder plate β_i; notice that a rotation of the half-wave plate by β_i will correspond to the polarisation plane of the incoming radiation rotating by $2\beta_i$. So, the modulation of the intensity $I(\beta_i)$ in the detector will be

[9]http://www.das.inpe.br/ claudia.rodrigues/polarimetria/reducao-pol.html. Access date: September, 2010.

$$s = \frac{I(\beta_i) - \langle I(\beta)\rangle}{\langle I(\beta)\rangle} = P\cos\left(2(\beta_i - \delta)\right) + s_N, \tag{2.42}$$

with δ is a phase angle depending on the orientation of the wave and the sky angle and instrumental axis. The polarisation angle will be $\beta_{max} = \delta = \chi$ for which $I(\chi) = I_{\max}$. The quantity s_N is a gaussian random noise component associated to the measurement. For each simultaneous measurement of the two orthogonal components, the signal S can be calculated from the $I_\perp$ and I as:

$$S(\beta) = \left(\frac{I_\perp - I_\parallel}{I_\perp + I_\parallel}\right)_\beta. \tag{2.43}$$

Now, the form in Equation 2.42 can be decomposed into two orthogonal components:

$$s(\beta) = (q + q_N)\cos 2\beta - (u + u_N)\sin 2\beta, \tag{2.44}$$

where $q = Q/I = p\cos 2\delta$ and $u = U/I = p\sin 2\delta$ are the normalised Stokes parameters. The values q_N and u_N are noise components in phase with $\cos 2\delta$, which are the final quantities desired from the measurement process.

Any residual instrumental + foreground polarisation can be discounted by calculating (in the way described above) the polarisation parameters of standard *unpolarised* stars of the field. The principles used to derive the individual Stokes parameters and their correspondent errors from these images are standard practice in the field but lengthy to treat properly and so will be omitted here. A comprehensive description of these procedures can be found, for example, in [193] and [241].

Chapter 3

Radiation Processes in Blazars

In this chapter we deal with the main processes of radiation emission that contribute to the high-energy flux observed from blazars and their relativistic jets. We start in Section 3.1 with an account of Fermi acceleration mechanisms, thought to be the responsible for the creation of the high-energy particles which will emit the nonthermal radiation observed from the jets. We then follow in Section 3.2 with a brief discussion of the aspects of the bulk flow of the jet plasma and their effect on the observational properties of the source. The Chapter is concluded in Section 3.3 with a detailed discussion of the two dominant radiation process in the jet: synchrotron radiation and inverse-Compton scattering.

3.1 Particle Acceleration

Active galactic nuclei produce the majority of their radiative output in the form of non-thermal emission. Having already introduced in Chapter 1 the main conditions which can lead to the production of gamma-ray emission, we will now concentrate on the details of the synchrotron and inverse-Compton processes which are believed to power the AGN spectrum and the emission from extragalactic jets, and to produce the GeV-TeV gamma-ray fluxes we observe from active galaxies. The non-thermal gamma-ray emission from jets requires the presence of very energetic particles, of energies up to 10 TeV or so; studying of the processes through which such particles are accelerated is therefore a pre-requisite to understanding the origin of the GeV-TeV gamma-rays. In fact, given the large energies involved and the rapid energy-loss times of the radiating particles, gamma-rays

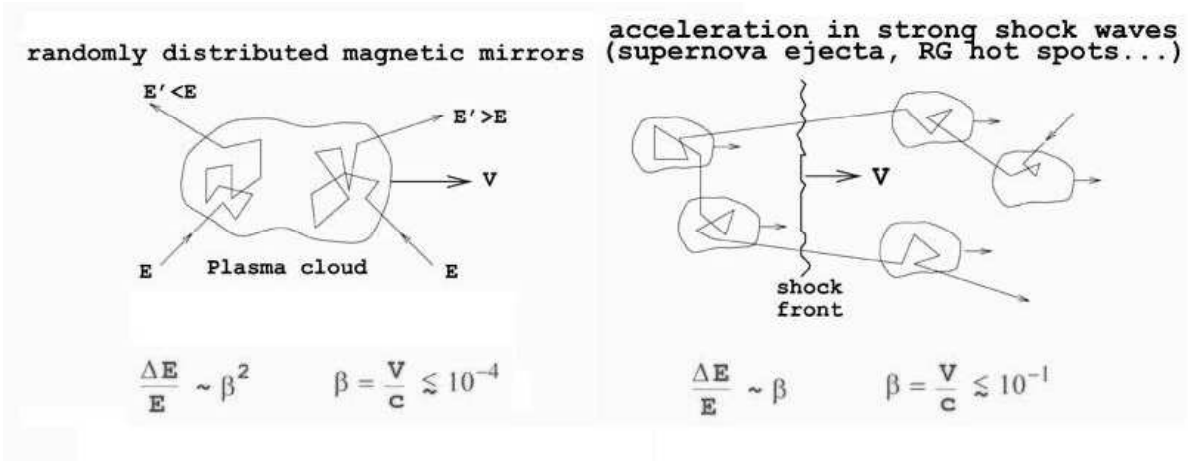

Figure 3.1: Schematic representation of the first (left panel) and second order (right panel) Fermi particle acceleration mechanisms.

can be thought of in this context as the ideal tracers of energetic particle populations and of particle acceleration sites in jets.

3.1.1 Fermi Processes

Electric fields are *a priori* the only way in which charged particles can be accelerated, since the Lorentz force of magnetic fields $q(\mathbf{v} \times \mathbf{B})$ is always perpendicular to the momentum of the particle and so does not do work. Static electric fields cannot nevertheless be maintained in astrophysical situations due to the high conductivity of astrophysical plasmas. But if the particle is in relative motion, then the induced electric field in the particle's reference frame $\mathbf{E} = -\partial\mathbf{B}/\partial t$ will be able to do the necessary work to produce acceleration.

Diffusive shock acceleration is believed to be the main mechanism through which particles are accelerated within the relativistic jets of AGN. The main theory behind this mode of particle acceleration are the so-called Fermi magnetic acceleration mechanisms, proposed by E. Fermi in 1949 [140], in which particles are accelerated by means of energy transfer from moving magnetised plasma clouds. Fermi's original intuition was that in an environment where the plasma density (and therefore the magnetic field density) are variable, a charged particle (e.g., an electron or a proton) will eventually "collide"

with randomly moving "magnetic mirrors" and be reflected, thus gaining or losing kinetic energy in the process. In the most likely case of a net energy gain after a series of such collisions, particles escape the system having been accelerated by an amount $\delta E = (V/c)^2\ E$ per collision, where E is the initial energy of the particle, and V/c the velocity of the scattering cloud or "magnetic mirror".

The probability of gaining or losing energy in the collision is proportional to the probability of head-on versus overtaking collisions with the scattering surfaces. Since these scale with the magnitude of the relative velocities ($v + V$ and $v - V$, respectively), it is easy to see that there is a (slightly, since $v \gtrsim V$) higher probability of head-on collisions and therefore a net energy gain in the process. Formally, allowing for all random angles of collisions possible, the particle's energy balance per collision would be:

$$\frac{E'}{E} = \frac{1 \pm 2V\beta\cos\vartheta + V^2}{1 \mp V^2}, \tag{3.1}$$

where V is the cloud velocity, βc the particle's velocity, ϑ the collision angle, and the upper sign in $\pm$ or $\mp$ is for head-on and overtaking collisions, respectively. The result for the average of many collisions is:

$$\langle \ln(E'/E) \rangle = 4V^2 - 2V^2\beta^2\cos^2\vartheta. \tag{3.2}$$

After N such collisions (in some of which the particle will stochastically lose energy to the scattering wall) the particle would have attained an energy $E = Mc^2\ \exp(V^2N/c^2)$, where M is the (very large) mass of the scattering cloud. The situation is illustrated in Figure 3.1, and this original mechanism is called 2$^{\text{nd}}$ order process because the energy gain scales with $(V/c)^2$. The great attractiveness of this mechanism is its prediction that, if the age distribution of particles in the system follows an exponential distribution, then the integrated effect of these collisions over time is to generate an energy spectrum for the whole population which obeys an inverse power law in energy, as regularly observed in the cosmic rays.

Diffusive shock acceleration

There exists another, more efficient way to accelerate particles by scattering off "magnetic mirrors"; this is the dominant mode in diffusive shock acceleration, which is thought to be operative inside the jets. The basic theory was developed by Bell in 1978 [76] and [77]. The main ingredient of this mechanism is the same as before, that is, the presence of a highly magnetised scattering surface, which here is provided by the compressed plasma at a shock front, as illustrated in Figure 3.1. The great attractiveness of this model comes from the ubiquity of shocks in (quasi-) relativistic astrophysical environments and the fact that this mechanism can produce power law particle distributions with a spectral index in energy of about -2.5, close to what is observed in cosmic rays and deduced from synchrotron emission spectra. It thus responds to the necessity of finding a likely acceleration mechanism that is universal.

In the present case, the shock front works as a "converging scattering region", which guarantees the process will be of the first order in (V/v). Bell's treatment assumes that the particles enter the system already with relatively high energy, so that the upstream flow can catch up with the shock. Furthermore, since the shock front is relatively thin compared to the gyroradius of the particles, once they reach the shock they can cross it without difficulty. The effect of crossing the shock is that the flow will become turbulent and the bulk kinetic energy will be converted into random motion, accelerating the particles. When the particles cross to the downstream side of the shock, they will be faster than the Alfvén speed of the plasma. This will generate Alfvén waves [44] which will prevent the particles from escaping by isotropising their velocities and scattering them back to roughly the Alfvén speed downstream of the shock, and the front will catch up with them again. As a result, Bell observed that energetic particles will cross the shock front many times, between the turbulent wake upstream and Alfvén waves downstream of the scattering surface, gaining energy from the head-on collisions with the shock at each time.

Mathematically, we can equate the parameters of the diffusing particle by observing that when it crosses from one side to the other of the shock, its energy *in the rest frame of the scattering centre* is given by the following Lorentz transformation:

$$E' = \gamma v(E + \beta \cos \vartheta), \tag{3.3}$$

where v is the particle's speed, $\beta = V/c$ is the relative speed between the upstream and downstream plasmas, and E and E' are the particle's energies before and after the crossing respectively; here $\gamma = \sqrt{(1 - v^2/c^2)}$ is the Lorentz factor of the particle. In the reference frame of the shock $V = V_s\,(\kappa - 1)/\kappa$, where κ is the compression factor of the shock. As pointed out before, the particles will go through a series of such crossings. This crossing rate was calculated by Bell, who observed that the rate of particles *crossing and recrossing* the shock is $1/4nv$, where n is the number density of particles and v the particle's velocity. Because the particle's energy isotropises after every crossing, some of the particles will be lost upstream of the shock, at a rate proportional to the ratio of the shock and the particle's velocity $V/v \sim V/c$. So the escape probability is $1 - (V/c)$, and after k crossings we will have $N = N_0\mathcal{P}^k$, where N_0 is the initial (injected) number of particles.

For such a particle, which has crossed the shock $k - 1$ times, the total energy gain in the $(k + 1)$th crossing will be:

$$E_{k+1} = E_k\left(\frac{1 + v_{k1}V\cos\vartheta/c^2}{1 + v_{k2}V\cos\vartheta/c^2}\right), \tag{3.4}$$

where the indices 1 and 2 refer to crossings from downstream and upstream, respectively. Thus the total energy gain after k+1 crossings is:

$$\ln\left(\frac{E_{k+1}}{E_0}\right) = \frac{4}{3}(k + 1)(\kappa - 1)\frac{V_s}{\kappa c}, \tag{3.5}$$

where the factor E_0 is the injection energy of the particle and the factor 4/3 results from the average of all possible angles of scattering between $[0, \pi/2]$, multiplied by 2 to account for the round trip.

The final power-law energy spectrum of the particles can be readily obtained by combining the escape probability with Equation 3.5 written in the form $E = E_0\beta^k$, to obtain the ratio $\ln\mathcal{P}/\ln\beta = \ln(N/N_0)/\ln(E/E_0)$, which gives:

$$dN = \left(\frac{k + 2}{k - 1} - 1\right)N_0\left(\frac{E}{E_0}\right)^{-\frac{k+2}{k-1}}. \tag{3.6}$$

For a strong shock and a completely ionised gas, corresponding to $r = 4$, we recover a distribution $N(E) \propto E^{-2}$, which is close to, but a bit harder than, the universally observed value of ≈ -2.5. Finally, we mention that this mechanism is a suitable explanation for the

origin of TeV gamma-rays, since the maximum energy attained by accelerated particles in the first order Fermi process can easily surpass the required values of 10 TeV or so [247].

3.1.2 Acceleration timescale and particle energies

An important quantity in the analysis of our observations in Chapters 5 and 6 is the concept of acceleration timescales. The acceleration timescale is defined as the time needed for the particle energy to roughly double. In the case of the first order Fermi-acceleration, this occurs approximately at every crossing+re-crossing of the shock front, so the acceleration timescale is $t_{\rm acc} \approx t_{\rm cycle}$, which in turn is the sum of the *residence times* upstream and downstream of the shock front $t_{\rm up} + t_{\rm down}$ [164]. Since the crossing from upstream is due to magnetic field deflection, the upstream time is inversely proportional to the shock's Lorentz factor Γ_s and the particle's gyrofrequency ω_B:

$$t_{\rm up} \sim \frac{1}{\Gamma_s \omega_B} \equiv \frac{\gamma_e m_e c}{q \Gamma_s B}, \tag{3.7}$$

where γ_e is the electrons' Lorentz factor, m_e the electron's rest-mass and q its charge. The term Γ_S is the Lorentz factor of the shock and B the downstream (uncompressed) magnetic field intensity. Now, the downstream re-crossing, which is due to scattering off the Alfvèn waves, will have a timescale dictated by the particle's diffusion time, which in the case of Bohm diffusion is simply inversely proportional to the gyrofrequency of the particle:

$$t_{\rm dn} \sim \frac{1}{\omega'_B} \equiv \frac{\gamma'_e m_e c}{q B'}, \tag{3.8}$$

where the primes are to distinguish downstream from upstream conditions.

From the Rankine-Hugoniot jump conditions (see for example [164]), we know that the shock compression of the magnetic field will be given by $B' \approx \Gamma_s B$, and so $t_{\rm up} \sim t_{\rm dn}$; thus $t_{\rm acc} \gtrsim 2t_{\rm up}$. Now, it will be explicitly discussed in Chapter 6 that, when spectral variations are observed accompanying flux variability in the source, this is a signature that the cooling times of the particles are shorter or of the order of the acceleration timescales, $t_{\rm cool} \lesssim t_{\rm acc}$. Therefore observations of particle cooling can be used to put constraints on the magnetic field intensities and Lorentz factor of the shocks.

These final considerations on the acceleration timescales can also be used to estimate the maximum energy attainable by the particles in shock acceleration. In the abscence of other energy loss mechanisms, the acceleration timescales $t_{\rm acc}$ can be estimated (by an analogous reasoning to the one above) to be shorter than the age of the system, which is associated for example with the adiabatic expansion of the system and its correspondent loss-times. Now, the latter has as an upper limit, the light-crossing time of the region R/c, so that:

$$\gamma_{e;\max} \approx \frac{qB\Gamma_s R}{m_e c^2}. \tag{3.9}$$

Observe that this is greater, by a factor of Γ_s, than an estimate that simply requires the gyroradius of the particle to be bounded within R. But this is the appropriate relativistic expression, since in fact the particle will typically execute only $1/\Gamma_s$ of its Larmor orbit before crossing the shock [164].

3.1.3 Shocks in Jets

A concrete realisation of the presence of shocks in jets can be seen in the form of inhomogeneities that are observed in the images of extragalactic jets throughout the spectrum, from radio to X-rays. In fact,the great majority of jets show localised patches of high-intensity emission, called "knots" (or hot spots when they coincide with external shocks at the jet termination point) along their length. M.J. Rees was the first to identify, in 1978, the knots in the jet of M 87 with internal shocks which develop due to irregularities in the flow speed [301]. In simple terms, he noted that if the flow velocity v_j changes by a factor $\Delta v_j/v_j \gtrsim M_j^{-1}\Gamma_j^{-2}$ on a timescale Δt, where M_j is the flow's Mach number and Γ_j its bulk Lorentz factor, than the faster material will be able to catch up with the slower flow ahead of it in a time $\sim v_j \Delta t/\Delta v_j$, creating a strong shock traveling with a speed $\sim v_j$. The fraction of kinetic energy which gets dissipated by the jet in the process was predicted by Rees to be $\sim \Gamma_j^2 \left(\Delta v_j/v_j\right)^2$, and so to be proportional to the jet's bulk Lorentz factor.

Another piece of observational evidence in favour of shocks existing all the way along the flow is the requirement for *in situ* particle acceleration, which is necessary to sustain the synchrotron emission throughout the jet, given the relativily fast cooling times of the

radiating particles in the presence of strong magnetic fields (see next Section). Similarly, the idea of "knots" as relativistically propagating shocks is in accordance with the "Doppler favouritism" which accounts for the high jet/counter-jet surface brightness ratios of the knots [46].

Another way of producing such brightness enhancements due to internal shocks is by the development of large-amplitude instabilities in the jet. Evidence for the existence of instability-driven shocks can be sought for example in the regular spacing of the "knots" in the inner kpc-scale jet of M 87 and other objects, which is consistent, for example, with the development of the fastest-growing large-scale modes of Kelvin-Helmholtz instability [73].

3.1.4 Interlude: The Bulk Flow

Following on the simple ideas for shock-in-jet models from the previous section, we could consider that an injection of plasma in the jet will start off with low bulk speeds and will propagate and accelerate along the jet collimation region (see Section 4.5) to a final Lorentz factor $\Gamma \sim \Delta\Gamma$. If $\Gamma \sim \Gamma_{\rm TeV}$, the minimum Lorentz factor necessary for gamma-ray emission from the radiation Doppler boosting requirements (see Section 4.5.2), then a fundamental constraint can be put (analogous to the one we will present in the context of our work in Chapter 6) to the site of gamma-ray emission [99]:

$$R = R_\gamma \gtrsim r_g \frac{\Gamma^2}{(1+z)}, \tag{3.10}$$

where R is a distance measured from the base of the jet, r_g is the gravitational radius of the SMBH, which defines a fundamental scale for the system, and z is the redshift of the source. The above mentioned expression means that as a consequence of the relativistic expansion of the source, any variation at the central engine on timescales r_g/c will be manifested in the flow as variability with a timescale $\sim \Gamma^2 r_g$, and that gamma-ray emission will only happen after a certain distance has been crossed, in which the flow has been sufficiently accelerated, typically at a linear scale $\sim (10^2 - 10^4) r_g$ [75]. Observe that to such fundamental size constraints one should add those resulting from the discussion of internal source opacity, which will be presented in Section 4.4.

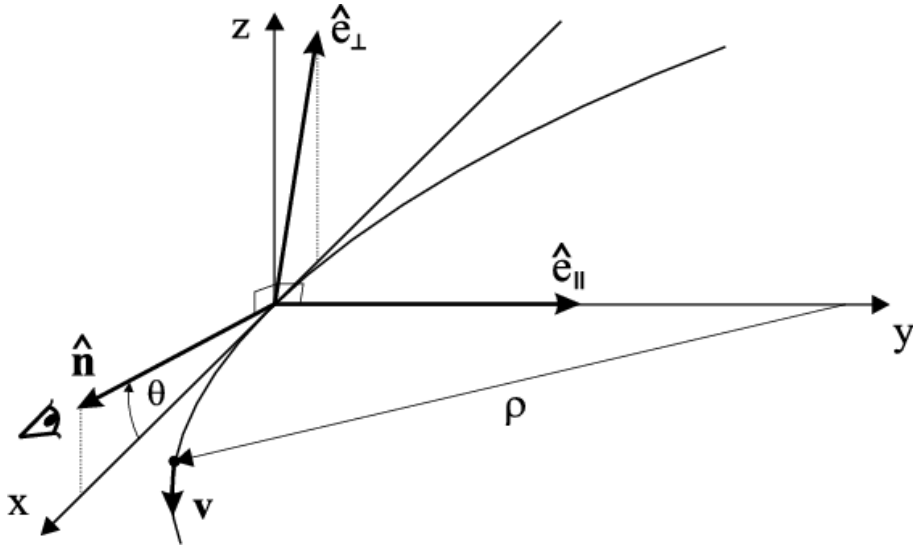

Figure 3.2: Geometry for the calculation of synchrotron emission.

3.2 Radiation Mechanisms in Blazars

3.2.1 Synchrotron Emission

Synchrotron radiation is the main mechanism responsible for the production of non-thermal emission in relativistic, high-energy sources. The theory of synchrotron radiation was developed in the early 50's to mid-60's and was reviewed in its more-or-less contemporary format by Ginzburg & Syrovatskii in two works in 1965 [175] and 1969 [176]. Below we present only the main aspects of the theory necessary to understand the contents treated in this work.

Synchrotron radiation is emitted by electrons and charged particles accelerated in a magnetic field **B**. In the classical limit, the power radiated by the electron is trivially given by Larmor's theorem [236]:

$$P = \frac{2}{3}\frac{e^2}{m_e^2 c^3}\dot{\mathbf{p}}^2, \tag{3.11}$$

where, e is the elementary charge, m_e is the electron mass and **p** is the momentum of the electron. The emitted radiation is monochromatic, of frequency equal to the Larmor frequency $e\mathbf{B}/2m_e c$.

The extension of the theory to relativistic speeds can be done by using the Lorentz invariant form of Equation 3.11 as originally derived by Schwinger in 1949 [316]. This can

be accomplished in a simple formal procedure, by considering the time derivative with respect to the proper time $d\tau = \gamma dt$, and accordingly replacing the momentum derivative $\dot{\mathbf{p}}^2$ by the relativistic invariant quantity $\mathbf{p}'^2 - (1/c^2)E'^2$. Here, the primed quantities represent derivatives with respect to the proper time $d\tau$. Thus, the expression for the relativistic-invariant Larmor formula is:

$$P = \frac{2}{3}\frac{e^2}{m_e^2 c^3}\left(\frac{E}{mc^2}\right)^2\left[\dot{\mathbf{p}}^2 - \frac{1}{c^2}\dot{E}^2\right]. \tag{3.12}$$

.

If an electron is moving in an uniform field (see Figure 3.2) its trajectory will be a circular path about the field line, and we retrieve the *betatron* formula [236]:

$$P = \frac{2}{3}\omega_B \frac{e^2}{r}\beta^3\left(\frac{E}{m_e c^2}\right)^4, \tag{3.13}$$

where $\beta = v/c$, $\omega_B = eB_\perp/\gamma m_e c$ is the cyclic (or Larmor) frequency and $r = \gamma m_e c v/eB_\perp$ is the Larmor radius of the motion. Here $B_\perp = B\sin\vartheta$, where ϑ is the pitch angle of the electron, that is the constant angle between the electron velocity and the magnetic field direction.

Equation 3.13 above is for the total intensity of radiation, integrated over all solid angles, and is therefore independent of the particular geometry of the emission (see Equation I.42 in [316]). The spectral distribution of the radiation, $P(\nu)$, on the other hand, will depend on the emission geometry, and will reflect the aberration effects of relativistic motion, departing therefore from the monochromatic approximation. In this respect, two further properties of the synchrotron radiation must be brought into the discussion: the anisotropy of the emission and its consequent frequency distribution.

Radiation anisotropy and spectral distribution

To see how the synchrotron radiation is anisotropic, consider the current $\mathbf{j}(\mathbf{R}, t) = ec\beta(t)\,\delta(\mathbf{R} - \mathbf{r}(t))$ and charge $Q(\mathbf{R}, t) = e\,\delta(\mathbf{R} - \mathbf{r}(t))$ densities of an isolated electron, where δ is the Dirac delta function. The corresponding retarded vector and scalar potentials are [283]:

$$\mathbf{A}(\mathbf{R}, t) = \frac{e\beta'}{R'_0(1 - \beta' \cdot \mathbf{R}'_0)} \tag{3.14}$$

$$\phi(\mathbf{R}, t) = \frac{e}{R'_0(1 - \beta' \cdot \mathbf{R}'_0)} \tag{3.15}$$

From these, the fields due to the moving charge can be computed directly by using the Lienard-Wiechert potentials above, calculated in the observer's reference frame. The fields at infinity are:

$$\mathbf{E} = \frac{e}{R'_0} \frac{\mathbf{R}'_0 \times [(\mathbf{R}'_0 - \beta') \times \dot{\beta}']}{c(1 - \beta' \cdot \mathbf{R}'_0)^3} \tag{3.16}$$

$$\mathbf{H} = \mathbf{R}'_0 \times \mathbf{E}, \tag{3.17}$$

from which we get the spatial distribution of the radiation [283]:

$$P_\Omega = \frac{c}{4\pi} E^2 R_0^2 = \frac{e^2}{4\pi c} \left[\frac{\dot{\beta}}{\Psi^4} + \frac{2(\mathbf{R}'_0 \cdot \dot{\beta}')(\beta' \cdot \dot{\beta}')}{\Psi^5} + \frac{(\mathbf{R}'_0 \cdot \dot{\beta}'^2)}{\gamma^2 \Psi^6} \right], \tag{3.18}$$

where $\Psi = (1 - \beta' \cdot \mathbf{R}'_0)$. It is clear from this expression that the power will not be emitted isotropically in all directions Ω, but will be highly concentrated towards the solid angles for which Ψ is small.

If the particle is highly relativistic ($\beta \approx 1$), we can expand the dot products $\beta' \cdot \mathbf{R}'_0$ in powers of the angle φ to the instantaneous direction of motion $(1 - \beta \cos\varphi) \approx 1 - \varphi + \varphi^2/2$. We readily deduce, from the fact that this expression will be of $O(1 - \beta)$ only for $\varphi \approx \sqrt{(1 - \beta)}$, that most of the power will be concentrated within a cone about the direction of motion of aperture $\varphi \sim 1/\gamma$. This result is consistent with what is expected from the simple transformation of solid angles due to relativistic aberration in the forward direction of motion.

The general trajectory for a charged particle moving with some initial velocity about a uniform field is that of a helix around the field lines, as shown in Figure 3.3. Given the anisotropic character of the radiation derived from Equation 3.18, an observer watching the particle's movement will see the radiation as a series of pulses which are apparent when the instantaneous direction of motion crosses the line-of-sight, with a period $T =$

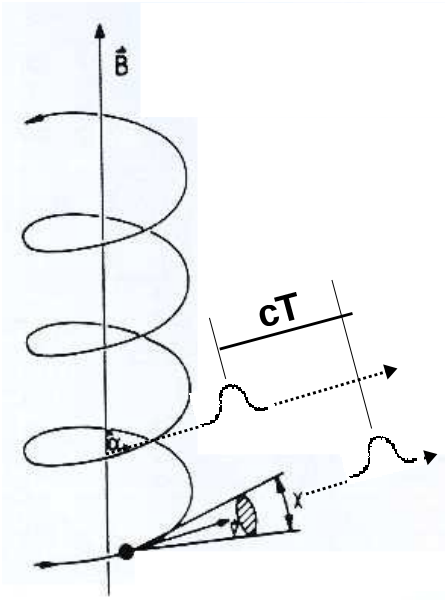

Figure 3.3: Pulsed synchrotron emission from an electron gyrating about an uniform magnetic field line.

$2\pi/\omega_B(1-\beta\sin^2\vartheta)$.

The narrowness of the radiation cone naturally implies that very high frequencies are emitted. This result can be obtained mathematically, following the reasoning presented in Ginzburg & Syrovatskii 1965 [175]. The radiation spectrum constructed from this sequence of pulses will consist of harmonics of the frequency ω_B. The frequency carrying the maximum power is defined by the width of the pulse $\Delta\tau$. For a cone of half-aperture $\varphi \sim 1/\gamma \simeq E/mc^2$ and $\beta \approx 1$, we have $\Delta\tau \simeq r\varphi/\gamma c = mc/eB_\perp\ (mc^2/E)^2$, where the term $1/\gamma$ in the first equality is to convert from the proper time of the electron to the observer's time. Thus, the frequency of the emission where most of the synchrotron power is radiated is:

$$\nu_m \sim \frac{1}{\Delta\tau} \simeq \frac{eB_\perp}{mc}\left(\frac{E}{mc^2}\right)^2 = \gamma^2\omega_B. \tag{3.19}$$

Now, to calculate the exact power distribution, observe that the series of EM pulses can be represented as a Fourier series of monochromatic waves of frequency $n(\omega_B/sin^2\vartheta)$ mentioned before [283]:

$$\mathbf{E}(t) = \Re\left(\sum_{-\infty}^{+\infty} E_n\ \exp\left(-i\frac{\omega_B}{\sin^2\vartheta}nt\right)\right), \tag{3.20}$$

where the amplitudes $\mathbf{E}_n$ are

$$\mathbf{E}_n = \frac{\omega_H}{2\pi \sin^2 \vartheta} \int_0^{\frac{2\pi \sin^2 \vartheta}{\omega_B}} \mathbf{E}(t)\ \exp\left(i \frac{\omega_B}{\sin^2 \vartheta} nt\right) dt. \tag{3.21}$$

To obtain the spectral distribution of the radiation, we thus have to use the expression for the field given by 3.16 in Equation 3.21 above, and then calculate the power as done before in Equation 3.18 as $P_{n\Omega} = (c/2\pi)|E_n|^2 R^2$. The calculations are straightforward but lenghty and require algebraic care; they are presented in full detail both in [316] and [353]. The final result is:

$$P(\nu) = \frac{\sqrt{3}}{4\pi} \frac{e^2}{r^2} \left(\frac{E}{mc^2}\right)^4 \frac{\nu c}{\nu_c^2} \int_{\nu/\nu_c}^{\infty} K_{5/3}(\eta) d\eta, \tag{3.22}$$

where K are Bessel functions of the second kind which govern the shape of the energy distribution in frequency (see Figure 7 in [175]). The critical frequency ν_c is defined as $3/4\pi\ \nu_m$. A corollary of the concentration of the power around ν_m is that for a given magnetic field intensity, all synchrotron photons of a given energy can be regarded as produced by electrons with approximately the same Lorentz factor γ. In this way we have an important one-to-one correspondence between the observed spectrum and the energy of the emitting particles that allow us to map the energetics of the source.

Integrating Equation 3.22 over all frequencies we have the total energy loss rate by the electron due to synchrotron radiation:

$$-\frac{dE}{dt} = \int P_\nu d\nu = \frac{4}{3} \frac{e^2 c B^2}{8\pi (m_e c^2)^4} E^2 = \frac{4}{3} \beta^2 \gamma^2 \sigma_T c U_B \tag{3.23}$$

which is proportional to the square of the electron's Lorentz factor and the magnetic field density $U_B = B^2/8\pi$, where $\sigma_T = (e^2/m_e c^2)^2$ is the Thomson cross section, and $\beta \approx 1$. The appearance of the Thomson cross section here underlines the quantum nature of the synchrotron radiation as the scattering of electrons off the virtual photons of the electromagnetic field. Using the electron energy in GeV and the magnetic field intensity in Gauss, we have that the loss rate is given by $-dE/dt = 1.5 \times 10^{-5}\ B_G^2 E_{GeV}^2$ erg s^{-1}. From this, we obtain the lifetime of an electron in a magnetic field (also called the synchrotron cooling time), defined as:

$$T_{\rm sync} = \frac{E}{dE/dt} = \frac{3}{4}\frac{(m_e c^2)^2}{2\gamma c e^2 B^2} \sim 6.2 \times 10^6 B_G^{-2} E_{GeV}^{-1} \text{ s}, \tag{3.24}$$

which shows that high-energy electrons cool faster. This fact will be responsible for introducing curvature in the spectrum and will be a signature of aged particle populations in steep-spectrum sources, as for example in the SEDs of large scale regions of active galaxies.

Radiation from an ensemble of Electrons

We saw in Section 3.1.1 that diffusive shock acceleration will give rise to a population $N(\gamma)$ of particles with exponential distribution of energies $m_e c^2 \gamma$:

$$N(\gamma)d\gamma = N_0 \gamma^{-p} d\gamma, \tag{3.25}$$

where the exponent $-p$ can be derived from the shock parameters as in 3.6, and has a typical value of ≈ -2.5. The synchrotron spectrum of a source will then be the integrated emission of this population of particles, which is given by the *synchrotron volume emissivity*:

$$\rho j_\nu = \int_{\gamma_{min}}^{\infty} P_\nu(\gamma) N(\gamma) d\gamma. \tag{3.26}$$

One way to calculate ρj_ν is simply to insert the expression for $P_\nu(\gamma)$ obtained from Equation 3.22 with $N(\gamma)d\gamma$ and proceed with the algebra. Another approach due to Shu 1991 [320] is to recall a result from the previous section, which showed that most of the power emitted by an electron with a given Lorentz factor γ is radiated at a particular frequency $\nu_m = 4\pi/3\nu_c = \gamma^2 eB/mc = \gamma^2 \omega_B$. We can then re-write Equation 3.22 in the form:

$$P_\nu(\gamma) = \frac{\sqrt{3}}{2}\frac{e^3 B}{mc^2}\phi_\nu(\gamma), \tag{3.27}$$

where the $\phi_\nu(\gamma)$ is a formal term which absorbs all the dependency on the frequency distribution, as a function of the electron Lorentz factor γ. We then replace $\phi_\nu(\gamma)$ by a delta function centered on the maximum emitting frequency $\nu_m = \gamma^2 \omega_B$, that is: $\phi_\nu(\gamma) =$

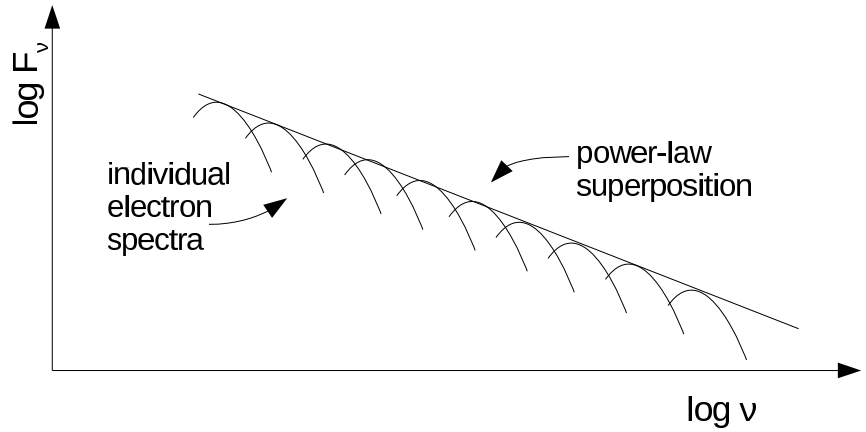

Figure 3.4: Wide-band power-law spectrum of a synchrotron source shown as the superposition of a sequence of mono-energetic synchrotron spectra.

$\delta(\nu - \gamma^2\omega_B)$. The idea behind this approximation is indicated in Figure 3.4, where it is shown how the superposition of the synchrotron spectrum of individual electrons gives rise to a wide-band power law spectrum characteristic of AGN. This result is obtained mathematically by integrating Equation 3.26 over gamma with the approximation 3.27, to obtain the synchrotron emissivity [320]:

$$\rho j_\nu \simeq \frac{\sqrt{3}}{2} N_0 \frac{e^3 B}{mc^2} \left(\frac{\nu}{\nu_c}\right)^{-(p-1)/2} . \tag{3.28}$$

This expression is accurate to a factor of order unity. The spectral index for the synchrotron spectrum of a population of nonthermal particles is then $\alpha = (p-1)/2$ and $\rho j_\nu \sim \nu^{-\alpha}$ is a pure power-law.

There are two additional factors which will modify the appearance of the synchrotron spectrum from a population of particles. The first one is the fact that since particles of higher energy cool faster, aged populations will not have an exponent that is constant over all ranges of electron Lorentz factors γ. After a time of the order of the synchrotron cooling time $T_{\rm sync}(\gamma_1)$, particles originally injected with energies $\gamma \gtrsim \gamma_1$ will have lost most of their energy and the spectrum will show a break in the power law at a frequency $\nu_{\rm break} = 3/4(mc^2/eBT_{\rm sync}(\gamma_1))$. In the νF_ν plot, this break frequency will roughly coincide with the *peak of the emission spectrum* of synchrotron radiation, and this fact will be used in Chapter 5 to calculate parameters for the acceleration of the bulk flow in the blazar PKS 2155-304 from energy-dependent time-delay measurements. The second factor is synchrotron self-absoprtion, which reflects the compactness of the source.

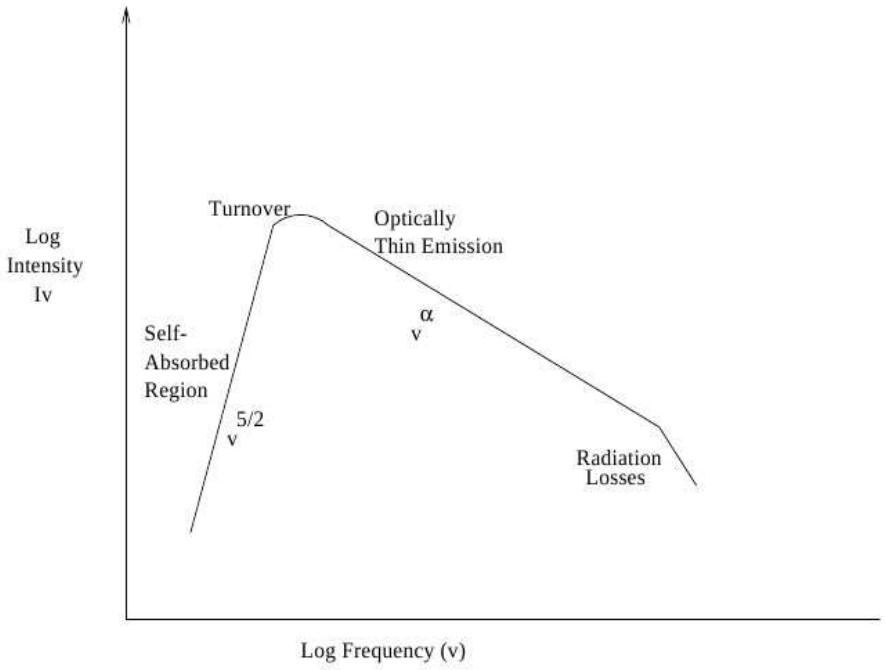

Figure 3.5: Spectrum of a compact synchrotron source showing the effect of synchrotron self-absorption.

Compactness of sources: synchrotron self-absoprtion

Radiation emission/absorption in a system of particles can be thought of as a Markov process, i.e. it is a memoryless stochastic process, in which the past and future states of the system are independent of the present state. This means that it must obey the principle of detailed balance, which states that *"in thermodynamic equilibrium, every elementary process is statistically balanced by its exact reverse"* [320], which is an equivalent to Kirchhoff's well-known thermodynamic statement from which the *blackbody limit* is derived, namely that the emissivity of a medium equals its absorption capacity. In fact, the power in Equation 3.28 diverges beyond the blackbody limit for low frequencies, which is physically impossible by the law of energy conservation.

For a synchrotron source of spectrum $\rho j_\nu \propto \nu^{-\alpha}$, a "brightness temperature" can be formally defined as $T_b = \rho j_\nu c^2/2k\nu^2$, where k is the Boltzmann constant. The brightness temperature is thus proportional to $\nu^{-(2+\alpha)}$, and defines the regime in which the radiation and the particles are in *thermal equilibrium*, that is $\gamma m_e c^2 \approx 3/2KT(\nu)$. This will happen for the lowest frequency photons of the system ($\nu < \nu(\gamma^*)$), for which the kinetic temperature of the electrons can then be written as $T_k = \gamma^* m_e c^2/3k = T_b$. Recalling that

$\gamma^* \approx (\nu/\omega_B)^{1/2}$, we have:

$$\rho\, \mathrm{J}_{\nu<\nu(\gamma^*)} = \frac{2kT_k}{c^2} = \frac{2m}{3\omega_B^{1/2}}\nu^{5/2} \propto \frac{\nu^{5/2}}{B^{1/2}}. \tag{3.29}$$

And the turnover frequency marking the passage between the high-frequency optically thin and low-frequency optically thick cases is $\nu(\gamma*) \approx \omega_B$.

These few results are all we need to understand the main physical effects of the synchrotron self-absorption. Detailed expressions for the absorption coefficient of the source κ_ν, which allow a more formal derivation of the source function $\rho\, j_\nu/\rho\kappa_\nu$ can be found, for example, in Rybicki & Lightman 2004 [305].

Polarisation of Synchrotron Radiation and Magnetic Field Structure

There is one last topic of synchrotron radiation to be treated, which is fundamental for the understanding the physics of extragalactic jets: its polarisation. Whereas the radiation of a non-relativistic particle is circularly polarised, synchrotron radiation from a single relativistically moving particle will be elliptically polarised. The result of this is that (by superposition) the emission of a system with some anisotropy in its geometry will have a certain direction that is favoured over the others, and the radiation from the particle distribution will be linearly polarised, which is a distinctive observational property of nonthermal emission in AGN and an important diagnostic of the source structure.

The basic reason for the elliptical character of the polarisation is again of a geometrical character. In the passage from the non-relativistic to the relativistic case, we have seen that the dipole radiation of the accelerated particle becomes beamed in the forward direction of motion into a cone of half-opening angle $\varphi \sim 1/\gamma$. This means that now the parallel field component (when the electron is moving towards the observer in its circular or spiral orbit) has a different time dependence within each pulse in relation to the perpendicular one. When deriving Equation 3.22 we implicitly ignored this vectorial character of the emission, expressed in the cross products in the expression for the electric field in Equation 3.16.

To recover this information, let us go back to Equation 3.22, for the spectral synchrotron power, and recall the following recurrence relation for the Bessel function $K_{5/3}(\eta)$

[316]:

$$\frac{2d}{d\eta}K_{2/3}(\eta) = K_{5/3}(\eta) + K_{1/3}(\eta). \tag{3.30}$$

Since K_α carries the angular information that was implicitly integrated out in Equation 3.22 [353], by inserting this relation in Equation 3.22 we can recover the two integral equations for $P_\perp(\nu)$ and $P_\parallel(\nu)$, the power perpendicular and parallel to the instantaneous direction of motion, respectively. In fact, integrating the relation 3.30 and calling (as Longair 1994 [247] does it):

$$F(x) = x\int_x^\infty K_{5/3}(z)dz \quad \text{and} \quad \mathrm{G(x) = x\ K_{2/3}(x)}, \tag{3.31}$$

where the variable transformation $x = \nu/\nu_c$ took place, we retrieve the powers:

$$P_\perp \nu = \omega_B j_\perp(\nu) = \mathrm{cons[F(x) + G(x)]} \tag{3.32}$$

$$P_\parallel \nu = \omega_B j_\parallel(\nu) = \mathrm{cons[F(x) - G(x)]}, \tag{3.33}$$

where it is easy to see that the total power is obtained simply by addition of $P_\perp$ and $P_\parallel$, since $P(\nu) = \mathrm{cons(x)}$. It is also simple to see that the degree of polarisation of synchrotron radiation (for a single electron) will be given, according to the definition from the previous chapter, by:

$$\Pi(\nu) = \frac{P_\perp(\nu) - P_\parallel(\nu)}{P_\perp(\nu) + P_\parallel(\nu)} = \frac{G(x)}{F(x)}, \tag{3.34}$$

which is simply the ratio of the Bessel functions in Equations 3.32. The asymptotic behaviour of both $F(x)$ and $G(x)$ for large and small x is given in Equations 3.40 of Pacholczyk 1970 [283], and imply that the polarisation can be very high – in fact for its maximum value at $\nu \sim \nu_c/2$, we have $\Pi \approx 75\%$.

Now, for a non-thermal particle population as in Equation 3.25, the integral of the population emissivity in Equation 3.28 will give a *linear* polarisation degree of [247]:

$$\Pi = \frac{\int_0^\infty G(\nu)\nu^{(p-3)/2}d\nu}{\int_0^\infty F(\nu)\nu^{(p-3)/2}d\nu}, \tag{3.35}$$

whose solution for a uniform magnetic field is presented in Longair 1994 [247] and equal to:

$$\Pi_0 = \frac{p+1}{p+7/3}. \tag{3.36}$$

For alternative geometrical configurations of the magnetic field, this value will change and we will have a net polarisaton $\Pi < \Pi_0 \lesssim 0.75$ [235]. Other effects such as a broken or curved power-law spectrum (see [279] and [309]) as well as the superposition of different particle populations will affect the appearance of the source's polarisation, introducing also the important phenomenon of spectral dependent polarisation which will be discussed in Chapter 6. Aberration due to bulk relativistic motion of the plasma can also *amplify* the source's polarisation by changing (compressing) the geometry of the magnetic field in the direction of motion in the observer's reference frame [83], but these are very extensive topics to discuss in detail here, and the aspects necessary for this work will be pointed out in the context of Chapter 6.

3.2.2 Inverse-Compton Emission

In a region of space where energetic charged particles are present, together with a high soft-photon field density, the inverse-Compton process will happen, whereby the high energy particles will scatter off the soft photons, boosting them to higher energies by transfer of momentum. This kind of scattering is the exact inverse of Compton scattering, because here the electrons are more energetic than the photons. Therefore the condition for inverse-Compton scattering to happen in astrophysical systems is that the magnetic fields present in the region be of moderate magnitude – otherwise the charged particles will cool catastrophically via synchrotron radiation and the photon up-scattering will be ineffective.

The elementary theory was developed by Compton in 1923 [107] as a quantum extension of J.J. Thomson's classical theory of X-ray scattering. Radiation scattering can be fully characterised by the ratio of the amount of energy radiated by the scattering system in a given direction to the energy flux density of the incident radiation [236]:

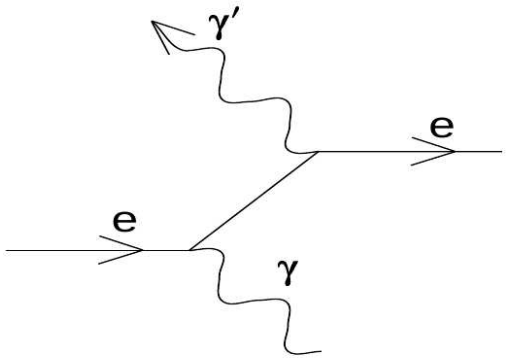

Figure 3.6: Diagrammatic representation of inverse-Compton scattering

$$d\sigma = \frac{\langle dS \rangle}{\mathbf{S}}, \tag{3.37}$$

where $\langle dS \rangle$ is the average radiated energy per solid angle and **S** the Poynting flux of the incident ray; $d\sigma$ is called the total scattering cross-section of the process.

For the non-relativistic case, $\langle dS \rangle$ is given by the dipole radiation formula $dS = (e^4/4\pi m^2 c^3)\ (\mathbf{E} \times \mathbf{n})^2\ d\Omega$, where $\mathbf{n}'$ gives the scattering direction, and $\mathbf{S} = c/4\pi\ E^2\mathbf{n}$ is the Poynting vector. From this we recover Thomson's scattering formula:

$$d\sigma_T = \left(\frac{e^2}{mc^2}\right)^2 \sin^2\theta\, d\Omega = r^2 \sin^2\theta\, d\Omega, \tag{3.38}$$

with $d\Omega = \sin\theta d\theta d\phi$, and θ is therefore the angle between the incident and the scattering directions and $\phi \in [0, 2\pi]$ the angle around the polar axis. As before, r is the gyroradius of the electron.

Quantum corrections will alter this cross-section, basically because of the momentum of the photon $h\nu/c$ which will induce a recoil of the electron: the scattering will no longer be elastic. Conservation of energy and momentum thus give, for the photon:

$$h\nu' = \frac{h\nu}{1 + \frac{h\nu}{mc^2}(1 - \cos\Theta)}, \tag{3.39}$$

where $\cos\Theta = \cos\theta\ \cos\theta' + \sin\theta\ \sin\theta'\ \cos(\phi - \phi')$ is calculated in the rest-frame of the electron. For ultrarelativistic electrons, relativistic aberration will imply that collisions will be effectively head-on and will give the energy of the photon in the centre of momen-

tum frame to be $h\nu \approx \gamma\, h\nu'(1 - cos\theta')$. This means an effective boost in the energy of the electron for the inverse-Compton scattering of $\gamma^2 h\nu$, the second γ factor coming in the expression when we change the reference frame back to the observer's frame. It can be readily seen that in the presence of very energetic electrons, the energy boost is going to be large and very high energy photons will result from the process. This is the mechanism by which gamma-rays are produced from soft optical-to-X-ray photons in blazars, giving rise to the double-bump SED seem in Figure 4.4.

The total scattering cross-section formula for unpolarised radiation consistent with Dirac's electrodynamics is the so-called Klein-Nishina cross section [225]:

$$d\sigma_{KN} = \frac{r^2}{2}\frac{h\nu'^2}{h\nu^2}\left(\frac{h\nu}{h\nu'} + \frac{h\nu'}{h\nu} - \sin^2\theta\right) d\Omega. \tag{3.40}$$

One can see that the effect of the term in brackets is to reduce the cross section from its classical value for large photon energies. Observe as well that away from the classical regime, $h\nu' \gg h\nu$, we can say that the energy loss due to scattering will be catastrophic, as will be shown further ahead (Equation 3.48), meaning that astrophysical sources cannot be sustained in this regime. When the scattering enters the ultra-relativistic ($h\nu \gg m_e c^2$) regime, the result is that the total cross section will simplify to [305]:

$$d\sigma^* = \frac{3}{8}\sigma_T \frac{m_e c^2}{h\nu}\left(\ln\left(2\frac{h\nu}{mc^2}\right) + \frac{1}{2}\right). \tag{3.41}$$

Conversely, if the photons involved in the sattering have $h\nu \ll m_e c^2$ then we retrieve the Thomson regime: $\sigma \approx \sigma_T(1 - 2\, h\nu/m_e c^2)$.

Inverse-Compton Power and Spectrum

Here we follow the approch of Blumenthal & Gould 1970 [87]. Let us first define $\epsilon = h\nu$ the energy of the photon in the lab frame, and ϵ' the equivalent quantity in the CM frame of the scattering. A relativistic electron of Lorentz factor γ moving through a radiation bath will see an energy flux, in its own rest frame, of $\gamma^2 c(1 - \beta\cos\theta)\mathcal{U}_{\rm rad} = \gamma^2 c(1 - \beta\cos\theta)\epsilon'/dn'$, where $\mathcal{U}_{\rm rad}$ is the radiation density of the bath[1]. We can then write the

[1]Here the term $(1 - \beta\cos\theta)$ is the angle dependence of the Doppler shift equation due to the scattering geometry, as shown in the previous section.

energy loss-rate of the electron [2]:

$$-\frac{\dot{E}}{E} = \int \sigma_T c\epsilon' dn' = \sigma_T c\mathcal{U}'_{\rm rad}. \tag{3.42}$$

Observing that dn/ϵ is a relativistic invariant, we can recall the expression of the preceding paragraph for the radiative energy flux, $\mathcal{U}'_{\rm rad} = \gamma^2 \int (1-\beta\cos\theta)^2 \epsilon\, dn$, so that we have the expression for the power due to a single scattering (for the efficient scattering regime $h\nu \ll m_e c^2$):

$$P_{Comp} = \frac{4}{3}\sigma_T c\beta^2\gamma^2\mathcal{U}_{\rm rad}, \tag{3.43}$$

from which we readily recall the IC-cooling time as:

$$T_{IC} = \frac{E_e}{\dot{E}} = \frac{3}{4}\frac{m_e c}{\sigma_T \gamma \mathcal{U}_{\rm rad}}. \tag{3.44}$$

Notice the striking resemblance between these last two expressions and their synchrotron equivalents 3.23 and 3.24 (when written in terms of σ_T and observing that the energy density of the magnetic field is $\mathcal{U}_B = B^2/8\pi$). This is not without a very good reason and shows the physical similarity of the two phenomena: the scattering of electrons on the photons of the radiation field and that between the charge and the virtual photons of the electromagnetic field, in the case of the synchrotron emission. So, in both cases, the total radiative power is simply a function of the density of the radiation field (either real or virtual), and the ratio of Compton (L_C) to synchrotron (L_S) luminosities for a given volume is given by:

$$\frac{L_C}{L_S} = \frac{\mathcal{U}_{\rm rad}}{\mathcal{U}_B}. \tag{3.45}$$

Now, recalling that the bulk of the synchrotron power comes out near the peak defined by the frequency ν_m, we have: $L_S \sim \nu_m F_{\nu_m} 4\pi r^2$. The synchrotron photons thus generated in a source of size R_S will have a density $\mathcal{U}_{\rm rad} \sim L_S/4\pi R_S^2 c$, so that in a volume that is emitting both synchrotron radiation and up-scattering these photons via the inverse-

[2] This equivalence is obtained by realising that the energy of the scattered photon in the observer frame is much larger than its energy before scattering [87]: $-dE_e/dt = d\epsilon/dt$

Compton process:

$$\frac{L_C}{L_S} \sim 8\pi \frac{\nu_m F_{\nu_m}}{\theta_S^2 c B^2}, \tag{3.46}$$

where θ_S is the angular size of the synchrotron source.

If we write this expression in terms of the brightness temperature T_b of the source in the mode indicated in Section 3.2.1, we arrive at $L_C/L_S \sim T_{b,12}^5(\nu_m)\nu_{m,\mathrm{GHz}}$, where T_b is measured in units of 10^{12} K and ν_m is given in GHz. This calculation shows that Compton losses become dominant in a source once the synchrotron brightness temperature reaches $\sim 10^{12}$ K, and then rises into the regime where catastrophic inverse-Compton cooling takes place. This fact is known as the "compactness problem" of radio sources, whereby very luminous and compact (as inferred from variability timescales) extragalactic radio sources would be expected to suffer catastrophic IC cooling, contrary to observations. This problem was solved by M.J. Rees with the hypothesis of superluminal expansion of the extragalactic radio sources, as will be discussed later.

Now, to conclude this section, let us briefly discuss the spectrum of the inverse-Compton emission for a single scattering particle; as for the power, we will not discuss the Klein-Nishina regime, since due to its strong suppression of the cross section it will not contribute appreciably to the source's flux (this fact will be important in interpreting the data of multiwavelength observations of PKS 2155-304 which we will present in Chapter 6). Furthermore, all the calculations for the Klein-Nishina regime follow exactly the same procedure, only changing σ_T for σ_{KN}.

Let us then assume a mono-energetic radiation bath in which the energetic electron of energy $\epsilon_0 = \gamma mc^2$ is immersed. The radiation energy flux is $(cdt\ dn/d\Omega)\delta(\epsilon - \epsilon_0)$. The scattering cross-section in the CM frame will be [87]:

$$d\sigma = \frac{1}{2} r^2 (1 + \cos^2\theta')\delta(\epsilon - \epsilon_0)\, d\epsilon\, d\Omega'. \tag{3.47}$$

This expression can then be used to calculate the energy distribution of scattered photons in the observer frame by integrating $dn'c\ d\sigma$ over all angles and energies. The result is given by Blumenthal and Gould 1970 [87], where γ is the initial Lorentz factor of the electron, ϵ the energy of the incident photon, ϵ' the energy of the scattered photon, and

$\hat{\epsilon} = \epsilon'/4\epsilon\gamma^2$ is the scattering energy in terms of its maximum value:

$$\frac{dN_{\gamma,\,\epsilon}}{dt\,d\hat{\epsilon}} = 8\pi r^2 c\; n(\epsilon) d\epsilon\; f(\hat{\epsilon}). \tag{3.48}$$

Here, $f(\hat{\epsilon}) = 2\hat{\epsilon}\;\ln\hat{\epsilon} + \hat{\epsilon} + 1 - 2\hat{\epsilon}^2$, which is a broad distribution in energy, has a maximum at low energies of the scattered electrons ϵ' (see Figure 3 in [87]). The upper limit for the scattered energy ϵ' in Equation 3.48, $\epsilon'_{max} = 4\epsilon\gamma^2$, corresponds to a head-on transfer of the electron's energy to the photon.

In the Klein-Nishina regime, as we have mentioned before, the scatterings are catastrophic. In fact most of the electron's energy is lost to the photon in the first few scatterings. This can be seen by noticing that in the ultra-relativistic regime, the energy dependency of the scattering is given by:

$$f_{KN}(\tilde{\epsilon}) = 2q\ln q + (1+2q)(1-q) + \frac{1}{2}\frac{(\Gamma_e q)^2}{1+\Gamma_e q}(1-q), \tag{3.49}$$

where $\Gamma_e = 4\epsilon\gamma/mc^2$ is proportional to the ratio of the photon to the electron energy in the observer's frame, and $q = \tilde{\epsilon}/\Gamma_e(1-\tilde{\epsilon})$. The ratio Γ_e will determine the domain of the scattering: classical for $\Gamma_e \ll 1$ and ultrarelativistic for $\epsilon \sim \gamma mc^2$. For this last case, $f_{KN}(\tilde{\epsilon})$ will peak for large values of $\tilde{\epsilon} \lesssim \Gamma_e/(1+\Gamma_e)$ (see Figure 4 in [87]). In the Thomson limit, multiple succesive scatterings will happen, and the rate of increase in the photon energy is given by solving the Kompaneets equation [228], which is a solution of the Focker-Planck equation for photons scattering off a non-relativistic thermal electron distribution:

$$\epsilon'(t) = \epsilon \exp\left(\frac{4kT}{mc^2}t_c\right), \tag{3.50}$$

where $t_c = (N_e\sigma_T c)t$ is the time between scatterings for a medium with electron number density equal to N_e. The energy increase of the photon is therefore exponential.

The IC spectrum from a power law electron ditribution

Since we know from Section 3.1.1 that in extragalactic jets a power-law distribution of energies is expected for the electron population (Equation 3.25), let us consider the IC spectrum resulting from scattering by such a particle distribution of an arbitrary photon distribution. This can be achieved by calculating the total Compton power by integrating

the product $N(\gamma)P_{Comp}(\gamma)d\gamma$ using the expression given in Equation 3.43 [267]:

$$P_{IC} = \int_1^{\gamma_{\max}} P_{\rm Comp}(\gamma)N(\gamma)d\gamma = \frac{4}{3}\sigma_T c\mathcal{U}_{\rm rad}\frac{K}{3-p}\gamma_{\max}^{3-p}, \tag{3.51}$$

which shows that the cooling, for large $\gamma_{\max} \gg 1$, will have a power law dependence on the particle energy of the electron population, as expected. The shape of the IC bump will therefore be very similar to that of the synchrotron radiation, albeit slightly more spread due to the γ^2 factor in the radiation boost. Rybicki & Lightman [305] give a comprehensive discussion of the IC spectra obtained from scattering off a number of different particle population distributions, as well as the effect of multiple scattering in the formation of the IC spectra, and the reader is referred to this reference for more details.

The polarisation of inverse-Compton emission

Finally, and in order to conclude our presentation on the radiative processes relevant for jet emission from blazars, let us briefly discuss the polarisation of the inverse-Compton radiation. Observationally, this topic is still in its infancy due to great technical difficulties, and polarimetry at γ-rays has not properly started yet. The only gamma-ray polarisation signal detected until now comes from the strong Crab nebula source, at 200 keV, with measurements by *INTEGRAL/IBIS* [154] althought there are promising projects for new ballon-borne instruments for soft-gamma-ray polarimetry such as PoGOlite, which are expected to be able to detect 10% polarisation level from $\mathcal{O}$(100 mCrab) flux sources [221]. Gamma- and X-ray polarimetry have nevertheless figured in the "Astronomy and Astrophysics 2010 Decadal Survey" and are expected to see some significant development in the coming years [260].

X-ray polarimetry also has its equivalent polarimetry mission proposed for the next generation of satellite-based instruments: POLARIX [110], but although X-ray polarimetry started much earlier with the measurement by Weisskopf et al. in 1978 of a significant $\sim$ 20% polarisation signal from the Crab Nebula [352], only a few marginal source detections followed in the past decades, including observational attempts of Cygnus A and Scorpius X-1 – for a brief technical and historical account see Tinbergen 2005 [332] and Matt 2010 [257].

Chapter 4

Blazars & Extragalactic Jets

Extragalactic jets provide the principal physical and observational link between supermassive black holes (SMBHs) and their cosmic environment. To study their properties in greater detail is therefore a pre-requisite to understanding the BHs themselves and the evolution of their host galaxies. The prospects for advances in extragalactic jet physics are increasingly promising, largely due to technical and observational developments in the field of gamma-ray astronomy. The relativistic jets of active galaxies are now understood to be the sites of the gamma-ray emission that was discovered from a number of such sources in recent years (see [345], [240], [239]). It could be argued that it is now becoming possible to give a more definitive answer to the question about the location of the sites of variable non-thermal emission in active galactic nuclei (AGN) and in so doing derive a more comprehensive picture of the jet's kinematical structure, as well as answering long-standing questions about the dominant emission processes and the jet composition in the inner regions of the these objects.

The surprisingly large luminosities detected from active galaxies in the TeV band have made this last observational window into the extragalactic universe a fundamental one. The extreme properties of AGN as seen at these energies reveal a wealth of astrophysical information unknown to the other observational bands and have forced a revision of many aspects of the physics of extragalactic jets. Our aim in this chapter is to give a brief introduction to active galaxies and their associated relativistic jets. It will be organised therefore in the following way: Section 4.1 will give a general presentation of AGN and their unification scenario; in Section 4.2 we return to the subject of the radiation mecha-

nisms, now applied to the specific framework of blazars. Section 4.3 will discuss blazar phenomenology in more detail, concentrating on their observational properties as seen in the gamma-rays. Section 4.4 will discuss the subject of gamma-ray opacity in blazars which is important to understand their spectra and some fundamental constraints to the escaping of TeV photons from these sources. We then move, in Section 4.5 to a brief discussion of the extragalactic jets and conclude, in Section 4.6 with a specific discussion of the object of interest to this thesis, the BL Lac object PKS 2155-304, the observations of which revealed many new important aspects of the physics of blazars and their associated relativistic outflows.

4.1 Active Galactic Nuclei

The realisation that bright and variable compact radio sources were extragalactic objects whose emission was dominated by non-thermal radiation from relativistically outflowing plasma was gradually achieved after their first discovery over 50 years ago. Curtis's observation in 1918 of a "ray" emanating from the centre of M 87 [117] was in fact the first, albeit early, clue towards the existence of a compact source of energy in the centre of galaxies, at a time during which the debate on the nature of the "spiral nebulae" as "island universes" was still taking place. Another indication of nuclear activity in some galaxies was the detection of emission lines from the bright (star-like) central regions of a few nearby sources by Seyfert in 1943 [317], whose properties – such as width and intensity of the Hydrogen lines – correlated with the absolute magnitude of the nucleus and the ratio of nuclear-to-total galaxy luminosity.

The subsequent development of radio astronomy in the post-WWII years rapidly led to the discovery of the first extragalactic radio sources, of which Cygnus A, with a peculiar double-lobe structure [211], was the first to have its optical counterpart found, thanks to observations by Baade & Minkowski [56]. The radio galaxy M 87 was another object to have its radio-to-optical emission studied in the early days of radio astronomy [58]. In this case, the highly polarised nature of the optical emission [57][1] provided a strong case for

[1] Polarisation degrees of the order of 30% were detected by Baade from the jet, extending all the way from the centre of the galaxy to the jet extremity.

the identification of the broadband emission as synchrotron radiation, which at the time had been succesfully used by Oort and Walraven to explain the non-thermal continuum observed from the Crab Nebula [282]. Burbidge's [93] detailed analysis of the energetics of the synchrotron emission from M 87 led to the conclusion that prodigious energies and powers were involved in the generation of the observed luminosity from the nucleus and jet. In fact, the bolometric luminosities of the AGNs are extremely high, ranging from $L_{\rm bol} \sim 10^{43} - 10^{48}$ erg s^{-1}. This synchrotron luminosity implied a total energy of 10^{58} to 10^{60} ergs in the form of particles and magnetic field[2], depending on the source and on the particular assumptions made. Burbidge readily observed these values to be superior to the total energy in the form of cosmic radiation and magnetic field in the Galaxy, having a mass-equivalent of 100-1000 $M_\odot$. Furthermore, the estimates for the energy content of the radio lobes, of up to 10^{61} ergs, imply the processing of a mass-equivalent in energy of $10^8 M_\odot$, at moderate conversion efficiencies of about 10%, with the large "residual" mass left to be collected at the bottom of a growing gravitational potential well[3].

The growing observational evidence in favour of the galactic nuclei being the engines of powerful radio sources, and the many difficulties on finding reasonable mechanisms (such as supernovae explosions) which could explain the stable release of such amounts of energy over long periods (of at least the order of 10^5 years as inferred from the linear scales of the jets, if we assume that the plasma is moving at speeds close to the velocity of light), led Hoyle & Fowler to postulate in 1963 [202] that the best way to power these sources was through gravitational contraction of matter around a densely packed stellar nucleus with mass up to $10^8 M_\odot$. This mechanism would release gravitational potential energy, $U_g \sim GM^2/R$ (which for $10^8 M_\odot$ is of the order of $U_g \geq 10^{42}$ erg for $R \sim 10^{15}$ cm and thus not far from the required values), which could be stored in magnetic fields toroidally wound during the accretion process by conservation of angular momentum[4] and then released when these fields "explode". The compactness of these stellar-like nuclei

[2]The value of 10^{58} erg was obtained in the case of equipartition between particles and magnetic field, an approximation assumed in many theoretical studies developed afterwards, but which is now understood not to be valid throughout the jet, which has an evolving structure.

[3]A result of this observation, that the accumulated accreted mass will lead to a growth of the SMBH, is that the AGN will evolve in time, depending mainly on the availability of accreting material. AGN evolution is an important topic for understanding the physics of active galaxies, but will not be discussed here. For an early introduction and further references, see [73].

[4]Thus providing a means for the production of relativistic particles by electromagnetic acceleration.

was fully realised after the discovery by Schmidt, in 1963, of the first quasi-stellar object (the quasar 3C 273 [315]), and the following detection of variability from it, which greatly constrained its size by means of light travel-time arguments to the scales of 10^{15} cm (< 0.1 pc) already quoted, and thus no bigger than that of the Solar System [244].

It was Lynden-Bell who in 1969 advanced a final argument towards the powering of quasars and extragalactic radio sources by means of the release of gravitational energy from a deep potential well [248]. He[5] noticed that accretion of matter onto a compact object was the most efficient mechanism of mass-energy conversion, with an efficiency of up to 40% for a maximally rotating Kerr black hole, in striking contrast with the 0.7% obtainable through nuclear reactions[6]. These theoretical developments constituted a decisive point towards the establishment and rise of the supermassive black hole paradigm in AGNs, which followed on to find further support from a wealth of additional observational evidence over the years.

Among these additional lines of evidence, the most interesting one is perhaps the link established between the existence of the relativistic jets and the deep gravitational potentials provided by SMBHs. The very existence of these jets requires such deep wells as anchors to grant the gyroscopic stability necessary to sustain their directionality over the long ages and across the large (Mpc) scales over which they extend, and to explain secular variability phenomena associated with the occurrence of torques at the base of the jet-accretion disc system, such as precession [95]. A more detailed account of the physics of extragalactic jets will be given in following sections.

The current AGN paradigm thus states that the nuclear activity is produced by infalling material onto a super-massive compact object via an accretion disc, and had all its essential ingredients set by the early 70's. This SMBH-accretion disc system releases a large fraction of its gravitational energy in the form of radiation, via heating of the accreting material (the standard model for which was proposed by Shakura & Sunyaev in 1973 [318]), and relativistic particles, which are accelerated by the release of some of the energy stored in magnetic fields during the accretion process, to give rise to the launching

[5] See also Salpeter 1964 [307] and Zel'Dovich & Novikov 1965 [357]

[6] See sections 7.7 and 7.8 in Frank et al. 2002 [158] for an extensive discussion of the topic.

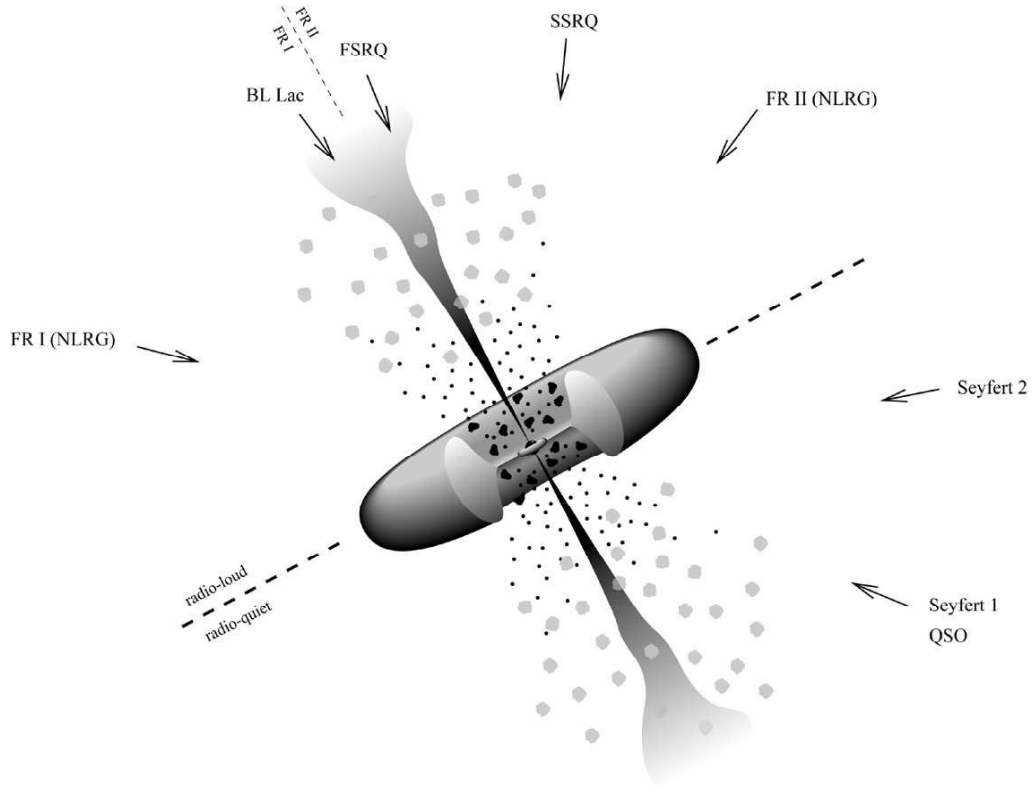

Figure 4.1: Unification scheme of AGN showing how the different classes of sources result from the relative orientation between observer and jet-accretion disk geometry. The scheme also show the divide between radio-quite and radio-loud sources and that between FRI (and BL Lac) and FRII (and FSRQ) radio-galaxies, which are thought to be of intrinsic origin as discussed in the text. The image was adapted from Urry & Padovani 1995 [336]

of the extragalactic jets. This basic scheme, which is illustrated in Figure 4.1, developed as a combination of ingenious multi-wavelength observations and theoretical insight, and is today the best-accepted model to explain the nature of active galaxies. A lot of its success rests not only in explaining the AGN phenomenon [303] but in correctly predicting the existence of passive SMBH in the centre of other, non-active galaxies (e.g., [319]), and specially the Milky Way [266].

4.1.1 AGN Classification and Unification

Figure 4.1 shows a diagram with the basic ingredients of the standard model of active galaxies and how it connects the different types of objects that are observed in the sky. From this image, the rich typological diversity of AGN can be readily understood if one notices that due to its complex morphology and axis-symmetrical geometry (as opposed to isotropy), the observer's view of the central source will radically depend on the relative point of observation. A sideways view, blocked by the dusty torus, will impede for example the observation of most of the central engine, and only indirect radiation reflected from the clouds in the narrow and broad-line region will be detected, resulting in narrow line radio galaxies (NLRG) and Seyfert 2 objects (Sy 2). As the observer's line-of-sight moves away from the torus, he gains a vantage point for direct observation of the accretion disc and the observed properties change radically – QSO[7], broad line radio galaxies (BLRG), Seyfert 1 (Sy 1) are now seen. This happens until a face-on view of the jet is attained and its non-thermal, featureless continuum emission starts to dominate the entire source's spectrum due to the strong boosting of the relativistically expanding emitting plasma: here blazars and flat spectrum radio quasars (FSRQ) are observed.

The basic ingredients of the standard AGN model

It is important to stress that this picture of the central engine, with all of its different constituent regions arranged in a particular geometry, is not directly accessible to observations. The compactness of the source and its complexity mean that our view of the

[7]Which we can subdivide into flat-spectrum radio quasars (FSRQ) and steep spectrum radio quasars (SSRQ), depending on their radio spectral index $S_\nu \propto \nu^{-\alpha}$, for $\alpha < 0.5$ and > 0.5 respectively, which is ultimately a function of the angle to the line-of-sight.

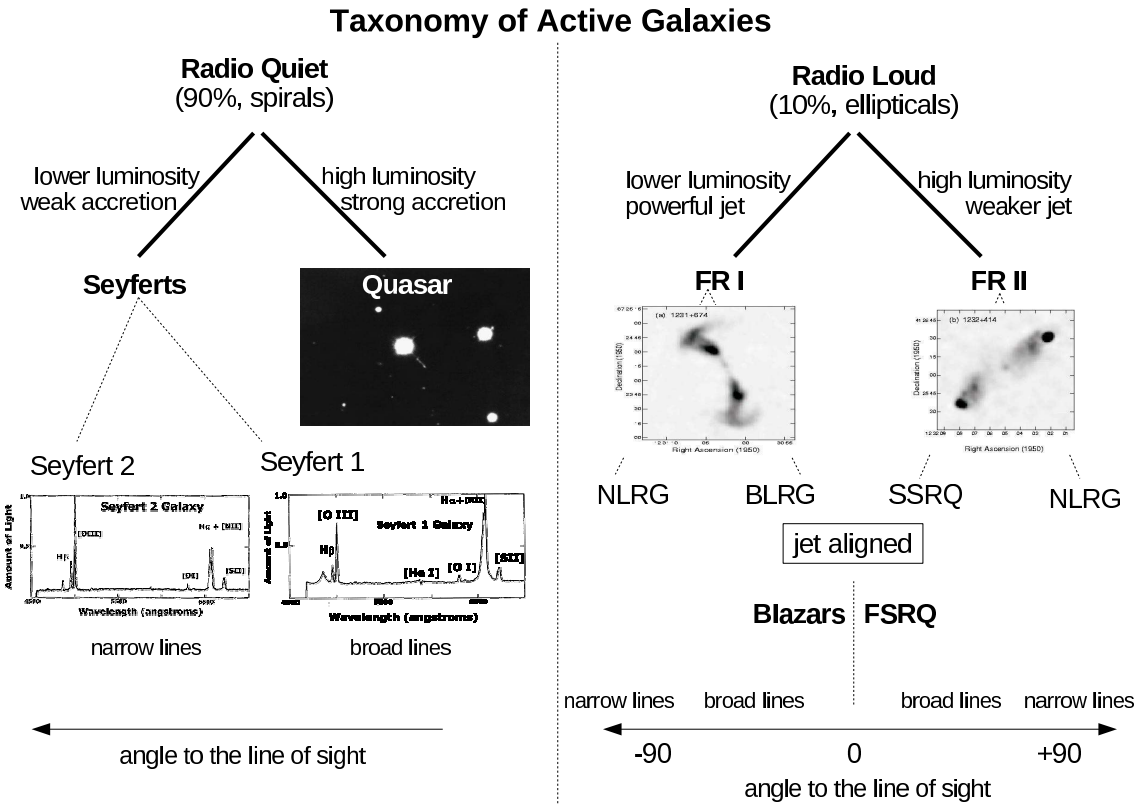

Figure 4.2: Simple taxonomic diagram for AGN, showing the main different populations of radio-loud and radio-quiet objects

AGN came about as a synthesis of many observational factors which together (and taking into consideration the relevant physics) allowed the plethora of sources to be explained with a minimum of resources. The jets are in fact the only ingredients in Figure 4.1 that were intially directly observed, whereas the rise of the hypothesis for a SMBH at the heart of the AGN was described in detail in the previous section as a natural implication of the demanding energetics of the system and the compactness of sources.

The existence of a large quantity of gas in the vicinity of the central engine is inferred from its essential role in the fuelling of the SMBH, but this nuclear gas is arranged in different regular structures. Dynamically, the most important is the material infalling into the SMBH from the surrounding medium which, due to radiative cooling, tends to lose its vertical support and organises itself as a disc whose radial structure is maintained by conservation of angular momentum. The material in the accretion disk will rotate differentially, with radial-dependent azimuthal velocities, and energy dissipation via “friction” will be one of the main elements governing the gas dynamics (see for example [267]).

Accretion-disc theory is a subject on its own right and won’t be extensively discussed

here. We just wish to emphasise that the infalling material in the disc will radiate by liberation of potential energy $L_{\rm rad} = dU_g/dt = (1/2)GM\dot{M}dR/R^2$, where the factor $1/2$ is to satisfy Virial's theorem. Additionally, assuming there is enough time for thermalisation to happen, the disc will radiate as a blackbody and we will have $dL_{\rm rad} = \sigma T^4 dA$, according to Stefan-Boltzman's law, and $dA = 4\pi R dR$. The temperature of the disc can thus be solved as [127]:

$$T^4(R) = \frac{GM\dot{m}}{8\pi\sigma R^3}, \tag{4.1}$$

where the radial dependence indicates that the spectrum of the disc can be seen as a sum of blackbodies for different dR, with a peak at $R_{\rm in}$, the internal radius of the disc. At this extreme of high temperatures the spectrum will obey Wien's law: $F_\nu^{\rm Wien} \propto \nu^3 \exp -h\nu/kT$ The outer disc, which is cool, will follow a Rayleigh spectrum with $F_\nu \propto \nu^2$. In between we will have:

$$F_\nu \propto \nu^{1/3} \int_0^\infty \eta^{5/3} \exp \eta - 1 d\eta, \tag{4.2}$$

where $\eta = h\nu/kTR_{\rm in}(R/R_{\rm in})^{-3/4}$. Observationally, the disc will therefore manifest itself as a hot blackbody continuum extending from blue/UV (the so-called blue-bump) to X-ray wavelengths, the latter from its most internal regions. X-ray variability will therefore be associated with the size scales of the central engine, which scale with black hole mass as shown for example from X-ray quasi-periodic variability (QPO) measurements in blazars [174]. Further out from the central engine, a thick torus will radiate thermally at infrared wavelengths by heating of the dust and reprocessing of the UV radiation from the disc. In bright blazars, these thermal sources of emission are rarely relevant for the SED since the spectrum is dominated by boosted, non-thermal emission from the jet as will be detailed in the following sections.

The emission line properties observed from active galaxies provide the fundamental clues to distinguish their emission regions as two different zones. These are all heated by radiation from the accretion disc, and there are in fact three types of emission lines which can be singled out in the observations: narrow (width $\lesssim$ 1000 km/s) and broad (width $\sim 10,000$ km/s) *permitted* lines as well as narrow *forbidden* lines. These lines

also present different ratios indicative of varying optical depths within the system. These different physical properties were later associated with the distance of the line emission region from the central engine, which will govern, among other things, the radiative flux they receive from the active nucleus.

The region deeper inside the gravitational well, the gas of which is hotter and experiences greater Keplerian velocities which imply a large broadening of the emission lines, is known as broad line region (BLR); due to its higher temperatures which increase the rate of collisional de-excitation of the atoms, this gas does not produce forbidden lines. Due to the strong proximity of these regions to the central source, these lines tend to be very luminous, being sustained by an intense flux of UV radiation from the AGN (hence the observed correlations between the line luminosities and the continuum flux). Conversely, the narrow lines come from an outer region of the AGN, called the narrow-line region. The velocities of the BLR gas[8] are so high that if due to thermal motions alone, the derived temperature of the gas would be $\sim 10^9$ K. This suggests that the widths of the emission lines from AGN must result from differential Doppler shifts due to motions of individual clouds, thus proposing a view that the gas is clumpy [233]. The presence of nuclear "clouds", i.e. that the media surrounding the core of AGN is clumpy, has been also inferred from mm-wave free-free absorption [1].

For its obscuration role, the dusty torus is another fundamental ingredient in the unification paradigm. The existence of the dusty torus, or for this purpose of any geometrical form of opaque material existing around the central engine, came about as an artifice to explain the lack of some emission features (particularly the absence of broad high-ionisation lines in the spectra) in Type 2 AGN [336]. The idea of obscuration of the central source and the BLR was strenghened by Antonnucci's [51] observation that in some Sy 2s these high-ionisation lines could actually be seen at low fluxes in polarised light, indicating the presence of a "hidden quasar" within Type 2 sources, which could only be detected as reflected light that is able to circumvent the dust obscuration. In fact, IR observations were able to penetrate some of this obscuration, partly revealing the infrared high-velocity gas emission, which is completely obscured in the optical. Estimates from IR observations

[8] And for that matter those of the narrow line region as well!

set the optical depth of this obscuring torus to an incredibly high visual extinction, in the range 25-50 mag (but in some cases much higher than that [347]). Direct imaging of the dusty torus was first obtained at optical wavelenghts in 1993, in an HST image of the galaxy NGC 4261 [209].

From what has been said, one can readily see that ultimately the properties of the nuclear emission will depend primarily on the mass supply rate $\dot{M}$ and the mass of the SMBH, $M_\bullet$. Flows with small $\dot{M}$ or towards large $M_\bullet$ will tend to have a low optical depth and will radiate gravitational potential energy inefficiently, thus producing powerful jets (kinetically speaking) which are optically weak. At the limit of small accretion rate, much of the gravitational energy can be extracted electromagnetically from the BH spin and generate jets that are Poynting-flux dominated where the material is accelerated and collimated. Quasars and Seyfert galaxies, on the other hand, arise in the case when $\dot{M}$ is large or $M_\bullet$ is small (as in spiral galaxies), and their flow tends to be radiative: we then have weak jets but bright optical nucleus. For more details on this simple one-parameter model of AGN see [73].

Unification

Observationally, a number of properties distinguish the different kinds of AGN throughout the electromagnetic spectrum: e.g., the radio and optical luminosities, the radio morphology, the presence or not of emission lines and their relative width. After radio galaxies, quasars were the first objects to be added to the zoology of AGN, as very luminous star-like objects that were systematically identified as the optical counterparts of radio-survey sources. However, not all quasars are radio-loud[9] (in fact, 90% are radio-quiet), as can be seen in Figure 4.2, but many were identified in optical surveys by their blue continuum colours (the spectral "blue bump" that has its origin in the thermal radiation from the accretion disc) and their characteristic broad emission lines ($\Delta\lambda/\lambda \sim 0.03$). From an optical standpoint, quasars can be thought of as high-luminosity Seyfert galaxies. The Seyferts, which are characterised by high-ionization emission lines, can themselves be separated

[9] Radio-loudness is defined in terms of the ratio of the 5 GHz radio flux to the B-band optical flux of the source, and includes objects with $F_{5\ \mathrm{GHz}}/F_B \gtrsim 10$

into two types depending on the width of these lines[10]: Seyfert 1s are observed at low angles and the broad-line clouds are visible (FWHM $\sim 10^4$ km s^{-1}), whereas the less luminous Seyfert 2s are seen at high inclination angle, and thus only the narrow-line clouds (FWHM $< 10^3$ km s^{-1}), more distant from the central engine, can be detected[11]. These radio-quiet AGNs constitute the vast majority of active galaxies and are hosted in spiral galaxies, with the exception of the radio-quiet quasars, which are hosted by ellipticals undergoing accretion at higher rates.

For the radio-loud AGN (see [336] for a detailed discussion of the unification of radio-loud AGN), the same distinction applies and the NLRG (and LINERS; low-ionization nuclear-emission-line regions) and BLRG are the loud counterparts of Sy 2 and Sy 1 galaxies, respectively. The absence of emission lines is the characteristic of blazars and FSRQ, which are also defined for their strong variability properties, which in optical gives the name to the class of optical violently variable (or OVVs), with typically sub-hour variability timescales. The main observational distinction between radio-galaxies and radio-loud quasars (FSRQ or SSRQ) is the optical brightness, a band at which radio-galaxies appear as underluminous objects ($M_V > -23$).

The diagram of Figure 4.1 also shows two clear divides, which are indicated by the dashed lines and are not related to geometry, but believed to originate in the intrinsic physical properties of the AGN. These dichotomies were established early on and contributed to the rise of the unified scheme of AGN. The first one to be identified was related to the distinction between high and low-luminosity radio sources. Fanaroff and Riley (FR) in 1974 found the positions of low and high brightness regions in extragalactic radio-loud sources to be correlated with their luminosity [137]. This led to the distinction between FR I sources, which are less luminous and have peak radio brightness in the nucleus, and FR II, more luminous and possessing bright lobes which dominate the radio flux. Today, this difference is understood to go beyond the radio appearance of the sources, to encompass the nature of the accretion mechanism at the central engine and to be directly related

[10]These line widths are commonly interpreted as the result of Doppler broadening due to bulk motion of the emitting gas clouds about the central object

[11]There exists in fact a continuum of intermediate Seyfert types which are known today and provide strong observational support for the geometrical connection between these objects. The observation of strongly polarised, weak broad lines in some Sy 2 is another piece of evidence in favour of the geometrical unification, since it most likely orignates as reflected emission from the obscured BLR. (see [52])

to the total kinetic power in the jet [358]. The FR Is in this case would have jets with a higher ratio of bulk kinetic energy to radiant energy, whereas FR IIs have a lower fraction of their accretion energy funneled into jet bulk kinetic energy [67], in accordance with Rees' interpretation of radio galaxies as "starved quasars" [302].

In this model, the different radio morphology is then linked to the intrinsic jet properties which result from the two accretion modes and may lead to deceleration in the inner kpc region (FR I) or not (FR II) [67]. The mechanism by which jet deceleration happens in FR I galaxies is still to be understood, but if the bulk kinetic energy of the material is dissipated radiatively at the inner jet by means of shocks [253] then the emission of TeV gamma-rays by these objects (and their aligned counterparts, the blazars) could be one defining factor for the morphology [165].

The optical and UV emission-line spectra and IR to soft X-ray continuum of most radio-loud and radio-quiet AGN are very similar and must therefore be produced in similar ways. The inclusion of radio-quiet sources – that side of the plot in Figure 4.1 which lacks a strong radio jet and is populated by the Seyfert galaxies and radio-quiet QSOs – in the unification scheme was nevertheless first realised by Antonucci in 1983 [51]. He hypothesised that in the same way as the optical polarisation angles in radio-galaxies were either perpendicular or parallel to the large-scale radio structure, reflecting the geometry of the scattering material, in Seyfert galaxies the different alignments of the polarisation angles seen in Types 1 and 2 could be interpreted as being due to a different scattering geometry, and thus a function of the observing angle. The radio power would thus remain as the main fundamental physical difference between the sources. The physical cause of the radio loud/quiet dichotomy is still a major source of debate and complexity, but it is now apparent that it is not linked to the host galaxy type as once thought, but rather to properties of the central engine such as BH mass and spin [264].

It is not proposed to go any further into the details of the different ingredients of the standard AGN model. The TeV emission from blazars, with which we are concerned in this work, is completely dominated by the processes going on within the jet, and for this reason we will now focus on this particular structure, detailing its general properties and the emission mechanisms by which gamma-ray emission is produced.

4.2 Emission Models for Blazars

As mentioned before, the bulk of the radiative flux of blazars (and all the GeV-TeV gamma-ray emission) is thought to originate inside the pc-scale jets of these objects. The models of γ-ray production can be classified in relation to the main contributor to the emission: hadronic models when the accelerated particles responsible for the emission are protons, or leptonic models, if the jet is dominated by electrons (and positrons). In fact, discriminating between the emission mechanisms occurring in the jets (hadronic vs. leptonic) is the key tool on deciding about the jet composition.

Leptonic models are presently favoured, and this preference is of a phenomenological character, that is, based mainly on the modelling of the source's SED, regardless of *a priori* arguments concerning the origin and type of the particles that compose the flow or the particularities of the particle acceleration mechanisms at play. The reasons to favour leptonic models are basically three-fold [27]: (i) to produce VHE γ-rays via inverse-Compton scattering of either self-synchrotron or external photon fields, electrons have to be accelerated to energies of $\gtrsim$ 10s TeV, which can be easily achieved in the models of shock acceleration discussed in Section 3.1.1; (ii) the expected particle and magnetic field densities in the jets, plus radiation-enhancement and boosting mechanisms (such as relativistic outflows) can easily produce the synchrotron and inverse-Compton fluxes necessary to explain the observations; (iii) and finally, the correlated character of the SED emission and its double hump structure is (with the caveat of a few "unexplained" events such as the TeV orphan flares [119]) well-fitted within the predictions of leptonic emission models.

In reality, events like the orphan flare or the extreme flare of PKS 2155-304 and the Compton-dominance observed from the BL Lac 3C 279 (see Section 4.3.2) attest to the fact that such a black-and-white distinction between hadronic and leptonic models is most likely an idealised simplification of the source, and in reality both types of processes (and specially different kinds of hadronic and leptonic mechanisms) might be happening together, and perhapes dominating the source's emission at different moments and in different source states.

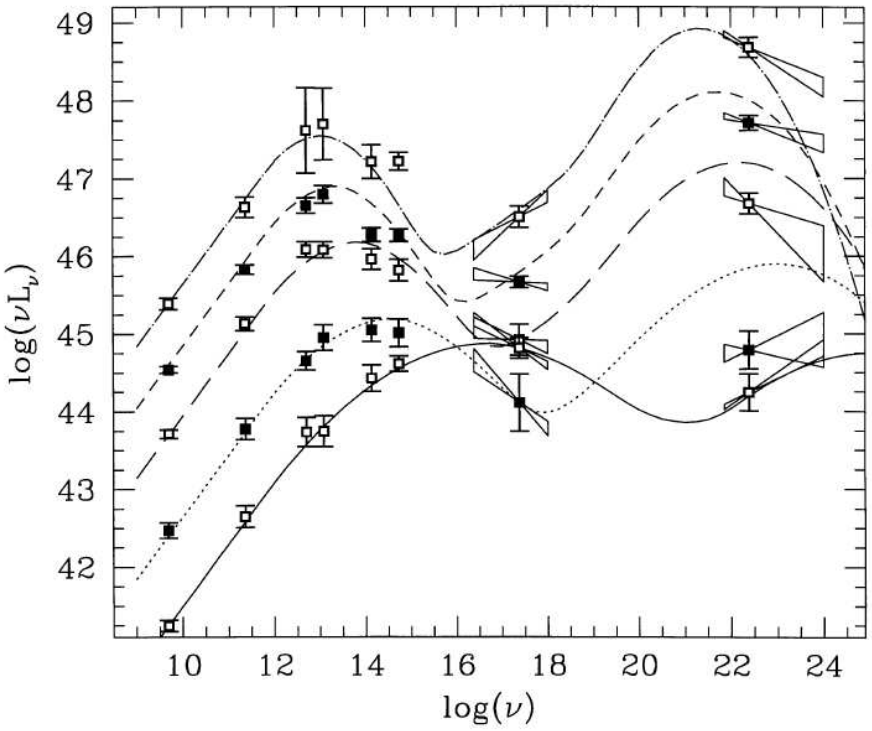

Figure 4.3: The blazar sequence: averaged SEDs for a complete blazar sample combined according to radio luminosity. The fitted curves are analytic curves obtained in the framework of the SSC model, i.e. (1) assuming that the ratio of synchrotron to IC peak frequencies is constant and (2) that the amplitude of the inverse-Compton peak is proportional to the radio luminosity. Figure from Fossati et al. 1998 [156].

4.2.1 Synchrotron Self-Compton Models

The basic ingredient of the leptonic blazar models is that the X-ray (of synchrotron origin) and the gamma-ray emissions (of inverse-Compton origin) are tied to the *same* population of relativistic particles in the jet. This is an attractive model, because the necessary energy for the radiating electrons (tens of TeVs) can be readily achieved through the shock acceleration mechanisms discussed in Section 3.1.1, and both emission channels (synchrotron and IC) are very efficient radiatively, that is, their cooling times are comparable to the dynamic times of these sources, inferred from the light-crossing times $R/c \lesssim$ hour. In fact, in the gamma-ray range, the cooling time $t_{IC} \propto E_e^{-1}$, whereas the energy boost due to the Compton upscattering is $\propto \gamma_e^2$, so that in terms of the photon energy the characteristic time goes with $E_\gamma^{-1/2}$, which means that the TeV gamma-rays will vary more rapidly than the GeV gamma-rays and should correlate with the behaviour of the most energetic X-ray photons, generated by this same population of high energy electrons.

In the consideration of the possible leptonic models, the central question is that of the origin of the target photons for the inverse-Compton scattering. The synchrotron self-Compton mechanism arises when the population of soft photons is provided by the synchrotron emission of the same population of particles participating in the IC up-scattering, and was first considered by Jones et al. 1974 [215].

In the SSC model, the fact that the synchrotron emissivity depends linearly on the electron distribution (see Chapter 3) means that the IC scattering will depend quadratically on the electron density: once due to the synchrotron emissivity dependence and the second time because it is scattering radiation already produced according to this dependence. This property will mean that if an increase in the source luminosity is registered due to electron injection, the variability of the IC bump will be bigger than that of the synchrotron one by a factor N_e – so that, if the injection of energetic particles is very large, a Compton dominance of the source can eventually be seen such as happened to PKS 2155-304 during the large flare of 2006 [112] and [32]. Observe that the increase of the magnetic field will have the opposite effect of decreasing the ratio L_C/L_S ($L_c \propto B^{-1/2}$ whereas $L_S \propto B$), while shifting the peak of the two distributions by equal amounts towards higher energies – see for example [70].

Observe as well that, as given by [206], there exists a basic kinematic condition for the IC scattering within the SSC mechanism, which for a given synchrotron photon energy ϵ_s and electron Lorentz factor γ_e restricts the range of allowed energies of the Compton photon ϵ_{IC}:

$$\epsilon_s \leq \epsilon_{IC} \leq \gamma_e \frac{4\epsilon_s \gamma}{(1 + 4\epsilon_s \gamma)}. \tag{4.3}$$

This rule is useful in deriving basic predictions from simple estimates about the synchrotron spectrum and the parent particle population.

Another characteristic property of the SSC mechanism is that since the synchrotron emission generates photons with energies $\epsilon \propto \gamma_e^2$, the energy of the IC photons will be $\epsilon \propto \gamma_e^4$, and so the spread in energy of the IC bump will be twice that of the synchrotron one, whereas the slope of the energy distributions, as we saw in Chapter 3, will be the same as long as the scattering happens in the Thomson limit.

Mathematically, we can recall the results 3.45 and 3.46 to derive the relation between

the Compton and synchrotron luminosities in the SSC scenario:

$$L_{IC} = \frac{2L_{\rm sync}^2}{R_S^2 B^2 c}, \tag{4.4}$$

which evidence the proportionality $L_{IC} \propto L_{\rm sync}^2$.

When we go to higher energies, an abrupt suppression of the IC bump will be seen, marking the entrance of the scattering in the Klein-Nishina regime. All these basic ingredients of the SSC emission can be seen in Figure 4.3.

4.2.2 External Compton Models

This alternative model, in which the origin of the seed soft photons is radiation fields external to the emitting region was initially proposed by Begelman & Sikora in 1987 [74]. The attraction of this method is that it can, by invoking external sources of radiation, supply an explanation for the high-energy bump when it does not obey the strict correlations stated in the previous section which are demanded by the SSC scenario. It is important to observe that, except for a certain amount of self-absorption that might affect the synchrotron and IC emissivity of the compact emitting region, it is hard to avoid that part of the radiation be emitted via the SSC channel, so it is quite likely that even when the EC mechanism is present, the SSC mechanism will contribute at some level to the emission.

In blazars, because of the dominance of the boosted jet emission, it is hard to directly observe other radiation fields, but from the knowledge of the AGN environment in general, we can devise the following possible sources of external seed photons: (i) emission from the accretion disc, most prominent in the UV [321]; (ii) re-processed emission from the accretion disc by the BLR, which will largely fall in the optical band [271]; (iii) the host galaxy red stellar continuum [325]; (iv) and of course, the cosmic microwave background.

An interesting variant of the EC model has been recently proposed by Ghisellini & Tavecchio 2008 [169] to try and explain the extreme VHE flare of PKS 2155-304. In this "needle in jet" scenario, the particles responsible for the synchrotron flux form a distinct population with the jet, travelling with enhanced Doppler factors, and they EC-scatter the radiation produced by the surrounding jet. This scenario proposes an interesting superposition of SSC+EC emission that is capable of explaining both the quiescent state of the

source as well as the extreme flaring activity (see Figure 2 in [169]).

4.2.3 Hadronic Models

The main difficulty with hadronic models, which usually disfavours them relative to their leptonic counterparts, is that for an efficient hadronic emission of VHE gamma-rays, capable of explaining the observed SED fluxes – and given the same basic "environmental" conditions within the jets as for the leptonic models – hadrons need to be accelerated to energies of up to 10^{20} eV[12]. Several different hadronic processes can contribute to the emission from blazar jets, but in general, they all ssume that the γ-ray emission is basically the final product of the interaction of the accelerated protons with either ambient matter (in so-called *matter-loaded* models), photon-fields (via photo-pion production) or magnetic fields (in proton-synchrotron models), so here too the physical characteristics of the jet can be inferred from modelling of the emission. A review of these models can be found in Böttcher 2007 [90], but for the sake of completeness a brief account of these three radiative mechanisms is given below.

Photo-pion production

If the development of the jet is such that a significant fraction of its kinetic power is converted into the acceleration of protons, beyond the threshold level for p-γ pion production, then electromagnetic pair-cascades can develop within the jet that will give rise to *gamma*-ray production. This threshold is given by $h\nu \simeq 0.03 E_{19}^{-1}$ eV, for a photo-pion cross-section of $\langle \sigma_{p\gamma} f \rangle \simeq 10^{-28}$ cm^{-2} [12]. The provenance of the target photons can either be the relativistic jet itself or external radiation fields such as from the accretion disc. The main reaction channels are [90]:

$$\begin{cases} p + \gamma \rightarrow p + \pi^0 \\ p + \gamma \rightarrow n + \pi^+ \\ p + \gamma \rightarrow p + e^+ + e^- \end{cases} \tag{4.5}$$

[12] In this sense, the verification that hadronic mechanisms are the actual responsible for γ-ray productions in blazars would represent a fundamental step in associating extragalactic jets with potential sites of UHECR production.

The first two reactions will later give rise to γ-rays from EM-cascades in two ways: π^0-decay into 2γ, and $\pi^{\pm}$-decay ($\pi^{\pm} \rightarrow \mu^{\pm} \rightarrow e^{\pm}$). The main constraint for such reactions is that they require protons to be accelerated to extreme energies, exceeding 10^{19} eV, and the efficiency of acceleration of protons to such extreme energies in compact regions is possible only in the presence of extreme magnetic fields $B \gg 1$ G. [12]. Differentiation between the different reaction channels can be based on the fact that the pion-cascades generate featureless spectra, in contrast to p-synchrotron cascades which are expected to produce double-bumped γ-ray spectra, the low-energy one contributing to the primary-synchrotron emission from electrons, whereas the γ-ray spectra would be fully dominated by the hadronic channel, given that the extreme magnetic fields do not favour up-scattering of the lower-energy radiation [90].

Matter-loaded models

As the name suggests, if the jet is dense in hadrons, proton-proton interaction cross-sections can be large enough so that the rate of p-p pion production in the system becomes sizeable. The minimum energy threshold for each proton is 290 MeV, and so the advantage of this scenario over photo-pion production is that particle acceleration to extreme energies is not required. Nevertheless this model has the disadvantage that observations seem to favour a plasma in the jet that is of relatively low density, and therefore the efficiency of this mechanism is likely to be too low to explain the observed time-variability and the high γ-ray fluxes observed in blazars [12]. It is important nevertheless to observe that while a low-proton density jet would disfavour such mechanism, it is still a likely scenario when part of the proton targets comes from external sources such as in the event of a collision of the jet with a dense cloud on its path and the consequent *entrainment* of the material.

Proton-synchrotron models

Proton-synchrotron radiation becomes an effective mechanism for the production of γ-rays, with high enough fluxes and characteristic cooling times 10^5 s, as necessary to fit the observational data, only for very energetic protons ($E \geq 10^{19}$ eV) and strong magnetic fields $\approx$ 100 G. If the particles are in a regime dominated by synchrotron losses (i.e.

$t_{\rm acc} = t_{\rm sy}$), than the spectral shape of the Doppler-boosted γ-radiation is given by the self-regulated synchrotron cut-off at $E_{\rm cut} \simeq 3\eta^{-1}\delta_{10}$ TeV. For a maximum particle acceleration efficiency ($\eta \sim 1$) and typical jet Doppler factors of $\delta \gtrsim 10$, the proton-synchrotron spectrum is expected to extend all the way to the TeV range [12].

The conditions for proton-sychrotron emission are very similar to those required for effective γ-radiation via photo-pion production. Because of that, if the system achieves the necessary conditions to radiate via the photon-pion mechanism, it will also have the necessary conditions for the protons to efficiently radiatively cool by synchrotron emission; it actually turns out to be the case that this last process will then dominate, meaning that efficient γ-ray emission in a hadronic scenario is a likely indication *in favour* of proton-synchrotron process and a sign of the *low efficiency* of the photon-pion mechanism. Only with protons with energy well below 10^{19} eV would the photon-pion mechanism dominate over the proton-synchrotron one [12].

In any case, both the particle energies involved and the values of B are so high (expected to exist only in the innermost regions of the jets) that it is challenging to explain how emission via this mechanism can be realised in practice, even if phenomenologically hadronic models can successfully fit some of the key features in the SEDs of blazars (e.g Mannheim 1993 [251]).

Interlude: curvature radiation

To conclude, there exists a last mechanism that can contribute to the proton radiation of gamma-rays. *Curvature radiation* is produced when a charged particle follows a curved path along a magnetic field line. It is different from synchrotron radiation inasmuch as here the magnetic field lines are not straight, but themselves curved, and as the particle experiences acceleration by following the curved trajectory of the line, electromagnetic radiation is given out. In this sense, curvature radiation can be treated as a generalization of magnetobremsstrahlung as discussed by Aharonian et al. 2002 [11]. The radiative loss rate for curvature radiation is given by:

$$\dot{\epsilon}_{\rm curv} = \frac{2}{3}\gamma_e^4 \frac{q^2}{R^2} c = \eta q B c \,, \tag{4.6}$$

where R is the radius of curvature of the field line and all other quantities are as defined previously. The quantity $\eta = 2/3(q/R)^2\gamma^4$, which should be compared to its synchrotron equivalent $2/3(q/mc^2)^2\gamma^2$, is termed "radiative efficiency" and defined in general terms in [11] as $\dot{\epsilon} = \eta qBc$, where $\eta B = E_{\rm eff}$, the effective equivalent electric field responsible for the acceleration. By comparing both the synchroton and the curvature radiation expressions, one sees that the curvature radiation losses are smaller than those for synchrotron radiation, as long as the energy of the particle satisfies the condition $E < qRB$, and thus provides a favourable emission mechanism[13]. The latter limit on the energy of the particle is that above which the particle's gyroradius is greater than the radius of curvature of the field line and so it makes no sense to speak about "curvature radiation" any longer.

Observe that this last condition is met with particular suitability when we speak of extremely strong magnetic fields. Such curved magnetic field lines of extreme intensity can exist in AGN environments in the vicinity of the central rotating supermassive black hole, creating an environment where curvature radiation would putatively dominate over synchrotron emission. For magnetic fields $\gtrsim$ 10 G, curvature radiation could produce photons of $\gtrsim$ TeV energies, with the advantage that the emitting regions, being constrained by the sizes of $r < R$, would be very compact, thus providing an instance for extremely fast variability (as observed in PKS 2155-304) in the vicinity of the central engine. As in synchrotron radiation, given the intensities of the magnetic fields at play, electron energy losses would be catastrophic, and only protons are expected to provide relevant contributions for the fluxes at TeV energies.

4.3 Blazars and TeV Emission

Active galaxies represent one third of the known VHE gamma-ray sources, with the vast majority of the detected objects belonging to the BL Lac (or blazar) class. The number of known extragalactic TeV sources has increased by a factor of at least 4× since 2003, just before the current generation of Cherenkov observatories became active. The distance of

[13]This can be expressed in an alternative way, as given in [11], by noting that the photon energy emitted by curvature radiation relates to that of synchrotron radiation by $\epsilon_{\rm curv}/\epsilon_{\rm sync} = r/R$, where r, as before, is the gyro-radius of the particle.

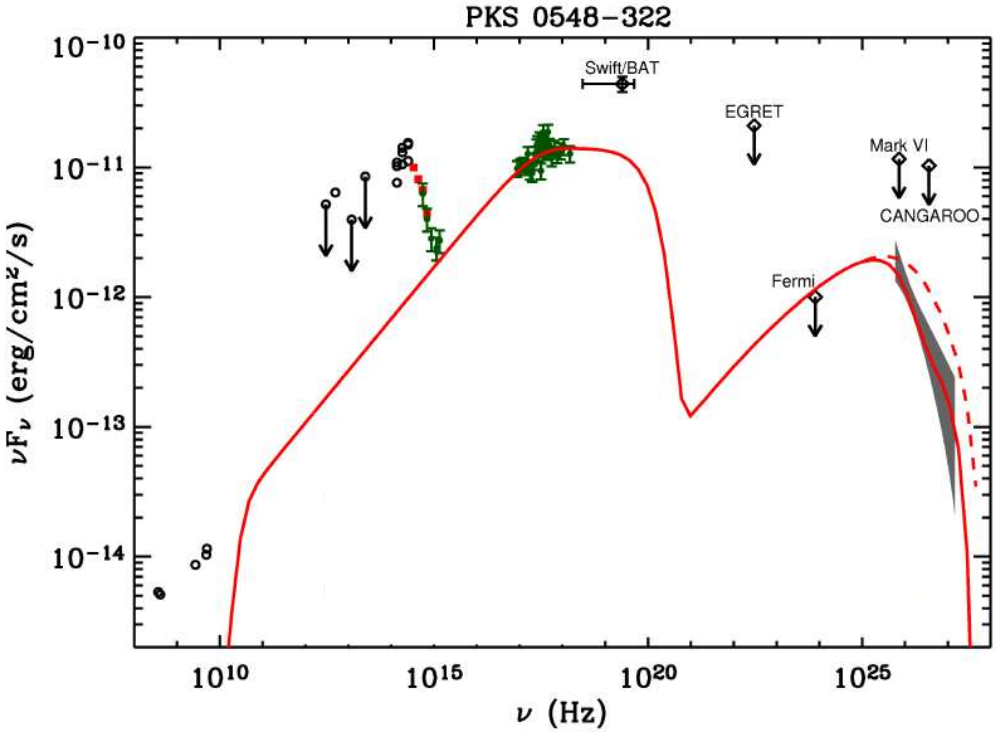

Figure 4.4: Spectral energy distribution (SED) of the TeV blazar PKS 0548-322, the most recently discovered VHE AGN. The typical SED of blazars is constituted of two dominant peaks which are interpreted as synchrotron and inverse-Compton emission from a population of energetic electrons. Notice the presence of an emission peak at low frequencies, of non-thermal origin and corresponding to the underlying galaxy emission over which the jet's double-humped synchrotron-IC SED is superposed. Figure adapted from [37]

the known sources has also increased considerably: while the first confirmed TeV AGN were "local" objects ($z < 0.05$, e.g. Mkn 421[14] and Mkn 501) the most distant object known to date, the FSRQ 3C 279 [41], is located at a redshift $z = 0.53$, much beyond the initial expectations for the detectability of the TeV sources with the current generation of instruments.

As mentioned before, blazars are radio-loud AGN which possess relativistic jets pointing close to the line of sight, and are therefore characterised by a dominant, featureless non-thermal continuum emission. As shown in Figure 4.4, the spectral energy distribution (SED) of blazars, which is seen extending from the radio to the TeV bands, presents two broad components in the νF_ν plane, that in the case of the TeV sources peak in the X-rays and the GeV-TeV band respectively. The positions of such peaks are variable, depending

[14]This was the first extragalactic TeV source discovered, detected with the Whipple telescope in 1992 [294].

on the state of the source[15] and can sometimes accompany the short-timescale variability that is characteristically observed from these sources[16].

In itself, the existence of VHE gamma-ray emission from these sources, which is variable on extreme (short) temporal scales, is important because it provides independent and unsurmountable evidence in favour of strong relativistic beaming being operational in the jets. As we will see later, because of γ-γ pair creation opacity, the VHE emission provides severe constraints on the location of the sites of the (kinetic) energy dissipation zones which characterise their jets (their parent population is that of the FR Is).

The bimodal SED of blazars is not the same for all sources, and in fact, the blazars themselves are subdivided in several categories, which form a multi-band continuum of spectral properties as evidenced by Fossati ei al 1998 [156]. In simple terms, the sources range from low-frequency-peaked (or radio-selected) BL Lacs (LBLs), more luminous (in bolometric terms) and whose synchrotron peak falls in the optical bands, to high-frequency-peaked (or X-ray selected) BL Lacs (HBLs), with synchrotron peak emission that lies in the keV range, reflecting therefore an anti-correlation between the synchrotron peak of the emission $\nu_s^{\rm peak}$ and the corresponding energy density at this frequency $\nu F_\nu(\nu_s^{\rm peak})$. It is this last class that composes the majority of TeV-detected blazar sources, with very few exceptions such as the FSRQ 3C 279 [41], the LBL BL Lac [40] and the IBL (intermediate class between LBLs and HBLs) W Comae [6]. This basic phenomenological scheme has been succesfully explained in its most general terms within the widely accepted synchrotron-self-Compton and external-Compton models (see Section 4.2 for details on these models) in which the SED sequence reflects an evolution of the physical properties that characterise the emission region, namely, the jet power and the intensity of the diffuse radiation field surrounding it and which serves as target photons for the Compton up-scattering.

Costamante & Ghisellini 2002 [111] have analysed in detail the broadband SED prop-

[15] In extreme active states these peaks can move dramatically towards higher-energies, with the inverse-Compton component falling well within the TeV band [232]. Their relative intensities can also vary by large amounts, an in some cases the bulk of the radiative output of the source is seen from the gamma-ray bands [32].

[16] Nevertheless, it is important to notice that this is not always the case with these objects, and in the most extreme varibility episode observed from PKS 2155-304 in 2006 [26], flux varibaility of $\sim 100\times$ were registered without spectral variability, pointing to a complex and maybe not unique variability mechanism in operation in these sources.

erties of a number of blazars and the position of the sources that had been detected to that date in the TeV band[17] to establish criteria for the search of other TeV-emitting BL Lac objects. This procedure, which was based on the presence of large X-ray and radio luminosities, has been very successful in guiding the searches with the current generation of ground-based instruments. The physics behind these criteria was in line with the main ideas behind the blazar sequence of Fossati (Figure 4.3), since the X-ray luminosity was tracing the density of seed photons and the strong radio fluxes were an indicator of the total power in the jets. The detection rate based on this recipe has been extremely high in the past few years, and in fact all the objects detected in this way were HBLs.

4.3.1 The blazar sequence rationale

As mentioned above the blazar sequence is a phenomenological classification of sources based on SED properties. Physically (see Section 4.5), the observed luminosity of blazars is enhanced by beaming according to δ^4, where δ is the bulk Doppler factor of the flow, $\delta \equiv [\Gamma(1 - \beta\cos\theta)]^{-1}$, for a jet viewing angle θ. Not only the luminosity, but also the frequency of the emitted photons is boosted by the same mechanisms $\propto \delta$ – that is to say, naively the expectation would be that both emissions increase, whereas the trend evidenced in the blazar sequence is of an anti-correlation.

In the leptonic scenario discussed in the previous section, the blazar sequence corresponds to a decrease in the energy of electrons emitting at the SED peaks whilst the energy density of the seed soft photons for IC scattering and source power grows [100]. Within this scenario, Ghisellini et al. 1998 [167] found a correlation between $\gamma_e^{\rm peak}$ for the electrons emitting at the peak of the distribution and $\mathcal{U} = \mathcal{U}_B + \mathcal{U}_{\rm rad}$, the total energy density of the jet. By observing that the radiative cooling rate is given by $\dot{\gamma}_e \propto \mathcal{U}\gamma_e^2$, they concluded that this had to do with cooling of the electrons, implying a "universal" cooling rate at the peak for all sources.

In the case of continuous particle injection and radiative cooling dominating at all energies (the case of the LBL), $\gamma_e^{\rm peak}$ will be $\sim \gamma_e^{\rm min}$, the minimum Lorentz factor of the injected particle population. Whereas for HBL, where radiative cooling is less strong

[17] Namely, Mkn 421 and Mkn 501, both detected by Whipple, 1ES 1959+650, 1ES 1426+428 (detected by HEGRA), 1ES 2344+51 (Whipple) and PKS 2155-304 (Durham)

because $\mathcal{U}$ is smaller, adiabatic losses will dominate and $\gamma_e^{\rm peak} \propto \mathcal{U}^{-1}$, explaining the reversed trend.

Today, with the large amount of knowledge gained in the understanding of blazars from multiwavelength, but specially gamma-ray studies, this simplified view of the blazar sequence is being challenged (see for example [170]), even though phenomenologically it still holds strong. The details of the problem are rather specific to be discussed here, but it should suffice to say that a one-parameter model based on the bolometric luminosity seems no longer sustainable and the physical properties of the central engine, such as the black hole mass $M_\bullet$ and the accretion rate $\dot{M}$ (or disc luminosity L_{disc}) must be taken into consideration. In fact, some of the key points of this new proposal have been recently confirmed in a study of the properties of the brightest detected *Fermi* blazars, in which a positive correlation was found between jet power and accretion disc luminosity [171], suggesting an important physical link between the accretion process and the jets.

4.3.2 The gamma-ray view of blazars

The majority of AGN detected by EGRET belong to the blazar population [276] (the exception being the radio galaxy Centaurus A). The main contributors to the EGRET blazar population are the FSRQ, which are more luminous and less polarised than BL Lacs, and tend to be more distant objects. The EGRET blazars showed variability on timescales of months, but the minimum timescales are clearly limited by the sampling of the observations and the observatory's limited sensitivity of $F(>1\text{GeV}) \simeq 2\times10^{-11}$ erg/cm^{2}s for the one year sky-survey typical integration times. Nevertheless, short flares on timescales of less than 10 hrs were detected from bright objects such as 3C 279 [276]. Regarding their spectral properties, EGRET blazars are well-described by a simple power law over the energy range 30 MeV to 10 GeV, with photon index $\Gamma \sim -2.2$ and no evidence of apparent cut-offs. These spectral properties are remarkably similar for objects over 3 orders of magnitude different in luminosity. No correlation was found in the EGRET sample between the photon indices and the redshift of sources, despite a strong luminosity-redshift correlation being found, which could be due to selection effects.

Of the over 100 AGN sources detected by *Fermi/LAT* in its first year of operation [150] the vast majority belongs to the blazar class. The new LAT data confirms, with larger

statistics, the EGRET results that the majority of the bright GeV BL Lacs are FSRQ with somewhat softer spectra than the HBLs detected in the same band, which typically present $\Gamma < -1$. Not only this spectral dichotomy is confirmed by the new LAT data, but also the expected trend between the GeV gamma-ray luminosity and the spectral slope, which is in the sense of "bright when harder". The recent *Fermi* observations were important also to constrain the peak of the IC emission in a number of sources, since typically the frequency of maximum IC-emission falls between the LAT ($E < 100$ GeV) and the ground-based bands ($E > 50$ GeV) [148].

There is neverheless a population of BL Lacs, charcaterised by very hard GeV-TeV spectra, that are not easily detectable by the gamma-ray satellites. In fact, perhaps the most interesting trait of EGRET or LAT objects for us is that they form a complementary sample to that of TeV sources, meaning that GeV-bright blazars are tendentially weak TeV emitters, and pertaining to the sample of radio/optical-selected rather than X-ray selected blazars. The GeV-TeV anti-correlation is associated with the high density of soft IR/optical photons in quasars, which provide an effective environment for IC production of gamma-rays, but also limit the maximum energy of the upscattered radiation, as manifested in the "redder as brighter" relation shown in Figure 4.3. Finally, GeV blazars tend to have superluminal parsec-scale jets, in contrast to the sub-luminal propagations that are seen from the TeV objects, most likely due to the jet deceleration mentioned earlier in this work. Apart from these intrinsic effects, the intergalactic absorption of TeV gamma-rays from distant sources will contribute to different spectral properties of both populations of sources.

The general observational properties of the population of TeV blazars are now being studied systematically, since a minimum statistics for these objects has been reached. These first synoptic studies have been conducted by Wagner 2008 [345] and Lenain et al. 2010 [240], and have confirmed the expected correlations between X-ray and gamma-ray luminosities, resulting from the synchrotron self-Compton (SSC; see Section 3.2) model used to describe the broad SED features. The sources were also shown to follow a harder-when-brighter spectral behaviour at energies $E > 100$ GeV. More interestingly, a possible correlation between black hole mass and gamma-ray emission has been detected, suggesting the existence of a possible threshold black hole mass for the onset of strong

jet activity, in gamma-rays as well as in radio [345]. Lenain et al. observed that a simple SSC model is indeed successful in reproducing the majority of the (time-averaged) SED of VHE AGN, and in particular HBLs, whereas other classes of blazars and FSRQs need a parameter space for modelling which is slightly different. According to Lenain et al., this is most probably down to the microphysics governing the acceleration mechanisms in these sources, as detailed in Section 3.1.

It is important to bear in mind that all these analyses are conducted with the sources most probably in a high-state. Given the relatively limited sensitivity of the ground-based Cherenkov telescopes, TeV blazars are usually observed when flaring, and except for one case which will be discussed later (namely, PKS 2155-304) in no other objects are we sure to have detected the object's low emission (or quiescent) state. For this reason, an intrinsic bias might exist in the aforementioned studies which prevents more definitive conclusions on the physics of the blazar jets being advanced.

4.4 Gamma-ray Opacity: Pair Production

The most important mechanism by which GeV-TeV gamma-rays are absorbed is photon-photon pair production, whereby the incident gamma-ray interacts with a softer photon to annihilate and produce an electron-positron pair: $\gamma_1 + \gamma_2 \rightarrow e^- + e^+$. The energy threshold of this interaction must of course be $h(\nu_1 + \nu_2)(1 - cos\theta) > 1.02MeV = 2m_e c^2$, corresponding to a threshold $E_{\gamma,TeV} = 0.26/E_{TeV}$. Since the incident gamma-ray carries most of the momentum before the reaction, the created electron-positron pair is highly beamed in the direction of motion of the gamma-ray, generating the potential of creating gamma-pair cascades in space [12].

The optical depth for absorption of a gamma-ray $h\nu$ in a soft-photon bath with number density $n(\epsilon, r)$ is:

$$\tau(\nu) = \int_r \int_\epsilon \sigma_{\gamma,\gamma}(\nu, \epsilon) n(\epsilon, r)\, d\epsilon\, dr\ , \tag{4.7}$$

where the cross section $\sigma_{\gamma,\gamma}(\nu, \epsilon)$ bares some resemblance with the functional form of the Compton scattering cross section, and an approximate form is given by Aharonian 2004 [12]:

$$\sigma_{\gamma,\gamma} = \frac{3\sigma_T}{2s^2}\left[\left(s+\frac{1}{2}\ln s-\frac{1}{6}+\frac{1}{2s}\right)\ln\left(s^{1/2}+(s+1)^{1/2}\right)-\left(s+\frac{4}{9}-\frac{1}{9s}\right)\left(1-\frac{1}{s}\right)^{1/2}\right]. \quad (4.8)$$

Here $s = h\nu\epsilon/m^2c^4$ indicates that the cross section depends only on the energies of both photons. Notice that when $s \to 1$, the cross section for pair production approaches $(1/2)\sigma_T(s-1)^{3/2} \approx 0$. Otherwise, when s is very high, $\sigma_{\gamma,\gamma} \to (2/3)\sigma_T(\ln(s)/s)$, thus decreasing for even higher s. The cross section has therefore a spectrum which is very sharp and relatively narrow, peaking for $s \sim 3-5$ (see Figure 5 in Coppi & Blandford 1990 [108]) with a value of $\approx 0.2\sigma_T$. This means that a very-high-energy gamma-ray in the range 0.1-10 TeV will be absorbed by a narrow band of IR-optical soft photons: the peak in terms of soft-photon energy is: $E_{\gamma,TeV} = 0.9/E_{TeV}$. Finally the optical depth to gamma-rays propagation is [108]:

$$\tau_{\gamma,\gamma}(\epsilon) \approx 0.2\sigma_T\epsilon^{-1}n(\epsilon,r)r. \quad (4.9)$$

4.4.1 Emission Site Constraints from Internal Source Opacity

The presence of soft photon fields from the central engine and the broad line region or the startlight of the host galaxy will have implications to the escaping of gamma-rays produced in the near vicinities from the source centre, as they will be a source of internal $\gamma-\gamma$ opacity. The presence of such sources of absorption will be relevant for putting physical constraints to the sites of gamma-ray emission. The $\gamma-\gamma$ opacity from such external radiation fields in blazars has been considered for example by Celotti et al. 1998 [99]. They observe that in order to estimate the physical constraints imposed by these external fields on the sites of gamma-ray emission, it is necessary to consider their compactness over different size scales in the source.

Because of the relativistic bulk flow experienced by the emitting plasma, the opacity constraints can be fomulated in terms of minimum values to the flow's Lorentz factor Γ, which alleviate the intrinsic constraints to the escaping of the observed gamma-ray radiation. For a given size scale of the emitting region $r_\gamma \sim \Gamma^2 c\Delta t_{\rm var}$, and for a soft photon flux (e.g. IR photons) $F_{\rm obs}(\nu_{IR})$, we have [99]:

$$\Gamma \gtrsim 1.2 \times 10^{4.5} F_{\rm obs}^{1/2}(\nu_{IR}) t_{\rm var}^{-1/2}. \tag{4.10}$$

This expression signifies that the gamma-radiation is produced at typical distances $R_\gamma \sim 4 \times 10^{19} F_{\rm obs}(\nu_{IR}) t_{\rm var}^{-1}$ cm. If we require nevertheless that the plasma propagate with more modest and typical Lorentz factors $\Gamma \sim 10$, severe constraints can in turn be put in the IR photon field of the source (e.g. such as that from a putative dusty torus around the central engine). Celotti et al. 1998 [99] used this reversed argument to estimate a more reasonable constraint for the site of TeV emission in the blazar Mkn 421 of $R_\gamma \gtrsim 3 \times 10^{12} t_{\rm var} \Gamma^2$ cm.

Another important intrinsic source of opacity will arise within the synchrotron self-Compton framework, which results from the opacity *inside* the emitting zone itself (i.e. within the blob). In the SSC model, a soft photon field will be generated by synchrotron emission co-spatially to the particle population which can potentialy absorb the Compton upscattered gamma-ray photons. Again, the size of the emitting blob can be derived by means of the variability timescale to be $r_\gamma \lesssim c t_{\rm var} \delta (1+z)^{-1}$. Taking into account the relevant Doppler transformations for the observed gamma-rays, this will mean that for a $\sim$ TeV photon ($\nu_{TeV} \simeq 1.2 \times 10^{26}$ Hz) the soft photon field that will mostly contribute to the absorption will have a frequency $\nu_{\rm soft} \sim \nu_{IR} \simeq 1.2 \times 10^{26} \nu_{TeV}^{-1} \delta^2$ Hz. So, for a given flux $F_{\rm obs}(\nu_{IR})$, the internal constraint on the Doppler factor will be [99]:

$$\delta \propto \left(\frac{F_{\rm obs}(\nu_{IR})}{t_{\rm var}} \right)^{1/6}, \tag{4.11}$$

which implies $\delta \sim$ 10-15 for the typically observed non-thermal IR fluxes in blazars.

Observe as well that due to the shape of the SED of blazars, according to which most of the synchrotron flux is emitted below ν_m (this parameter is defined in Chapter 3), a lower limit on δ which puts the frequency of the absorbing soft photons $\nu_{\rm soft} > \nu_m$ will guarantee that the blob is essentially intrinsically transparent to high-energy gamma-rays. Such considerations are discussed in detail for example by Begelman et al. 2008 [75] in the context of the large flare of PKS 2155-304, for which extreme $\Gamma \gtrsim 50$ are shown to be required. Internal gamma-ray absorption might also play a fundamental role in the "artificial" hardening of the observed intrinsic blazar spectrum, as discussed by Aharonian et al. 2008 [31].

4.4.2 Propagation Through the EBL

Early in this section we arrived at the conclusion that a soft IR photon field would strongly absorb photons of ∼ TeV energies; in fact, because of the sharp peak in the cross section shown in Equation 4.8, there is practically a one-to-one mapping of the gamma-ray photon energy and the absorbing radiation [199]: $E_{TeV} \approx 0.7\lambda_{\mu m}$. The local universe is immersed in a broad-band radiation bath called the extragalactic background light (EBL; see Hauser & Dwek 2001 [190]) made up of a number of distinct components of different astrophysical origins. Among them, the presence of an intense, albeit innacurately determined, IR component due to integrated and redshifted starlight (1-5 μm) and reprocessed radiation by dust (100-200 μm) will influence observations at the VHE bands by strongly suppressing flux in a differential manner along the gamma-ray spectrum of extragalactic sources. In fact, the accurate measurement of the EBL is one of the important constributions that very-high energy gamma-ray astronomy can give to cosmology, and this can be done basically by comparing the observed spectrum of gamma-ray blazars with the expected blazar models to estimate the amount of absorption suffered during propagation [199].

The optical depth of the EBL, $\tau_{EBL}(E;z)$ is described by Equation 4.9, and will modify the intrinsic spectra of gamma-ray sources $\Phi_{obs}(E) = \Phi_{int}(E)e^{-\tau_{EBL}(E;z)}$. A fundamental consequence of an intense level of EBL is that an extragalactic gamma-ray horizon will exist, beyond which the Universe becomes opaque to observations at TeV energies. The recent observations of gamma-rays from increasingly distant blazars and extragalactic sources has nevertheless contributed to refine the predictions for the EBL energy density from near-IR to optical wavelengths, and the revisions have favoured the lowest theoretical estimates. In terms of the appearance of the source spectra, the expected peak in the shape of the EBL in the near-IR ($1 - 3$ μm) means that the 1 TeV photons will suffer more attenuation than softer, 0.2 TeV photons, and so the spectrum of distant blazars will be steepened in a manner which is proportional to the redshift of the source [20]. The diverse spectra of nearby sources can then be used as a reference point for limits on the hardness of the VHE blazar spectra which can then be used to test the different predicted levels of EBL density by trying to reconstruct the intrinsic gamma-ray spectra of distant objects [20]

More recently, Mazin & Raue 2007 [259] have collected spectral information on all

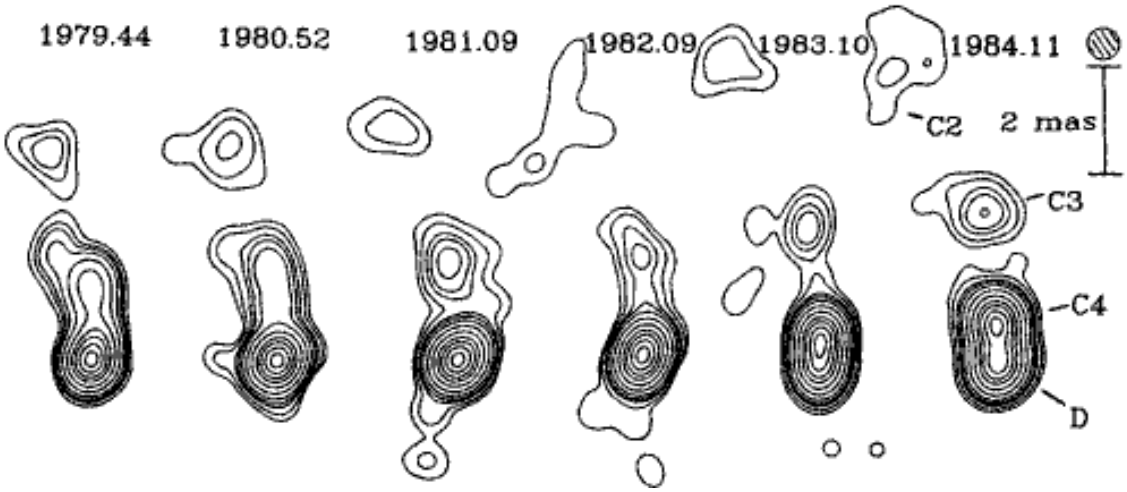

Figure 4.5: Series of radio images of the quasar 3C 345 at 10.7 GHz over the span of five years showing evidence for expansion of jet features within the jet at apparent relativistic speeds exceeding 7c. Credits: J. Biretta

gamma-ray blazars observed to that date and used basic assumptions regarding the physics of gamma-ray blazar emission to derive independent constraints for the EBL in the range $\sim$ 1-80 μm, which approximated very well to the lowest-limit from phenomenological EBL models. The most distant TeV source known to date, the FSRQ 3C 279, at redshift $z = 0.54$, pushes the VHE gamma-ray horizon to larger distances than would have been expected few years ago, corroborating the growing evidence towards a "transparent" Universe for gamma-rays [41]. In all these studies, the effects of the intrinsic source-opacity are an important and often unknown factor, which complicate the problem but must be taken into consideration [329].

4.5 Extragalactic Jets

4.5.1 Geometrical Structure and Superluminal Motion

The observation of superluminal motion in the jet of extragalactic radio sources came as the demonstration of J. Terrell 1964 [330] and M.J. Rees's predictions in 1966 [299] that the non-thermal emission from compact extragalactic sources originated in plasma experiencing relativistic expansion which would boost its emission and thus alleviate the energetic difficulties and constraints implied by short-timescale variability. The effect is based on the fact that if a portion of radiating plasma (blob), emitted from a stationary

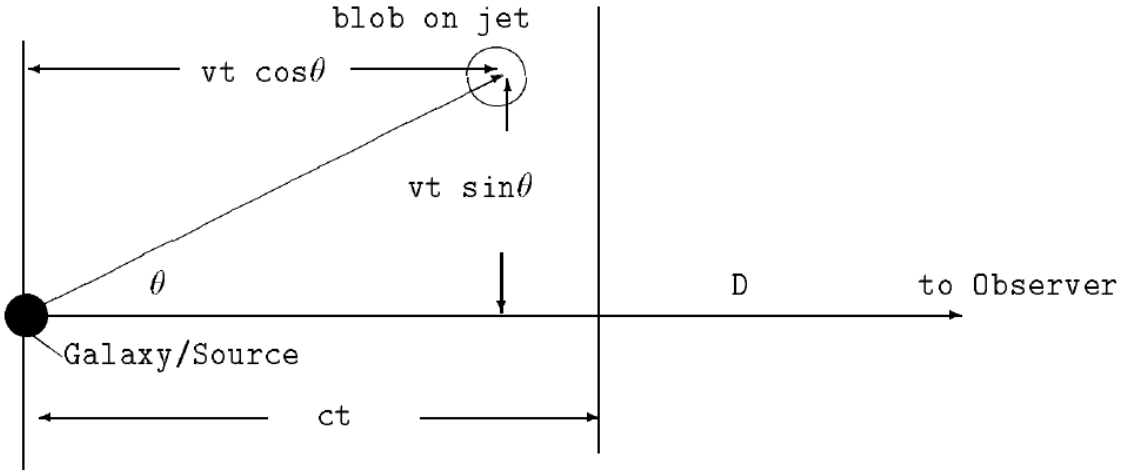

Figure 4.6: Geomtry of superluminal motion. Credits: G. Smooth lecture notes (UC Berkeley).

central source at distance D, moves away from the core with a velocity $v\beta c$ on an angle θ to the line of sight, then the photons which are emitted at a later time t_e will cover a distance $D - vt_e \cos\theta$ rather than D (see Figure 4.6).

This geometrical configuration has the direct consequence that the interval $\Delta t_{\rm obs}$ which the observer measures between two poisitions of the source is shortened by a factor $(1 - \beta\cos\theta)$ over the corresponding time interval in the blob's frame. As a result, the apparent speed of the moving jet features projected at the plane of the sky will be:

$$v_{\rm app} = \frac{vt_e \sin\theta}{\Delta t_{\rm obs}} = c\frac{\beta\sin\theta}{1-\beta\sin\theta} \tag{4.12}$$

In this geometrical configuration, the apparent projected speed $v_{\rm app}$ can be greater than 1 when the denominator becomes small, that is, for relativistic speeds $\beta \approx 1$ and when the blob motion is in close alignment to the line of sight $\cos\theta \approx 1$. With these limits into account we can re-write:

$$\beta_{\rm app} = \frac{v_{\rm app}}{c} \simeq \frac{2\theta}{\Gamma^{-2}+\theta^2}, \tag{4.13}$$

where $\Gamma = 1/\sqrt{1-\beta^2}$ is the Lorentz factor of the blob, and the approximations $\beta \simeq 1 - 1/2\Gamma^2$ and $\cos\theta \simeq 1 - \theta^2/2$ have been used [256]. For the case of blazars or closely-aligned sources, where the jet is viewed almost face-on, i.e. $1/\Gamma < \theta \ll 1$, we have $\beta_{\rm app} \simeq 2\theta^{-1} \gg 1$ and large superluminal motions can be registered such as shown for the

quasar 3C 345 on Figure 4.5.

4.5.2 Relativistic Boosting

An important consequence of this relativistic expansion (we will revisit this topic in Chapter 6 in the context of our own work) is the Doppler boosting of the emission; in fact, this was the main reason, related to the energetics of the source, for the prediction of the relativistic expansion in extragalactic sources. Again, if the source of emission is moving with $v = \beta c$ at an angle θ to the line of sight, the intrinsic emission parameters will be modified when registered by the observer according to the laws of relativistic aberration [245].

For an optically thin source of size s at a distance D, the synchrotron flux can be written as $S_\nu = \int j_\nu s d\Omega = D^{-2} \int j_\nu dV$, where $j_\nu s$ is the synchrotron emissivity given in Chapter 3 and dV the volume of the emitting source. The flux boost due to relativistic motion is therefore related to the transformation law of the emissivity from the rest frame j'_ν to the observer's frame j_ν:

$$j_\nu = n_e \frac{dW}{dt d\Omega d\nu}, \tag{4.14}$$

where n_e is the electron density. Let us define the Doppler factor $\delta = \Gamma^{-1}(1 - \beta \cos\theta)^{-1}$. Thus, the different components of Equation 4.14 above will transform as [256] (see also [304]):

- frequency: $\mathrm{d}\nu = \delta d\nu'$
- power: $\mathrm{dW} = \delta dW'$
- time: $\mathrm{dt} = \Gamma dt'$
- number density: $\mathrm{n} = \Gamma n'$
- solid angle: $\mathrm{d}\Omega = \delta^{-2} d\Omega'$

All these together will imply $j_\nu = \delta^2 j'_\nu$, and so the flux from a power law distribtuion in frequency with spectral index α will experience a Doppler boosting due to relativistic motion of:

$$S_\nu(\nu) = \frac{\delta^{3+\alpha}}{D^2} \int j'_\nu(\nu) dV', \tag{4.15}$$

which implies, for an spherical source that the boost in luminosity will be of $L = \delta^4 L'$. Because the Doppler factor is a very sensitivie function of the viewing angle (e.g., for blazars $\theta < \Gamma^{-1} \rightarrow \delta \simeq \Gamma$ and otherwise $\theta > 1 \rightarrow \delta \simeq \Gamma^{-1}$), Equation 6.27 will introduce a large difference between sources depending on geometrical factors alone, as we said in the discussion that openened this chapter.

4.6 The VHE Blazar PKS 2155-304

At a redshift $z = 0.117$, PKS 2155-304 is the prototypical southern-hemispehere TeV-emitting BL Lac object. First discovered in the X-rays in 1979 [184] by the *HEAO 1* because of its synchrotron emission which peaks in the soft X-ray band, this HBL is one of the brightest gamma-ray sources in the sky. Because of its intense emission and variability properties the source has been extensively studies along the years, specially in the context of comprehensive MWL campaings (see for example Urry et al. 1997 [337]). In radio its spectral properties are typical of compact radio sources, with a flat spectrum characteristic of the superposition of a series of compact, self-absorbed synchrotron components (see Chapter 3). In gamma-rays the source was first detected by the *EGRET* instrument onboard *CGRO*, between 30 MeV and 10 GeV [344], and its photon index at this high-energy band is hard ($\Gamma = 1.71 \pm 0.24$) indicating that the IC component peaks in the MeV gamma-ray region.

PKS 2155-304 was the third extragalactic source to be discovered in the TeVs, by the Durham Mark VI telescope, in 1997 [101]. The Durham results were later confirmed by observations with the H.E.S.S. telescopes still before the completion of the full array, in 2003, at a strong detection level of 45σ [15]. Since then, this source has been regularly observed by H.E.S.S. at a number of different intensities and spectral states. In fact, due to its strong emission, PKS 2155-304 is the only extragalactic H.E.S.S. source which is detectable at any moment in which it is observed, after integration times of ~ 1 hour when in the lowest state.

PKS 2155-304 was the subject of several multiwavelength campaigns involving TeV

observations along the past decade. The first one was conducted by H.E.S.S. in 2003 along with *RXTE*, the optical telescope ROTSE and in radio with the Nancay antenna [15], when the source was seen to be at a low state throught the electromagnetic spectrum, with VHE fluxes $\sim$ 0.2 Crab. The photon index observed by H.E.S.S. at low states is extremely soft $\Gamma = 3.37 \pm 0.07_{\rm stat} \pm 0.10_{\rm syst}$. The SED of PKS 2155-304 was modeled by a number of different leptonic and hadronic models, but frequently SSC models fit well the time-averaged SED at low states. As will be discussed in Chapter 6, this simple modelling approach fails when time-dependent information is included and in Chapter 5 we will present data from extreme high states which cannot be explained by one-zone SSC models.

In fact, during the summer of 2006, PKS 2155-304 exhibited unprecedented flux leves accompanied by strong variability [26] at minute timescales. A detailed analysis of the temporal properties of PKS 2155-304 at VHE energies is presented in [2]. Further discussion of the source and previous observations, in particular a detailed presentation of its optical polarimetric properties, will be given in Chapter 6.

Chapter 5

Time Variability and Spectral Dispersion in Blazars

Blazars are usually detected in the gamma-ray band when in a high state. These high states are dominated by strong and burst-like flaring episodes that are characterised by very short variability timescales due to the fast cooling times of the ~ 10 TeV electrons[1]. Furthermore, the limited photon statistics that are associated with these objects at VHE energies mean that the information on the time variability comes oftentimes in the form of poorly or under-sampled light-curves. The use of unbinned methods, which are capable of utilising all the information content of the time-tagged event lists recorded by the telescopes, without recourse to binning, is therefore justified. It also provides the best statistical tools for the study of short variability events. In this chapter the statistical aspects of this work will be presented.

These were initially developed with the intent of finding an optimal method to detect short flares within limited photon samples. The studies then evolved to the development of a new method, called the Kolmogorov distance method, that is specially designed to look for energy-dependent time variability signatures in limited photon data at high energies. After discussing in detail this new method, which proved to have excellent performance for the proposed task, we will apply it to the data on the large flare of PKS 2155-304 observed in 2006, to study two different effects. First, to test for quantum gravity sig-

[1] A detailed study on the characteristics of the gamma-ray variability in blazars can be found in Giebels & Degrange 2009 [173] and Abramowski et al. [2].

natures in the energy dependent propagation of photons (a realisation of the so-called time-of-flight experiments) and second, to put some constraints on the internal acceleration mechanisms in extragalactic jets, which lead to the production of gamma-rays of very high energy. The analysis of the H.E.S.S. data relative to this Chapter was already discussed in Chapter 2.

Some of the theoretical background work related to this chapter was presented in the 4th Heidelberg Symposium in High-Energy Gamma-ray Astronomy (Gamma 2008) [62]. The initial work on the statistical algorithm for energy-dependent dispersion was presented at the 31st International Cosmic Ray Conference (ICRC) in 2009 [63] and in a number of talks at National conferences. A paper on the application of the method to the TeV blazar PKS 2155-304 is being submitted shortly to Astroparticle Physics.

5.1 Bayesian Studies of Time Variability: Unbinned Statistical Methods

5.1.1 Fundamentals of Bayesian statistics

The laws of probability inference were shown by Cox [114] to be derivable from two fundamental axioms, obeying the rules of Boolean logic:

Axiom 1: *The probability of an inference (X) on given evidence (I) determines the probability of its contradictory ($\tilde{X}$) on the same evidence.*

$$\mathrm{prob}(\mathrm{X}|\mathrm{I}) + \mathrm{prob}(\tilde{\mathrm{X}}|\mathrm{I}) = 1 \tag{5.1}$$

Axiom 2: *The probability on given evidence (I) that both of two inferences (X and Y) are true is determined by their separate probabilities, one on the given evidence, the other on this evidence with the additional assumption that the first inference is true.*

$$\mathrm{prob}(\mathrm{X}, \mathrm{Y}|\mathrm{I}) = \mathrm{prob}(\mathrm{X}|\mathrm{Y}, \mathrm{I}) \times \mathrm{prob}(\mathrm{Y}|\mathrm{I}) \tag{5.2}$$

Bayes' Theorem follows trivially from Axiom 2 by exchanging propositions X and

Y in Equation 5.2 and noticing that $X \cdot Y = Y \cdot X$:

$$\text{prob}(\text{X}|\text{Y}, \text{I}) \times \text{prob}(\text{Y}|\text{I}) = \text{prob}(\text{Y}|\text{X}, \text{I}) \times \text{prob}(\text{X}|\text{I}), \tag{5.3}$$

from which follows:

$$\text{prob}(\text{X}|\text{Y}, \text{I}) = \frac{\text{prob}(\text{X}|\text{I})\text{prob}(\text{Y}|\text{X}, \text{I})}{\text{prob}(\text{Y}|\text{I})}. \tag{5.4}$$

In logical terms, Bayes' Theorem states that every proposition (X or Y) implied by a given hypothesis (I) is irrelevant under that hypothesis to every other proposition. In purely statistical terms we can think of X as a proposition (or model) and Y as an observation (or piece of data), where I is some knowledge or information about the system under study, for example that it is governed by a certain probability distribution. Bayes' theorem is therefore telling us that at every new observation of the system (when new data Y is accumulated) our opinion prob(X|Y, I) on a given assertion about it, X, is updated according to what we already knew (or believed) about it, prob(X|I), and the likelihood that this previous idea X (together with the information I) explain the new data taken, prob(Y|X, I) (derived from model fitting or regression). Observe here that the term prob(Y|I) is irrelevant for any assertions about X (by Axiom 2). This analysis process described in the Bayesian theorem is sometimes called "learning process" or "logical inference".

Following this explanation, the individual terms of the theorem have particular names, which highlight their meaning in the inference process [183]: prob(X|Y, I) is the posterior probability of X; prob(X|I) is the prior probability of the hypothesis X; prob(Y|X, I) is the likelihood function of X, that is the probability of obtaining the data Y if the hypothesis X and the prior information I are true; and prob(Y|I) is simply a normalisation factor, which being independent of the hypothesis under test X, is usually irrelevant for model comparison. This last term can be written (by Axiom 2) as:

$$\text{prob}(\text{Y}|\text{I}) = \sum_{\text{i}} \text{prob}(\text{X}_\text{i}|\text{I})\ \text{prob}(\text{Y}|\text{X}_\text{i}, \text{I}), \tag{5.5}$$

and is simply the probability for $Y|I$ integrated over the entire set of parameters X_i of the model under study. This last operation 5.5 in Bayesian jargon is referred to as *marginalisation*, because all the nuisance parameters of the model (i.e. uninteresting for the infer-

ence process in question) are eliminated by integration.

Because prob(Y|I) is always the same for all X, this term is unimportant for comparing the odds ratio $\mathcal{O}_{ij}$ between two models X_i and X_j. The odds ratio can be written as the ratio of the posterior probabilities for each model:

$$\mathcal{O}_{ij} = \frac{\text{prob}(\text{X}_\text{i}|\text{Y}, \text{I})}{\text{prob}(\text{X}_\text{j}|\text{Y}, \text{I})} \equiv \frac{\text{prob}(\text{X}_\text{i}|\text{I})}{\text{prob}(\text{X}_\text{j}|\text{I})}\mathcal{B}_{ij}, \tag{5.6}$$

where the first factor is called the *prior odds ratio* and $\mathcal{B}_{ij}$ is the *Bayes factor*, which is simply the ratio of the two likelihood functions for X_i and X_j, usually obtained from fitting the model to the data.

In the case that the prior's odds are equal for both models (i.e., one does not have a strong *a priori* preference for any of the models – the modeller is an uninformed subject and the prior is said to be *uniform* in the model's parameter space), only the Bayes factor (the mathematical incarnation of Occam's razor) is relevant for identifying the best model to fit the data. In such cases the inference problem can be reduced to a *maximum likelihood* approach, in which the solution as to which of $X(\theta_i)$ or $X(\theta_j)$ better corresponds to the observed reality is obtained by maximising the likelihood function $\mathcal{L}(\theta) = \text{prob}(\text{Y}|\theta, \text{I})$ to find the best-fit vector of parameters $\hat{\theta}$.

It is this maximum likelihood approach which will be used in the Bayesian blocks model for searching flares in high-energy light-curves, discussed in the following section, whereas our own method to find the energy-dependent dispersion parameters in these same light-curves will draw from another approach, namely "metrics minimisation". This approach is appropriate only if one is working in a probability space with well-defined metrics, so that distances between probability distributions can be specified.

5.1.2 Change-point detection of gamma-ray flares

As astronomical observations move into the highest energy windows, such as GeV and TeV gamma-rays, it becomes increasingly clear that an unbinned data analysis is preferred. The application of unbinned methods to high-energy data analysis is often justified on the basis that binning can overcome the problem of the paucity of the data, but by its very nature this practice inevitably results in loss of information and can greatly

limit the temporal resolution and potential of the analysis, specially in the regime of low counts found in high-energy astronomy. Moreover, unbinned algorithms, which do not rely on any kind of smoothing or representation of the data by continuous functions, are usually well suited for the analysis of local and aperiodic light-curve features, such as bursts or flares in AGN or GRB observations. In the case of gamma-ray datasets, where the counting rates can be very limited and the data consist of a series of time- and energy-tagged events, unbinned methods naturally constitute the preferred choice of tools for the analysis.

Change point algorithms are an optimal approach for studying aperiodic or stochastic variability episodes such as those commonly present in light-curves from blazars. The change-point problem is defined as the identification of the instant in a given Poisson sequence where the process's rate changes; usually the unknown parameters in the problem are the prior and posterior rates, the location of the change point, and the number of change points in the sequence. The object of inference is therefore how best to model the event sequence by a step-function with an arbitrary number of pieces.

Let us thus formulate the change-point problem in Bayesian terms, following the description presented in Green 1995 [181]. Suppose we have a countable collection of candidate partition models (or piecewise step functions) $\{\mathcal{M}_k, k \in K\}$. Model $\mathcal{M}_k$ is described by a vector $\theta^{(k)}$ of unknown parameters, such as listed above; the number of such parameters determines the *dimension* of the model n_k. Call Y the dataset. The joint distribution $(k, \theta^{(k)}, Y)$ is expressed by the Bayes theorem in the form:

$$p(k, \theta^{(k)}, Y) = p(k)\ p(\theta^{(k)}|k)\ p(Y|k, \theta^{(k)}), \tag{5.7}$$

which is simply the product of the model probability, the prior on the model and the likelihood. Thus for example, if Y is a Poisson sequence of length $[0, L]$, the range of models $\mathcal{M}_k$ with $k \in \mathcal{K} = \{0, 1, 2, ...\}$ indicates that there are exactly k change-points in the sequence. To parameterise the resulting step function, we need to specify the position of each change-point and the value of the step-function for each of its pieces, and so $\theta^{(k)}$ is a vector of length $n_k = 2k + 1$. In practice, if all we desire is to detect the presence of flaring events, we need only be concerned with the change-point position, and can treat the other parameters of the model as nuisance parameters that get integrated out in the

writing of the likelihood function. The Bayes factor for the model choice is thus given by the ratio $p(k_1|Y)/p(k_0|Y) \div p(k_1)/p(k_0)$, which Green observes to be independent of the prior $p(Y)$, as we have seen before in Section 5.1.1.

Bayesian Blocks

With the problem formally defined, we now present an optimal search algorithm, called *Bayesian Blocks*, due to Scargle 2001 [311] and Jackson et al. 2004 [207], which is an ideal method for flare detection in high-energy light-curves[2].

The "Bayesian blocks" algorithm which we will use here to identify individual burst episodes in the large flare of PKS 2155-304 in 2006 [26] was proposed as a method for detecting *local* structures in a photon sequence and characterising intensity variations of a stochastic quality in a time series. The optimal search algorithm developed by Jackson et al. is the preferred method for implementing this search. This dynamic algorithm has a computational cost that goes with $O(N^2)$ and is always guaranteed to find the optimal partition for a given choice of prior. It is also shown by Scargle et al. [313], in a more detailed study of the method, that this approach is relatively insensitive to the particular value of the prior within a broad range of "sensible choices"[3], and this is a very desirable property of the method. In the following few sections I will present the theoretical background associated with this method, including my own extensions to it, before proceeding to an application to the large flare of PKS 2155-304.

As already mentioned, the algorithm is based on the fitting of piecewise constant models to the data, each piece (block) being of constant Poisson rate and yielding a step-function representation of the signal. Each block indicates therefore a different "state of emission" of the source. The properties of the bursts are determined in a non-parametric fashion from the width and amplitude of the blocks, independently of any pulse-shape model, which can be fitted to the light-curve *a posteriori*, using the non-parametric in-

[2]The method has now been implemented as part of the *Fermi* standard analysis software [61] and a C++ version of the algorithm has been jointly implemented for the Durham version of the H.E.S.S. analysis software by H. Dickinson and myself. Relevant, non-published material about the method and further developments can be found at: astrophysics.arc.nasa.gov/ jeffrey/. Date of last access August/2010.

[3]This sensible choice has been heuristically quantified by M. Novak (private communication) and states that the optimum prior for block segmentation, γ, is given approximately by the logarithm of the number of data points in the series, $\gamma \sim \ln N$.

formation obtained in the way described here. The particular strength of the model is in its local character, which renders it effective in identifying bursts in large and complex datasets and in its direct applicability to time-tagged event data, i.e. datasets composed of the individual photon time-stamps, as usually recorded in high-energy astronomy experiments. This allows for the best use of the total information available in the light-curve and to the search of short timescale variability. We now proceed to the exposition of the algorithm.

Block fitness: evidence for a constant Poisson rate model. Let us first derive the likelihood function for the constant rate model describing the block. For that we use the fact that the elementary event of photon detection obeys a discrete Poisson counting process (PCP) and the distribution of the number of counts n in an interval δt is described as:

$$P(k|PCP, \Lambda) = \frac{\Lambda^n e^{-\Lambda}}{n!}, \tag{5.8}$$

where $\Lambda \equiv \lambda\, \delta t$ is the (constant) count rate in the given interval, and $\lambda \geq 0$ is the count rate per unit time [s^{-1}]; k indicates the block (or change-point) k. The elementary interval δt is identified with the temporal resolution of the observations (a "tick" of the detector's clock).

0-1 event data mode: The strength of the proposed method is fully exploited with the use of *time-tagged event data* (TTE)[4], where the raw light curve is described in terms of the detection times ("ticks") of individual photons and can be probed down to the shortest timescales. In addition, such a treatment frees us from any binning anomalies that can be very relevant in our case, where the low count rates tend to force the bin sizes to be of comparable width to the relevant temporal scales of variability of the source. The time series can then be parameterised as a set of N photon arrival times:

$$D_{TTE} : \{t_n,\ n = 1, 2, 3, ..., N\}, \tag{5.9}$$

[4]This is different from binned data in the sense that no duplicated time-tags are allowed and usually the intervals δt are much smaller than the astrophysical timescales of interest.

where n represents each individual count and N is the total number of photons detected in the observation. Introducing an integer time index m so that $t_m = m\delta t$, for $m = 1, 2, 3, ..., M$, $M \geq N$, we can reconstruct the light curve as a sequence of detection/non-detection 0-1 events:

$$D_{TTE} : \{m_n,\ n = 1, 2, 3, ..., N\}, \tag{5.10}$$

meaning that the photon n is detected at time $m_n\delta t$ and the duration of the whole interval is given by $T = M\ \delta t$. Let us call such a 0-1 event X_m. Now, we associate with the non-detection a probability $P\{X_m = 0|\Lambda\} = p_0 \equiv e^{-\Lambda}$, and with the detection a probability $P\{X_m = 1|\Lambda\} = p_1 \equiv 1 - p_0$. Since the detections of individual photons are independent processes, and no correlations exist between the number of photons in two different, non-overlapping intervals, the block likelihood is given by the product of the likelihood functions for the individual intervals that compose it. The joint probability distribution for all events X_m is thus given by:

$$P(D_{TTE}|\mathcal{M}(\Lambda, T)) = \prod_{m=1}^{M} P(X_m|\Lambda) = p_1^N(1 - p_1)^{(M-N)}, \tag{5.11}$$

corresponding to N detections (1s) and $M - N$ null events (0s) in the interval T. Since Equation 5.11 is independent of Λ, we can change the description of the problem so that p_1 is the new model parameter. In this representation the uniform normalised prior is simply:

$$P(p_1|\mathcal{M}) = \begin{cases} 1 & \text{if } 0 \leq p_1 \leq 1 \\ 0 & \text{otherwise} \end{cases} \tag{5.12}$$

To evaluate the global likelihood, we follow Bayes' theorem; the product of the prior and the likelihood in Equation 5.11 gives:

$$\int P(D_{TTE}|\mathcal{M}(p_1))\ P(p_1|\mathcal{M})\ dp_1 =$$
$$= \int_0^1 p_1^N(1 - p_1)^{M-N}\ dp_1 = B(N + 1, M - N + 1), \tag{5.13}$$

where B is the Beta function, which in the case of a single-rate model reduces to:

$$\mathcal{L}(\mathcal{M}|D_{TTE}) = \frac{\Gamma(N+1)\,\Gamma(M-N+1)}{\Gamma(M+2)} = \\ = \frac{N!\,(M-N)!}{(M+1)!} \tag{5.14}$$

Binned event data mode: The light curve is composed of cells (bins) in which multiple photons are stored, the distribution of the number of counts in a bin following that of Equation 5.8. We parameterise the light curve as:

$$D_{BIN} : \{n_m, m = 1, 2, 3, ...M_k\}, \tag{5.15}$$

where n_m is the number of counts in bin m and $\mathcal{M}_k$ is the number of bins in block k. With this notation, we can re-write Equation 5.11 so that the likelihood for the block is, recalling the "memoryless" property of the Poisson process:

$$\mathcal{L}_k = \prod_{m=1}^{M_k} \frac{\Lambda^{n_m} e^{-\Lambda}}{n_m!}. \tag{5.16}$$

We define $N_k = \sum_i n_i$ the total number of counts (or photons) in block k, so that:

$$P(D_{BIN}|\mathcal{M}(\Lambda)) = \frac{\Lambda^{N_k} e^{-\Lambda M_k}}{\prod_{m=1}^{M_k} N_M!}. \tag{5.17}$$

Notice that the denominator $\prod_{m=1}^{M_k} N_M!$ is the same irrespective of the details of the interval partition and can thus be dropped for model comparison purposes; finally we arrive at the following likelihood function for the constant rate model of block k in binned data mode:

$$\mathcal{L}_k = \Lambda^{N_k} e^{-\Lambda M_k}. \tag{5.18}$$

A maximum likelihood analysis gives the following posterior for the block:

$$\mathcal{L}_{max} = \left(\frac{N_k}{M_k}\right)^{N_k} e^{-N_k}. \tag{5.19}$$

This result is useful because it shows exactly what the partitioning model is doing

when treating the data in a time-tagged event format: it is evaluating the temporal density of photon counts, represented by the dependence on the ratio N^k/M^k, according to the Poisson process that governs it (e^{-N^K}). In so doing it looks for regions where the variations in density differ significantly from those expected from simple statistical fluctuations, indicating a true rate change.

Sampling for exponential flares

The likelihood functions derived in the last two paragraphs are for piecewise constant rate models. Due to the burst-like character of variability, these are good approximations to fitting the light-curve, because the rate changes in high-energy flares tend to be dramatic and to happen on very short timescales. For well-sampled bursts though (like the rare case of the large flare of PKS 2155-304), where the profile is well-resolved and contains many events (i.e., $N \gg 20$ counts per block) this approach can lead to errors in the partition because the algorithm will tend to subdivide a single burst into two or more blocks unless the prior for division is chosen to be very restrictive. As a possible solution to this difficulty we propose to include some information on the burst profile in the likelihood function. So, in this paragraph we derive the likelihood function for an exponentially-varying Poisson rate, which we will apply to the search algorithm in the application to PKS 2155-304 in Section 5.1.4. The function will be derived for unibinned event data. This represents an extension to Scargle's original work.

Let us start by stating the rate function $\Lambda = \lambda(t)\delta t$ for a time-varying Poisson process:

$$\lambda(t|\alpha) = \lambda_{0,k}\, e^{\alpha\delta t}, \tag{5.20}$$

where $\alpha \in \mathbb{R}$ and the baseline rate $\lambda_{0,k}$ is the same for all t within the block k and can be defined however is convenient; if we choose to obey *continuity* between the blocks, $\lambda_{0,k}$ could be defined for example as: $\lambda_{k-1}(t^*|\alpha) = \lambda_{0,k-1}\, e^{\alpha\delta t^*}$, where t^* is the end-time of block $k-1$. As in the previous cases, δt is defined in relation to a finite data cell m and for simplicity we take δt to be equal for all cells m . A given time in the series is thus written as: $t_i = m_i\delta t$, whereas the entire interval of the light-curve is $T = M\delta t$, where M is the total number of data cells. Thus, the probability of 0-1 events in a given datacell m is given by:

$$\begin{cases} p(X_m = 0|\Lambda) = p_0 = e^{-\lambda_i} \\ p(X_m = 1|\Lambda) = p_1 = \lambda_i\, e^{-\lambda_i} \end{cases} \tag{5.21}$$

or more conveniently:

$$\ln p = \begin{cases} -\lambda_o\, e^{\alpha_k t_i} & \text{if } X_m = 0 \\ ln\lambda_0 + (\alpha_k t_i - \lambda_0\, e^{\alpha_k t_i}) & \text{if } X_m = 1 \end{cases} \tag{5.22}$$

where we use α_k to designate that α changes for each block in the partition. The passage to the log-likelihood will simplify the algebra and is permitted because it is a monotonic transformation.

For deriving the block likelihood, we follow the same procedure as before and write the product of the likelihood for 0-1 events for each cell:

$$\ln \mathscr{L}_k = \sum_{i=1}^{M} \ln p_m = \sum_{i=1}^{N} \ln p_{1,m} + \sum_{j=1}^{M-N} \ln p_{0,m}. \tag{5.23}$$

After some algebra, the log-likelihood reduces to:

$$\ln \mathscr{L}_k = N \ln \lambda_0 + \alpha_k \sum_{j=1}^{N} t_j - \lambda_0 \left(\sum_{i=1}^{M} e^{\alpha_k t_i} \right). \tag{5.24}$$

Recalling that $t_j = m_j \delta t$, the second term in this expression can be written as $N\alpha t$, and given that the sum in the third term is over a continuous range of cells, it can be replaced by:

$$\lambda_0 \left(\sum_{i=1}^{M} e^{\alpha_k t_i} \right) = -\lambda_0 \left(\int_t e^{\alpha_k t}\, dt \right). \tag{5.25}$$

We then arrive at the block log-likelihood function for an exponential flare profile:

$$\ln \mathscr{L}_k = N \ln \lambda_0 + \alpha_k N \delta t - \frac{\lambda_0}{\alpha_k}(1 - e^{\alpha_k t}), \tag{5.26}$$

which can be maximised on the parameters of interest as done for Equation 5.19, provided nuisance parameters are eliminated, and used directly in the dynamical algorithm described below.

5.1.3 Dynamical Algorithm

The algorithm discussed below solves the problem of finding multiple change-points optimally by partitioning an ordered sequence of discrete data cells into a set of blocks characterised and distinguished from their immediate neighbours by the value of the Poisson rate parameter. Let us first proceed with some useful definitions.

The *data space* in our case is the time interval (not necessarily continuous) over which observations have been made. It is composed of a set of N discrete data cells $C_n \equiv \{x_n, t_n\}$, where x_n is the independent variable with which the time coordinate t_n is associated. Data cells are in univocal correspondence to the counts in the sequence (or 0-1 events) and need not be uniformly ditributed in time.

A *block* is a set of adjacent cells and is written $\mathcal{B}(n, m) \equiv \{C_n, C_{n+1}, ..., C_m\}$. The edges of the block are marked by the change-points and are characterised by discrete jumps on the value of the rate variable. The fitness function of the individual block is the elementary statistical problem solved in the last section. The *change-points* (cpt) define the location and extension (width) of each block and are the sole parameters of the likelihood function giving the posterior probability to be maximised in the partitioning process. Every block starts with a change-point, so that $n_{\rm blocks} = n_{\rm cpts}$ and the first data cell is always a change-point.[5]

Finally, a partition of the interval $\mathcal{I}$ is a set of N non-overlapping blocks with change-points whose union is equal to the whole interval:

$$\mathcal{P}(\mathcal{I}) \equiv \{N_{\rm blocks}, {\rm cpt_k}, {\rm k} = 1, 2, 3, ..., {\rm N_{blocks}}\} \tag{5.27}$$

There exist 2^{N-1} ways of partitioning the data cells into a set of 1 to $n_{\rm cells}$ blocks, and the algorithm does it at a cost $O(N^2)$.

Salmenkivi & Mannila 2005 [306] propose a simple way in which to reduce the computational cost of the algorithm to only a fraction of this value. Their procedure, which we incorporate in our algorithm, is to modify the code to allow only a subset of all events to be a change point. The choice is made heuristically, by evaluating beforehand the

[5]Note that the change-points must always be drawn from the set of time coordinates of the data cells, i.e. must correspond to an event.

"likelihood" of occurrence of a change point at a given position in the time series. For this, a window w is used around each event m, with extremes $t_l = t(m) - t(m-w)$ and $t_r = t(m+W) - t(m)$. Our heuristic function for the decision on the "suitability" of a given point m_i to be a change-point is defined as:

$$h(m) = \frac{t_r - t_l}{t_r + t_l}. \tag{5.28}$$

Notice that h is simply a measure of the "variation on the photon density along the window", and the higher this variation, the better a candidate for a change-point m is. The threshold value of h, which will define the selected points in the sequence that will be tested for change-points during the partition process, is best determined via simulations, either of an arbitrarily chosen subset of the dataset under study (via bootstrap for example), or a Monte Carlo-generated independent realisation of the same dataset.

Finally, the *optimal partition* of the interval is the one that maximises the *global fitness function* for all blocks; if the blocks and data-cells are all independent, the fitness is additive over the blocks, and the global quantity to be maximised is:

$$F(\mathscr{P}(\mathcal{I})) = \sum_{k=1}^{N_{\text{blocks}}} f(\mathcal{B}_k), \tag{5.29}$$

where $F(\mathscr{P}(\mathcal{I}))$ is the total fitness and $f(\mathcal{B}_k)$ is the fitness of each individual block. The algorithm is generic and independent of the statistics describing the fitness function, but the choice of prior for the number of blocks in the model must be additive in the number of blocks so that the algorithm can be applied. This excludes for example that one uses the interesting Poisson prior for the flares multiplicity. This is because the factorials of the number of bursts that will appear in the denominator of the prior do not have an additive property[6].

Before proceeding to a description of the code, two results which are fundamental for the implementation of the dynamic algorithm must be quoted [207]:

[6]It has been suggested to me by Dr. Peter Craig from the Mathematics Department of Durham University, that the use of a Kalman filter might be the best way to incorporate a Poisson prior without changing the dynamical nature of the algorithm, but due to time restrictions this line of research was not pursued further.

Lemma (Principle of Optimality): *Let a subpartition $\mathscr{P}'(\mathcal{I})$ be composed of any subset of adjacent blocks $\mathcal{B}'$ of the optimal partition $\mathscr{P}(\mathcal{I})$. Then any such subpartition $\mathscr{P}'(\mathcal{I})$ is also an optimal partition of the subset of $\mathscr{P}(\mathcal{I})$ that it covers.*

Corollary: *Removing the last block of an optimal partition leaves an optimal partition of the remaining set of blocks.*

The partitioning algorithm

The following description refers to our particular implementation of the algorithm, which is presented in the Appendix. The proof that this procedure gives the optimal partition can be found in *Theorem 2* of [207].

We start with the first data cell, adding a new cell at each step of the calculation until the whole interval has been treated. At step R the algorithm finds the optimal partition of the interval comprised of data cells $\mathcal{I}_R \equiv \{C_1, C_2, ..., C_R\}$. The case $R = 1$ is trivial for there is only one partition possible; the fitness function of this data cell is calculated by the subroutine *MAKE BLOCKS* and is stored in the first cell of the array *optimum*, which stores the values of the fitness function of the optimal partition at each step. This array is recursively used by the subroutine *PARTITION* to re-calculate the best partition at each new inclusion of a data cell.

Now suppose we have completed step R, having obtained the optimal partition $\mathscr{P}(\mathcal{I}_R)$; for finding $\mathscr{P}^{\rm opt}(\mathcal{I}_{R+1})$, we calculate the array *lastblock*, which contains the fitness of all the putative last blocks starting at r and extending up to the end of the current interval, $R + 1$, with r ranging from 1 to $R + 1$.

Using the block fitness additivity property (Equation 5.16), the fitness of $\mathscr{P}^{\rm opt}(\mathcal{I}_{R+1})$ consists of the fitness for $\mathscr{P}^{\rm opt}(\mathcal{I}_{r-1})$ plus that of the array *lastblock*$(r, R + 1)$. The new optimal partition has got a last change-point r^*, still to be determined. This new change-point is given by $r^* = argmax[fitness(r)]$ and the array *fitness* is calculated at each step as: $fitness(r) = lastblock(r) + optimum(r-1)$. At each step, the locations of the last change-point determined are stored in the array $C_{\rm nbins\times nbins}$ composed of the cell locations of the change-point.

The last important thing to notice is in respect of the prior probability distribution for

the number of blocks. Scargle 1998 [311] proposed a geometric prior both for algebraic convenience and because it naturally favours minimum-parameter models, by penalising the partition of the interval into many blocks. The geometric prior assigns increasingly smaller probabilities for the inclusion of newer blocks in the model [109]:

$$P(N_{\text{blocks}}) = P_0 \gamma^{-N_{\text{blocks}}}, \quad 0 \leq N_{\text{blocks}} \leq N \tag{5.30}$$

so that $\ln P \propto -N_{\text{blocks}} \ln(\gamma)$, since the normalisation constant is not important for model comparison. The prior is additive and so its inclusion in the model is done simply by subtracting $\ln(\gamma)$ from the fitness function of each new block created. The term acts therefore as a penalising factor (akin to Occam's razor) for the segmentation of the interval. Simulated data by M. Nowak[7] suggests an optimal value for the prior of $\gamma \approx N$, the number of data cells, but, as always, a specific Monte Carlo study for finding the best value of γ for each particular data set under consideration is suggested.

For the proof of a theorem which shows the applicability of the Bayesian blocks algorithm to Cherenkov telescope data, please see Barres de Almeida et al. 2008 [62]. This proof will not be presented here for concisiveness, since it is very specific and slightly off-topic.

5.1.4 Application to PKS 2155-304

The Bayesian blocks algorithm was used to detect the individual bursts composing the large flare event observed by H.E.S.S. from PKS 2155-304 on the night of 28$^{\text{th}}$ July, 2006 (MJD 53944) [26]. The VHE data were analysed to extract the raw times and energy-tags of individual photons, using the DurhamLightCurve routine of the H.E.S.S. software, developed by H. Dickinson [123]. Data reduction proceeded according to the standard H.E.S.S. analysis as described in Aharonian et al. 2006 [19] and Benbow 2005 [78], and outlined in Chapter 2. Events were selected using "standard cuts" with an energy threshold of 170 GeV throughout the night (mean zenith angle $\approx 13°$). A total of 5,364 post-cut events were retrieved from the three 28-min observation runs (mean rate ~ 1 Hz),

[7] www.space.mit.edu/CXC/analysis/SITAR/, last accessed in 2008.

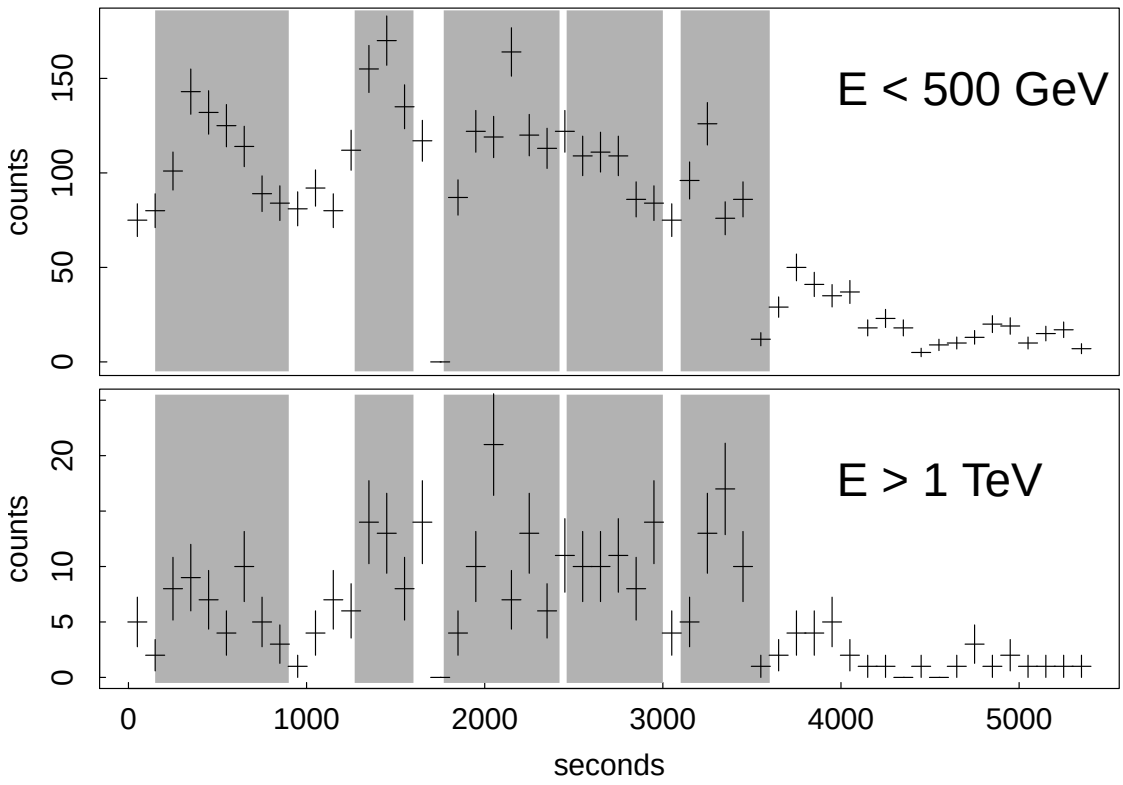

Figure 5.1: Light curve of PKS 2155-304 big flare event of MJD 53944 [**?**], for photons above 170 GeV. The data (crosses) are binned in one minute intervals, and the time is counted from the first event. The grey shades mark the location and extent of the five major bursts (BF 1-5) on which we conducted the dispersion analysis. These were selected using the Bayesian blocks algorithm with a variable Poisson rate, as described in Section 5.1.2. Note that the positions of the change-points in the two data subsets ($E < 500$ GeV and $E > 1$ TeV) fall in very similar, consistent, positions.

which were all accepted as photons; the highest energy event recorded was 7.4 TeV. The error in a single event energy reconstruction is dominated by systematic uncertainties and is estimated to be of the order of 15% throughout the entire energy range. As discussed in the original analysis by the H.E.S.S. collaboration [26], the source presented little or no spectral variability during the night, and for simplicity we will adopt a simple power law spectrum $\Gamma \simeq -3.5$ for all analysis in this chapter.

The results of the application of the Bayesian block algorithm (using our exponential flare likelihood function 5.26) to the data are shown in Figure 5.9. The optimal prior to blocks division used was $\ln \gamma = 8$, close to Nowak's rule. The different blocks are marked by the alternating white and shaded areas in the plot. As discussed before, the prior

$\ln\gamma$ can be though of as a "sensitivity" parameter determining the "fineness" with which features in the light-curve can be distinguished. Given the large range of amplitudes we are dealing with in this particular dataset, the choice of the prior was made so that we could get the most uniform partitioning throughout the time series. The particular value of $\ln\gamma = 8$ also reproduces the flares detected with H.E.S.S. and described in the original analysis paper [26] – in fact, the same partition is obtained for $\ln\gamma$ in the range 5-8, demonstrating the stability in the choice of the prior. The fact that this final partitioning model reproduces the original H.E.S.S. analysis is convenient because it will be used for the study of the Kolmogorov distance method in the next section, which we can then compare directly with other analysis of energy-dependent dispersion performed by the H.E.S.S. on this same dataset.

5.2 Energy-dependent dispersion in blazars

Having found and discussed an adequate method to detect burst-lke features in the light-curve of high-energy sources, we now move to the discussion of another kind of statistical algorithm. This will be used to detect energy-dependent dispersion in lightcurves of high-energy sources and will allow a more in-depth view of the physics of the source's emission and of radiation propagation over cosmological distances in the Universe.

5.2.1 Unbinned Methods: Motivation

The search for temporal lags between emission from different energy bands is common practice in astronomy. Methods are traditionally based on cross-correlation of the binned time-series, and sometimes rely on a particular parameterisation of the light-curve, for example by modeling the data according to a pre-determined choice for the light-curve profile. The research into methods for the study of energy-dependent dispersion in the light-curves of gamma-ray sources has gone through a prolific period in recent years, motivated by the prospects of testing for signatures of violation of local Lorentz invariance.

Astrophysical observations provide one of the most privileged instances for searches of quantum-gravity (QG) effects to be conducted. One of the possible experiments, based on the measurement of the time-of-flight for photons of different energies, was first sug-

gested by Amelino-Camelia et al. (1998) [47] and is based on the search for an energy-dependent speed of light in a vacuum from GeV-TeV photons propagating over cosmological distances. Because of the very-high energies at which QG effects are expected to become manifest (around the Planck scale, $E_{\rm QG} \approx E_{\rm P} \simeq 10^{19}$ GeV) and the consequently small magnitudes of its signatures observable at astrophysically accessible energies (for $E_\gamma \sim 1$ TeV, the correction to the speed of light due to quantum gravity is of about $10^{-15}c$), the searches require extremely sensitive measurements. Another important aspect of time-of-flight experiments is that since the effects on the variations of the speed of light manifest as integrated time-delays over the distance travelled by the photons, observations of distant (and therefore weak) sources are necessary. In fact, to first order, the magnitude of the delays expected from QG variations in the speed of light is $\delta t \propto E_\gamma / E_{\rm QG} \sim$ 10 s/TeV.Gpc. This means that the searches have to be conducted over correspondingly narrow variable features in the light-curve (thus disfavouring binning) and in order to be sensitive to small spectral dispersions within very limited photon lists.

The use of high-energy photons for performing the measurements is a requirement due to the form of the energy-dependence of the perturbation on the photon momentum due to QG, which is given by $c^2p^2 = E_\gamma^2[1 + \xi E_\gamma/E_{QG} + O(E_\gamma^2/E_{\rm QG}^2)]$ [47]. In other astrophysically relevant situations, such as for example the search for energy-dependent time delay signatures from ongoing particle acceleration at the source, studies at high energies are also to be preferred, and therefore the same limitations regarding the photon statistics apply.

5.2.2 Dispersion Cancellation Algorithm

A number of different approaches exist that are specifically designed for these kinds of tests, such as likelihood methods [255] and modified cross-correlation functions applied to the individual photon events [243]. A particularly attractive and simple algorithm to solve the problem of detecting energy-dependent time lags in statistically limited photon lists was independently proposed by Scargle et al. (2008) [312] and Ellis et al. (2008) [133], the former being derived originally to search for QG signatures from neutrino propagation. The algorithm works directly on the time- and energy-tagged events and tests for the presence of energy-dependent lags by searching for a non-zero parameter τ^* [s/TeV] that

optimally cancels any spectral dispersion present in the light-curve. An advantage of this approach is that it makes no *a priori* assumption on the statistical nature of the dataset (i.e. it is a non-parametric test), being therefore of great generality.

The search for the *dispersion cancellation*[8] parameter τ^* is done by assuming a particular functional dependency between the relative temporal lag δt between two photons and their energy difference ΔE_γ. In general, if the dispersion is small compared to other relevant variability timescales of the astrophysical system under study, the exact functional form of the dispersion is of little importance, as the dependency can be treated perturbatively and expressed as the first-order terms of a series expansion, without the necessity of an exact physical description of the process being available. We thus have:

$$\delta t_i = -\tau E_i^\alpha \tag{5.31}$$

Here, α defines the dominant term on the series for the energy dependency of the time lag, usually taken to be $\alpha = 1$. The *dispersion cancellation* algorithm simply cycles through a range of possible values for τ, looking for the τ^* that extremises an appropriately chosen cost function, so as to quantify as well as possible the abscence of spectral lags.

The energy dependence of the arrival times of photons can obviously only be detected in the presence of transient features or bursts, which allow for the identification of energy-dependent structures in the light-curve. A number of different *cost functions* have been tested for this purpose. They all use some kind of measure of sharpness of the burst profile as the value to be maximised in the search for the correct cancellation parameter (see examples in [133], [42] and [312]). The principle behind the maximum sharpness choice is that an energy-dependent dispersion will always introduce additional width to the light-curve, broadening the burst profile as a result. An energy-dependent dispersion (that is, photons of different energies being systematically delayed or sped up) is always an asymmetric effect, and the maximally sharp burst configuration will be retrieved when the temporal sequence of events is again randomised in energy, corresponding to the exact cancellation of the dispersion. Observe that this approach will always give a unique so-

[8] This name was coined by Scargle et al. (1998) in the context of their particular version of the test, but I will adopt it here with greater generality.

lution for each given dispersion model, because in the case of under- or over-corrections of the dispersion (as given by the magnitude of τ), the asymmetric effect will either still be left present or be re-introduced in the opposite direction, and the burst will remain broadened in respect to its original width.

In the following section I present an alternative measure or cost function for the determination of the optimal cancellation parameter, based on the Kolmogorov metric. Unlike the *maximum sharpness* measures mentioned above, this approach concentrates on the effect that the asymmetric photon dispersion will have on the shape of profile, *viz.* it will provide a non-parametric measure for the relative skewness of the profile at different energy ranges which will scale with E^{α}.

5.2.3 The Kolmogorov distance method

Given two random variables X and Y in $\mathbb{R}$, a simple measure of the difference between their respective probability distributions is the *Kolmogorov distance* D_K, introduced by Kolmogorov as a metric for random variables in probability space [227]. For $F_X(x) = \text{prob}(\text{X} \leq \text{x})$ and $F_Y(x) = \text{prob}(\text{Y} \leq \text{x})$, the cumulative distribution functions (CDFs) of X and Y, the Kolmogorov metric is defined as the maximum vertical distance between the two distributions:

$$D_K \equiv \sup_{x \in \mathbb{R}} |F_X(x) - F_Y(x)| \tag{5.32}$$

The situation is illustrated in Figure 5.2. Since F_X and F_Y are probability distributions, D_K is bound to the interval [0,1]. It is well known from the properties of the Kolmogorov-Smirnov test that the Kolmogorov distance is insensitive to the tails of the distributions, where the CDFs converge on the values of 0 and 1, and which describe the probability of extreme events [293]. In fact, D_K will tend to fall around the central regions of the CDF, therefore near to the peaks of the profiles, where their accumulated discrepancy is maximum. This is a useful property because it means that the measure naturally attributes a greater weight to the most transient parts of the light-curve.

For a sufficiently rich event list (this concept will be properly quantified in the next section) the light-curve can be separated in low- and high-energy bands, forming two

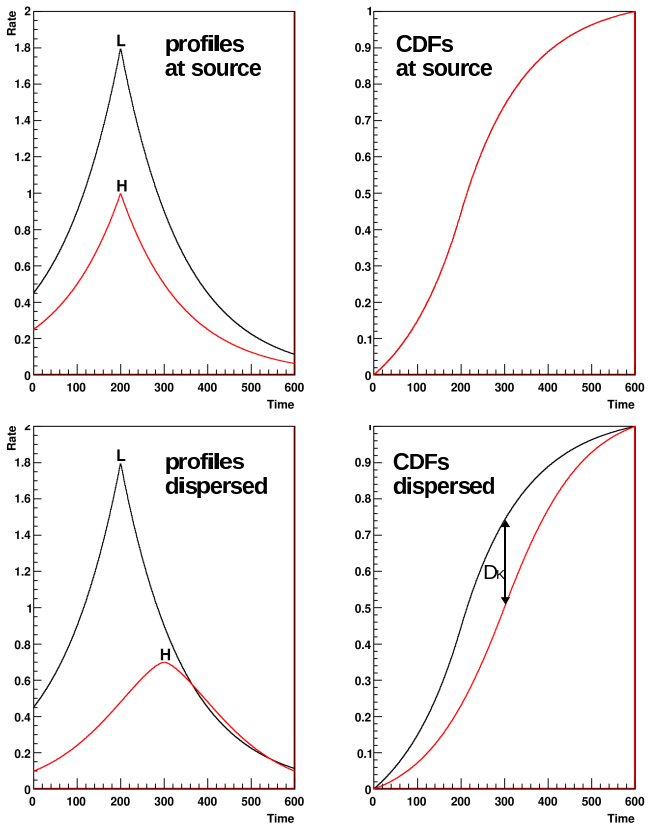

Figure 5.2: Cartoon of the effect of the energy-dependent dispersion on the shape of the low (L) and high (H) energy profiles. Observe that the systematic shift of the high-energy curve relative to the low-energy one is accompanied by a smearing out and skewing of the burst. Notice in particular the dispersion effect around the peak of the profile, suggesting the most transient part of the burst is the best region to search for dispersion. The panels to the right show the correspondent discrepancy of the CDF, after normalisation to compensate for the different intensities at both energies. The maximum vertical distance is indicated, corresponding to the Kolmogorov measure D_K.

independent datasets. In the absence of any spectral dispersion, the basic assumption that the temporal sequence of events is randomised in energy should hold and the profiles (apart from some arbitrary intensity scaling that can be eliminated by normalisation) should superpose. If, however, spectral dispersion is present, the profiles will look skewed relative to each other and their *cumulative* discrepancy can be measured by the distance between the two CDFs as defined in Equation 5.32.

In the context of the dispersion cancellation algorithm, the operation described by Equation 5.31 is applied simultaneously to all events in both profiles for a range of parameters τ. The dispersion parameter τ^*, retrieved as the one which minimises the Kol-

mogorov distance D_K between the the two CDFs, will be the measure sought for:

$$\tau^* : D_K(\tau^*) = \min_{\tau \in \mathcal{T}} \sup_{t \in \mathbb{R}} |F_L(t) - F_H(t)|, \tag{5.33}$$

where t are the event times and L and H refer to low and high-energy photons, respectively, and $\mathcal{T}$ is the set of all parameters τ tested.

The applicability of the *Kolmogorov metric* as an appropriate cost-function is based on the fact that a random distribution of events in energy – for example in a Poisson process whose rate function is independent of energy – will give rise to indistinguishable time profiles when two sub-samples in energy are considered. This is exactly equivalent to saying that a random distribution of events in energy will lead to a maximally sharp burst, and therefore the choice as to which measure is the most appropriate for a given problem should be investigated in each case, and preferably be informed by Monte Carlo studies.

Light Curve Representation

We now have to define how to construct the CDFs from the original event sequences, so that the algorithm can be applied. Given that the Kolmogorov metric is a measure for probability distributions, the event sequence must first be normalised. Since the dataset is composed of time/energy-tagged events, the cancellation will be applied to every photon individually so that none of the available information is left unused. The simplest choice for representing the data is to then construct empirical CDFs for both the low- and high-energy profiles as step functions from the original event sequence, according to the following rule:

$$CDF : \; F(t_i) = i/N, \tag{5.34}$$

where t_i is the time of the ith event in the sequence, and N is the total number of events in the sequence. In this construction, the height of each step is constant and equal to N^{-1} (the CDF is normalised to fall between 0 and 1), and the length of each step equals the waiting time between events in the sequence, and is therefore variable. All the timing information of the temporal sequence is thus explicitly preserved in this representation.

A different representation for the dataset was proposed by Scargle et al. (2008) [312],

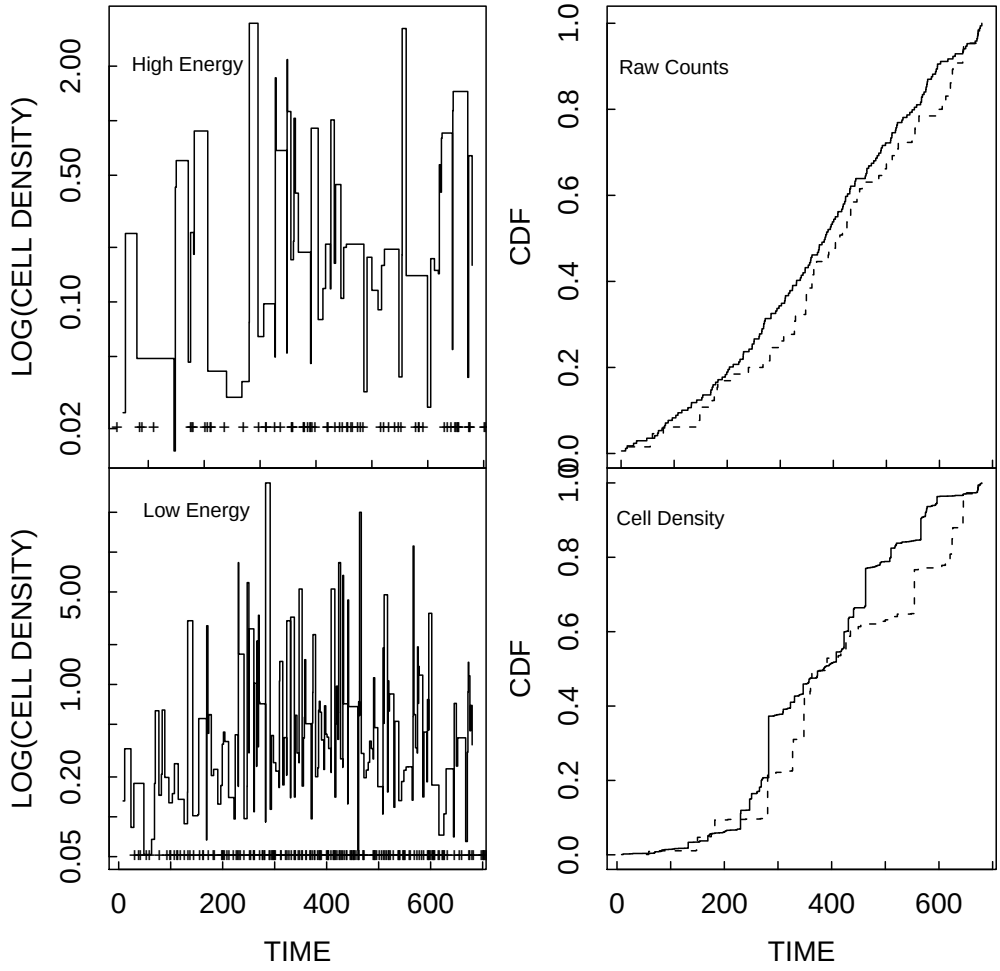

Figure 5.3: Choice of light-curve representation. The panels on the left show the cell density representation for the low- and high-energy components of flare BF1 of PKS 2155-304. The right panels show the correspondent CDFs for the two light-curve representations discussed (full line for the low-energy and dashed line for high-energy). Note that the *raw events* representation shows considerably less "ragged" CDFs that the *cell density* one, and is therefore more appropriate for using to calculate the Kolmogorov distance cost-function.

and can be used as an alternative way of constructing the CDF. In this representation, the dataset is tesselated so that the photon sequence is represented by a series of cells of width dt_i constructed around each event i. A cell density is then defined by the rule $x_i = 1/dt_i$, which can be interpreted as the instantaneous rate of the process at time t_i, and normalised into a discrete probability distribution: $p_i = x_i / \sum x_i$. The CDF in this case will be:

$$CDF : F(t_i) = \sum_{t < t_i} p_i, \tag{5.35}$$

For the application of the Kolmogorov distance metric, it is found that the first repre-

sentation in Equation 5.34 is more appropriate. This is because the magnitude of the cell density's representation can be dominated by spikes resulting from very small inter-event times in some cells, that will introduce excessive "raggedness" in the CDF representation. This can be seen in the right panel of Figure 5.3 which compares the low- and high-energy CDFs from a real burst profile, extracted from a VHE flare of PKS 2155-304 observed with H.E.S.S.. In this case, both profiles superpose, but as it can be seen the cell density representation results in additional fluctuations in the constructed CDFs. A way to circumvent this problem within the cell representation is to adopt a logarithm scale for the density – for example $x_i = \log(1/\mathrm{dt_i})$ – which recovers better the shape of the profile.

5.2.4 Monte Carlo Studies

To study the performance of the algorithm on recovering the dispersion parameter, a series of Monte Carlo simulations was performed to cover the entire parameter space likely to affect the detection of spectral lags. For each set of parameters tested – e.g. number of events, burst symmetry, width, energy resolution – 10,000 bursts were generated, each containing 500 events, to which the algorithm was applied. Probability distributions were built from the recovered dispersions, from which the mean reconstructed value and its empirical RMS were estimated. All simulations were performed with a relative step of 0.01τ, covering a range of $\Delta\tau \gg \tau$, which was usually of the order of, or larger than, the burst width itself.

Burst simulation

Individual bursts were simulated using the generalised Gaussian shape from Norris et al. [280], apropriate for describing the pulse shapes observed from AGNs [26]:

$$I(t) = I_{max} \exp\left[-\frac{|t - t_{max}|^{\kappa}}{\sigma_{r,\,d}}\right] \tag{5.36}$$

where t is the time into the flare, t_{max} is the time of maximum flux I_{max}, σ_r and σ_d are the signal rise (for $t < t_{max}$) and decay (for $t > t_{max}$) times respectively. The "peakiness" of the profile is given by the parameter $\kappa > 0$, a low value of which means we have a sharply peaked pulse, and $\kappa = 2$ corresponds to the pulse shape of a Gaussian.

The event times are generated by random draws from a distribution described by Equation 5.36. To each event time, an energy tag is then randomly attributed with $E_\gamma > 200$ GeV, this being the energy threshold of the current generation of ground-based gamma-ray telescopes. The energy tags used in this section were generated following a photon index $\Gamma = -2.5$, typical of extragalactic sources in the VHE range. Then, to simulate the energy dependent dispersion, a systematic delay τ is applied to each photon.

The dispersion algorithm is subsequently applied in order to retrieve the introduced dispersion. There is considerable uncertainty in the reconstructed energy of the gamma-ray photons as observed by the IAC telescopes. To simulate this effect, after introducing the dispersion τ to the true energies, but before applying the algorithm to retrieve it, the observed energy of each detected photon is re-drawn from a Gaussian distribution with mean equal to the true energy of the photon and σ equal to the energy resolution of the observations (in general between 10 – 20%). Another important caveat in the simulations is that if one is simulating a non-isolated burst, then it is necessary to allow for "confusion" during the cancellation process. This is done by allowing events from outside the burst being investigated to enter the window used to construct the CDFs for the Kolmogorov test, or conversely by allowing events to leave the burst window when the dispersion correction is applied.

Performance of the Method

We now test the analysis performance of the method by discussing the four main factors that are expected to affect the sensitivity for the detection of energy-dependent dispersion: burst width, energy resolution, burst intensity and asymmetry. We will consider here only the case of an isolated Gaussian burst. The superposition of multiple bursts or burst shapes different from Gaussian will be discussed when the method is applied to real data from PKS 2155-304, in the next section.

The first parameter analysed is called the "sensitivity factor" [47], and is defined as the ratio of the expected lag magnitude δt to the width of the transient feature Δt over which the search is conducted:

$$\eta = \frac{\delta t}{\Delta t} \tag{5.37}$$

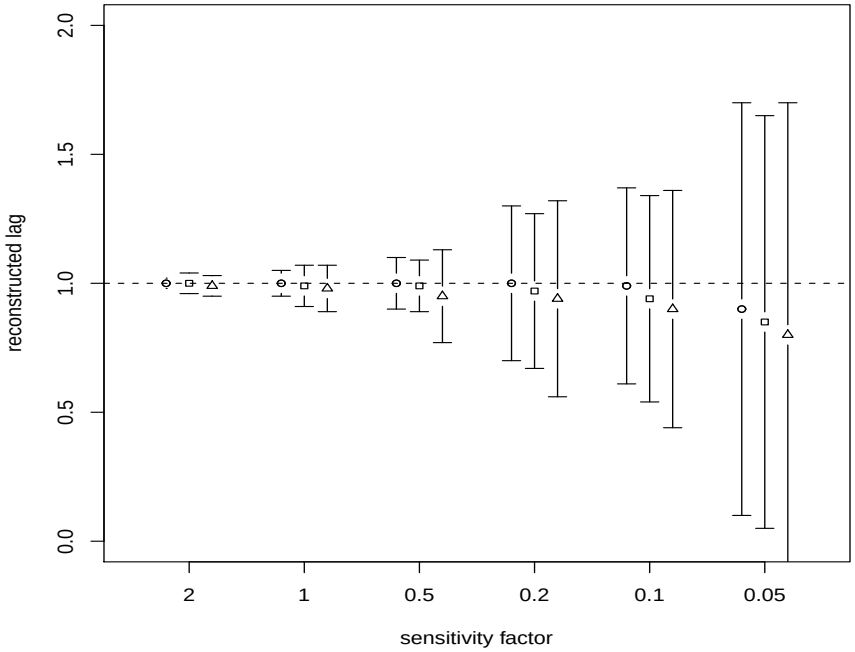

Figure 5.4: Sensitivity of the Kolmogorov distance algorithm in relation to the ratio lag/ burst width for 0% (open circle), 10% (open square), and 20% (open triangle) energy error. The results are from sets of 10,000 MC simulations of Gaussian profiles containing 500 events, for an energy threshold of 0.2 TeV and spectral index $\Gamma = -2.5$. The low and high-energy bins were defined such that the energy difference between the two is ~ 1 TeV in average.

This ratio is the main measure which quantifies the shortest lag that can be probed by the method, for a given burst width. To quantify the sensitivity of the Kolmogorov metric approach we follow the simulation procedures described in the previous section: 10,000 Gaussian burst profiles of 500 events each, with a low-energy threshold of 200 GeV and spectral index $\Gamma = -2.5$. We also included in our analysis the effect of the energy resolution, which is a great limiting factor in ground-based gamma-ray measurements. This uncertainty will directly affect the dispersion correction and will limit the sensitivity of the method (see Section 5.2.4).

The results of the Monte Carlo simulations are shown in Figure 5.4, where the error bars correspond to the RMS of the distribution of recovered parameters. One can see that the result of a lower sensitivity factor η is an increase in the uncertainty of the reconstruction of the true dispersion parameter, which grows slightly in the presence of errors on the photon energy. For the Gaussian model tested, the method can recover the dispersed lag

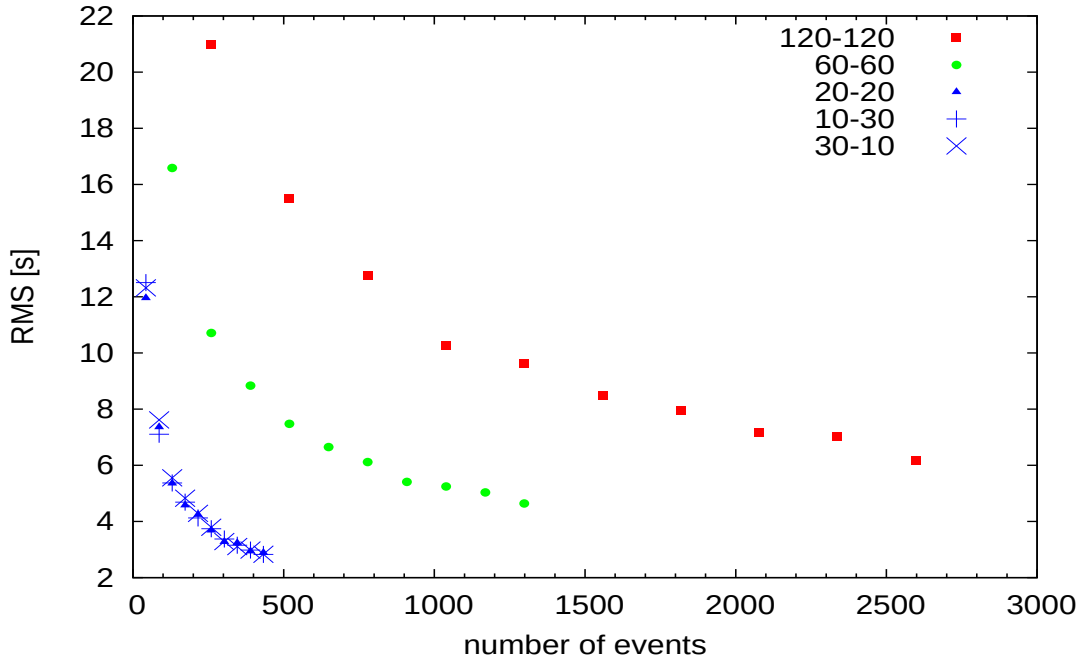

Figure 5.5: Sensitivity of the method in relation to the width of the burst and the number of events in it. The labels in the key define respectively the rise and fall times of the profile, in seconds. The results are from MC simulations of 10,000 bursts generated from a generalised Gaussian shape (see Section 5.2.4) with maximum event rate of 1-10 per second.

with significance above 3σ down to $\eta \approx 0.2$, corresponding to a lag of 25% of the burst width.

The energy resolution does not change this detection limit by much. The main effect of the energy resolution is to introduce a systematic underestimation of the value of the recovered dispersion parameter. The under-estimation happens because an uncertainty in the energy of the photon introduces additional "raggedness" to the CDF, making it difficult to distinguish one CDF from another, and a plateau in the minimum value of D_K will be achieved earlier in the cancellation process, while the two profiles are still some distance apart in the parameter space of τ. These results are likely to be dependent on the particular light-curve shape, and special simulations should be done for each particular dataset to be tested in order to estimate the RMS appropriately.

The burst intensity is another factor that will affect the sensitivity of the algorithm, since it will limit the photon statistics available to construct the CDFs. This is shown in Figure 5.5 and was tested by simulating sets of 10,000 Gaussian profiles with different number of events, between 50-3000, for 3 different burst widths with rise/decay times

between 10-120 s, corresponding to η in the range $1 - 10$. For a given burst width, the effect of increasing the number of events in the light curve is to reduce the RMS of the recovered dispersion parameter; from a certain number of events onwards, and depending on the width of the burst, the distribution tends towards a plateau and little inprovement in the RMS is obtained by further increasing the event number. As noticed before, the sharper the burst, the earlier this plateau is reached. Finally, we have also tested for effects of profile asymmetry by maintaining the total burst width and varying the ratio of rise/decay time of the flare. The results plotted in Figure 5.5 shows that the method is not affeted by burst asymmetry, but only to those parameters that determine its overall width (or sharpness).

When analysing transient events within a real light-curve it is important to consider the effects of under-sampling the burst. Until now we have treated isolated, simulated bursts, for which we were confident that all events were included in the analysis. However, if the burst is not isolated but is adjacent to a lightcurve with some structure it might be difficult to define with precision its start and end times. This becomes important in the present analysis because the existence of energy-dependent lags will imply that the most-lagged events might fall outside the analysis window, affecting the reconstruction. Also, if the burst is on the edge of an observation run, and thus data are missing for part of the flare, this loss of information is also likely to affect the performance of the reconstruction.

To test for these effects and assess if a proper reconstruction of the lagged light-curves is still possible in these circumstances, we performed two sets of simulations, using as before a Gaussian burst with 500 events and spectral index $\Gamma = -2.5$ above 200 GeV; an energy resolution of 20% was applied to mimic the real observational situation. For the first set, represented in Figure 5.6, the analysis considered a series of windows around the peak position of the burst of widths equal to 1, 2, 3 and 5 σ, to simulate different degrees of under-sampling. In this case a "transparent window" has been applied, meaning that though the CDFs are built only with the events that at each given time fall within its boundaries, for each different value of τ applied in the cancellation process events are allowed to pass thourgh the window's boundary.

The result is that a strong under-sampling of the burst affects the accuracy of the reconstruction, increasing the RMS by up to 20%, when only the central 1 σ around the

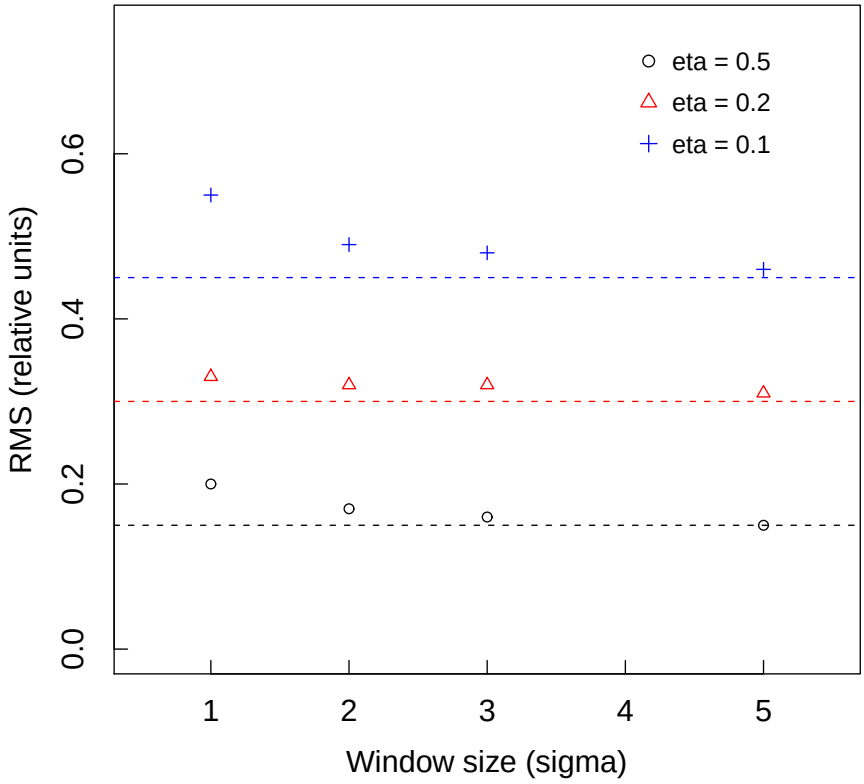

Figure 5.6: Sensitivity of the Kolmogorov distance method in relation to the size of the "transparent" window used to construct the CDFs from the burst profile. The labels in the key define different data sets with different sensitivity factors $\eta = 0.5,\ 0.2,\ 0.1$. Notice that too narrow a window (1-2σ) around the peak of the flare has the effect of degrading the RMS of the reconstructed lag even further. For windows as wide as $\sim 3\sigma$ around the flare peak, little effect is noticed in the worsening of the reconstructed RMS. The results are from MC simulations of 10,000 bursts generated from a generalised Gaussian shape (see Section 5.2.4), and an associated energy error for each event of $\sim 20\%$.

burst peak is used to build the CDF. This degrading effect can be understood by observing that a very narrow window will mean a strong undersampling of the high energy profile and a consequently ill-defined shape for the CDF. The effect is present for all the range of sensitivity factors tested, being more pronounced for smaller η. The results suggest therefore that one should attempt to include as much of the burst as possible into the analysis, i.e. an arbitrary choice of a narrower subsection of the burst to artificially reduce η does not improve the results due to a corresponding loss of information about the shape. CDFs.

Similar results are obtained when, as shown in Figure 5.7, we include an "opaque win-

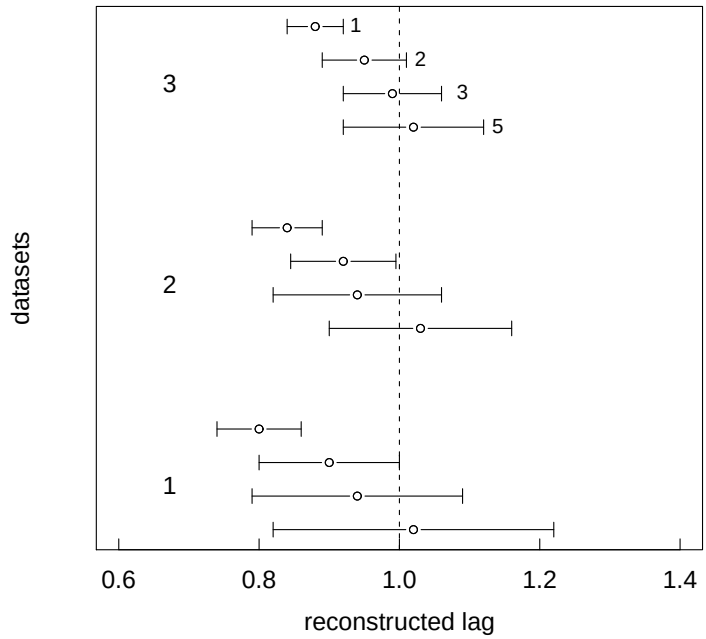

Figure 5.7: Sensitivity of the Kolmogorov distance method in relation to the size of the "opaque" window used to construct the CDFs from the burst profile. The different datasets 1, 2 and 3 correspond to η = 0.1, 0.2, 0.5 respectively, and it is apparent from the plot that the lag reconstruction is most affected by the presence of a "hard" window in the case when the sensitivity factor is small, because in this case more information is lost in the higher number of high energy events that fall outside the window. The numbers 1-5 within each dataset are for windows of 1-5 σ, respectively. Apart form the degradation ot the RMS, the presence of an "opaque" window also affects the absolute value of the reconstructed lag, which didn't happen with the transparent window. This is because the photons which fell outside the window after dispersion are not recovered during the cancellation process. Notice that too narrow a window (1-2σ) around the peak of the flare has the effect of degrading the RMS of the reconstructed lag even further. Again, for windows as wide as $\sim 3\sigma$ around the flare peak, little effect is noticed in the RMS or the value of the reconstructed dispersion parameter. The results are from MC simulations of 10,000 bursts generated from a generalised Gaussian shape (see Section 5.2.4), and an associated energy error to each event of $\sim$ 20%.

dow" instead. By this we intend to simulate a burst that is under-sampled at the detection level, rather than in the analysis procedure, for example when observation is interrupted before the full event is registered. In this case, the fact that we lose more high energy events means that not only will the RMS be worsened, but the lag will be reconstructed wrongly. The three different datasets represented in Figure 5.7 are for sensitivity factors η equal to 0.5 (1), 0.2 (2) and 0.1 (3), so notice that the case of smaller η is the most affected, simply because in this case most high-energy events are permanently lost from the burst window. Within each dataset, points 1-5 indicate the size of the window in units of σ.

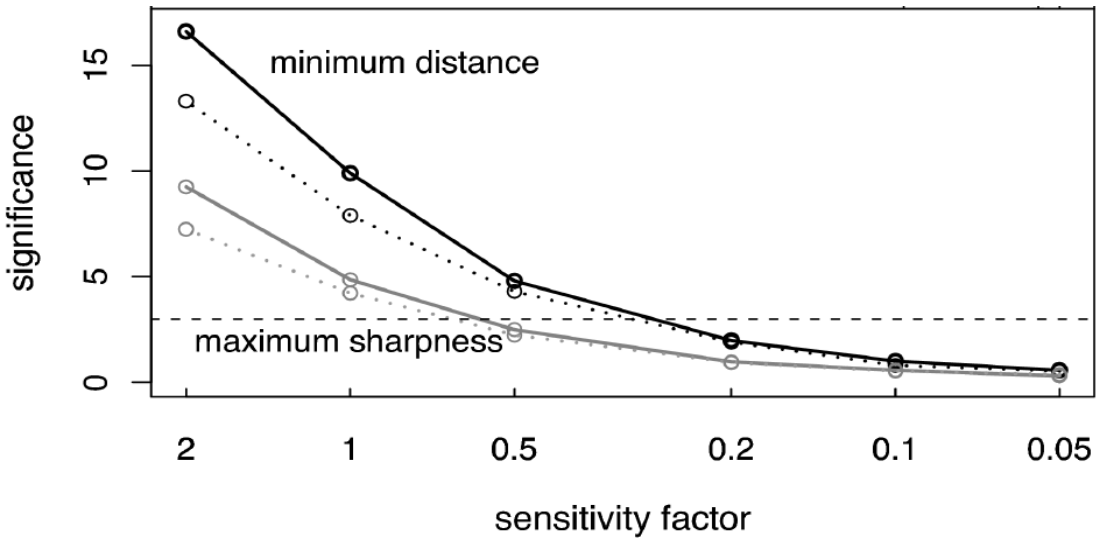

Figure 5.8: Comparison of the sensitivity for detecting a lag between the minimum distance Kolmogorov method [63] and the maximum sharpness methods of [133], [42] and [312], for a range of sensitivity factors η. The solid lines are for the case of no energy reconstruction error and the dotted lines correspond to energy uncertainties of 20%.

In the same way that events pertaining to the burst can be selected out of the analysis window, events not pertaining to the burst can also contaminate the analysis during the cancellation procedure. This is expected to produce the same kinds of effects as the case treated in Figure 5.6 and has to be taken into consideration. To conclude, a last plot (Figure 5.8) compares the performance of the Kolmogorov distance method to the maximum sharpness approaches discussed in previous sections, and shows the excellent performance of this new approach, which justifies its choice from now on.

In the next section we will apply the method to a large flare of the TeV blazar PKS 2155-304. Given the many factors presented in this section and shown to influence the reconstructed RMS, a Monte Carlo study of the particular dataset to be studied is necessary.

5.3 Application to PKS 2155-304

The dispersion algorithm was applied to each of the major burst features in the dataset, BF 1-5, generating five sets of independent measurements. Figure 5.9 shows the complete flare light curve, with the time windows as derived from the Bayesian block analysis of Section 5.1.4 indicated by the grey shades. The widths of the search windows were

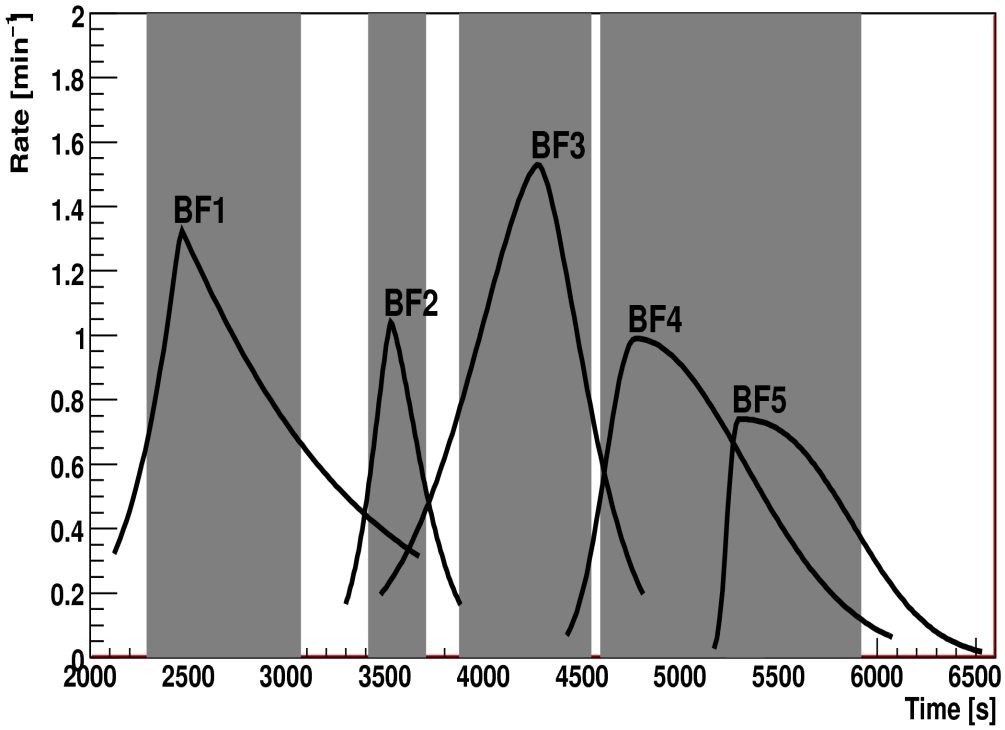

Figure 5.9: Modeled light curve of the PKS 2155-304 big flare event of MJD 53944, for photons above 170 GeV. The grey shades mark the location and extent of the five major bursts (BF 1-5) on which we conducted the dispersion analysis. These were selected following the Bayesian blocks light-curve analysis presented in Section 5.1.4 advanced by the H.E.S.S. collaboration. The black curves show the model fits for BF 1-5 using a generalised Gaussian profile with the parameters presented on Table 1 of [26], which were used in the Monte Carlo simulations to derive the confidence intervals for our dispersion analysis.

derived from the rise and decay times of each event according to the generalised Gaussian fit function 5.36, following the parameterisation in [26]. The profiles of the curves fitted to each burst are represented by the dark lines superimposed to the data and they were used to generate sets of simulated flares from which to derive confidence intervals for the dispersion parameter via Monte Carlo simulations, exactly as decribed in Section 5.2.4.

Before proceeding with the generation of the profile's CDFs to the application of the method, a few things need to be decided upon. The first is the choice of the window that will define the temporal boundaries of the burst. From the studies of the dependence on the sensitivity factor η, which is the most important parameter in determining the magnitude of the RMS and therefore the sensitivity of the method, we have seen that the smaller the ratio of lag to burst width, the better the reconstruction of the dispersion parameter. This

Flare	t_{max} [s]	Max. Rate [Hz]	σ_r [s]	σ_d [s]	κ
BF1	2460	1.33	173	610	1.07
BF2	3528	1.04	116	178	1.43
BF3	4278	1.53	404	269	1.59
BF4	4770	0.99	178	657	2.01
BF5	5298	0.74	67	620	2.44

Table 5.1: Parameters used for the generalised Gaussian fit to the PKS 2155 flare simulations. The third column (Max Rate) refers to the maximum count rate of each burst, corresponding to its peak flux at time $t_{\max}$. The parameters σ_r and σ_s are the rise and decay times of each burst and κ a measure of its "peakiness" (see text).

readily excludes the use of the entire light curve (as done for example in [28]) on the basis that this would be equivalent to perfoming the analysis in a burst of equivalent width equal to the total duration of the time series [63]. The separate analysis of the three individual runs that compose that night's observation is also discouraged for the same reason – we would again be (somewhat arbitrarily) increasing the width of the features to be studied. On this point it is important to remark that the fact that there are gaps in the data between the runs is not a problem in itself, because the effect of the interruption of data taking in the middle of a given burst[9] can be taken into consideration for the estimation of the RMS by using a "hard window", which mimics the permanent loss of information due to loss of photons.

Also, the sensitivity curves in Figures 5.6 and 5.7 show that a window as short as 3σ around the peak of the flare gives an RMS close to the optimum value, while concentrating the most around the peak of the burst, which is desirable if we want to minise any contaminations due to overlapping flares. We therefore decided to place the limits around each burst (whose parameters are given in Table 5.1) at 3σ. All windows used for the analysis were "transparent windows", except for those marking the end of run 1 (the right window of BF-2) and run 2 (the right window of BF-5). This same set up was used not only for the data analysis, but also in the Monte Carlo simulations, so that the estimated RMSs are all consistent.

[9] Such as BF-2 and BF-5, which extend beyond their respective run times, as can be seen for example in Figure 5.9, where at the end of BF-2 there follows a bin with zero counts near he mark of 2000s and at the end of BF-5 there follows one bin with near-zero counts at $\sim$ 3500 s.

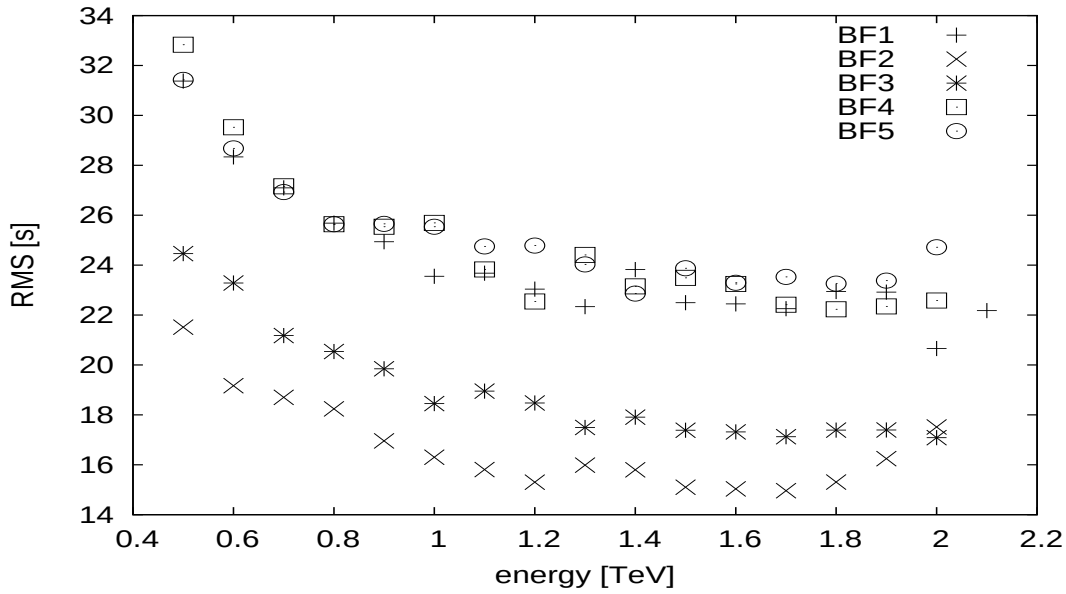

Figure 5.10: Effect of the choice of the energy cut for the high energy band on the accuracy of the determined dispersion measure based on Monte Carlo simulations of the burst profiles BF1-5.

The second point to consider is regarding the choice of where to place the low- and high-energy boundaries that will define the two CDFs to be compared during the cancellation process. This choice is made so that the difference in the mean energy between them is maximised (this will increase the average lag we will be testing and will thus improve η), while keeping good photon statistics in both bins for the analysis. We have verified that due to the steeply-falling spectral index of the photon distribution, the analysis is less sensitive to the choice of the low-energy boundary, provided that this is set comfortably above the threshold energy of the observations. Again, confidence intervals should always be derived for the specific dataset with which one is working, either from Monte Carlo simulations or bootstrapping. We thus searched for an optimal high-energy cut. For this Monte Carlo events were generated from the distributions BF 1-5 (Table 5.1).

Figure 5.10 shows the results of our analysis on the effect of the choice of the high-energy cut on the RMS of the re-constructed dispersion parameter. The curves show the presence of an optimal plateau around and above 1 TeV. At the low-energy end, the RMS shows a steep rise because the average energy of the photons in the high-energy bins differs little from those of the low-energy one and it becomes difficult to distinguish between the two CDFs. For flares BF-2 and 5 (where the hard window is present) we also

see an increase of the RMS for cuts above 2 TeV, and this is simply caused by lack of statistics due to information loss from the highest energy photons.

Analysis Results

The search for spectral lags was performed for each of the five bursts with energy cuts $E_1 < 500$ GeV and $E_2 > 1$ TeV. A linear relation between the lag and energy of the photon ($\alpha = 1$ in Equation 5.31) was adopted, which took into account both physical models discussed below. The time windows used for the inspection were determined from the rise and decay times of each burst, from half to maximum amplitude, as derived by [26] using $t_{r,d} = (ln2)^{1/\kappa}\sigma_{r,d}$. The corresponding number of events within each energy band, and the mean energy difference $< \Delta E >$ between the low- and high-energy profiles, are also presented in Table 5.2.

Flare	Window [s]	events < 0.5 TeV	events $> E_{cut}$	$< \Delta E >$ [TeV]	lag [s/TeV]
BF1	556	376	43	1.48	-3 ± 5
BF2	228	211	29	1.35	3 ± 7
BF3	534	372	59	1.48	-4 ± 6
BF4	695	344	62	1.34	10 ± 8
BF5	591	217	48	1.34	8 ± 5

Table 5.2: Temporal window and low- and high-energy boundaries used for the construction of the CDFs for each burst from PKS 2155-304. $< \Delta E >$ is the mean energy difference between the low-and high-energy CDF. The last column lists the optimal cancellation parameter τ^* retrieved from the analysis. The errors are the 66% confidence interval around the mean value, determined from MC simulations.

The errors in the reconstructed lags (in s/TeV) were determined from Monte Carlo simulations performed for each individual burst. Figure 5.11 shows an example of the MC analysis for the flare BF2, here simulated in the absence of spectral lags. The upper panel shows the distribution of the recovered dipersion parameters for the 10,000 simulated bursts, from which confidence intervals were derived. The lower panel shows the histogrammed values of the Kolmogorov distance D_K for each different dispersion parameter τ tested. The presence of a minimum near the true value of $\tau = 0$ is clearly visible. Here we have used a value of $\tau = 0$ to exemplify the derivation of our confidence intervals, but Figure 5.12 shows that the algorithm has a linear response on the accuracy of the

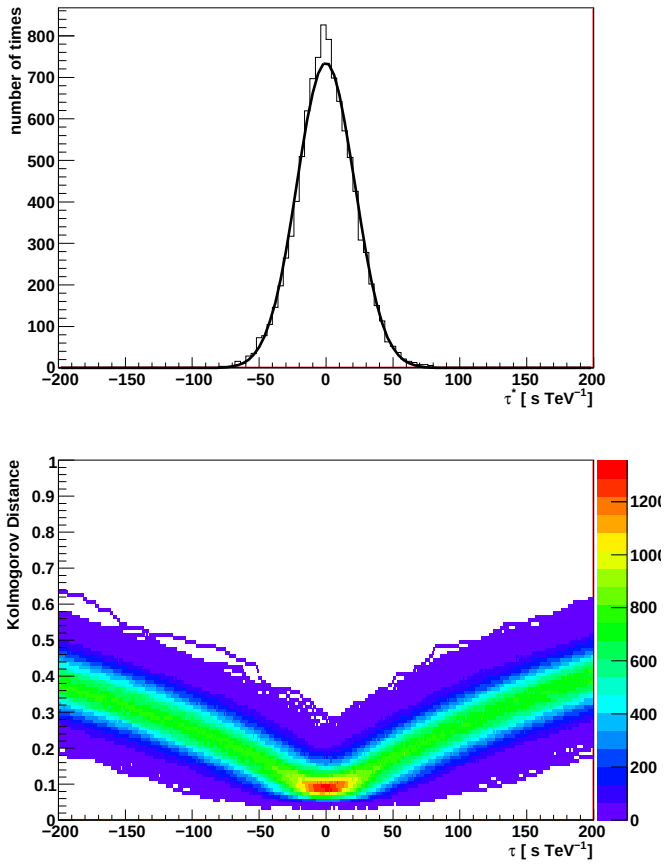

Figure 5.11: Simulation of 10,000 events for the profile of BF2, with no dispersion introduced. The top panel shows the distribution of the best fit τ^*, whereas the bottom panel shows the histogrammed Kolmogorov distance calculated for each value of the dispersion tested.

recovered dispersion parameter over a large range in parameter space. For energy differences $\gtrsim$ 1 TeV between the profiles, the method is sensitive (above the 2σ-level) to lags as short as $\sim 30-75$ s/TeV, depending on the particular feature considered, corresponding to average dispersions of $\lesssim$ 10% of the width of the burst. The curves representing the results of the searches for energy-dependent dispersions for each burst are presented in Figure 5.13.

In none of the flares was a significant spectral dispersion found within the probed time-windows. In the next two sections we derive 2-σ limits for the quantum gravity energy scale and the acceleration timescales t_{acc} for particles in the jet of PKS 2155-304, discussing the implications of these results.

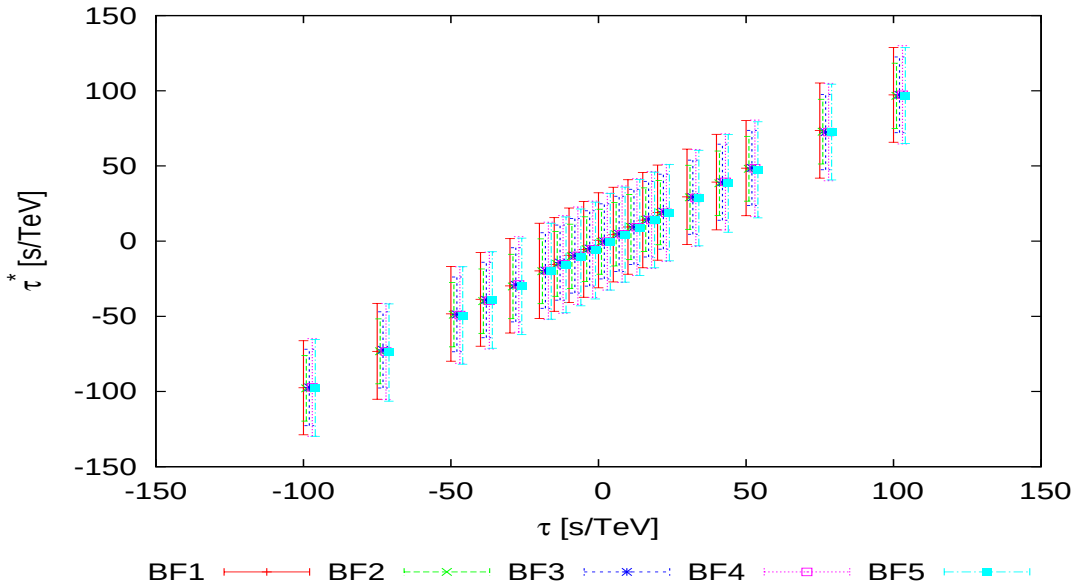

Figure 5.12: The accuracy to which the method can recover a fixed dispersion parameter introduced into the light-curves representing the PKS 2155-304 flares. Each point is the average dispersion estimated from 10000 simulated lightcurves and the errors represent the RMS of the recovered dispersion measure. Values corresponding to different flares are offset slightly on the x-axis for visual clarity. The 1-σ width of the simulated burst was of 100s.

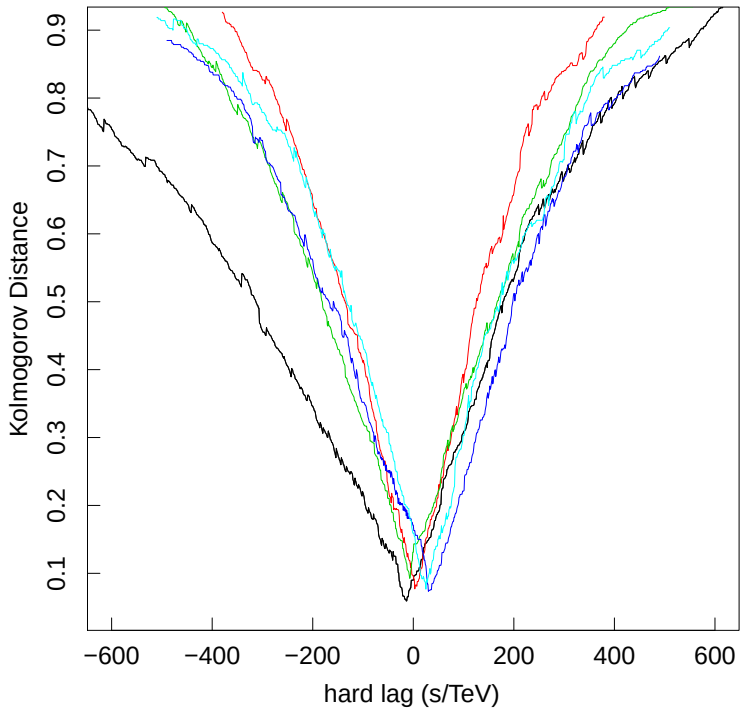

Figure 5.13: Kolmogorov distance profiles for the search of energy-dependent dispersion in the bursts BF1-5 of PKS 2155-304. The analyses were performed in steps of 1 s/TeV.

5.4 Application I: Quantum Gravity

Lorentz invariance is one of the principles behind relativistic field theories such as electromagnetism and general relativity [236]. Historically formulated as the transformation that maintained the invariance of Maxwell's equations, with the development of special relativity, it came to be understood as a fundamental symmetry of nature, on which depends the validity of the postulates of relativity [128]. It is a property also known to be maintained in quantum field theory (QFT) once it was shown by Jordan and Pauli in 1928 [219] that commutators in quantum mechanics conform with the Lorentz group. Attempts to a quantisation of gravity have nevertheless been faced with fundamental theoretical difficulties due to the way in which the gravitational field description in general relativity radically differs from that of QFT and many approaches to quantum gravity (QG) do not maintain Lorentz covariance as a fundamental symmetry [258]. Before discussing something about searches for QG signatures in Lorentz invariance volation (LIV), I will briefly present two "classical" results that give some "intuition" to the rather complex and abstract issue of LIV.

Gravity and the uncertainty principle

The first example is derived from Adler & Santiago 1999 [7], and proposes to give an intuitive understanding regarding the nature of space-time at very small scales from heuristic arguments. Let us first observe that the fundamental constants of nature c, $\hbar$ and G, define, among themselves, a natural scale (called the Planck scale [292]), defined by dimensional analysis in the following manner:

$$L_P \equiv \sqrt{\frac{G\hbar}{c^3}} \simeq 1.6 \times 10^{-35} \text{ m} \tag{5.38}$$

$$E_P \equiv \sqrt{\frac{\hbar c}{G}} \simeq 1.2 \times 10^{19} \text{ GeV} \tag{5.39}$$

$$T_P \equiv \frac{L_P}{c} = \sqrt{\frac{G\hbar}{c^5}} \simeq 0.5 \times 10^{-43} s \tag{5.40}$$

called the Planck length, energy and time, respectively.

From its construction, the Planck scale is suggestive of an *extreme* physical scale at

which quantum, relativistic and gravitational effects are all relevant to the description of the system: therefore we are in the domain where general relativistic and quantum mechanical effects are "unified", i.e. a theory of quantum gravity is necessary. Observe that this scale involves extremely high energies, and as such should apply to the very early universe or in collisions of highly energetic elementary particles. This is also the domain of very small scales, and is relevant for example for the description of the cloud of virtual particles that surround any real particle and can have arbitrary energy, due the Heisenberg uncertainty principle.

In fact, if we consider the effects of the gravitational field at the quantum scale, it is possible to derive a modified uncertainty principle from which a minimum, absolute, position uncertainty arises in the measurement process and which is of the order of the Planck length. Originally, Heisenberg's uncertainty principle results from considering the process of measurement of the position of an electron, which is done by scattering an electromagnetic wave of wavelength λ off the particle. The precision of the position measurement is thus $\Delta x \approx \lambda$. In addition, the photon momentum will impart an uncertainty in the electron's momentum during the scattering of the order of the photon's own momentum $\Delta p \approx p = h/\lambda$. The position-momentum uncertainty relation is thus obtained:

$$\Delta x \, \Delta p \approx \lambda \left(\frac{h}{\lambda} \right) \approx \hbar \tag{5.41}$$

Let us now consider the effect of the gravitational field. The field equations of general relativity are given by Einstein's equations [129]:

$$G_{\mu\nu} = -\left(\frac{8\pi G}{c^4} \right) T_{\mu\nu} \tag{5.42}$$

Following the proposal of [7], we can write the metric tensor $G_{\mu\nu} \approx \delta g_{\mu\nu}/L^2$, where $\delta g_{\mu\nu}$ represents the deviation of the metric from flatness due to the gravitational field and L^2 is a factor for correct the dimensionality of the expression, and represents the characteristic size of the interaction region of the photon-electron scattering (equivalent to λ in Heisenberg's original derivation). Similarly, from dimensional considerations, the field tensor $T_{\mu\nu}$ can be written as:

$$\left(\frac{8\pi G}{c^4}\right) T_{\mu\nu} = \left(\frac{8\pi G}{c^4}\right) \frac{E}{L^3} \approx \frac{Gp}{c^3 L^3}, \tag{5.43}$$

recalling that the energy is $E = pc$, the estimate for the metric deviation is:

$$\delta g_{\mu\nu} \approx \frac{Gp}{c^3 L}. \tag{5.44}$$

Adler & Santiago observe that since this is a deviation of the metric, it corresponds to a fractional uncertainty in all position measurements within L, which can be identified with a position uncertainty:

$$\frac{\Delta x}{L} \approx \delta g_{\mu\nu} \approx \frac{Gp}{c^3}. \tag{5.45}$$

Now, for, $\Delta p \approx p$, we can write $\Delta p \approx E_P/c = \sqrt{\hbar c^3/G}$, and so, using 5.45, we arrive at $\Delta x \approx L_P$, from which we conclude that the minimum absolute uncertainty to which a particle can be located in space is the Planck scale.

This observation is a heuristic way of realising Wheeler's concept of quantum foam [354], according to which at very small scales the metrics of space-time are expected to be affected by the variable energy content within a small region of space that arises as a result of the quantum fluctuations of the vacuum. Particles (e.g. photons) propagating through this "foamy spacetime" will notice these effects, which will in turn affect their path and propagation through space. In the next example we will see that this deviation of the metric can be understood by another classical analogy as being equivalent to the arising of a non-trivial spectral index for the vacuum. Since the deformation of the metric will depend on the energy content of the space at each point, this "vacuum spectral index" will be energy-dependent, and therefore one would in this case expect the photon propagation to be energy-dependent as well.

Equations of electrodynamics in the presence of a gravitational field

To see how the aforementioned non-trivial spectral index comes about, let us consider an example from Landau & Lifshitz's *Classical Theory of Fields* [236], which was later re-interpreted by Ellis et al. 2000 [130]. For this consider the perturbed metric of the last section:

$$G_{\mu\nu} = \begin{pmatrix} -\delta g_{oo} & \delta g_{01} & \delta g_{02} & \delta g_{03} \\ 0 & 1 & 0 & 0 \\ 0 & 0 & 1 & 0 \\ 0 & 0 & 0 & 1 \end{pmatrix} \tag{5.46}$$

which represents a deviation from the flat spacetime diag$\{-1, \delta_{\mathrm{i,j}}\}$. The perturbation is of the form $G_{0i} = \delta g_{0i}$ and is proportional to the momentum recoil due to gravity and therefore a function of the photon's energy, by Equation 5.44. Landau's exercise is to look at the effect of this non-diagonal metric for the solution of Maxwell's equations. The electromagnetic field tensor in special relativity is written as:

$$F_{ik} = \frac{\partial A_K}{\partial x^i} - \frac{\partial A_k}{\partial x^k}, \tag{5.47}$$

where A is the electromagnetic potential. The covariant form of Maxwell's equations then follows [236]:

$$\frac{\partial F_{ik}}{\partial x^l} + \frac{\partial F_{li}}{\partial x^k} + \frac{\partial F_{kl}}{\partial x^i} \tag{5.48}$$

$$F^{ik}_{;k} = \frac{1}{\sqrt{-\gamma g_{00}}} \frac{\partial}{\partial x^k} \left(\sqrt{-\gamma g_{00}} F^{ik} \right) = -\frac{4\pi}{c} j^l \tag{5.49}$$

From the fact that the above pair of equations for the sources j^l contains the term $\sqrt{-\gamma g_{00}} \sim \sqrt{-\gamma \delta g_{00}} \neq 1$, Landau observes that there exists a formal analogy between the form of these equations with those describing the electromagnetic fields in a material medium. Now, the solutions for the fields also follow an analogy with the fields in a medium with non-trivial magnetic and electric permeability (see Feynman 1963 [153] and Ellis et al. 2008 [134]):

$$\nabla \times E = -\frac{1}{c\sqrt{\gamma}} \frac{\partial}{\partial t} (\sqrt{\gamma} \mathbf{B}) \tag{5.50}$$

$$\nabla \times B = \frac{\sqrt{h}}{c\sqrt{\gamma}} \frac{\partial}{\partial t} \left(\sqrt{\gamma} \frac{\mathbf{E}}{\sqrt{h}} \right) + \frac{4\pi}{c} \mathbf{s} \tag{5.51}$$

where $\mathbf{s} = Qdx^{\alpha}/dt$ and $\delta g_{00} = h$, to unify notations with [236].

The modified dispersion relation that results from these is given by [130] to be:

$$k^2 - \omega^2 - 2h(E)k\omega = 0, \tag{5.52}$$

from which the energy-dependent speed of light results:

$$c(E) = c(1 - h(E)) + O(h^2), \tag{5.53}$$

and $h(E) = O(E/E_P)$, from 5.44. One can therefore write the spectral index for the vacuum as $n_\circ - 1 \sim E/E_P$, where E is the photon's energy.

The importance of searching for LIV signatures for testing quantum gravity models is that this seems to be a fundamental phenomenological effect of the theory, the basis of which is rooted in the fundamental principles of a quantum theory of gravity. From the experimentalist's point of view, this result is very appealing, because the energy-dependent propagation of photons provides with one of the very few instances in which QG theories could be directly tested.

5.4.1 Energy-dependent propagation: time-of-flight experiments

Even if breaking of Lorentz symmetry in QG happens only at extreme energies, and therefore deviations from a constant speed of light $\delta c \propto E/E_P$ are expected to be very small (of the order of $10^{-15}c$ for a photon of 1 TeV), astrophysical observations of high-energy gamma-ray photons propagating over cosmological distances (from sources such as AGNs or GRBs) can prove adequate to probe these effects, because the accumulated delay in the propagation can become noticeable [47]. Although the calculations of the preceeding section give a justification to the expected dependency of the speed of light on the energy of the photon, they do not provide an exact expression for the dispersion relation, and different approaches to quantum gravity can actually predict different analytical forms for this dependency [258].

This deficiency of the theory does not represent a problem for the performance of our tests. Since we are working with photons of energy $E << E_P$, the exact form of the dispersion relation is not important, but only its dominant terms, which can be obtained

from the first order factors in a series expansion about E [47]:

$$E^2 - c^2\mathbf{p}^2 \simeq -p^2c^2\left[\frac{E}{\xi E_P}\right]^n. \tag{5.54}$$

This corresponds to energy-dependent velocities $c' \approx c(1 - \xi(E/E_P))$. Here, $\xi \sim 1$ is the dimensionless parameter to be probed by the experiments, which sets the QG energy scale in relation to E_P. As already mentioned, and pointed out by Amelino-Camelia, the propagation of signals of different energies over large distances L will introduce a measurable relative lag δt in the arrival time of the photons:

$$\delta t \approx \xi\frac{\Delta E}{E_P}\frac{L}{c}. \tag{5.55}$$

In the absence of other sources of dispersion, the measurement of a non-zero spectral lag would therefore be a direct signature of vacuum dispersion. Observe that the magnitude of the lag is directly proportional to the size of the energy difference ΔE and the source's distance L. The expression above is only valid for nearby sources. For cosmological sources the expansion of the universe must be taken into account and so the delayed paths must be calculated with reference to the particle's comoving trajectory. The photon's path in the comoving trajectory can be calculated by writing the Hamiltonian for the comoving momentum [208]:

$$c' = \frac{d\mathcal{H}}{dp} = \frac{d}{dp}\left(E(1+z)\sqrt{1-(1+z)^n\left(\frac{E}{\xi E_P}\right)^n}\right). \tag{5.56}$$

The comoving path for the photon is given by $x(t,p) = \int_0^t v(E)dt'$, so that in terms of the redshift we can write [208]:

$$x(z,E_0) = \frac{c}{H_0}\int_0^z \left(1 - \frac{1+n}{2}\left(\frac{E_0}{\xi E_P}\right)^n (1+z')^n\right)\frac{dz'}{\sqrt{\Omega_m(1+z')^3+\Omega_\Lambda}}, \tag{5.57}$$

where E_0 is the redshifted particle energy measured at present, and Ω_m, $\Omega_\Lambda$and H_0 are the cosmological parameters measured today.

The comoving distances for the two photons of different energies are equal, but observe that the proper distances differ, because during the delay of the most energetic pho-

tons, the expansion of the universe will progress and this will affect the proper distance. Jacob & Piran 2008 [208] estimate that this effect is of the same order of magnitude of the delay due to the energy difference and so it is very relevant. The time delay consistent with cosmological propagation is therefore:

$$\Delta t = \frac{\Delta z}{H_0} = \frac{1+n}{2H_0}\left(\frac{E_0}{\xi E_P}\right)^n \int_0^z \frac{(1+z')^n dz'}{\sqrt{\Omega_m(1+z')^3+\Omega_\Lambda}}. \tag{5.58}$$

The magnitude of this delay is of the order of 10 s/TeV.Gpc, or about 4s in the case of PKS 2155-304, for $\xi \sim 1$ and $n \sim 1$, corresponding to first order effects.

Searches for LIV with gamma-ray observations

Despite no positive identification of QG-related dispersion effects exist to date, the sensitivity of time-of-flight measurements has increased considerably due to the improvements in both satellite and ground-based gamma-ray detection sensitivities, and the constraints and limits on LIV have become increasingly stringent. In fact, experiments are now approaching the critical energy range of the Planck scale [48] and recent *Fermi* measurements of two distant gamma-ray bursts (GRB 080916C [141] and GRB 090510 [142]) were the first to have tested LIV to this scale.

Before discussing our results, let us take a brief look at the history of the search for LIV signatures with gamma-ray observations. Schaefer, in 1999 [314], was the first to apply the idea put forth by Amelino-Camelia et al. [47] to gamma-ray observations, and using an extremely short (200 ms) flare of GRB 930131 observed by *BATSE* and *EGRET* (20 keV - 200 MeV), derived a limit of 8.3×10^{16} GeV on the energy scale for a frequency-dependent speed of light, a value which was nevertheless subject to considerable uncertainty given the lack of a redshift measurement for the GRB. From the very beginning, it was understood that, despite providing constraints, studies based on individual objects could not provide a definitive evidence for QG effects because it would not be possible to disentangle the propagation delays from possible intrinsic lags with origin at the source's emission mechanism or geometry (see [338] for a discussion of intrinsic spectral lags in GRBs).

Posterior searches have therefore concentrated mostly in observing populations of

GRBs at different distances, looking for an evolution of the delays with redshift that would be compatible with the propagation effect described by Equation 5.58. The success of this type of study has been directly linked to the energy scale of the observations. Studies using wavelets to select transient peaks by Bolmont et al. 2006 [89] using 0.5-400 keV data from HETE-2, excluded energies below 2×10^{15} GeV from the possible range of E_{QG}. Two studies by Ellis et al. (see [130] and [131]), used keV to MeV *BATSE* and *OSSE* observations of a sample of GRBs with known redshifts to look for z-correlated delays, and derive more rigorous limits for $E_{QG} \geq 6.9 \times 10^{15}$ GeV from a regression analysis. Later on, similar analysis by the same group in 2006 [132], including a larger sample from *Swift* observations, obtained a statistically robust limit of 0.9×10^{16} GeV to the scale of validity of Lorentz invariance. The most constraining limits until the launch of *Fermi* in June 2008 came from observations of a bright and very short 15 ms feature from GRB 021206 ($z \sim 0.3$), observed by *RHESSI* in 2004 [88], where the abscence of a dispersion in the peak position of the flare between 1-17 MeV led to a lower bound of 1.8×10^{17} GeV for the QG energy scale.

The most stringent limits on E_{QG} to date come from *Fermi* observations of single gamma-ray burst events, whereby evaluating the time difference between the arrival of the most energetic photon in the dataset ($13.22^{+0.70}_{-1.54}$ GeV for GRB 080916C [141] and 31 GeV for GRB 090510 [142]) and the start time of the burst, limits of $E_{QG} > 1.3 \times 10^{18}$ GeV/c^2 (for GRB 080916C) and $E_{QG} > 1.45 \times 10^{19}$ GeV (for GRB 090510) were derived. The first of these limits is within 10% of the Planck scale, and was obtained by assuming the maximum possible delay for the arrival of the 13.2 GeV photon ($\Delta t = 16.54$ s) was due to QG dispersion, which is a very conservative approach. In fact, it seems to be the case that the high-energy emission from GRBs with a LAT detection (e.g., 080825C, 081024B [48]) all have a delayed onset to the start of the VHE emission, the origin of which is still unclear [188]. In the case of GRB 080916C, the delay in the onset of the LAT emission could be as large as ~ 4.5 s, which would imply a significant revision of the limits on E_{QG}.

More important was the result of May 2009 on GRB 090510 [142], for which, under similar premises for the analysis, a delay on the arrival of a 31 GeV photon of only 0.829s puts a limit of E_{QG} of $\sim 1.2 E_P$, therefore beyond the expected energy scale for

the manifestation of these effects. This result strongly *disfavours* any QG models which predict a spectral variation on the speed of light due to the quantum nature of space-time (at least for first-order effects, i.e. $n = 1$ in Equation 5.58). Despite this important result, additional limits of the same order, population studies and measurements with different kinds of objects are desirable. As a matter of fact, a recent study of the precursors of *Swift* short gamma-ray bursts by Troja et al. 2010 [335] has looked into this; the authors have concluded that $\sim 8-10\%$ of short GRBs display early emission episodes, with times as early as 13 s before the GRB in the case of GRB 090510. They also conducted a detailed analysis of the spectral delays in GRB 090510 based on these new findings and concluded that knowledge of the 13 s-advanced precursor significantly reduces the constraints put before to $E_{QG} > 0.09 M_P$, leaving the quest for an unequivocal counter-evidence for LIV open. Other possible effects testable with astrophysical measurements are still to be made; examples are given in e.g., [226].

VHE Observations: Very high energy observations with ground-based atmospheric Cherenkov telescopes (ACTs) have great potential to contribute to these investigations. Even if the ground-based gamma-ray detection of GRBs is a difficult task with the current generation of ACTs, the higher energy range of the observations (by 3-4 orders of magnitude) mean that VHE AGN observations can essentially probe QG to similar scales as satellite observations of GRBs [346].

The first limit to the energy scale of QG from ground-based VHE observations was derived in 1999 by the Whipple collaboration. The abscence of delays in the registered arrival times of photons of > 2 TeV relative to the low-energy ones from Mkn 421 was used to derive a limit of 4×10^{16} GeV [71]. The most constraining AGN limits are from recent observations with the MAGIC and H.E.S.S. telescopes of Mkn 501 and PKS 2155-304 respectively ([42] and [28]), which extended the scale for the linear term of QG-induced dispersion to 0.2×10^{18} GeV in the case of the MAGIC measurement and 0.7×10^{18} GeV for the H.E.S.S. measurement. In fact, it is relevant to note that MAGIC measured an *actual* lag from Mkn 501 for events with energy > 1 TeV, of 0.030 ± 0.012 s/GeV. Nevertheless, the inconclusive association of this systematic delay with QG-induced dispersion forced the interpretation of the results as an lower-limit on E_{QG}. Potential spurious sources of

Flare	$< \Delta E >$ [TeV]	$\tau_{95\%}$ [s/TeV]	E_{QG} [$\times 10^{18}$GeV]
BF1	1.42	44	1.09
BF2	1.23	30	1.60
BF3	1.40	36	1.33
BF4	1.25	50	0.96
BF5	1.29	48	1.00

Table 5.3: Quantum Gravity energy scale limits derived using the five bursts from the PKS 2155-304 large flare. The parameter $\tau_{95\%}$ corresponds to the shortest lag that the method can probe with a 95% significance for each individual burst, as determined from MC simulations. The last column shows the correspondent lower limits for the QG energy scale.

dispersion which can interfere with a direct measurement of QG effects in time-of-flight experiments in the gamma-ray regime include both external factors, such as the cascading of photons due to interaction with the extragalactic background light (EBL) in the presence of weak intergalactic magnetic fields [277], as well as intrinsic delays on the production and escaping of high energy photons from the source. The association of a measured dispersion with LIV must therefore be able to distinguish between these effects, most probably via consistent measurements from a sample of sources over a range of redshifts, and taking into account the known source systematics.

5.4.2 Results from the Kolmogorov distance method

We now use the results presented in Table 5.2 of Section 5.3 to derive new limits for the quantum-gravity energy scale from the large TeV flare of PKS 2155-304. As can be seen from the results for τ^*, in none of the five individual bursts BF1-5 have we seen a significant ($> 3\sigma$) lag of the high energy photons. The non-detection allows us nevertheless to put a lower limit to the QG scale by quoting the value of E_{QG} which corresponds to the shortest lag for each burst to which the method is sensitive with 95% significance ($\tau_{95\%}$) confidence. These values can be estimated from the RMS values derived from Monte Carlo simulations in Section 5.3 (as shown for example in Figure 5.10), and then converting them in terms of $\xi^{-1}E_P$ according to Equation 5.58. The results are presented in Table 5.3.

Since the tests on all bursts BF 1-5 represent independent measurements, this analysis provides 5 independent limits for the QG-scale. The most constraining limit comes (as

expected) from the shortest of the flares observed, BF-2, followed by BF-3, which is the most intense. The results for BF 4 and 5 are the worst because these flares are considerably broader than the other ones. In considering therefore a final value for the new limits on E_{QG}, we need not combine these individual results. The most restrictive limit is given by the best of the five measurements, which corresponds to $\xi^{-1}E_P > 1.6 \times 10^{18}$ GeV.

This value is of course no match for the most recent Fermi measurement,but are still the most constraining limits to E_{QG} derived from blazar measurments, by a factor of 2, obtained by H.E.S.S. from this same dataset. All these factors point to the power of the Kolmogorov method which we developed in detecting spectral dispersion in high-energy astrophysical data.

As a final note to this section, one should keep in mind a few aspect related to these kinds of measurements and their consequences to QG models. The first of them is that the negative results reported here and their correspondent lower limits on E_{QG} do not in any way disprove the existence of effects of LIV. Their implication is only that of excluding a certain range from the energy scale where QG might be manifested. One important aspect of the QG models is that, though unknown, the energy scale for its manifestation is expected to be of the order of E_{Planck}; in this sense, an energy limit as measured by Fermi of 1.2 E_{Planck} represents a real challenge (albeit not a definitive one) for these models. Nevertheless, such limits are always qualitativily different from a "true" non-detection of the effect. This is because the possible influence of other unaccounted effects to the delay of photons and uncertainties about the source emission process can potentially mask the results. A genuine measurement or disproof of LIV from cosmological photon propagation needs therefore to rely on repeated and consistent measurements from a number of sources, preferentially within a broad range of redshifts. Certainly, a claim of detection of such effects will require a clear measurement of the lag's redshift dependency law, given by 5.58. Finally, the disproof of any manifestation of LIV at the Planck scale, far from being an trivial result, is a fundamental and important confirmation of the validity of the postulates of relativity up to extreme scales (akin to those which existed in the very early universe), for which there are no convincing theoretical justifications to date.

5.5 Application II: *in situ* acceleration

In the final section of this chapter we use the same results to study another effect: that the dispersion be of intrinsic origin. Relaxing the constraints on the required statistical significance of the detection, we derive some parameters for the acceleration of the flow in the jet of PKS 2155-304. These kinds of studies in blazars are an even more promising application for the Kolmogorov method than QG searches, because the expected magnitude of the lags are higher for these effects. The higher expected lags are also the reason why we allow ourselves to relax the constraints on the significance threshold for lag detection to 1σ only in the following analysis (which we admitedly do in a non-conservative way).

5.5.1 Size and physical nature of the emitting region

Very fast variability such as observed here for PKS 2155-304 gives us valuable information about the properties of the high-energy emission sites. Drawing from the discussions of relativistic bulk motions in Chapters 3 and 4, and based on evidence of superluminal expansions such as measured with VLBI (see [290] and [291]), which imply moderate Doppler factors for the pc-scale jet of $\gtrsim 10$, upper limits to size of the emission zones can be derived from causality arguments linked to the minimum variability timescales $t_{\rm var}$, taking into consideration the cosmological redshift of the source, z:

$$R \leq \frac{c t_{\rm var} \delta}{(1+z)}. \tag{5.59}$$

From the smallest variability timescales observed in this flaring event of MJD 53944, $t_{\rm var} = 173 \pm 28$ s, the size of the emitting region is constrained to $R\delta^{-1} \lesssim 4.5{\times}10^{12}$cm = 0.3 AU, or for $\delta \sim 10$, $R_{10} \simeq 3$ AU. As discussed in Chapter 4, the jets of blazars are presumably powered by accretion onto a SMBH, whose characteristic size (or Schwarszchild radius, $R_g = 2GM/c^2$) dictates the natural dynamic scales of the system [86]. Notice that these scales are "fixed" for the system, since the central engine is at rest, irrespective of the bulk outflows of the regions in the jet. For a mass of the SMBH of PKS 2155-304 $M \sim (1-2) \times 10^9 M_\odot$ [82], we have:

$$\frac{R}{R_g} \leq \frac{c^3 t_{\rm var}\delta}{2GM(1+z)} \sim 0.8 - 2\times 10^{-2}\delta, \tag{5.60}$$

which in order to satisfy the dynamical constraints imposed by the central engine would require outflows with Doppler factors $\delta > 50$, much above what is typically expected for blazars and at least 5 times superior to the Doppler factors of the pc-scale jet, implying strong deceleration of the flow in the passage from the inner to the pc-scale jet. These very fast timescales are an *objective* observational fact and, as presented in Chapter 4, represent a dynamical problem to the jet models only as far as the variable regions remain dynamically attached to the scale of the central engine, that is, if these timescales are for an entire cross-section of the jet. A quick response to this problem was drawn by Begelman et al. 2008 [75] and Ghisellini & Tavecchio 2008 [169], who dissociate the gamma-ray emitting zones from the dynamical constraints of the central engine by suggesting they develop within the flow as energetic regions with enhanced Doppler factors. The arguments were given at the end of Chapter 4, and a possible realisation of this scenario will be presented in the final section of Chapter 6. In any case, this discussion allows us to develop a picture of the emitting region (or compact emitting blob) which can be used for the study of the implications of the energy-dependent delays.

5.5.2 Energy dependent time-delays:

Let us return to Table 5.2, where for the first three bursts BF 1-3 no lag was found, but for BF 4-5 marginal 1σ-threshold delays between the $\gtrsim 1$ TeV and $\lesssim 500$ GeV events were seen. If we are to grant these measurements some relevance, for the sake of the exercise at least, then we could test the hypothesis of an intrinsic origin, for which these lags are a signature of gradual particle acceleration in the jet. The time delays between the peaks of the flares are therefore $\Delta\tau_{\rm BF4} \simeq 14 \pm 9$ s and $\Delta\tau_{\rm BF5} \simeq 11 \pm 6$ s.

In the first scenario [39], let us consider that the delay is due to the difference between the acceleration times of electrons to the energies necessary to emit 0.5 and 1 TeV photons:

$$\delta\Delta\tau_{\rm BF} = \tau_{\rm 1TeV} - \tau_{\rm 0.5TeV}, \tag{5.61}$$

where δ is to correct for the referential transformation of the times and τ refers to the acceleration times of the electrons. Assuming that the acceleration time is of the order of the cooling time in an SSC model, we have [39]:

$$\xi\Delta\tau_{\rm BF} = 0.1\frac{\Delta E_{\rm TeV}}{B\delta^2}, \tag{5.62}$$

where B is the magnetic field at the emitting region, ξ [TeV/G] is a measure of acceleration efficiency, and $\Delta E_{\rm TeV}$ is the difference in energy between the flares, given in Table 5.2 as $\langle E\rangle$. In terms of the unknown parameters ξ and δ, and assuming a typical magnetic field $B \lesssim 0.5$ G [252] we have

$$\delta^2 = 0.2\xi^{-1}\frac{\Delta E_{\rm TeV}}{\Delta\tau_{\rm BF}}, \tag{5.63}$$

which imply $\delta^2_{\rm BF4} = 0.02\xi^{-1}$ and $\delta^2_{\rm BF5} = 0.025\xi^{-1}$. For the typical Doppler factors for blazars $\delta \gtrsim 10$, we have acceleration efficiencies $\xi \sim 10^{-4}$ G/TeV, which are of similar magnitudes to the values derived for Mkn 501 [39] and a factor 10^3 lower than required to explain the gamma-ray flux of the Crab Nebula, implying therefore inefficient particle acceleration is taking place.

To develop a second and final scenario for our analysis, let us consider the accelerating blob model of Bednarek & Wagner 2008 [69]. Again here an SSC emission model is assumed. The difference of this scenario in relation to the previous one is that here we suppose that the macroscopic acceleration of the flow (or better, the blob within the flow), and not the microscopic acceleration of the electrons, is causing the energy-dependent time delays. We can imagine that this acceleration is happening, for example, in the innermost jet, where a twisted magnetic field configuration could work for a gradual acceleration of the flow, such as proposed by Marscher et al. 2008 [254]. In this scenario, the blob accelerates from a Lorentz factor $\Gamma_{\rm min}$ to $\Gamma_{\rm max}$ and it is this that causes the time delay between the low and high energy flares.

Now, let us recall that in Chapter 3 we showed that the IC power was related to the

synchrotron power by $P_{\rm IC} \propto \mathcal{U}_{\rm rad}\gamma_e^2 N_e$, where the radiation density in the case of SSC emission is that of the synchrotron flux $\delta\mathcal{U}_{\rm sync}$, and N_e is the number density of particles. Including the effect of the Doppler boost of the flow $\delta = \gamma(1-\beta\cos\theta)^{-1} \simeq 2\gamma$ (see [69]), we have: $P_{IC} = 4\gamma^2\mathcal{U}_{\rm sync}\gamma_e^2 N_e$.

Now, recall (also from Chapter 3) that the energy of the synchrotron photon can be approximated as originating from the electrons at the spectral break of the population's energy distribution. From the considerations above, the existence of such characteristic energy for the parent particle's energy will also be valid for the IC photons, and we can assume that when the blob accelerates from $\Gamma_{\rm min}$ to $\Gamma_{\rm max}$, the maximum energy of the gamma-ray photons will also go from $E_{\gamma,\rm min}$ to $E_{\gamma,\rm max}$, according to $E_\gamma \simeq m_e\gamma_e\Gamma$ [69].

Since a distance βc will be covered in the time dt necessary for this aceleration to happen, where $\beta = \beta(t)$ is the velocity of the blob, it is possible, given certain assumptions about the dynamics of the jet and the structure of the magnetic field (see Bednarek & Wagner [69]) to use the low to high energy time-delay $\Delta\tau$, to estimate the distance crossed by the blob during its acceleration:

$$X_{\rm acc} = c\Delta\tau(2\Gamma_{\rm min}\Gamma_{\rm max} - 1). \tag{5.64}$$

Now, $\Gamma_{\rm min}$ can be assumed, based on lower-limit values measured for the flow via VLBI, to be ~ 10. Sticking to the dynamical considerations of Bednarek & Wagner 2008 [69], which were formulated for the case of a rapid flare of another blazar, namely Mkn 501, very similar to PKS 2155-304, we have the additional condition that $\Gamma_{\rm max}/\Gamma_{\rm min} \approx 10^{2/3}$. and so $\Gamma_{\rm max} \sim 50$. With these values and using $\Delta\tau_{\rm BF4} \sim \Delta\tau_{\rm BF5} \sim 15$ s, as before, we have $X_{\rm acc} \gtrsim 10^{14}$ cm $\sim 10^{-3}$ pc for the size of the acceleration zone traversed by the blob.

This value is surprisingly small, and in particular of the same order of magnitude as the Schwarszchild radius of the central SMBH, meaning that in principle the acceleration region responsible for the production of gamma-rays could be located right at the base of the jet, very close to the central engine. Given that other factors such as opacity due to soft photons might impose more restrictive conditions to the escaping of high-energy photons from these regions, this is not likely to be the case. This result would imply, nevertheless, that once the opacity conditions are satisfied, while still within the jet acceleration and collimation zone (for example as suggested in the model of Marscher et

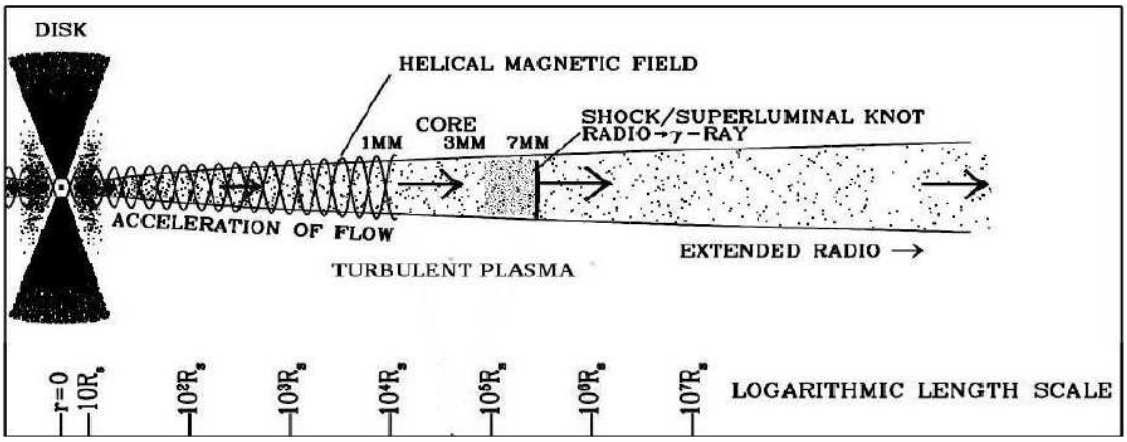

Figure 5.14: Pictorial model for the inner jet structure of blazars. Credits: A. Marscher (adapted).

al. 2008 [254] presented in Figure 5.14) the blob would quickly gain the necessary flow speeds for gamma-ray emission to happen. This means that in terms of the location of the emission sites, the opacity conditions are likely (in this particular case at least) to put stronger constraints on its proximity to the central engine than the values derived here from acceleration considerations.

In Marscher's BL Lac model, the size implied for this acceleration zone can be regarded as an upper limit. In their calculations, they have related the acceleration time directly to the final 240° rotation of the blob crossing a twisted magnetic field line, as revealed by optical polarisation rotation measurements. This association corresponds to a size-scale ≈ 0.025 mas $\sim 10^{-2}$ pc, or $\lesssim 10^{16}$ cm ($< 100 R_g$), which in the context of the previous discussion constrains the size of X_{acc} between few-100 R_g.

Marscher suggests, in the case of BL Lac, that once this acceleration happens the kinetic energy of the flow becomes too large compared to the magnetic energy density, so that turbulence develops and the flow decelerates, meaning that no more VHE gamma-ray emission is possible from downstream of the standing-shock at the VLBI radio core. If this is correct, than our very restrictive values for X_{acc} would constrain the gamma-ray emission to come from a region of a few R_g upstream from the radio core, where the acceleration of the flow is maximal due to continuous collimation and magnetic acceleration.

In conclusion, we have developed in this chapter a statistical method to study energy-dependent time delays in ubinned light curves of high-energy observations which is sen-

sitive enough to allow us to perform a series of tests about the mechanisms of generation and propagation of gamma-ray radiation from extragalactic sources. The cases presented here are examples of possible studies which can be done with the method, although the analysis of the quantum gravity hypothesis provided itself important results, namely the best-constraining limits to date on the violation of Lorentz invariance from AGNs.

Chapter 6

Multiwavelength Polarimetric Campaign on PKS 2155-304

In this chapter the analysis and results of a coordinated 11-day multiwavelength campaign on the VHE blazar PKS 2155-304 are presented. The campaign, conducted in the Summer of 2008 between MJD 54704-54715, was jointly organised by members of the *High Energy Stereoscopic System* (H.E.S.S.) and the *Fermi Large Area Telescope* (Fermi/LAT) collaborations, in what constituted the first coordinated observations of this object ever to cover its spectral energy distribution (SED) from optical to the GeV-TeV gamma-ray bands. In particular, the gamma-ray observations provided the first simultaneous GeV-TeV SED coverage of any BL Lac object, permitting a complete and direct view of the shape and temporal behaviour of the full inverse Compton (IC) component of the emission. Another unique feature of this campaign is that we succeeded in obtaining – for the first time for any BL Lac – optical polarimetric measurements contemporaneous with VHE observations. The object was found to be in a low state at all spectral bands covered, which allowed the placing of strong constraints on the origin of the quiescent emission of this prototypical VHE source. The optical polarimetric observations proved extremely useful in providing complementary information that was invaluable for an in-depth modelling of the source structure. The accompanying X-ray observations were performed with the *Rossi X-ray Timing Observatory* (RXTE) Proportionl Counter Array (PCA) instrument and the *Swfit*/XRT telescope.

The chapter will be organised in the following way. In Section 6.1 we will give a brief

description of the campaign. Since we already discussed in detail the observational techniques relevant for this work and have also given a detailed account of the high-energy view of blazars, we will proceed on Section 6.2 to a detailed description of the polarimetric view of PKS 2155-304. The high-energy multiwavelength analysis and results are presented in Section 6.3 and data analysis and results of optical polarimetry results are shown in Section 6.4. We conclude in Section 6.5 with a discussion of the quiescent state of PKS 2155-304 and the implications of our work to understanding the physics and modelling of the source and a discussion of the prospects of this kind of work on TeV Blazars. The worked presented here is published in two papers – Barres de Almeida et al. 2010 [65] and Aharonian et al. 2009 [35] – and the polarimetric part is inserted within a large project for the optical polarimetric monitoring of TeV Blazars and other AGN. Section 6.6 is an epilogue, attempting to model the optical polarisation variability by means of geometric arguments instead of a inhomogeneous synchrotron source, as discussed in the main papers.

6.1 Description of the Campaign

This work constitutes the third multiwavelength campaign performed with the H.E.S.S. experiment on the prototypical TeV blazar PKS 2155-304[1], and was organised as a joint venture by members of the H.E.S.S. and the Fermi/LAT collaborations in the months preceding the launch of the *Fermi* Gamma-ray Space Telescope on the 11th June, 2008. The observations were therefore motivated by the possibility of finally putting definitive constraints on the different SED models of high-energy BL Lacs, by accurately measuring for the first time and simultaneously the entire inverse-Compton peak in the 100 MeV-10 TeV range. Since the H.E.S.S. experiment detects the source in a low state within $\sim$ 1 hr, significant daily detections are always guaranteed, and the source was targeted for an 11-day multiwavelength campaign. A summary of the observations is presented in Table 6.1

The H.E.S.S. observations of PKS 2155-304 took place during MJD 54701–54715,

[1] Previous multiwavelength campaigns with H.E.S.S. are the 2004-2005 campaign [15] and simultaneous multi-band observations of the second exceptional flare of this object in July 2006 [32].

Table 6.1: Summary of 2008 observations of PKS 2155-304

Observatory	Spectral Band	MJD of Observations
H.E.S.S.....	0.2 – 10 TeV	54701–715
Fermi/LAT.....	0.2 – 300 GeV	54704–715
RXTE/PCA.....	2 – 10 keV	54704–713
Swift/XRT.....	2 – 10 keV	54711–715
ATOM.....	R, V, B	54704–715
LNA/Brazil.....	I, R, V	54710–716

for a total of 42.2 hr. After applying the standard H.E.S.S. data-quality selection criteria, an exposure of 32.9 hr live time remained (MJD 54704–54715), at a mean zenith angle of 18°.3. The dataset were calibrated using the standard H.E.S.S. calibration method [13] according to description in Chapter 2. PKS 2155-304 is one of the primary monitoring targets for the *Fermi* Large Area Telescope (LAT [54]) and is continually observed by the instrument in its normal survey mode. For this campaign, a series of dedicated pointing observations was taken. LAT analyses was performed with the *Fermi* Science tools, now publicly available from HEASARC and described in [61]. A likelihood analysis approach was used. Only class-3 events, with the highest probability of being photons, and coming from zenith angles 105° were selected for analysis. Diffuse emission was excluded according to standard models provided by the Fermi Collaboration which are created based on the Galactic cosmic-ray propagation code GALPROP. The extragalactic diffuse emission and residual instrumental background have been modelled as an isotropic power-law component which was added to the likelihood fit. Only photons within a 10° radius centered on the source coordinates were used in the analysis, and the final selected energy range was between 0.2-300 GeV, therefore with $\sim$ 100 GeV overlap with the H.E.S.S. data.

A total of 75 ks of exposure was taken with RXTE, spread over 10 days coinciding with the scheduled times of H.E.S.S. observations; the data were taken with the Proportional Counter Array (PCA [210]) and were analysed according to standard procedures provided by HEASARC[2]. An additional 6.4 ks exposure with *Swift* was also made towards the end of the campaign, using the X-ray Telescope (XRT [94]), and for this dataset pre-processed standard products were used.

[2]RXTE data analysis proceudres are described at http://heasarc.gsfc.nasa.gov/docs/xte/.

During the multiwavelength campaign, a total of 106 Bessel BVR filter observations were taken with the 0.8 m ATOM optical telescope [191] located on the H.E.S.S. site. Integration times between 60 s and 200 s were used. Photometric accuracy was typically between 0.01 mag and 0.02 mag. Automatically processed photometric data provided by the ATOM team were used as well.

Complementary optical polarimetric observations were conducted during the second half of the campaign, between MJD 54710–54716, and constitute the main highlight of this work. The observations were made with the 1.6 m Perkin-Elmer telescope at the Pico dos Dias Observatory of the National Laboratory of Astrophysics (OPD/LNA, Brazil), using the high-precision CCD imaging polarimeter IAGPOL in linear polarisation mode [250]. A total of about 100 (non-strictly) simultaneous multiband images were taken in the VRI filters, except for the last night of the campaign when only R-band measurements were made. Data analysis was described in detail in Chapter 2. The configuration of the polarimeter provides simultaneous measurements of the ordinary and extraordinary rays, which allowed for observations under non-ideal atmospheric conditions, since any atmospheric contributions will affect both rays equally, and any sky contribution is expected to cancel out in the process. Standard polarisation stars from Smith et al. 1991 [323] and Rector & Perlman 2003 [298] were used for calibration. Single polarisation images were integrated from 8× 150 s exposures, each at a different position of the polarimetric wheel; a precision better than 1% in the polarisation degree was achieved. The temporal resolution of consecutive measurements in the R band (which was the most intensely monitored band since it provides the lowest integration times) was of the order of 15 min, whereas V and I images were taken at the beginning and end of each night to monitor the spectral evolution of the source's polarisation properties. Data reduction was made with a specially developed package for LNA polarimetric data, PCCDPACK [285].

6.2 The Polarimetric view of PKS 2155-304

The high-energy peaked BL Lac object (HBL) PKS 2155-304 has been the target of several polarimetric observations along the years, from radio to ultraviolet frequencies, which accumulated a wealth of information on the polarisation properties of the source.

In fact, optical polarisation measurements of this object were first obtained by Griffiths et al. [185], shortly after the discovery of the optical counterpart of the *HEAO A-3* X-ray source H 2154-304 in 1978 [184]. The linear polarisation of the optical flux, together with the variable emission and broadband featureless power law continuum, helped the rapid identification of the source as a new member of the BL Lac class.

6.2.1 Optical Polarisation Properties

The first series of systematic studies of PKS 2155-304 in polarised light were done with the 3.8-m United Kingdom Infrared telescope (UKIRT) on Mauna Kea, between 1979 and 1983, by Impey et al. ([204], [205] and [201]). The source was observed in the *J*, *H* and *K* infrared bands showing a relatively stable and mostly low degree of linear polarisation of $\lesssim$ 3% and an equally stable polarisation position angle between 120°-130°. A strong thermal excess was also identified superposed on the polarised non-thermal flux from the two-colour IR plot [205].

The first simultaneous broadband polarisation measurements of PKS 2155-304 were performed by Brindle et al. [91] and Mead et al. [265] in IR and optical (from *K* to *U* bands) using the now defunct Mark I and Mark II Hatfield dual-beam polarimeters [115], mounted on the 3.9-m Anglo-Australian Telescope (AAT) and the UKIRT. The observations revealed the source to be in a relatively higher and more variable polarised state than seen in previous campaigns, with the polarisation degree assuming values typically between 3 – 7% [333] and presenting variability on both intra and inter-night timescales. These variations were accompanied by changes in flux and polarisation position angle (P.A.) on all nights, with the P.A. varying within the entire range of available angles, but assuming preferential values between 90° and 140° ([324] and [333]). Dominici et al. [126] investigated the existence of such preferential values for the polarisation, using historical data from the literature, and identified a variable component with a long timescale trend in P.A. that has been systematically decreasing during the last decades, possibly due to global geometric changes in the direction of the relativistic jet. No episodes of large and continuous rotation of the polarisation angle (such as the 90° or 180° swings observed in other BL Lacs) have ever been registered for this source, presumably due to insufficient sampling. The presence of large amplitude variability in the

polarisation degree seems to correlate with epochs of high photometric fluxes but there exists no consistent connection between the magnitude of these two quantities, as discussed for example by Smith et al. [324].

Before the measurements described here, the short-timescale polarisation variability was probed by Tommasi et al. [333] and Andruchow et al. [50] using the Complejo Astronomico El Leoncito (CASLEO, Argentina) 2.15 m telescope, with a resolution of about 15 min. Generally, daily variations did not exceed a factor of ~ 1.2 in amplitude for P and $\sim 20^\circ$ in P.A., but extreme polarimetric flux variations (up to a factor of 2) and P.A. rotations of 90° were registered during some of the intranight observations by [333]. Variations in the polarisation degree P and position angle P.A. do not necessarily correlate at either intra or inter-night timescales.

A variable level of positive[3] frequency dependent polarisation (FDP; $d\log P/d\log\nu > 0$) was also detected from the source during the highly polarised states ($P \gtrsim 10\%$). FDP was later also observed by Smith & Sitko [322], Smith et al. [324] and Allen et al. [45], extending up to the UV wavelengths, and always in the sense of $d\log P/d\log\nu > 0$, with a median of $P_U/P_I \simeq 1.2$. The *Hubble Space Telescope* Faint Object Spectrograph (FOS) measurements of Allen et al. [45] between 1360-3300 Å yielded strong evidence that the UV polarised flux is produced by the same synchrotron mechanism responsible for the optical polarisation; the greatest evidence for this was the lack of abrupt changes in P and P.A. between the optical and ultraviolet frequencies. Smith & Sitko [322] used this fact to constrain the contribution of an accretion-disc dominated UV continuum to the BL Lac emission, concluding that the FDP is intrinsic to the synchrotron source rather than the result of dilution by a non-thermal unpolarised component. A similar argument is valid for the host galaxy's contribution ([136] and [81]), for which the red stellar continuum of an elliptical galaxy could explain the sense of the FDP but not its time variability or the presence of a frequency dependent position angle (FDPA). In fact, marginal levels of FDPA were also present in some of the data collected by [91] and [322], with maximum rotations of about 5° over the entire IR to UV spectrum. FDPA measurements present no trend for a positive or negative $d\theta/d\nu$. Tommasi et al. [333] were the only people

[3]That is, in the sense of a higher polarisation degree towards the bluest frequencies.

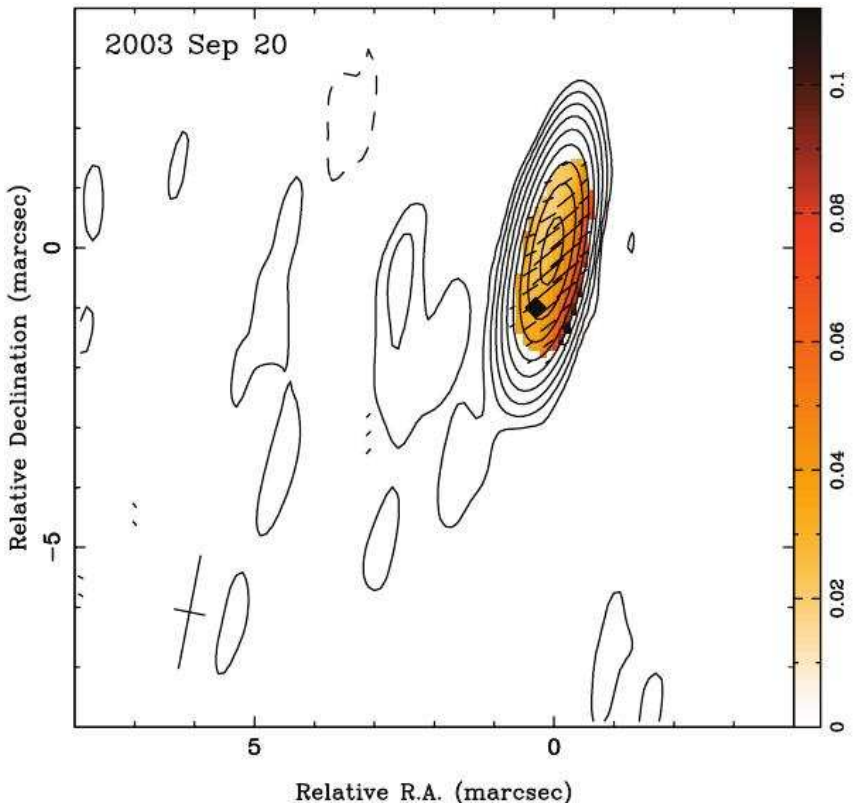

Figure 6.1: VLA image of PKS 2155-304 at 15.4 GHz by Piner et al. [291]. The tick marks show the magnitude of the polarised flux (with a scale of 0.2 mas mJy^{-1}) and the direction of the EVPA. The colours show the fractional polarisation, with the scale indicated to the right of the images.

to probe for circular polarisation in PKS 2155-304, with negative results, and they set an upper limit of 0.2% at the 3 σ level. One should bear in mind, however, that the absence of significant circular polarisation in homogeneous synchrotron source scenarios is expected, since the degree of circular polarisation should be a factor of γ_e less than the linear, where γ_e is the electrons' Lorentz factor, typically $> 10^3$ in blazars [309].

6.2.2 Radio Jet Observations

In radio frequencies, the parsec-scale jet of PKS 2155-304 was imaged twice at 15 GHz by Piner et al. ([290] and [291]) using the Very Long Baseline Array (VLBA) with a linear resolution of approximately 0.5 pc. The VLBI image shows a jet that starts southwest of the core at a position angle of $\approx$ 150° in 2000, and by 2003 seems to have rotated to the new position of $\approx$ 160°. The only pc-scale polarisation image of this source to date is the one made at 15 GHz by Piner et al. [291], presented in Figure 6.1, where a

single jet component is resolved downstream from the radio core, moving with a derived bulk Lorentz factor $\Gamma \sim 3$. Polarised flux was detected coming from the core component alone, as indicated by the coloured area, at a mean level of 2.9 %; the polarisation vector (at a P.A. $\approx 131°$) was seen to be about 30° mis-aligned with the jet-projected position angle.In the optically thin regime this is evidence for the presence of a dominant magnetic field component roughly transverse to the flow. The best-fit size to the core component is 0.23 mas, corresponding to a linear size of ~ 0.5 pc. The polarisation degree of the core exhibited a spatial gradient between 3-8% that increased in the upstream direction.

6.2.3 Implications for the source structure

The observational studies of PKS 2155-304 and BL Lacs in general have shown that the linearly polarised near-IR to UV continuum is most easily explained by emission from incoherent, optically thin synchrotron radiation [45]. As is typical for X-ray selected BL Lacs (XBLs or high-frequency peaked BL Lacs, HBLs) – as opposed to radio-selected BL Lacs (RBLs or low-frequency peaked BL Lacs, LBLs) – PKS 2155-304 presents a relatively low polarisation degree ($P \lesssim 10\%$). This fact alone could lead one to consider the existence of a strong unpolarised component which dilutes the more highly polarised and variable emission. The presence of such a strong unpolarised continuum has nevertheless been disfavoured by the observations of Smith et al. 1992 [324]. They noted an absence of any significant changes to the source's spectral index and FDP during a ~ 0.8 mag increase in the optical brightness which suggested that any unpolarised background contribution – from the host galaxy or other unpolarised AGN components such as the "big blue bump" – must be negligible ([322] and [45]).

The observed variability timescales also suggest that thermal radiation cannot be the source of the emission [324], and in fact the rapid changes seen in polarisation attest to an origin for the BL Lac continuum in compact zones, smaller than ~ 1 lt-day across. Allen et al. 1993 [45] also observe that the variability timescales argue against scattering processes being responsible for the polarised flux as well, since the scattering material could hardly change its distribution about the continuum source so rapidly. The polarisation properties of the source thus seem to indicate an origin for the IR-UV flux in a compact synchrotron source. The detailed properties of this non-thermal source need to be able to explain not

only the presence of rapid variability in the polarisation and the presence of FDP, but also the consistent lack of correlation between changes in brightness and the polarisation characteristics of the source.

Frequency Dependent Polarisation

An intrinsic origin for the FDP points to a picture of the emitting region as an inhomogeneous synchrotron source, since a homogeneous (i.e. aligned magnetic field structure and uniform particle distribution) zone of magneto-bremsstrahlung radiation would have frequency-independent properties [175]. According to Nordsieck 1976 [279] and Björnsson & Blumenthal 1982 [84] frequency-dependent polarisation will appear if the flux spectral distribution α steepens with frequency. However, Allen et al. 1993 [45] observed that such a form for the frequency-dependence $P(\nu) \propto (1 - \alpha(\nu))/(5/3 - \alpha(\nu))$ greatly underestimates the amount of FDP that is seen for the source, given its weak spectral curvature. An additional frequency dependence of the degree of ordering of the magnetic field is thus necessary to explain the spectral polarisation properties.

An alternative scenario to this picture would be a two-component model such as proposed by Ballard et al. 1990 [59]. A sharp high-energy spectral cutoff, as expected from shock-accelerated electron distributions in the variable polarised components, would then naturally lead to FDP, but would also predict a maximum polarisation at the cutoff frequency ν_c that has never been observed for PKS 2155-304. Courvoisier et al. 1995 [113] measured the spectral index of the polarised component between the U-I bands and found an unabsorbed spectrum, flatter than that of the unpolarised component, indicating that such a spectral break for PKS 2155-304 would have to happen at higher frequencies. Another weakness of such a proposal is that these two components would have to vary together if little or no concurrent changes in α are to be seen, as in the data of Ballard et al. Two-component synchrotron models were also studied by Brindle et al. 1986 [91] to explain the timing characteristics of the polarised emission of PKS 2155-304. A model where only one of the synchrotron components is polarised has been considered by Smith et al. 1992 [324], but they concluded that an unphysical relation between the brightness and spectral indices of the two components would be necessary to account for the constancy of the FDP observed over a range of different photometric flux levels, thus dis-

favouring such a scenario. It is clear therefore that the development of a model capable of accounting for all the range of complex polarisation behaviours observed from the source is not an easy task.

Polarisation Time-Variability

Extreme variability events where the degree of linear polarisation changes by a factor of 2 in one day while the P.A. rotates by 90° [333] suggest the presence of two significantly polarised components of different P and P.A. Tommasi et al. 2001 [333] combined their measurements with historical data to propose a model for PKS 2155-304 consisting of a stable component endowed with a regular magnetic field, usually dominant, responsible for the preferred P.A. of $\sim 115°$. Secondary components can then arise due to perturbations in the jet, which change the general ordering of the magnetic field and induce rotations in P.A. and variability in the polarised flux. The overall low level of polarisation is explained by the presence of several of these "patches" in the jet, each with a size comparable to the coherence length of the magnetic field. The total polarisation in this case is given by $P_{max}/\sqrt{n}$, where n is the number of "patches" and P_{max} the maximum theoretical polarisation of each individual sub-region ($\sim 70\%$). Ghisellini & Lazzati 1999 [168] envisaged that this ordered field component could be the geometrical result of a jet observed slightly off-axis.

An additional property of the polarised emission of BL Lacs that strongly constrains the source models and should be taken into consideration is the usual lack of correlation between the variations in polarised and photometric flux; in particular, the relative amplitude of the polarised flux variation over timescales of a few days tends to be much larger than that of the total flux in the same band ([324] and [113]). The distinct behaviour of the two light-curves means that it is not possible to account for the total flux variations by those of the polarised flux alone, and both components of the emission must vary in time. Conversely, the problem of the variation of the polarised flux cannot be reduced to that of its dilution on a variable and unpolarised background component. Courvoisier et al. 1995 [113] note that the spectrum of the polarised component does not vary together with its flux, and that this indicates that the flux variability cannot be dominated by changes in the physical parameters of the emitting region, such as particle spectrum or acceleration

efficiency and magnetic field ordering. Rather, they favour a scenario where variations are the result of changes in the beaming factor (either the bulk Lorentz factor or orientation) of the emitting region.

Relation to X-rays and Radio VLBI

In relation to the broadband SED of PKS 2155-304, Smith et al. 1992 [324] studied their results in the light of the inhomogeneous SSC model of Ghisellini et al. 1985 [166]. They noted that the rapid variations in the polarised flux are of a similar time scale to those seen in soft X-rays, which are predicted by Ghisellini et al. to originate from synchrotron rather than IC emission. Nevertheless, more detailed analysis conducted by Courvoisier et al. [113] using contemporaneous X-ray data showed that the X-ray and optical polarised emission are mostly likely not to be co-located.

Finally, note that the existence of a preferred position angle in optical similar to that of the mm-wave core favours the presence of a dominant or large-scale component with a regular magnetic field which is associated with both emissions. Furthermore, similar values of the polarisation degree seen in both bands and the lack of polarised emission from other parts of the jet in the VLBI images, suggest the unresolved polarised optical emission originates in the pc-scale radio core. This hypothesis will be adopted in the subsequent analysis, motivated by recent studies which used VLBI maps to compare the optical polarisation properties of the jet with the radio images, and associating the variable emission of blazars with the 43 GHz VLBI core (see [246], [220], [162]).

6.3 Multiwavelength Campaign: analyses and results

Now we present the results of the multiwavelength campaign as in the first paper (Aharonian et al. 2009 [35]) without the information on the optical polarimtery which will be added to the discussion later on.

Multiwavelength light-curves

Figures 6.2 and 6.3 show the multiwavelength runwise and nightly average light-curve data for all the measurements of the campaign. The average H.E.S.S. integrated flux level

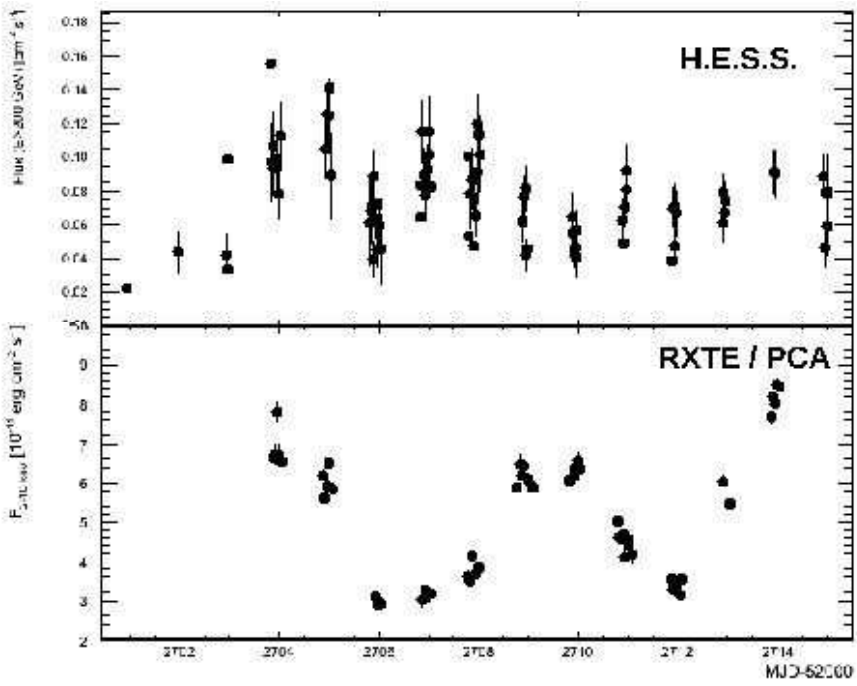

Figure 6.2: Runwise light curves for the entire campaign on PKS 2155-304, presenting H.E.S.S. and RXTE data.

above 200 GeV is of $(5.56 \pm 0.13_{\mathrm{stat}} \pm 1.11_{\mathrm{syst}}) \times 10^{-11}$ cm^{-2}s^{-1}, corresponding to ~ 0.2 Crab and about 50% higher than the historical minimum VHE flux level during the quiescent state of 2003 [15]. Characterisation of the source variability was done using the positive excess variance $\sigma_X S^2$ and fractional rms variability F_{var} measures presented in [341]:

$$\sigma_{XS}^2 = S^2 - \overline{\sigma_{err}^2} \tag{6.1}$$

$$F_{\mathrm{var}} = \sqrt{\frac{\sigma_{XS}^2}{\overline{x}^2}}, \tag{6.2}$$

where S^2 is the time series variance, x are the individual flux values, σ_{err} is the sample variance and the bars over the letters indicate averages. For the VHE data, we found $F_{\mathrm{var,VHE}} = 23\% \pm 3\%$. These values should be compared with the results of the long-term quiescent state constrained by H.E.S.S. with three year observations from 2005 to 2007, which found a stable low-state flux level of $F_{\mathrm{low,VHE}} = (4.32 \pm 0.09_{rmstat} \pm 0.86_{\mathrm{syst}}) \times 10^{-11}$ cm^{-2}s^{-1} and a corresponding rms $_{\mathrm{low,VHE}} = 0.9 \times 10^{-11}$ cm^{-2}s^{-1} [2], and the analysis of

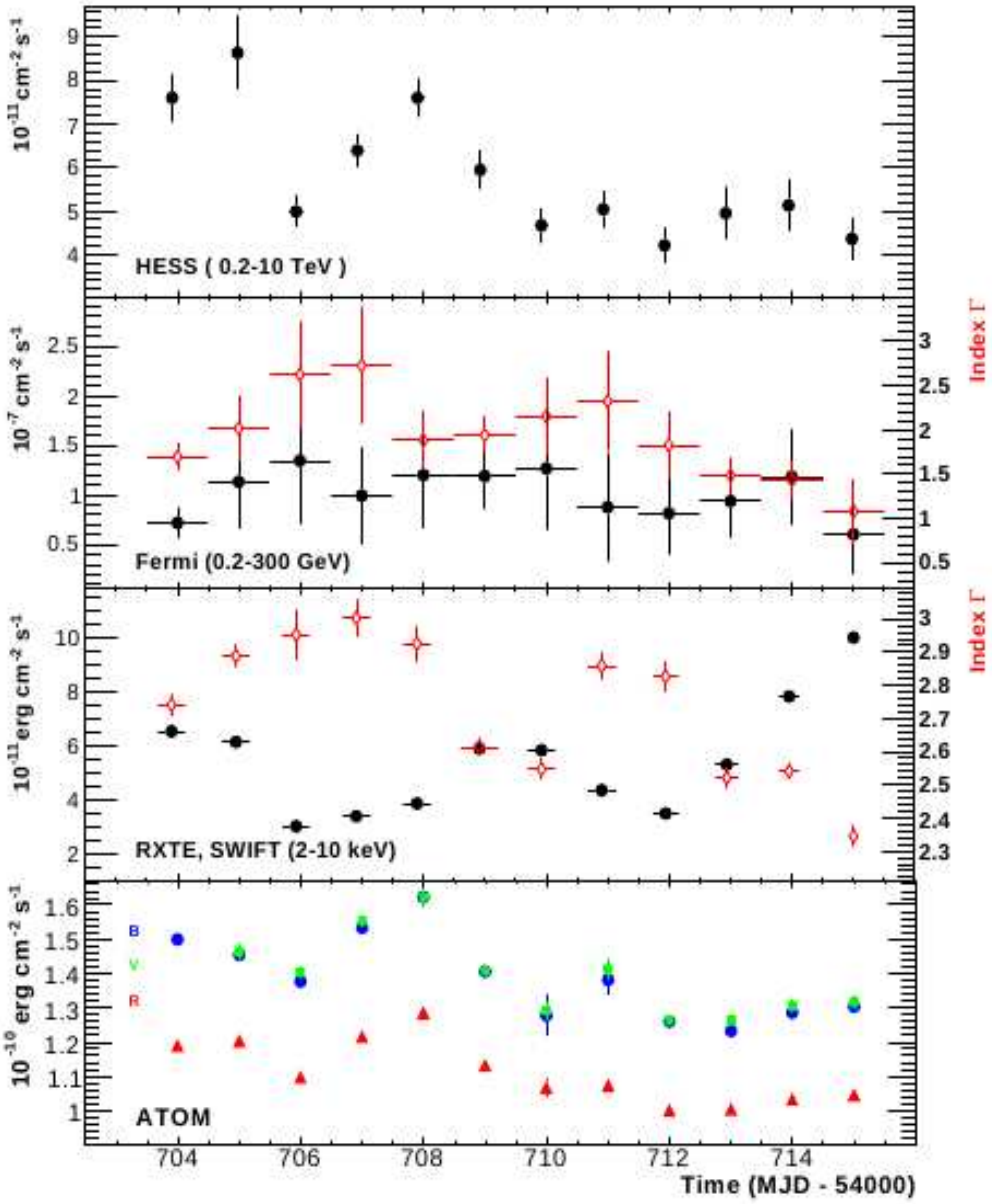

Figure 6.3: Light curves for the entire multiwavelength campaign dataset. The *Fermi* and X-ray (RXTE/PCA and Swift/XRT) panels also show the spectral index measurements (in red) for each night. The colour-coded ATOM datapoints are for B (blue circles), V (green squares) and R (red squares).

which suggests that this quiescent state has an intrinsic variability level associated with it. This variability was studied by Giebels and Degrange and found to be compatible with a lognormal process that they suggest governs the variability from jets in BL Lac objects [173].

The *Fermi*/LAT light-curves for the range 0.2–300 GeV were constructed by averaging all the intranight points and their times are exactly simultaneous with the H.E.S.S. data

points. A light curve fit to a constant finds a χ^2 probability of 0.95, therefore consistent with a constant flux, and the same normalised excess variance analysis gives an upper limit for the variability of $F_{\rm var,GeV}20\%$ at the 90% confidence level, according to the analysis method detailed in [139].

X-ray light curves of RXTE/PCA and *Swift*/XRT both show a higher degree of variability than the H.E.S.S. light curve and are consistent with each other, with flux-doubling episodes on timescales of days. The lowest flux level registed during the campaign in the 2-10 keV band was $3-6\times10^{-11}$ erg cm^{-2}s^{-1}, compatible with the sources low state observed by [15]. The high fractional variability is nevertheless not compatible with that seen at HE gamma-rays, with $F_{\rm var,keV} = 35\% \pm 0.05\%$. If the two bands were connected within a simple single-zone SSC model framework, then variability flux levels would be expected to be very similar and related to changes in the single particle population which would reflect equally in the synchrotron and in the inverse-Compton radiation channels. The fact that these do not match is already a sign that the SSC model might not be the most appropriate description of the source's quiescent SED, and two options can be envisaged to solve this problem: either there is a component of the inverse-Compton emission which is external-Compton in origin and the external soft-photon field is variable, or we need to consider a multi-zone model by means of which two or more particle populations are responsible for producing the observed optical to gamma-ray spectrum. We will return to this issue in the future, aided by the optical polarimetric information.

Spectral analyses

The H.E.S.S. time-averaged spectrum was derived using the forward-folding method described in Chapter 2. The VHE data is well-described by a power law of the form $dN/dE = I_0(E/E_0)^{-\Gamma}$, with a differential photon flux at $E_0 = 350$ GeV of $I_0 = (10.4 \pm 0.24_{\rm stat} \pm 2.08_{\rm syst})\times10^{-11}$ cm^{-2}s^{-1}TeV^{-1} and spectral index $\Gamma = 3.34\pm0.05_{\rm stat}\pm0.1_{\rm syst}$. The VHE spectrum therefore shows no evidence of curvature, as is usual for the low state of this source, but the spectral index here is significantly harder than the long-term quiescent state properties derived by the H.E.S.S. Collaboration, where $\Gamma_{\rm quies} = 3.53 \pm 0.06$ [2]. This is in good accord with the derived spectral trend of "softer when brighter" that was derived for this object from the long term data (see Figure 7 in [2]). After correction for

EBL absorption using the model P0.45 given in [20], an intrinsic photon index $\Gamma_{\rm int} \approx 2.5$ was derived.

The time-averaged *Fermi* spectrum also follows a simple power law with $I_0 = (2.42 \pm 0.33_{\rm stat} \pm 0.16_{\rm syst}) \times 10^{-11}$ cm^{-2}s^{-1}MeV^{-1} and $\Gamma = 1.81 \pm 0.11_{\rm stat} \pm 0.09_{\rm syst}$ and $E_0 = 943$ MeV. This photon index is compatible with the EGRET measurement of 1.71 ± 0.24 during a GeV gamma-ray flare in 1995 [344], but is much harder than the 2.35 ± 0.26 index quoted for the source in the "Third EGRET Catalogue" [189].

Finally, the 4-10 keV PCA and the 0.5-9 keV XRT data were combined and fitted in XSPEC, using a broken power-law model with a multiplicative factor for each instrument to account for cross-calibration uncertainties and non-simultaneous observations. With a fixed Galactic hydrogen column density $N_H = 1.48 \times 10^{-20}$ cm^{-2}, the parameters obtained were: $\Gamma_1 = 2.36 \pm 0.01$, with $E_{\rm break} = 4.44 \pm 0.48$ keV, and a high-energy index $\Gamma_2 = 2.67 \pm 0.01$, for a unabsorbed 2-10 keV flux of $F_{\rm keV} = 4.99 \times 10^{-11}$erg cm^{-2}s^{-1}, which is twice the value registered for the lowest state in 2003 [15].

Let us now turn to the presentation and discussion of the optical polarimetric data, after which we shall return to the discussion of our results on the wider multi-wavelength context of this campaign.

6.4 Polarimetric Observations of PKS 2155-304 in 2008

Figure 6.4 shows the R band light-curve for the total flux, polarisation fraction and electric vector position angle (EVPA) for all six nights of the optical campaign. A complete journal of the polarimetric observations can be found in Table B.1. The data presented in this figure represent the directly observed quantities, not corrected for the unpolarised contribution of the stellar continuum. For the remainder of the analysis, flux estimates for the host galaxy of PKS 2155-304 as quoted in [125] (see also Table 6.2) were used to subtract the unpolarised contribution to the total emission, leading to an estimate of the intrinsic polarisation of the AGN light according to the expression [333]:

$$P_{\rm int} = P_{\rm meas}\left(1 + \frac{F_{\rm host}}{F_{\rm AGN}}\right) \tag{6.3}$$

Table 6.2: Host galaxy contribution for PKS 2155-304.

Filter	Flux (mJy)	References
B	1.5	Bertone et al. (2000) [81]
V	3.1	Falomo et al. (1991) [136]
R	4.8	Fukugita et al. (1995) [160]
I	7.6	Falomo et al. (1991) [136]
J	14.6	Kotilainen et al. (1998) [230]
H	22.5	Kotilainen et al. (1998) [230]

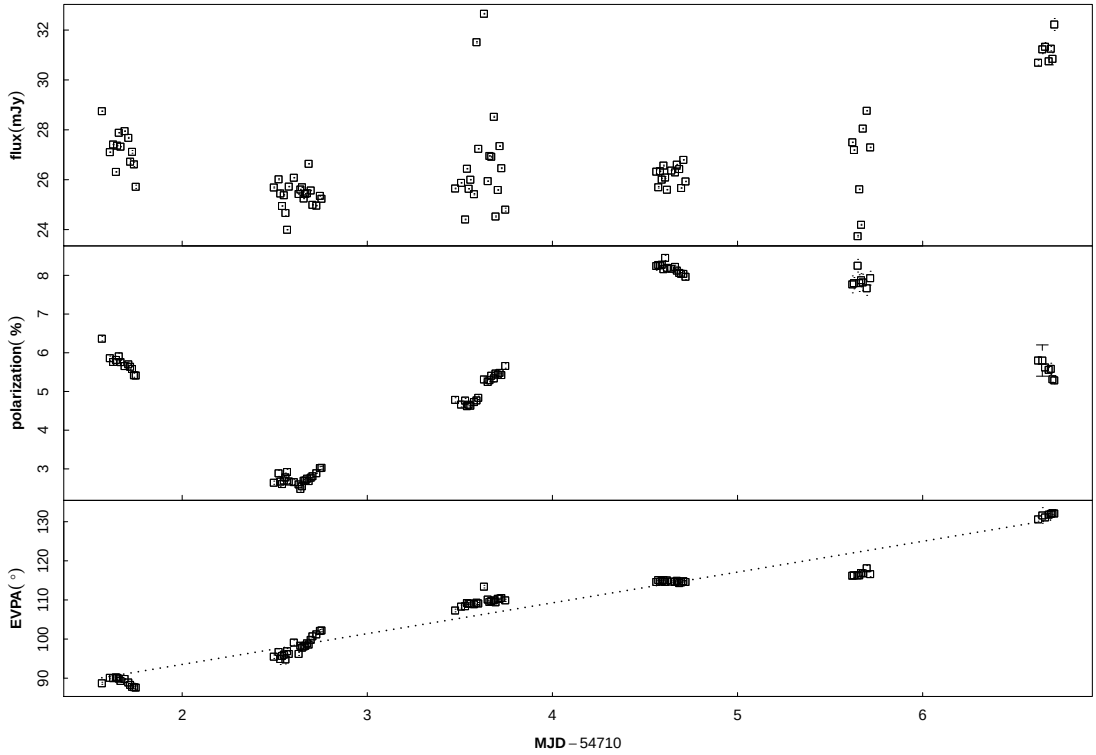

Figure 6.4: R-band optical light-curve for PKS 2155-304 from 01 to 07 September 2008, showing the total flux variability (*upper panel*), fractional polarisation degree (*middle panel*) and EVPA rotation (*lower panel*). Each data point corresponds to an integration time of about 15 min. The flux points and polarisation degree are not corrected for the host galaxy contribution. Error bars are of the order of the size of the points.

The source was observed for three to six hours during each night with a minimum temporal resolution in the R band of $\sim$ 15 min, resulting in a week of well-sampled intranight light-curves. The overall flux behaviour is qualitatively distinct from the changes in the polarisation properties of the emission (particularly the polarisation degree), as noted before by Courvoisier et al. 1995 [113] and Tommasi et al. 2001 [333] for this same object. Flux variability is dominated by intranight activity, superimposed on a base-

line level which increases towards the end of the campaign and is in agreement with the multi-band measurements from the ATOM telescope presented in [35].

Microvariability Analysis

A Lomb-Scargle power spectrum analysis [310] reveals that the total and polarised flux micro-variabilities in the R-band are describable as random fluctuations. The power spectrum distributions (PSD) for the three quantities is well-described by a red-noise (or Brownian motion) power law followed by high-frequency Poisson white noise. The respective noise power levels showed that the variability timescales are limited by the temporal resolution of the measurements. To quantify the presence of micro-variability at each night of the campaign, we used a standard χ^2 test for variance in a normal population, as proposed by [223] and discussed in a review by [124]. According to this criterion, given N observations over a certain period of time, the source is classified as variable if the chance probability of exceeding the value

$$X^2 = \sum_{i=1}^{N} \frac{(S_i - \langle S \rangle)^2}{\epsilon_i^2} \tag{6.4}$$

is $< 0.1\%$, where ϵ_i^2 is the standard error of the i-th measurement and $\langle S \rangle$ is the weighted average of S, defined by

$$\langle S \rangle = \frac{\sum_i \epsilon^{-2} S_i}{\sum_i \epsilon^{-2}}. \tag{6.5}$$

If the measurement errors are random and follow a normal distribution, X^2 is χ^2-distributed with $N - 1$ degrees of freedom and the critical error for the test is given by $\chi^2_{0.001,\ N-1}$, presented in Table 6.3 along with the other parameters used here to quantify the variability. These parameters give measures of both the amplitude and timescale of microvariability for the total flux and each of the Stokes parameters for linear polarisation; they include the fluctuations index μ, the fractional variability index FV and the time between extrema in the intranight light-curves Δt, and are defined below, where σ_S is the standard deviation of the dataset:

Table 6.3: Optical and polarimetric micro-variability analysis results.

				Flux			Stokes Q			Stokes U		
Date (2008)	N	Δt_{obs} [h]	χ^2_{N-1}	μ %	FV	Δt [h]	μ %	FV	Δt [h]	μ %	FV	Δt [h]
01.Sep	13	4.25	34.5	2.86	0.06	3.49	4.26	0.08	4.39	110.	1.20	2.57
02.Sep	21	6.75	46.8	2.13	0.05	2.07	4.24	0.09	1.50	31.4	0.47	2.28
03.Sep	19	6.25	43.8	8.05	0.14	2.21	6.01	0.09	2.20	11.0	0.18	3.66
04.Sep	14	4.50	36.1	1.42	0.02	1.98	1.64	0.03	2.01	1.80	0.03	2.01
05.Sep	8	3.00	26.1	6.88	0.10	0.96	4.40	0.08	0.96	2.05	0.03	1.45
06.Sep	7	1.75	24.3	1.68	0.02	1.21	20.3	0.26	1.29	3.50	0.05	1.38

$$\mu = 100\,\frac{\sigma_S}{\langle S \rangle}\ \% \tag{6.6}$$

$$FV = \frac{S_{max} - S_{min}}{S_{max} + S_{min}} \tag{6.7}$$

$$\Delta t = |t_{max} - t_{min}| \tag{6.8}$$

All quantities presented significant intranight variability throughout the campaign, with $X^2 \gg \chi^2_{0.001,\ N-1}$. Though the intranight variations dominated the behaviour of the total flux light-curve, both the Stokes Q and Stokes U parameters also showed very high relative variability indices, sometimes higher than the photometric flux.

Figure 6.5 shows the variability track of the polarised flux in the $Q - U$ plane, as indicated by the arrows following the chronological order of the variations. The general appearance of these plots gives an important visual insight into the chaotic nature of the short-timescale variability, as first discussed by Moore et al. 1982 [273] for the case of BL Lacertae. The intranight tracks of the linear Stokes parameters seem to follow a random walk (as already indicated by the PSDs), with little excess net displacement from start to finish of the observations relative to the typical amplitude of the excursions at each step. Significant changes in the Q and U fluxes happen at multiple timescales, showing that there is no single characteristic scale for the intranight variations, as would be expected from a turbulent origin for the rapid variability.

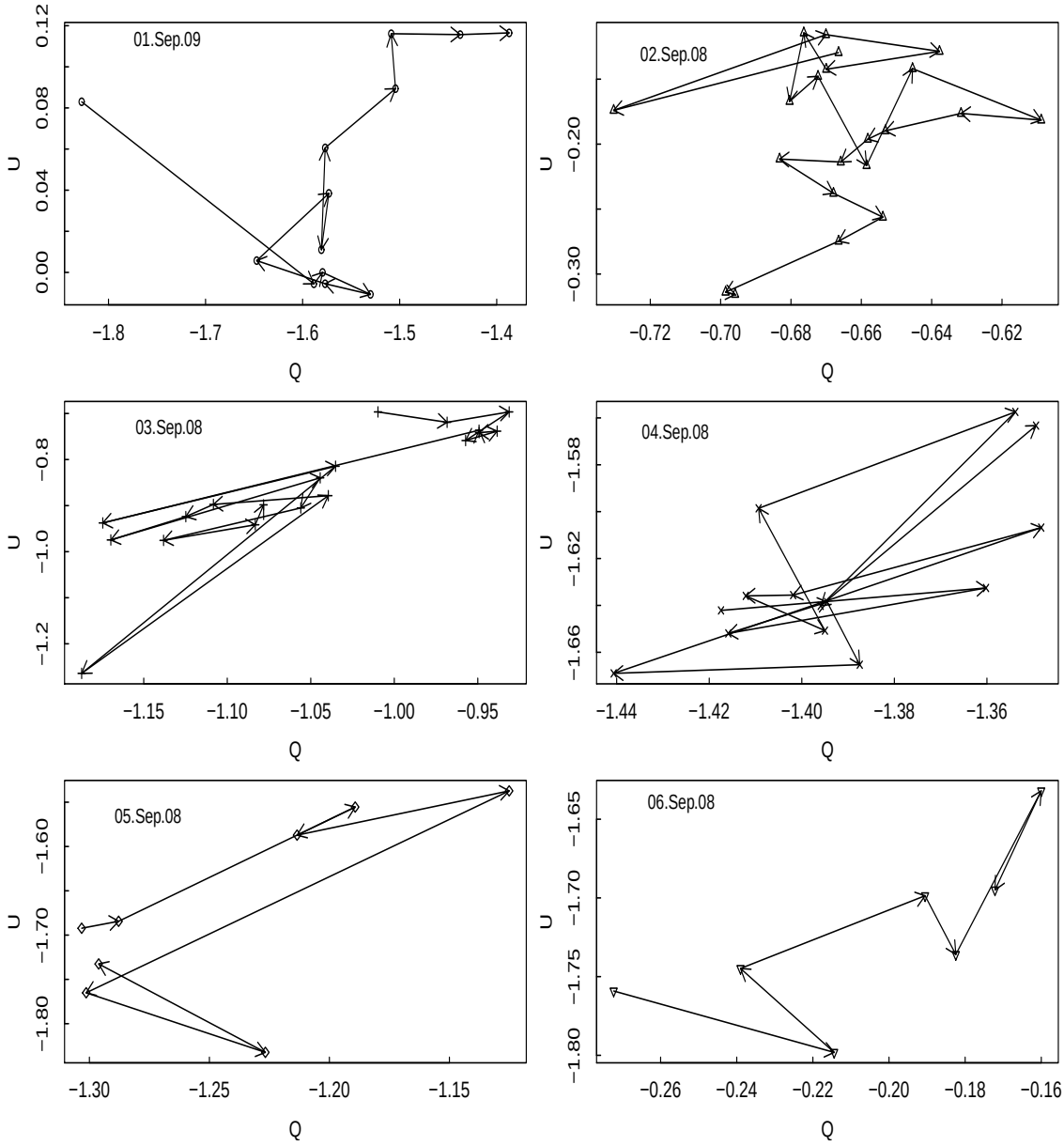

Figure 6.5: The intranight polarimetric variability of PKS 2155-304 in the Stokes $Q-U$ plane for each night of the LNA optical campaign. The points represent each individual flux measurement of the linear polarisation quantities. The arrows indicate the chronological order in which variability happens. Errors are of the order of the size of the points.

Description of Polarisation Quantities

Although presenting some intranight activity, the temporal behaviour of the polarised flux was dominated by internight variations, over which the random, shorter-timescale fluctuations are superimposed. The relative amplitude of the polarised flux variability is much larger than that of the total photometric flux as evident from Figure 6.4, varying by a factor of 3 during the campaign. The host-galaxy-corrected polarisation degree varied

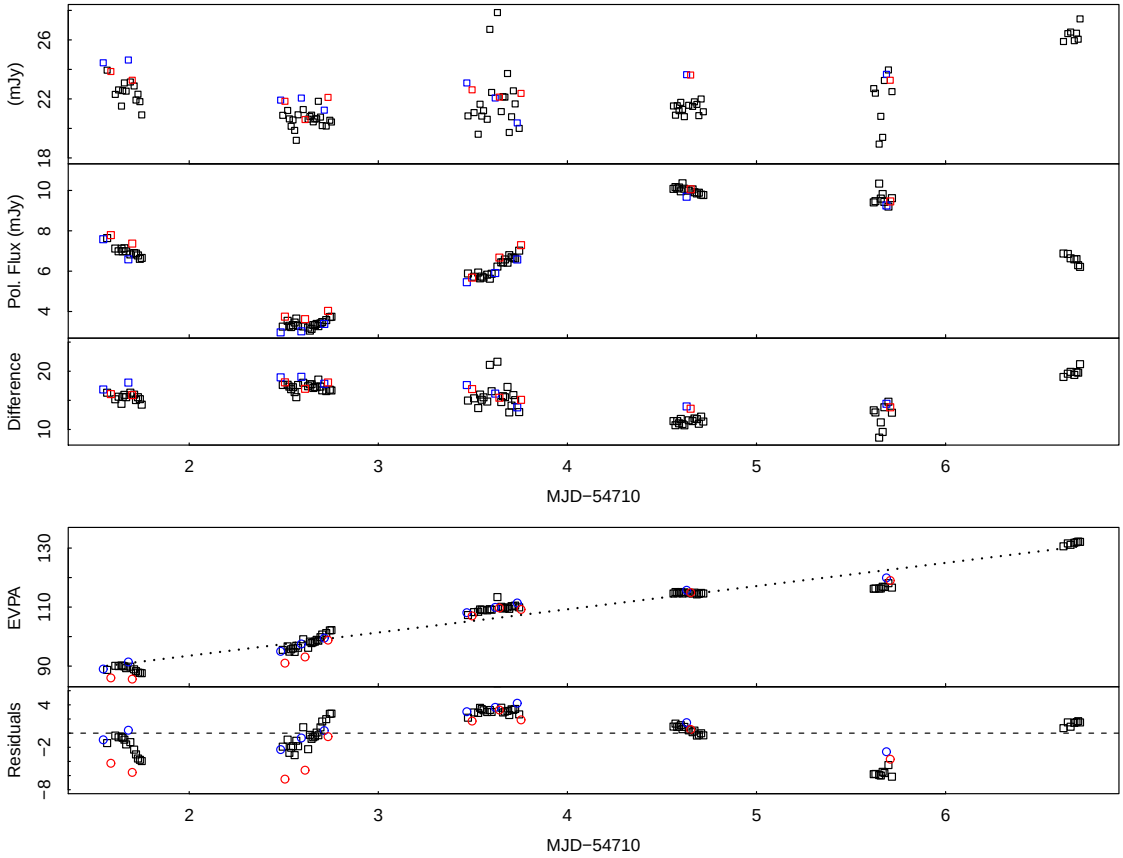

Figure 6.6: Multiband optical lightcurves for PKS 2155-304 in optical. The first three panels show: the host-corrected photometric flux *(top)*, the total polarised flux *(middle)*, and the unpolarised flux, corresponding to the difference between the two previous panels *bottom)*. The last two panels show the EVPA *(top)* and the residuals of the subtraction of a constant-rate rotation trend of $\approx 7^{\circ}$ per day to the overall position angle behaviour *(bottom)*. Observe that the deviations from a constant trend are highly significant and do not follow any clear "sinusoidal" or oscillatory behaviour around the mean. Black points correspond to R-band measurements, blue points to the V-band and red points to the I-band.

smoothly between 3-11% along the six nights of observations, within the range typically registered for this source and similar to that seen for the radio core. A very similar "oscillatory" behaviour for the polarisation fraction can also be seen in the optical light-curves of Courvoiser et al. 1995 [113], but the behaviour of the polarisation vector is very distinct at both epochs.

Figure 6.6 presents a more detailed look into the photometric and polarisation light-curves of the source, now with all the quantities corrected for the host-galaxy contribution. As pointed out before, the polarised flux variability is dominated by the long-term changes in the polarisation degree. Subtraction of the polarised component of the photometric flux shows that a significant fraction of the optical variability comes from changes

in the polarised flux, but that this cannot entirely account for the changes registered for the source. This means that there is substantial evolution of the unpolarised flux that is contributing to the optical variability. Such changes could in principle be either from a *completely* unpolarised component or result from variations in one or more *partially* polarised components, and its origin can only be clarified within the framework of a comprehensive model for the emission. It is nevertheless important to note that dilution of a constant polarised component on a variable, unpolarised background cannot account for the observed behaviour of the polarisation degree, which changes in an uncorrelated fashion with respect to the total flux, specially when the day-to-day variations are considered. This fact alone argues against the presence of an unpolarised background dominating the variability.

Finally, throughout our observations the EVPA underwent a quasi-linear counterclockwise rotation of about 40°, at a rate of $\approx 7°$ per day. The deviations of the EVPA rotation from a strictly straight-line (see the bottom panels of Figure 6.6) are not compatible with a "sinusoidal" or regular oscillatory variation about the mean linear trend. These oscillations also lack any clear correlation with the flux or polarisation behaviour (e.g., the "oscillations" seem in the polarisation degree and the EVPA are out of phase), suggesting they are probably not linked to geometrical changes in the viewing angle of the emitting region, which would imply corresponding flux variations due to aberration effects. The evident lack of correlation between the evolution of the polarisation parameters and the flux behaviour is a common property in many BL Lac observations in the optical bands [269], and must be explained if we are to attain a satisfactory model of the source.

6.4.1 Modelling of the Polarised Emission

Given the structural complexity of BL Lacs, with extended and inhomogeneous jets and different possible regions contributing to the emission at optical or near-optical wavelengths (such as accretion disc, BLR, etc.), the study of its variability is greatly complicated by the impossibility of spatially resolving the different parts of the system. In fact many different regions of the AGN are thought to be contributing to the source's emission simultaneously. The temporal variability of the emission is thus the best way in which

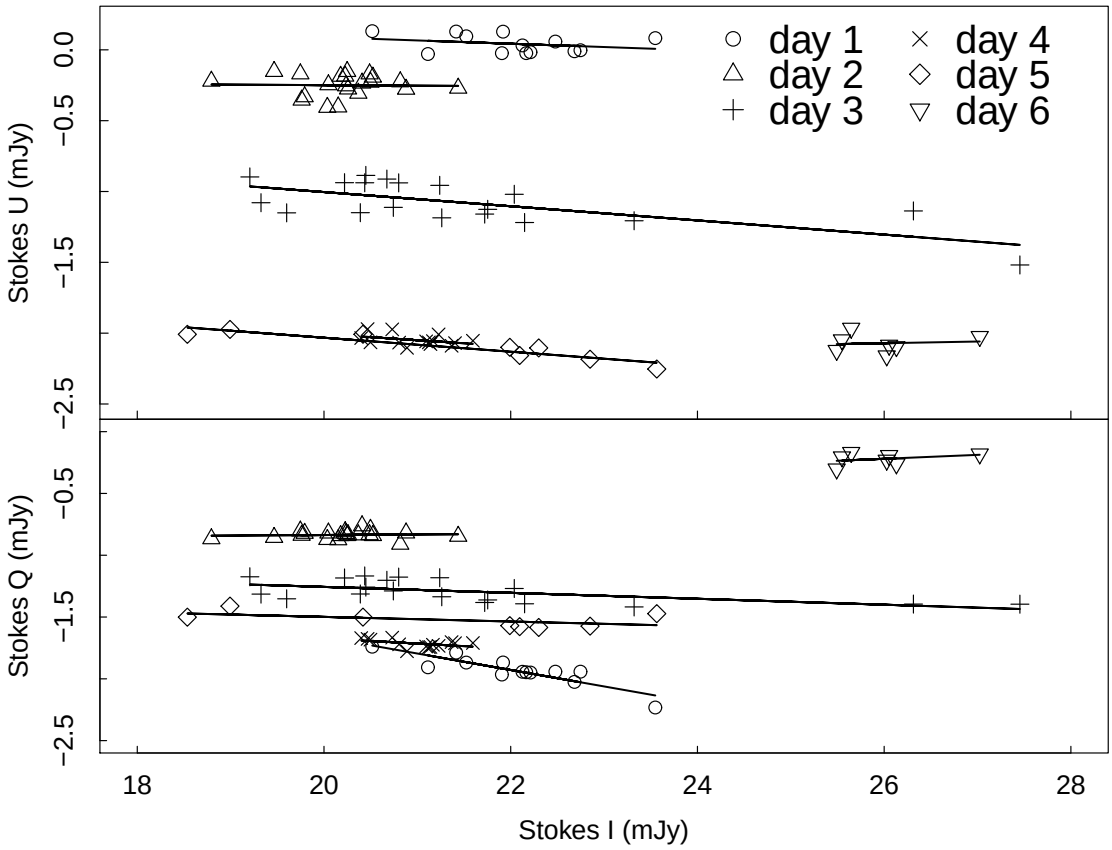

Figure 6.7: Polarised versus total flux relation for the six nights of the optical campaign. The straight lines are fits to the data used to derive the polarisation properties of the variable component. Error bars are of the order of the size of the points and are not apparent in this plot.

valuable information about the internal structure of the source can be extracted from the observations, and a better picture of the objects can emerge. Multiwavelength data greatly adds to such studies, and the presence of polarimetric information introduces an additional layer of constraints on the distinction between multiple active emission sites.

As presented in Section 2.2.1, the state of the linearly polarised radiation is fully described by the Stokes parameters I, Q and U. Without loss of generality, we can decompose the emission as the superposed contribution of a variable and a constant component, by writing $I = I_{\rm var} + I_{\rm cons}$, as proposed by Hagen-Thorn and Marchenko 1999 [186]. From this follows:

$$Q = Q_{\rm var} + Q_{\rm cons} = I_{\rm var}\,(p_{\rm var}\cos 2\chi_{\rm var}) + Q_{\rm cons} \tag{6.9}$$

$$U = U_{\rm var} + U_{\rm cons} = I_{\rm var}\,(p_{\rm var}\cos 2\chi_{\rm var}) + U_{\rm cons} \tag{6.10}$$

where $Q_{\rm cons} = I_{\rm cons}\ p_{\rm cons} \cos 2\chi_{\rm cons}$ and $U_{\rm cons} = I_{\rm cons}\ p_{\rm cons} \cos 2\chi_{\rm cons}$ are the non-variable Stokes parameters of a constant emission component, which one could think as emission from the extended source. If the terms in parenthesis in the above expressions are also constant in time, and only the photometric flux I_{var} varies, then these relations represent a straight line in the Q-I and U-I planes. Any temporal changes in the polarisation degree are in this case the result of variations on the flux of a polarised emission component, whose polarisation properties are kept constant in time. In fact, the terms in parenthesis correspond to the normalised Stokes paremeters of the variable component, $u_{\rm var} = U_{\rm var}/I_{\rm var}$ and $q_{\rm var} = Q_{\rm var}/I_{\rm var}$, which must naturally obey to the relation $q_{\rm var}^2 + u_{\rm var}^2 < 1$. Therefore, from the linear fits to the variability data in the Q-I and U-I planes, the polarisation properties of the variable component can be directly and univocally derived.

If the polarisation properties of this variable emission source were also time-dependent, then the flux measurements would not obey a linear relation in the Q-I and U-I planes, unless there existed an inversely proportional dependence between the flux and the polarisation degree of its emission. This relation, if rather unphysical for a single source, could in principle be achieved by the superposition of two or more variable synchrotron components, but not without a careful fine-tuning that renders it improbable. A linear temporal relation between the Stokes parameters Q, U and I can therefore be taken as firm indication of the presence of a *single variable* synchrotron component with *constant* polarisation paremeters being responsible for all the variability observed from the source, within the correspondent time interval of the observations.

As discussed by [186], this analysis is therefore a powerful test for understanding the intrinsic source structure as it allows the separation of the different components that together contribute to the emission, providing a hypothesis under which to construct a model or scenario for the source. Figure 6.7 shows that although the aforementioned relation is not obeyed by the entire dataset collectively, intranight measurements taken individually clearly follow a linear trend. This suggests that the flux microvariability could be either the result of a single variable component whose Stokes parameters evolve on longer timescales than those of the intranight monitoring, or represent the manifestation of several different components with different polarisation properties dominating the emission on each night. The smoothness of the temporal evolution of the polarisation parameters

Table 6.4: Polarisation parameters of the variable component.

MJD	$p_{\rm var}$ (%)	$\theta_{\rm var}$ (°)	$I_{\rm var}$ (mJy)
54711	12.5 ±1.3	84.9 ±5.6	2.3 ±0.6
54712	1.0 ±0.6	70.0 ±12.0	2.0 ±0.2
54713	5.6 ±1.4	102.2 ±7.0	3.8 ±0.6
54714	7.5 ±1.4	120.1 ±6.4	1.8 ±0.8
54715	6.8 ±1.3	123.6 ±6.2	5.8 ±0.8
54716	3.4 ±1.9	125.4 ±6.5	7.5 ±1.0

seen in Figure 6.4 seems nevertheless to disfavour the presence of a great number of components, each active at different times. In particular, the fact that the polarisation properties of PKS 2155-304 change more slowly than the total flux argues against the polarised flux being the resultant contribution of a large number of independent components.

From the fits to each set of intranight measurements presented in Figure 6.7, relative Stokes parameters were determined as the slopes of the lines and these were used to model the polarisation properties for the variable component, $p_{\rm var}$ and $\theta_{\rm var}$, presented in Table 6.4. Although an appropriate physical description for this variable component has not yet been given, the observational motivation behind its identification is to single out a particular region of the source through which *all* photo-polarimetric variability can be explained and to then test this hypothesis by means of a more formal modelling of the emission.

The polarisation degree of the variable component as determined from Figure 6.7 varied in the range 1-13% during the campaign, reaching a minimum on the second night, when its intrinsic polarisation almost disappeared. Although the temporal evolution of $p_{\rm var}$ and $\theta_{\rm var}$ broadly follows the same trend of the integrated source's polarisation, it does not match exactly the observed parameters in Figure 6.4. This mis-match in the polarisation properties suggests the presence of another polarised component by which this variable emission is "diluted". This is particularly evident from the fact that the EVPA derived for the variable component does not agree with the values measured for the source's polarisation angle at all epochs.

The interplay between a *constant polarised* component, associated with the underly-

ing jet, and a *variable* one due to the propagation of a relativistic shock inside the jet, has been proposed by a number of authors to explain a variety of variability behaviours in blazars (e.g., [201], [296], [92]). Given the scarcity of multi-band data we will seek here to model solely the data from the R-band. The polarisation properties of the superposition of two optically thin synchrotron components can be directly derived from Equations 2.33, noticing the scalar additivity of the Stokes parameters:

$$p^2 = \frac{Q^2 + U^2}{I^2} = \frac{(Q_{\rm var} + Q_{\rm cons})^2}{I^2} \tag{6.11}$$

$$\tan(2\chi) = \frac{U}{Q} = \frac{U_{\rm var} + U_{\rm cons}}{Q_{\rm var} + Q_{\rm cons}} \tag{6.12}$$

where $I = I_{\rm cons} + I_{\rm var}$, and Q and U are defined as $Q = I\ p \sin(2\chi)$ and $U = I\ p \cos(2\chi)$. From this results [201]:

$$p^2 = \frac{p_{\rm cons}^2 + p_{\rm var}^2\ I_{\rm v/c}^2 + 2\ p_{\rm cons}\ p_{\rm var}\ I_{\rm v/c} \cos 2\xi}{(1 + I_{\rm v/c})^2} \tag{6.13}$$

$$\tan 2\theta = \frac{p_{\rm cons}\ \sin 2\theta_{\rm cons} + p_{\rm var}\ I_{\rm v/c}\ \sin 2\theta_{\rm var}}{p_{\rm cons}\ \cos 2\theta_{\rm cons} + p_{\rm var}\ I_{\rm v/c}\ \cos 2\theta_{\rm var}} \tag{6.14}$$

where $\xi = \chi_{\rm cons} - \chi_{\rm var}$ and $I_{\rm v/c}$ is the ratio of fluxes of the variable and constant components.

In order to determine the values for the parameters of the constant component and the ratio of fluxes $I_{\rm v/c}$, a procedure similar to that of Qian 1993 [296] is followed. Given the uncertainties in $p_{\rm var}$ and $\chi_{\rm var}$, and the complex trigonometric relations in Equations 6.14 which prevent a straightforward analytical solution, the fitting process had to be done iteratively. The second night, where the contribution of the variable component was likely to be the smallest, was chosen as the starting point, and the model above was used to find the best fitting values for the parameters p and χ for both the variable and constant components. This was done automatically, searching the entire parameter space and looking into minimising the model residuals. This procedure gave an estimate for the flux level of the constant underlying jet component, $I_{\rm cons} \approx 20$ mJy. Its polarisation degree p_{cons} was also estimated from the same dataset to be $\sim 3\%$. The best fit value for $\chi_{\rm cons}$ corresponding to these polarisation parameters was of $\approx 120°$. Analysis then proceeded by applying

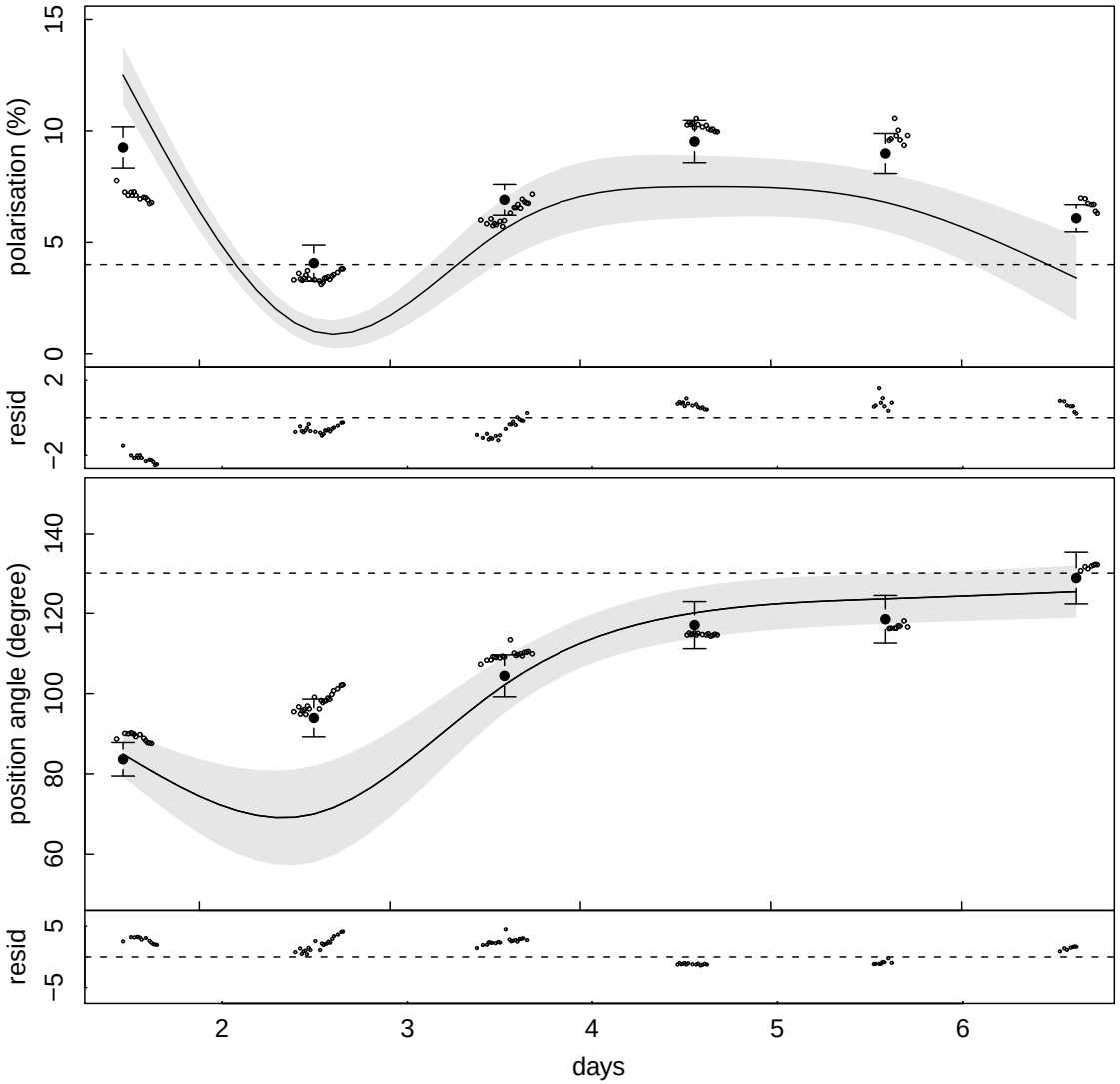

Figure 6.8: Results of the two-component synchrotron model fitted to the optical polarimetric observations of PKS 2155-304. Small points correspond to the observational data points and the large filled circles are the model calculated values for each night of the campaign, using the parameters of variable and constant component as present in Table 6.4 and in the text. The model points were obtained using the law of superposition of two polarised components, described by Equation 6.14. The smooth solid line is a spline interpolation through the parameter values for the variable component, and illustrate its temporal evolution. Grey shades represent the confidence intervals, calculated according to the errors in Table 6.4 and extended according to a spline interpolation. Dashed lines represent the best-fit value for the constant component to each parameter. The small plots below each of the main graphs are the residuals of the model fit to each night. Notice that since the model fit is for the nightly averages, it is not intended to account for the intranight variability in the polarisation parameters. The plot for the polarisation angle clearly shows the gradual alignment of the variable component to the direction of the constant component. Observe as well that the start of this gradual alignment coincide with the increase in the percentage polarisation of the variable component, which grows and then fades on the final night of the campaign, and is responsible for the observed variability of the source's polarised flux

this set of values as a starting point to fit each individual night. The parameters of the constant component were allowed to vary within the same error range of those of the variable component as quoted in Table 6.4, since they limit the accuracy to the model fitting. The values of the variable component which minimise the residuals while keeping these pre-determined bounds, i.e. $I_{\rm cons} \approx 18 - 22$ mJy, $p_{\rm cons} \approx 1 - 5\%$ and $\chi_{cons} \approx 110 - 130^{\circ}$ were looked for in each night's data.

A good indication of the appropriateness of this model in describing the entire dataset is that a reasonable fit for each night was obtained without the need for the parameters of the constant component to greatly depart from the 1σ error bounds mentioned above, which can be regarded as reflecting the accuracy of the measurements. Final confidence intervals for the polarisation parameters of the constant component were estimated from the night-to-night variations in its best-fit parameters, and are given by $p_{\rm cons} = 4 \pm 2/10^{\circ}$. They are therefore compatible with a set of constant parameters throughout the campaign within the observational errors. This best-fit model is shown in Figure 6.8. For all nights $I_{\rm v/c} < 1$, indicating that the background component dominates the photometric flux emission. The values of $I_{\rm var}$ derived for each individual night are presented in Table 1, corresponding to 15-45% $I_{\rm cons}$, and the temporal evolution of both modelled components is also shown in Figure 6.8.

The derived parameters for the constant component are found to match the regular values of the polarisation parameters compiled in [333] for PKS 2155-304, suggesting its association with a persistent optical jet component. The degree of polarisation $p_{\rm cons}$ is also similar to the minimum values measured for this source at 43 GHz and in historical optical data, and the corresponding position angle is well-aligned with the radio-core EVPA as determined by Piner et al. (2008) [291]. This coincidence also attests to the presence of a field component in the jet which is common both to the radio and optical wavelengths and persistent in time, and whose direction is transverse to the flow, as expected from a shock-compressed tangled field.

From the second night of the campaign onwards, the position angle of the variable component rotated continuously from 70° (i.e. approximately 90° mis-aligned with the jet-projected P.A.) to 120°, in close alignment with the direction of the persistent jet component. The rotation of $\chi_{\rm var}$ could be interpreted as the gradual alignment of the field of

a new "blob" of material encountering a shock in the core that re-organises its field. The maximum value observed for the source's polarisation degree coincides with the epochs of greatest alignment between the two fields, and the start of the rotation in $\chi_{\rm var}$ marks the onset of the increase on the baseline photometric flux seen towards the end of the campaign. Such a scenario, where both optical position angles $\chi_{\rm var}$ and $\chi_{\rm cons}$ tend to align with the direction of the radio EVPA when the observed polarisation is high, was considered before by Valtaoja et al. 1991 [340] for the quasar 3C 273 during a radio-to-optical flare. In such a scenario a correlation is expected between the optical and polarised fluxes which is marginally observed in our dataset, and more observations of more active states are necessary to better establish the validity of the correlation for this object.

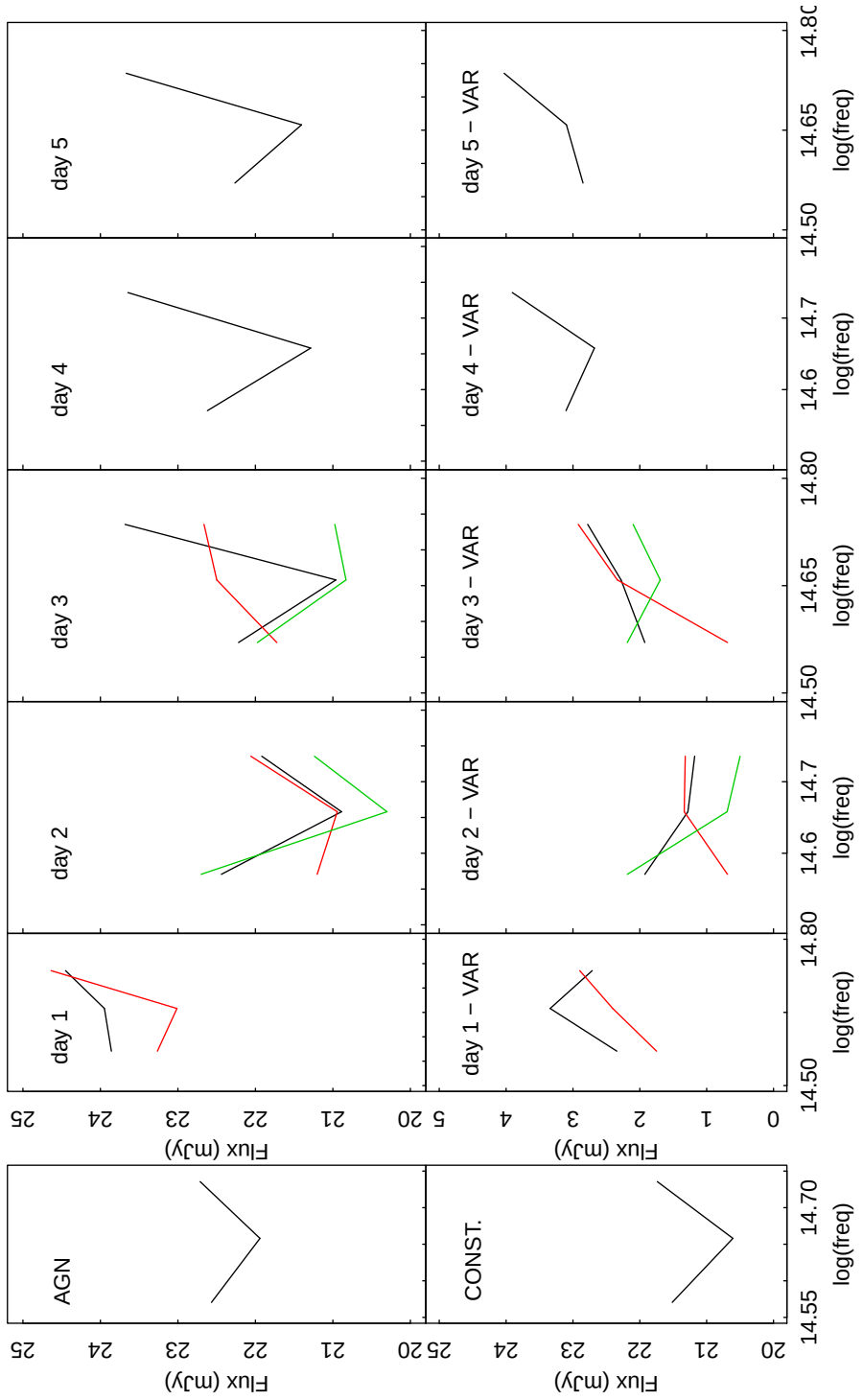

Figure 6.9: Optical spectra of PKS 2155-304 for the 5 days of the optical campaign with V, R and I multiband information. The two left hand side plots show the host-galaxy subtracted average intrinsic spectrum of the source (*top*) and the spectrum of the constant component associated with the extended jet in the model of Section 6.5 (*bottom*). The remaining plots show the total intrinsic spectra for each day (*top*) and the spectra for the variable component alone (*bottom*). Notice the presence of strong intranight spectral variability, associated with the flux microvariability discussed in Section 6.4.2 and the evolution of the variable component, which presents an increase in flux towards the final days of the campaign, accompanied by an increase in the relative amount of flux in the V band relative to the I band.

6.4.2 Origin of the Flux Variability

As noted before, the observed flux variability happens on two different timescales, its amplitude being dominated by intranight variability, superimposed on a background level that steadily increases towards the end of the campaign, and which we have associated with the evolution of a variable (or shocked) component in the model of the previous section.

Microvariability

To try to identify the physical origin of these variations and in particular the nature of the flux microvariability, we observed that the intranight flux changes were accompanied by changes in the spectral index. The daily evolution of the source's spectra, as measured in the V, R and I bands, can be seen on Figure 6.9. The source presented colour variations both in intranight timescales and in the nightly averages. The intranight $(V-I)$ colours varied in the range 0.12-0.27, with greatest amplitude in the third night of the campaign, when the variability was the greatest. Colour variations can be linked to radiative cooling of electrons in a magnetised plasma, implying synchrotron lifetimes of the order of the intraday timescales of a few hours. The synchrotron lifetime in the observer's frame, written in terms of the observed photon frequency in units of GHz, ν_{GHz}, is given by (see Chapter 3):

$$t_{\rm sync} \approx 1.1 \times 10^4 \left(\frac{1+z}{\delta\, \nu_{GHz}\, B_G^3} \right)^{1/2} \quad \text{hours} \tag{6.15}$$

For $t_{\rm sync}$ equal to the timescale of intranight variations in the R band, and using typical Doppler factors for PKS 2155-304 of about $\delta \sim 30$ (e.g., as for the compact components in Katarzyński et al. 2008 [222]) we obtain a magnetic field $B \lesssim 0.5$ G for the variable component. The fact that we see changes in the $(V-I)$ colours simultaneously with the intranight flux variations suggests that these can be taken as a direct signature of particle acceleration and cooling at the source, with $t_{\rm acc} < t_{\rm sync}$. An upper limit to the size of the acceleration region r_s can be set using causality arguments which bound r_s to the variability timescale $t_{\rm var}$. Taking into account relativistic effects due to the flow possessing a Doppler factor $\delta = (\Gamma - \sqrt{\Gamma^2 - 1}\, \cos\theta)^{-1}$, where Γ is the Lorentz factor with which the

emitting plasma is moving, at an angle θ with respect to the line of sight, we have:

$$r_s < \delta\, t_{\rm sync}\, c/(1+z) \approx 10^{16}\ {\rm cm} \sim 5\times 10^{-3}\ {\rm pc}. \tag{6.16}$$

Marscher & Gear 1985 [252] considered the observational properties of shock-induced variability in relativistic jets. As indicated above, synchrotron losses will determine the distance travelled by an energetic electron emitting due to interaction with a magnetic field of intensity B. In the optically thin regime the radiating frequency of the electron is $\nu_{GHz} \gtrsim \nu_*$, the turn-over frequency of the synchrotron spectrum due to self-absorption. The co-moving distance x in which the electron radiates most of its energy is given by:

$$x \approx 0.4 B^{-3/2} \nu_{\rm GHz}^{-1/2} \left[\frac{\delta}{(1+z)}\right]^{1/2} \beta_{\rm rel} \quad {\rm pc}, \tag{6.17}$$

where $\beta_{\rm rel}$ is the velocity of the shock front in the frame of the shocked gas (typically ~ 0.1, for a post-shock Lorentz factor $\Gamma_s \sim 1.1$). For such values, the co-moving distance is very similar to the radiating distance in the observer's frame $x_{\rm obs} \sim \Gamma_s\, x$, and therefore the minimum variability timescale (for a given observing frequency ν) associated with the synchrotron cooling is given by:

$$\Delta t \sim \frac{x}{c}\,\frac{(1+z)}{\delta} \sim 0.03\, h^{-4} \left(\frac{\nu}{\nu_*}\right)^{-1/2} \quad {\rm days}, \tag{6.18}$$

where $B \sim 0.5$ G and $\delta \sim 30$ are adopted, for a redshift of 0.116. Here, $h \sim 0.72$ [159] is the Hubble parameter, introduce in the cosmological time-dilation in relation to the luminosity distance of the object. Adopting a turn-over frequency for PKS 2155-304 of $\nu_* \lesssim 15$ GHz, corresponding to the longest-wavelength from which optically thin radiation was observed by VLBI from the radio core (see [290] and [291]), we have $\Delta t_{var} \sim 1$ hour, in the R-band. This variability timescale corresponds to a shock thickness of

$$x \sim 2\times 10^{-4} h^{-5} \left(\frac{\nu}{\nu_*}\right)^{-1/2} \simeq 5\times 10^{-3} \quad {\rm pc}. \tag{6.19}$$

This value, being of the same order of the estimates based on the R-band intranight flux variations, points to an origin for the flux microvariability as the result of particle

acceleration taking place at a shock front, with high magnetic field due to plasma compression. Magnetic fields of the order of the ones estimated here ($B \lesssim 0.5$ G) have also been considered by Marscher & Gear 1985 [252] as typical estimates for the field intensity in blazar cores, and are of the same order of magnitude of those recently found to explain the low-activity state of Fermi/LAT-detected blazars [145]. In the SED model of Katarzyński et al. 2008 [222] such values for the B-field and Doppler factor are also associated with the variable shocked components, as opposed to the extended jet which had lower values for both parameters.

Internight Variations

In the model presented in Section 6.5, the long-term increase of about 5 mJy in the "baseline" flux level of the variable component towards the end of the campaign was associated with a flux increase of the variable component. The intrinsic (host-corrected) average nightly $(V-I)$ colours for the source varied between -0.17 to -0.01 mag, and were bluest towards the end of the campaign, correlating with the increase observed in the baseline photometric flux level. If we assume that the intrinsic colours observed for the second night (when the source's flux was the lowest; $(V-I)_{\rm cons} = -0.01$) are representative of the colours of the extended jet component, then we can explain the changes in the average nightly colours as the superposition of a redder, stable spectral component (due to the jet) and a bluer one, variable on both intranight and internight timescales, and due to the shock. In this case, the changes in colour by $\Delta(V-I) = -0.16$ mag, associated with the brightening of the source during the last nights of the campaign would be due to the relative increase in the flux of the variable component, as expected from the evolution of a growing shock. The scenario is clearly illustrated in Figure 6.9 where the evolution of the variable component is shown as presenting a brightening in the total flux towards the end of the campaign, accompanied by an increase of flux in the V band relative to that of the I band. This evolutionary trend of the spectrum is compatible with the idea of a shock growing in intensity towards the end of the campaign due, for example, to the increase of the magnetic field intensity or the particle density, both factors that enhance the synchrotron emissivity of the source.

6.4.3 Magnetic Field Structure

Synchrotron emission from an optically thin plasma will produce radiation that is naturally linearly polarised, with a degree of polarisation which is dependent on the following quantities, integrated within the resolved dimensions of the source: the amount of ordering of the magnetic field, its spatial orientation and the pitch-angle distribution of the radiating electrons, the latter assumed to be uniform, as discussed in Chapter 3. In the optically thin regime, the polarisation is a direct indicator of the state of the magnetic field B inside the emission volume. If the source is inhomogeneous its observational properties will result from the integrated characteristics of all different emitting regions, and will generally lead to a decrease of the net polarisation degree while revealing the scale of any large-scale anisotropy or symmetry in the structure of the magnetic field [217]. Furthermore, any asymmetry in the physical properties of the source, such as a jet viewed slightly off-axis, will naturally introduce a net polarisation due to the geometrical and projection effects even if the source possesses an isotropically tangled field structure, for example (see discussion in [327] and references therein). Wavelength or time-dependent polarisation properties will result from inhomogeneities and can be used to trace the internal structure of the source. Turbulence in the flow is one such possible source of inhomogeneities, affecting the magnetic field structure and breaking its overall coherence beyond some characteristic sizescale l_B [218].

Polarisation Variability

The absence of correlation between the variations of the polarisation degree and photometric flux and in particular the lack of counterparts in the polarisation degree for the microvariability suggests that the timescales of evolution of the magnetic field are decoupled from those of particle acceleration by the shock.

To investigate the magnetic field structure in our shock-in-jet scenario, we follow a stochastic analysis proposed by Jones et al. 1985 [217]. He shows that the spatial scale of magnetic field disorder l_B can be directly estimated from the intrinsic degree of polarisation of the source κ, after correcting for the contribution of any unpolarised emission. Here we adopt the properties of the underlying component in the model of Section 6.5 as representative of the underlying jet parameters. We take the internight

scatter in the polarisation degree to be of the order of the uncertainty in the parameter p_{cons}, that is $\delta p \sim 2\%$. We may then model the polarised flux at a given wavelength as coming from statistically independent regions, distinguished by the coherence length of the field. We can estimate the coherence length of the large-scale field as being

$$l_B = \left(\frac{\kappa\,\Pi_0}{\delta p}\right)^{-2/3} l \sim 0.15\,l, \tag{6.20}$$

where $\Pi_0 = 0.7$ is the polarisation fraction of a perfectly ordered field region, and l is the size of the emitting source. If the optical emission comes from a region with size of the order of the VLBI radio core, then $l \approx 1$ mas [291] and $l_B \approx 0.3$ pc.

Geometry of propagation of relativistic shocks This linear scale can be compared with shocked-jet models [252], in which variations are linked to the distance along the jet travelled by the relativistic shock in the time between two extrema of the light curve. The geometry of the shock propagation was studied by Rees in 1967 [300]. Suppose that an observer sees a variable cosmological source at a redshift z, so that the measured variability timescales are correspondingly dilated by a factor $(1 + z)$ from the intrinsic variability scale Δt.

If the shock follows the material ejected isotropically from the source with relativistic speed $\beta \sim 1$, the direction of motion of each point in the expanding sphere relative to the line of sight will introduce an aberration to the shape of the surface occupied by the ejecta which is proportional to the Doppler shift. The surface at time t will be given by $r = c\,\beta\,t/(1 - \beta\cos\theta)$. Note that, analogous to what is seen in the kinematics of superluminal motion, the fastest apparent velocities are for angles to the line of sight $\sim \arccos\beta$, and that these velocities, being equal to $c\Gamma$ – where $\Gamma = (1 - v^2/c^2)^{-1/2}$ is the Lorentz factor of the flow – can greatly exceed c. Variability events can therefore be observed in the light-curves of relativistically propagating emitters which are related to intrinsic structures of the source that are larger than the corresponding light-travel time arguments would imply (see [331] and references therein). The locus at time t of material ejected with a Doppler shift δ can then be written as [300]

$$\left(\frac{R}{t}\right) = \frac{\delta\,\Gamma\,c\,\beta}{(1+z)}, \tag{6.21}$$

and so an observed variability timescale Δt corresponds to a propagation distance in the source:

$$\Delta R = R_2 - R_1 = \frac{\delta_s \, \Gamma_s \, c \, \beta_s \, \Delta t}{(1+z)}, \tag{6.22}$$

where the subscript refers to the shock parameters.

Interpretation of the polarisation lightcurve Using values derived by [290] and [291] for the shock speed ($\beta_s = 1-4$), bulk Doppler factor ($\delta_s \sim 3$) and Lorentz factor ($\Gamma_s \approx 3$), and taking $\Delta t = 2$ days, the timescale between extrema in the polarisation lightcurve, we obtain $\Delta R \approx 0.3$ pc for the distance travelled by the shock. This distance, being consistent with the field turbulence scale l_B, suggests a connection between the internight variations observed in the polarisation degree and the spatial changes in the magnetic field, induced by inhomogeneities in the jet. As pointed out by Qian et al. 1991 [295], if these inhomogeneous structures are "illuminated" by the shock through amplification of the magnetic field and increased electron density, they will induce changes in the integrated polarisation parameters. The timescales for these variations are thus not necessarily associated with the fast variations in flux observed due to particle acceleration and cooling at the shock front. On the other hand, the increase in the total optical flux that is seen towards the final nights of the campaign can still be associated with these inhomogeneities since changes in the electron density or in the strength of the shock as it progresses through regions of evolving magnetic field properties can enhance the emissivity of the variable component.

In three recent papers (see [261], [262] and [263]), McKinney performed general-relativistic MHD simulations of jets which show the development of current-driven instabilities beyond the Alfven surface (10^3 gravitational radii, r_g). His simulations show that these instabilities can induce the formation of structures in the jet (which he called "patches" – see Figure 6.10) characterised by an enhanced Lorentz factor and distinct physical properties to the rest of the jet, such as magnetic field and particle density, which can drive internal shocks. The typical sizes of these "patches" in the jet can be as large as $\sim 10^3 r_g$, which in the case of PKS 2155-304 is equivalent to 0.1-0.2 pc, and thus not very different from the estimated coherence length of the field derived above. If such structures indeed develop in the inner regions of AGN jets, they could provide the right scale of in-

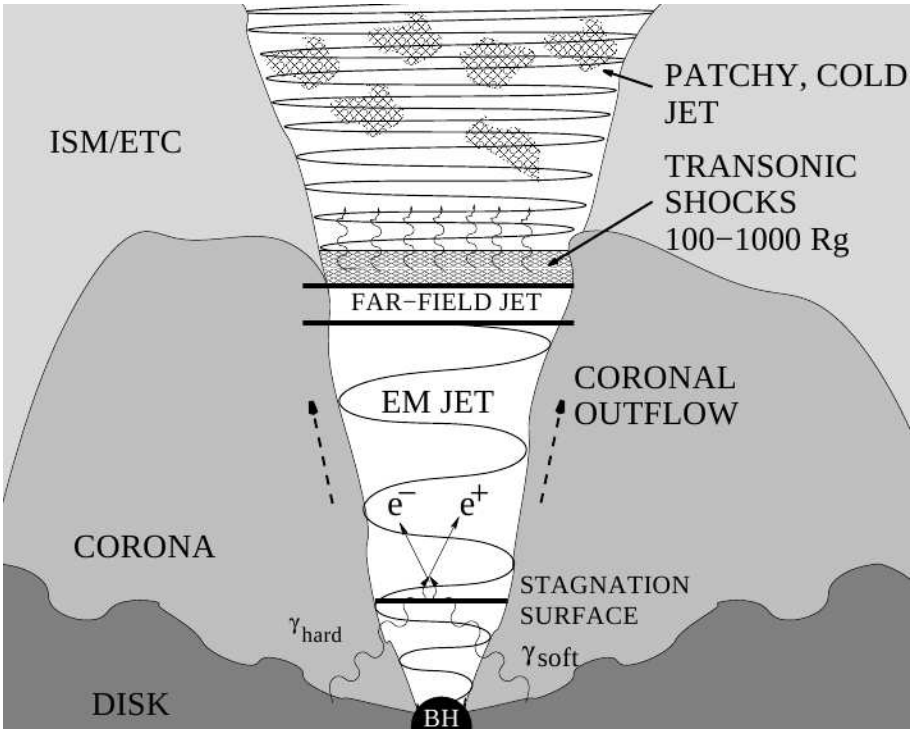

Figure 6.10: Schematic picture of AGN jet model and shock-heating radiation emission, as proposed by J. McKinney (2005) [262]

homogeneities necessary to explain the variations in flux and polarimetric properties that we observe as the timescale necessary for the shock to traverse one of these "patches".

In the picture presented here, particle acceleration and cooling happening at the shock front are responsible for the fast flux variability. Variations in the polarisation degree are associated with the propagation of this same shock through an inhomogeneous plasma, compressing and re-ordering its otherwise tangled field [234]. The longer timescales for the change of the polarisation degree thus result from the shock encountering portions of the jet which have different magnetic field properties, leading to a changing ratio of ordered to chaotic magnetic field intensity, as derived from the integrated source emission. It is important to stress that this scenario can naturally explain the lack of correlation between the photometric and polarised fluxes whilst associating the origin of both phenomena with the same physical region, namely an evolving shock. If the scenario proposed is correct, than polarimetric properties can serve as important diagnostics of the structure of the magnetic field in the source, on scales that are directly related to those of the variability of the polarised flux and thus capable of providing tighter constraints on the location and nature of the emission sites.

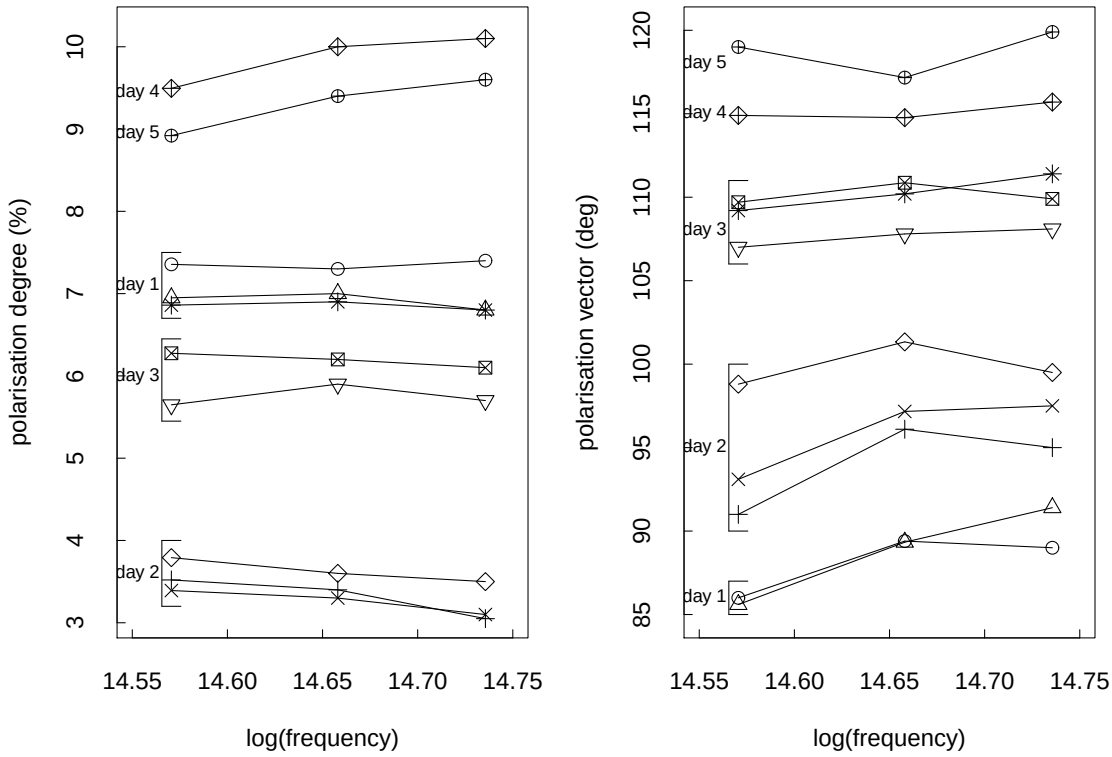

Figure 6.11: Frequency dependence of polarisation degree (FDP; *left panel*), and frequency dependence of polarisation angle (FDPA; *right panel*). Each sequence of points of the same type is connected by a solid line and represents quasi-simultaneous I, R and V measurements of the polarisation quantities. The annotations to the left of the data points indicate the dates of the campaign corresponding to each set of measurements. On the *left panel*, the vertical scale orders the measurements according to total intensity of polarisation and show that FDP increasing with frequency is present at high polarisation levels. The *right panel* shows that FDPA is present only in the first few nights, when the discrepancy between the polarisation angle of the constant and variable component is greater. In the later dates of the campaign, as the contribution of the variable component to the polarised flux increases and becomes dominant, FDPA vanishes.

6.4.4 Frequency Dependent Polarisation

Spectral dependence of the polarisation parameters is a common feature of blazars and its study gives information about the structure of the synchrotron source. To search for the presence of FDP we use the I and V band measurements taken at the beginning and end of each night, within approximately 30 mins of observations in the R-band. Ginzburg & Syrovatskii 1965 [175] showed that the polarisation of radiation from a homogeneous synchrotron source with a power-law distribution of electron energies is frequency-independent, and so the presence of FDP is indicative of inhomogeneities in the particle distribution or magnetic field structure of the source (see also [83]). Curvature in the spectrum of electrons or the superposition of two or more independent components

with different spectral indices would also naturally lead to FDP (Nordsiek 1976 [279]). For technical details and theoretical demonstrations of some of these facts, please refer to Chapter 3.

FDP can be manifested in relation to both the polarisation degree and the polarisation vector (FDPA), but our dataset contains little systematic indication of the latter (see Figure 6.11). An appreciable level of FDPA ($\chi_I - \chi_V \lesssim 5^\circ$) is only seen during the first and second nights of observations (please refer also to Table B.1 in Appendix B.1), after which it vanishes as the polarisation angle of the variable emission gradually aligns with the direction of the extended component. At the end of the campaign, the contribution of the variable component to the polarised flux is dominant, this being another factor which contributes to the suppression of FDPA. The temporal evolution of the FDPA is therefore a sign of the relative (mis-)alignment of the different synchrotron sources composing the source and contributing to its non-thermal emission and is an important indication of the dynamical evolution of the plasma. Note that this last observation implicitly assumes that the two components must have intrinsically different FDP so that FDPA can be manifested, and that this will usually be the case if their physical nature is different, for example for any parameters relating to the age of the two populations of radiating electrons.

The polarisation degree p has nevertheless shown significant dependence on the observing frequency, and a trend of increasing polarisation with freqeuncy is apparent when the source is at a high polarisation state (see again Figure 6.11). The magnitude of the observed FDP, measured as p_V/p_I, varied from 0.8 at low polarisation levels to 1.1 when the polarisation was the hightest. This trend in FDP has been observed before for this source and the $p(\nu) - p$ dependency was discussed in detail by Holmes et al. 1984 [201]. The authors note that this trend of increasing frequency dependence with increasing polarisation is not valid only for individual sources but is a common feature for blazars, the correlation being valid for the source populations as well. Statistical studies by these authors also showed that the dependence is stronger when $p > 10\%$, and that there is a tendency for inversion of p_V/p_I from > 1 to < 1 when the source polarisation decreases dramatically, i.e. below 5%.

No significant intranight variations in the FDP are observed, in connection with changes

in the spectral index. This can be understood from the fact that the flux of the extended component, with roughly constant polarisation and spectral properties, is dominant, and therefore masks the intranight changes which would be induced in association with flux microvariability. In fact, only for the third night, where the amplitude of the intranight variations were largest, have we seen any significant signature for intranight changes in the degree of FDP. On the other hand, when the longer-term increase in the photometric flux of the source is combined with an increase on the intrinsic polarisation degree of the variable component, as seen towards the final nights of the campaign, the dependency becomes noticeable.

It is important to stress that the data presented in Figure 6.11 are corrected for the host galaxy's contribution according to [125], and it is clear that a constant source of unpolarised emission such as the red stellar continuum cannot account for the observed time-variability of the FDP (see [323] and [324]). A similar argument can be invoked to rule out contributions from thermal accretion disc emission, whose effect would be to dilute the observed blue trend [322]. These arguments point to a FDP which is intrinsic to the synchrotron source.

In this case, a positive FDP, associated with an increase in the polarisation degree and optical flux, can be directly associated with the temporal evolution of a growing shock in the jet as discussed by Valtaoja et al. 1991 [339]. In their model, a shock is responsible for the production of highly polarised radiation with a flat-spectrum distribution that will appear superposed on the low-level polarised emission from the extended jet, which has a steeper spectrum corresponding to an aged electron population (see Figure 6.12). The newly-developed shock will therefore introduce an excess of high-frequency radiation from freshly accelerated particles which, being more polarised than the extended component, will lead to a strong FDP towards the blue, coinciding with a maximum in both flux and polarisation degree (compare the scenario presented in Figure 6.12 to the multiband source evolution as seen on Figures 6.9 and 6.11). As the shock-accelerated electrons cool, the flux decreases and the spectrum of the shocked component steepens, causing the excess contribution of the highly polarised synchrotron component to shift towards the red, supressing or changing the sign of the FDP that now is greater towards the red. Figure 6.11 shows this trend very clearly, as we observe FDP increasing towards

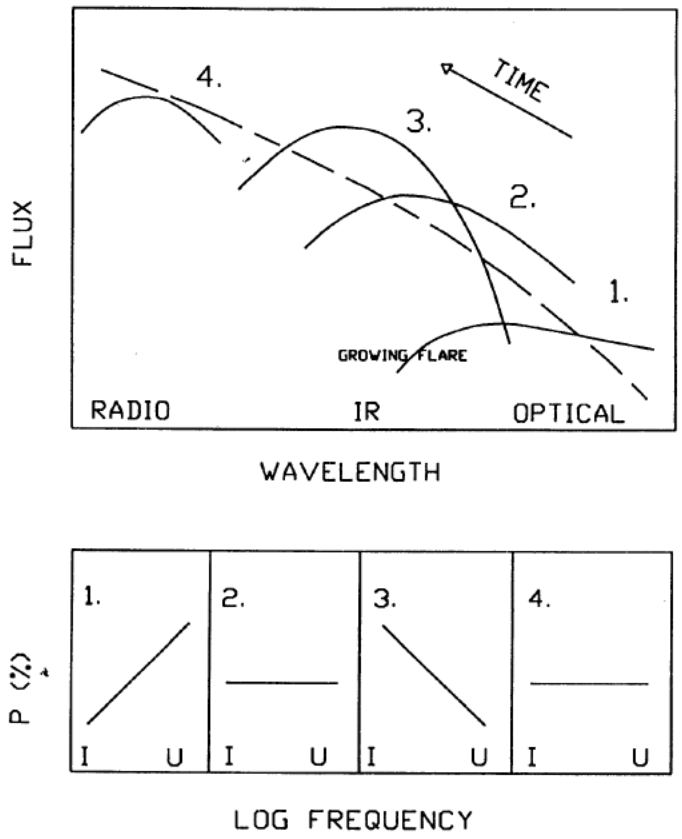

Figure 6.12: Scenario for production of variable frequency-dependent polarisation based on a shock-in-jet model of Valtaoja et al. 1991 [339]. The upper part of the figure shows the radio to optical spectrum of the jet component (*dashed line*) and the shock component during different stages of its evolution (*solid lines*). The bottom panels show schematically the resulting FDP corresponding to each of the four stages of the shock development presented. This figure should be compared to Figures 6.9 and 6.11 for a clear view of the situations at the source.

the blue during the high states which inverts towards the red when the polarised flux is minimum.

6.4.5 Timescales of Magnetic Field Evolution

Björnsson 1985 [85] suggests that multiple-component models can be regarded as an approximation to what is in reality a more complex synchrotron source whose properties vary from one point to another, and in which one or more components dominate the emission at given epochs. More insight into the structure of the source's magnetic field structure can then be obtained following an argument by Korchakov & Syrovatskii 1962 [229] which we outline below.

Changes in the degree of polarisation p of a synchrotron source are directly related

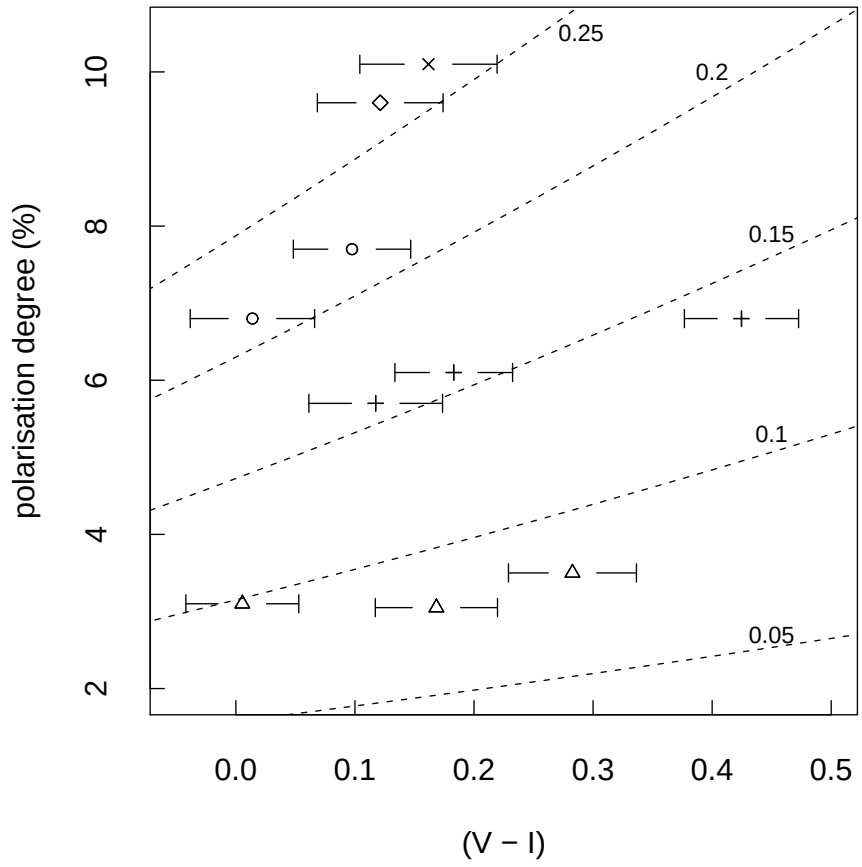

Figure 6.13: Plot of the V-band polarisation degree versus V-I spectral index. The dashed lines indicate positions of constant degree of ordering of the magnetic field B_0/B_c, as indicated by the labels. Same symbols refere to data taken during a specific night:day 1 (○), day 2 (△), day 3 (+), day 4 (×) and day 5 (⋄). No multi-band observations are available for the last night of the campaign.

to the evolution of the magnetic field structure in the emitting region, which consists of the superposition of an ordered (B_0, provided by the shock) plus a chaotic magnetic field component (B_c). Those authors show that the magntiude of p at any given time depends only on the spectral index of the emission $\alpha = (\gamma - 1)/2$ and the amount of field ordering $\beta = B_0/B_c$. At the limit of small β, we have:

$$p = f(\gamma)\beta^2 = \frac{(\gamma + 3)(\gamma + 5)}{32}\,\Pi_0\,\beta^2. \tag{6.23}$$

Here, $f(\gamma)$ is a slowly varying function of α [309], and $\Pi_0 = (\gamma + 1)/(\gamma + 7/3)$ is the polarisation degree of a perfectly uniform magnetic field. The observed range of spectral indices, resulting from the acceleration and cooling of particles in the variable shock component, imply only a narrow range for $f(\gamma)$ (= 0.5-0.8), which is in itself insufficient to

explain the entire range of variations observed in p. This means that significant internight changes of the degree of field ordering must also be present to account for the observed polarisation variability, as also expected from the discussion of an inhomogeneous jet in the previous Sections.

The variation in the degree of ordering of the field is shown in Figure 6.13, where dashed lines correspond to different fraction of B_0/B_c, calculated from the equation above. During our observations, β varied between 10-25%. Figure 6.13 also shows that values for α corresponding to the same night tend to align along the directions of constant β indicating that changes in the spectral index happen on shorter timescales than those of the magnetic field and that therefore the timescales for particle cooling and acceleration are decoupled from those of changes in B. If the ordering of the field is provided by shock compression, the relative amount of ordering can be related to the shock strength at a given instant. In this sense, one can notice that the increase in flux level seen towards the end of the campaign correlates with the two nights with higher B_0/B_c.

6.5 Conclusion: The Quiescent State of PKS 2155-304

6.5.1 Analysis of the quiescent state SED

As we discussed in Chapter 3, the broadband SED of blazars can usually be described by synchrotron self-Compton models, which seem to reproduce well the characteristics of their spectra. Implicit to these models, and a fundamental ingredient to test their validity, is the correlation expected from the time variability in the different bands of the emission across the electromagnetic spectrum. In particular, typical jet parameters usually imply that the electrons responsible for the X-ray emission are usually associated with the production of VHE emission via the synchrotron and inverse-Compton mechanisms, respectively [60]. This single-zone SSC picture has recently found difficulty in explaining the observed variability pattern of BL Lacs in a high state as revealed by simultaneous H.E.S.S./Chandra observations of a second exceptional gamma-ray flare from PKS 2155-304 [32].

Thanks to the completeness of the data coverage of this campaign both in the time and the spectral domain, we were able to test this fact in detail for the quiescent state

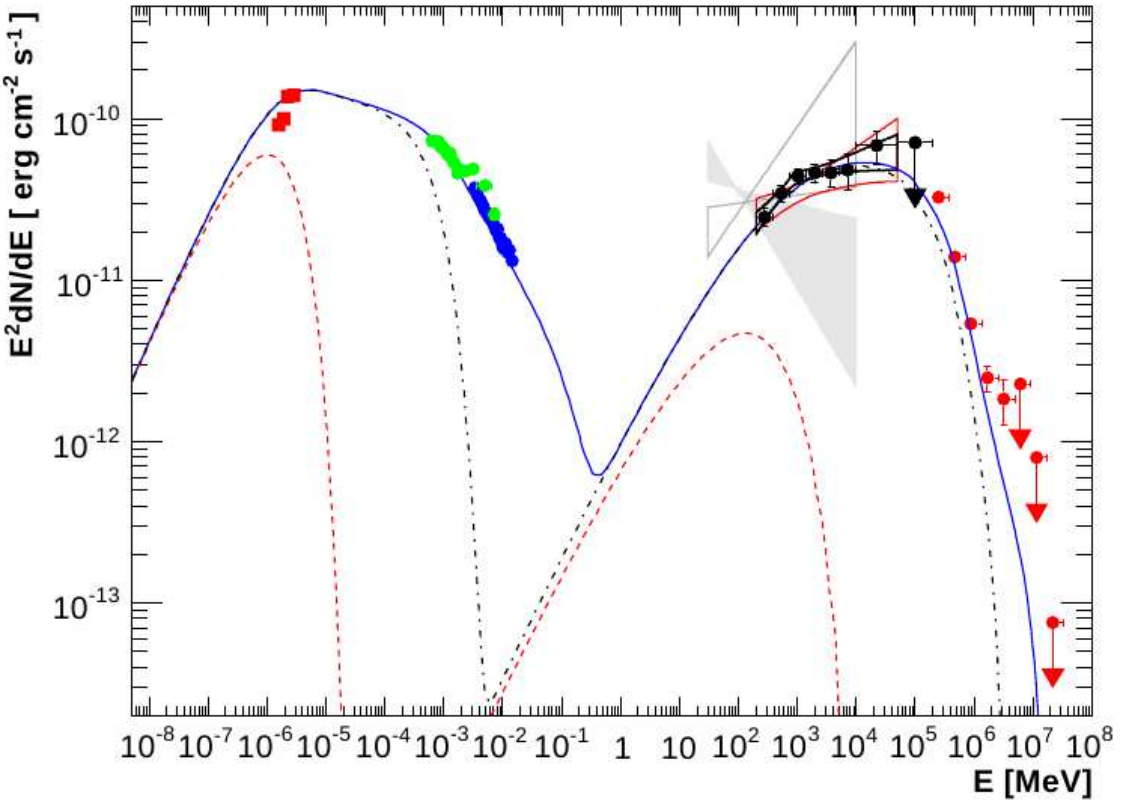

Figure 6.14: Spectral energy distribution of PKS 2155-304 during the MWL campaign. The red butterfly represents the *Fermi* spectrum from MJD 54704–54715, while the black points cover the period MJD54682–54743. The *Fermi*–LAT spectral break is strongly constrained at ~ 1 GeV. The gray butterflies are archival data from EGRET. The solid line is a one-zone SSC model fit to the time-averaged data, whereas the dashed and dot-dashed lines are the same model without electrons above certain Lorentz factors $\gamma_1 < \gamma_2$ (see text). Red squares are optical data from ATOM. Green points are *Swift*/XRT data and blue points RXTE/PCA. Red circles are VHE data from H.E.S.S. The P0.45 extragalactic absorption model used to reconstruct the H.E.S.S. spectrum at source is present at [20]. The SSC code and fits presented here were are from [35].

as well. Figure 6.14 shows a SSC fit to the time-averaged data of PKS 2155-304. The model fit, which was performed by colleagues in the H.E.S.S. and Fermi collaborations, has parameters as indicated in the row "model" of Table 6.5. These parameters, which correspond to the "blue fit" in Figure 6.14 have very similar values to those of the steady large jet component as described in the SSC fit of PKS 2155-304 by Katarzyński et al. 2008 [222] and which represent the extended jet emission, as opposed to the compact zones also present in their model, and which was responsible for the observed gamma-ray flares during the high-state. Without including any timing information in our analysis, it seems therefore that the extended jet emission can be described very well by the low-state SED, whereas the high-states of the source such as observed by H.E.S.S. in [26] and [32]

Table 6.5: SSC model parameters for the SED of PKS 2155-304.

model	p_i	γ (max)	N_e	R (cm)	δ	B G
SSC fit	1.3, 3.2, 4.3	$10^{6.5}$	6.8×10^{51}	1.5×10^{17}	32	0.018
($\gamma < \gamma_2$)	–	2.3×10^5	–	–	–	–
($\gamma < \gamma_1$)	–	1.4×10^4	–	–	–	–

result from the presence of more energetic regions within the jet which emit via external-Compton interaction with other parts of the jet, such as described in the "jet-in-needle" model of Ghisellini & Tavecchio 2008 [169] or the multi-blob model of Katarzyński et al. 2008 [222].

To probe the timing information, observe that although the optical, X-rays and VHE data present a significant degree of variability (with the X-rays varying more than the VHE emission by a factor of 35% vs. 20%), the GeV *Fermi* data show no significant temporal variation during the observations (the fractional variability was derived previously in this Chapter with an upper limit of 20%).

The last two rows of Table 6.5 correspond to the two dotted curves in Figure 6.14, and represent fits with the same physical parameters as the "main model" but with different values of γ_{max} for the electron population. Values of $\gamma > \gamma_2$ represent the energy of the electrons responsible for the X-ray synchrotron emission, and it is clear from Figure 6.14 that the omission of these electrons from the SSC fit cause little or no variations in the IC peak, showing that the X-ray emitting electrons are actually *more energetic* than the VHE-emitting ones. Furthermore, this lack of impact on the IC flux is a clear indication of a fact discussed in Chapter 3, *viz.* that very high energy particles will not contribute to the IC flux because the scattering will fall in the Klein-Nishina regime which will suppress any flux contribution to the TeV energies. This analysis of the energetics can readily explain the lack of correlation between the X-ray and the VHE variability in this case. The fact that we see spectral variations in the X-rays and none in the TeVs is another sign of the higher energy of the X-ray-emitting electron population, which suffers a faster cooling.

In the absence of spectral variability, the mechanisms that would produce the observed flux variability in the VHE band are well constrained: they could be driven either by parti-

cle injection or escape from the emitting region, or by adiabatic losses due to expansion of the region. It could also be the case that changes in the seed photon density are driving the variability. This last possibility seems more favourable for two reasons: 1. the electrons emitting at TeV are in the weak cooling regime ($\gamma < \gamma_2 = 2.3 \times 10^5$), and 2. we register a correlation between the VHE and the optical variability, with correlation coeficients of the order of ~ 0.8 (see Figure 6.3).

The difficulty with this simple picture is that any variations in the optical band should also be reflected in the *Fermi* LAT observations, which shows no significant flux changes. This can be seen by the fact that if we exclude from our SED fit of Figure 6.14 the electrons with $\gamma > \gamma_1 = 1.4 \times 10^4$, which are those responsible for the synchrotron emission at optical bands and above, than *both* the GeV and TeV fluxes are heavily suppressed. That is, for the single-zone SSC model, the electrons that produce the optical-soft X-ray emission also produce the bulk of the IC component. The fact that we find no indication of this in the temporal behaviour of the data suggests that the optical emission may be associated to a separate population of electrons than those responsible for the gamma-ray fluxes. If so, then they probably occupy a distinct region in the jet, i.e. with different physical parameters. In order to gather clues as to the solution of this difficulty, we must turn to the results of the polarimetric data in the previous section, which allow us to disentangle the internal source structure.

6.5.2 Source structure and emitting regions

Let us briefly revise the implications of the optical polarimetric observations for the multiwavelength analysis of the source described above. Supported by correlated optical and radio VLBI polarisation properties, we have shown that the optical synchrotron emission from PKS 2155-304 is consistent with having an origin at the radio core. The structure of the quiescent state jet was then modelled as an inhomogeneous synchrotron source consisting of an underlying jet with tangled field which is locally ordered by a shock compression of the flow, where particle acceleration takes place.

It is a common feature of BL Lacs that the flux and polarisation variations show no obvious temporal correlation. Our analysis of the possible sources of variability within a shock-in-jet model have concluded that the flux microvariability can be interpreted as

direct signature of particle acceleration and cooling at the shock front. This picture is supported by observations of the spectral index on timescales of a few hours. The longer timescales of the polarisation variability are nevertheless associated with the propagation of the shock along a structured jet with changing physical properties. This picture was suggested to be linked with results of general-relativistic MHD simulations by McKinney, which predict the formation of instability-induced "patches" in the jet at sub-parsec scales.

Now, concerning the discussion of the SED and the multiwavelength time-variability, our model for the optical emission shows that most of the optical flux originates in the weakly polarised, stable jet component, whereas the photo-polarimetric variability results from the development and propagation of a shock in the jet. This multi-zone scenario supports the picture advanced in the previous section that an inhomogeneous model is necessary to explain the temporal behaviour of this blazar in the quiescent state. Whereas most of the optical flux has its origin in the extended jet component, the variable optical emission seems to originate in a shock component, with higher Doppler factors and magnetic field intensities than modelled by Katarzyński et al. 2008 [222] for the extended jet. A consequence of this scenario is that the optical polarimetric emission is potentially a better tracer of the high-energy emission, revealing the importance of optical polarimetric monitoring in multiwavelength campaigns.

In fact, if the variable and polarised optical and TeV emissions are indeed associated, then the radio core could be identified as the source of the quiescent TeV flux, much in the same way as Giebels et al. 2002 [172] propose that the quiescent X-ray flux originates in the unresolved components of the pc-scale radio jet. In the case this association holds, the IC flux would be correlated rather with the behaviour of the variable shock component, responsible for the polarimetric variability, than the extended jet component. Before concluding this chapter, let us briefly look into an alternative model for the polarisation variability, based on relativistic aberration effects of a geometric origin.

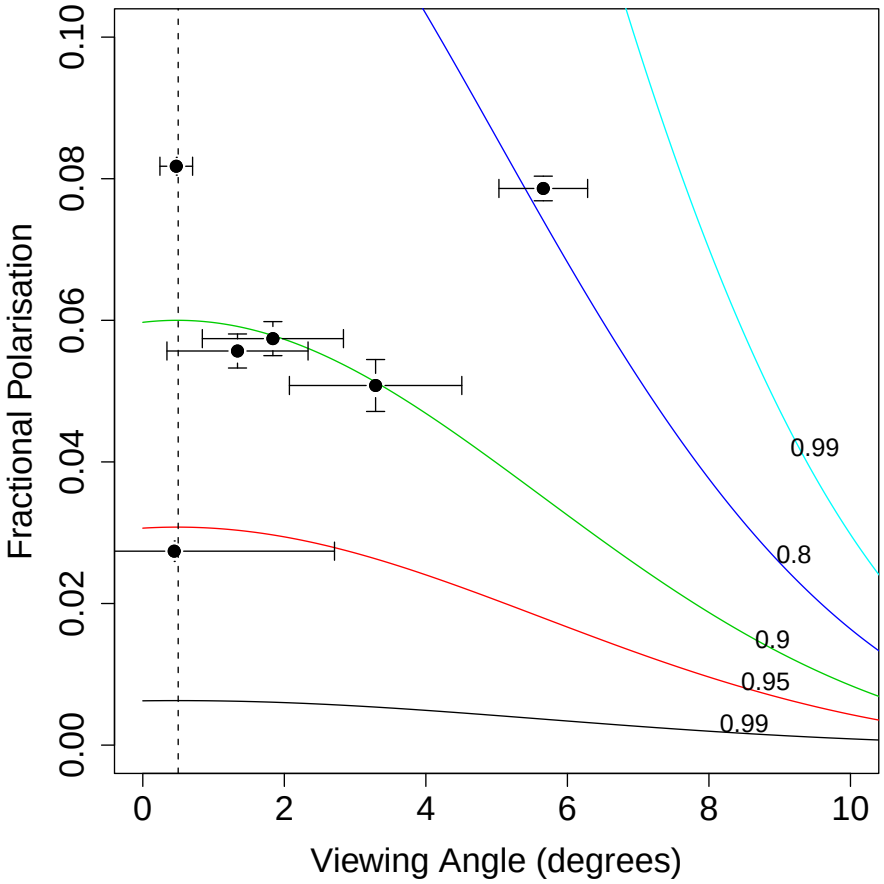

Figure 6.15: Geometrical model for the changes in the polarisation degree of PKS 2155-304 due to relativistic aberration of a shock with changing angle to the line-of-sight. The different curves indicate different compression factors k for the shock as indicated by the numerical labels. The points are estimated measurements of the aberration effects from the observations assuming that the hypothetical variations of the viewing angle are reflected in the oscillations about the linear rotation trend observed for the EVPA in the R-band light curve. These points represent the nightly averages and do not carry information regarding the microvariability of p. The vertical dashed line marks the jet angle to the line-of sight of $\approx 4.2°$ as calculated from VLBI images [290] and corrected for relativistic aberration according to Equation 6.25.

6.6 Epilogue: Do geometric effects play a role in the polarimetric variability?

Theoretical calculations of an internal shock model for the origin of the polarisation variability in extragalactic jets performed by Hughes et al. 1985 [203] consider the effect of aberration on the magnitude of the polarisation degree. In their model, the degree of polarisation of a shocked component is dependent on the compression factor of the shocked plasma, k, the aberrated viewing angle θ' and on the post-shock acceleration particle en-

ergy distribution index, α, according to:

$$P \approx \frac{\alpha+1}{\alpha+7/3}\frac{(1-k^2)\cos^2\theta'}{2-(1-k^2)\cos^2\theta'}, \tag{6.24}$$

This expression is derived assuming $\alpha \approx 3$, which allowed for a simple analytical solution, but Hughes et al. observe that the geometrical effects on the polarisation depend only very weakly on this parameter and so the approximation is valid (see Figures 3 and 4 in [203]). The viewing angle of the shock in the observer's frame θ', subject to relativistic aberration due to a bulk Lorentz factor Γ of the flow, is given by:

$$\cos\theta' = \frac{\cos\theta-\beta}{1-\beta\cos\theta}, \tag{6.25}$$

where $\beta = (1-\Gamma^{-2})^{1/2}$ is the relativistic velocity of propagation of the shocked plasma. The bulk velocity of the flow can be inferred from the speeds of the jet components in VLBI images, such as obtained by Piner et al. (see [290] and [291]) for PKS 2155-304 at 15 GHz. These authors have studied the jet properties of a number of VHE-emitting BL Lac objects and concluded that at pc-scales the flows are only mildly relativistic $\Gamma \sim 2-4$. These observations refer to the movement of components downstream from the radio core – thought in blazars to be several 10^2-10^3 gravitational radii distant from the central AGN – where the emission is optically thin and the flow has expanded sufficiently for these components to be resolved at the mas-scale, and correspond to the bulk jet flow, Γ_{jet} (see [155]). It is a caveat of this analysis that the aforementioned values do not necessarily correspond to the speeds at the innermost regions of the jet. These regions, responsible for the extreme behaviour observed from BL Lacs from optical to TeV energies (see the models of Katarzyński et al. 2008 [222], and Ghisellini & Tavecchio 2008 [169]) possess high Doppler factors as deduced from variability measurements and SED modelling. Even at low states, the optical-to-X-ray emission of PKS 2155-304 requires shocked material with Doppler factors $\delta \gtrsim 10$ to fit the observations (e.g., [35] and [155]), meaning that the shocks in these extreme emitters strongly deccelerate by the time they reach the pc-scales, a few mas from the central engine, possibly due to strong, efficient transference of the bulk kinetic energy of the plasma into particle acceleration which is then radiated away by emission of high-energy photons (see [177] and [178]).

In order to reproduce these minimum requirements on the Doppler factor required by the emission models of $\delta \sim 10$, and to remain consistent with the viewing angle estimates for PKS 2155-304 of $\theta = 4°$, as estimated by Piner et al. 2004 [290] from VLBI measurements, we have:

$$\delta = \frac{1}{\Gamma_{\rm jet}(1 - \beta \cos\theta)}, \tag{6.26}$$

which for $\Gamma_{jet} \sim 3$ gives $\beta \simeq 0.97$. Observe that the correspondent Lorentz factors for these innermost emitting zones is greater than Γ_{jet}, and of the order of 5.

Figure 6.15 shows the effect on the polarisation fraction of a change in the viewing angle θ as a function of the compression factor of the shock, k. The changes in the viewing angle θ were directly estimated from the oscillations seen in the EVPA about the straightline trend, as shown in Figure 6.6 and correspond to $\Delta\theta \lesssim 5°$. In this it is assumed that, whereas the linear trend is due to the evolution of the two-component system, the deviations from this trend are the result of changes in the viewing angle of the shock due to inhomogeneities in the path of the flow, which we take to be equally probable and therefore symmetric in all directions. Thus the changes of the EVPA in the plane of the sky are a direct estimate of the deviations in relation to the line-of-sight. As discussed by Andruchow et al. 2003 [49], the dependency of p on $\Delta\theta$ is potentially strong, and small changes of the viewing angle can produce large variations in the degree of polarisation. As a combination of the relatively modest speed of the flow, and the fact that the jet is viewed in close alignment to the line of sight, at an angle similar to the magnitude of the angle aberrations, the changes in the polarisation degree amount to not more than a few degrees in this case, and as can be seen from Figure 6.15 the values of p favour compression factors for the shock $k \sim 1$.

Geometrical modelling of the light-curve

Although this simple geometrical relativistic analysis shows that in principle the magnitude of the day-to-day changes in the polarisation degree could be accommodated within a geometrical model, a more detailed analysis is necessary to confirm that the entire photo-polarimetric behaviour of the light-curve could be reproduced by this model in a manner similar to the observations. For this I follow an analysis performed by Haggen-Thorn et

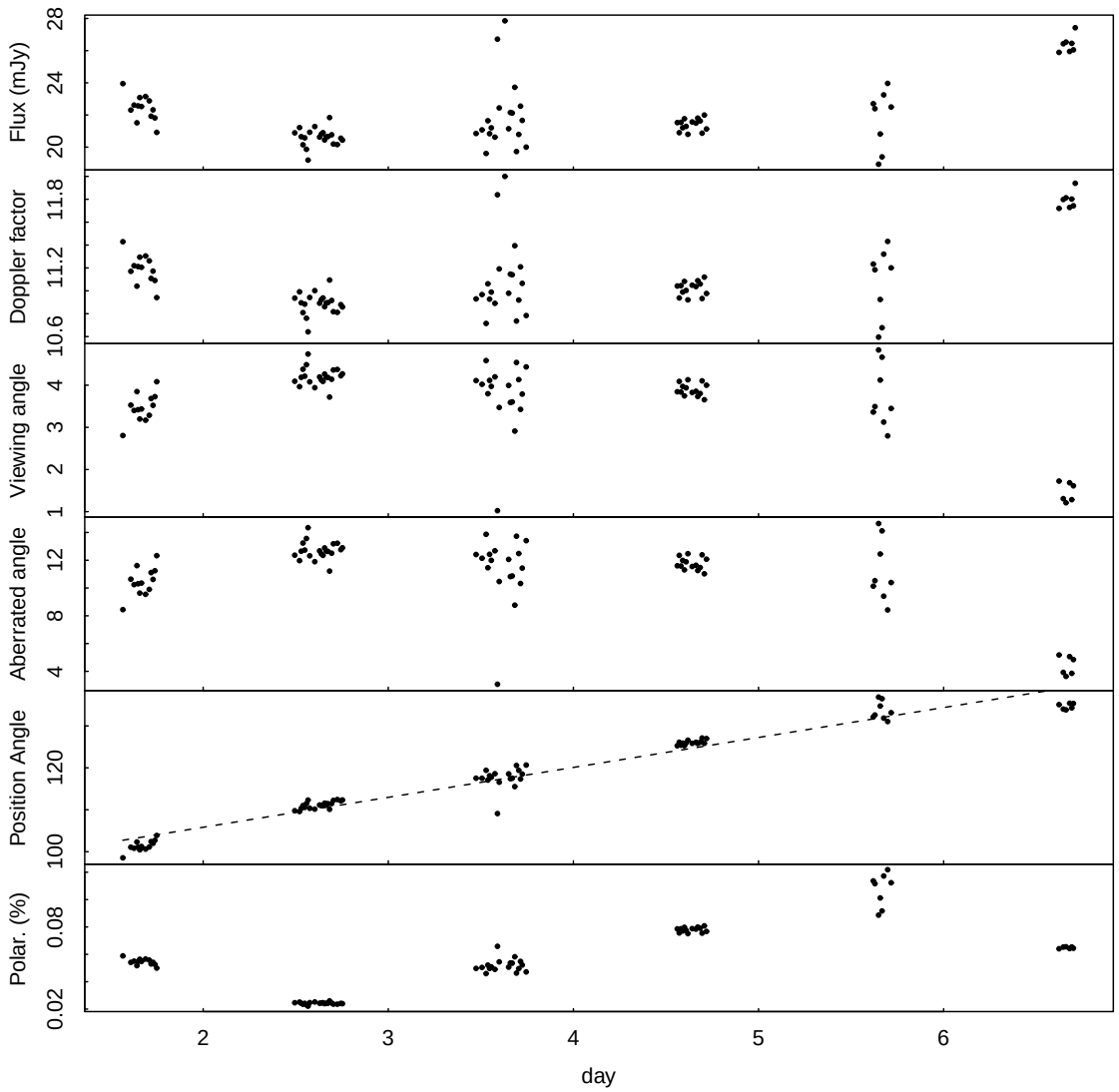

Figure 6.16: Reconstruction of the optical photo-polarimetric parameters and light curve behaviour from the geometrical model.

al. 2008 for the blazar AO 0235+164 [187].

The first parameter one has to consider when modelling the light-curve is the effect of the aberration on the boosting of the optical flux F, which is described by:

$$F = F_0 \nu^{-\alpha'} \delta'^{(2+\alpha')} \delta^{(3+\alpha)}, \tag{6.27}$$

where F_0 is the intrinsic flux, δ' is the Doppler factor of the shocked plasma in the rest frame of the shock front, assumed $\approx$ 1 and corresponding to a non-relativistic speed $v \ll c$. The flow is assumed to have a constant bulk Lorentz factor $\Gamma \sim 3$ which is the Doppler factor of the shock front in the observer's frame. If we assume, in accordance

with the previous section, that the shock speed $\beta \sim 0.97$ is constant in time and that the bulk Lorentz factor of the flow is also unchanging, δ will be solely a function of the viewing angle θ, according to $\delta = [\Gamma(1 - \beta \cos\theta)]^{-1}$.

The intrinsic flux F_0 can likewise be estimated by inversion of Equation 6.27 with the assumption (see [187]) that $F_0 = F_{max}\ \nu^{\alpha'}/\delta_0^{(3+\alpha')}$, where F_{max} is the maximum flux observed in the R-band, and $\delta_0 \simeq 11.5$ is the Doppler factor corresponding to the maximum degree of polarisation of the source, obtained for the un-aberrated angle $\theta'_0 \sim 0.5°$. Using the daily average values for the shock compression as derived from Figure 6.15 we can then use Equation 6.27 to derive the Doppler factors for each flux measurement, which can then be used to calculate the viewing angle variations and the correspondent light-curve of the polarisation degree.

The results are shown in Figure 6.16. As it can be readily seen from a comparison with the original light-curve, the observational parameters can be well reproduced by this alternative model, once the total flux light-curve is taken into account in the context of the assumptions adopted in this section for the jet, in accordance with VLBI observations. This shows that variations on the viewing angle of the shock of only a few degrees, can also be used to explain the polarisation properties and temporal behaviour of the source. This result suggests that both the inhomogeneous synchrotron model and the geometrical model have some degree of degeneracy, and this is in fact not surprising given that, as pointed out by Björnsson 1982 [83] many of the effects of an inhomogeneous synchrotron source are equivalent to those one would expect from relativistic motion aberration. Given the limited span of our dataset and our somewhat restricted analysis due to lack of better-sampled multi-band data, these two scenarios cannot be distinguished. In principle, this distinction should be possible with a better and longer-timespan data sampling and this is certainly an area to look into in future analysis.

In conclusion, in this chapter we have presented the results of a multiwavelength campaing on the blazar PKS 2155-304 made when the source was in a low-state. This campaign had two main novelties to it: first the use of *Fermi* data on the first campaign ever to completely sample the IC-bump of a BL Lac object, strongly constraining its SED properties; secondly, the presence of optical polarimetric data, for the first time taken

simultaneously to VHE gamma-ray observations. The optical polarimetric observations allowed us to interpret the results of the SED modelling in a new light and confirm its results that a multi-zone or inhomogeneous synchrotron source is necessary to explain the time-dependent behaviour and structure of BL Lac objects, even when in quiescent state. We were also able to constrain the optical polarimetric emission (and by consequence the correlated gamma-ray emission) to probably originate within or near the radio core in the pc-scale jet, which is associated to the site of internal shocks where *in situ* particle acceleration is taking place. This unique MWL campaign serves therefore as a model to further studies of BL Lacs, stressing the importance of the use of gamma-ray data to properly sample the IC-bump and the inclusion of unique information on the source structure that can be provided only by polarisation measurements. We plan to continue to use this approach for the study of other BL Lac objects.

Chapter 7

Conclusions & Future Perspectives

In this work I have studied multiwavelength aspects of the variability of the prototypical VHE-emitter BL Lac object PKS 2155-304, concentrating particularly on its gamma-ray and polarimetric emission. In doing so, I have proposed a new observational approach to the study of extragalactic jets as an essential line of investigation if one wishes to disentangle the physical structure and location of the sites of VHE emission, *viz.* the use of contemporaneous optical or radio polarimetric data in high-energy multiwavelength campaigns. By applying this strategy I was able to produce further evidence towards the fact that the quiescent state SED of BL Lac objects, and in particular of the source PKS 2155-304, requires a two-zone model for its time-dependent properties to be properly modelled, even if a single-zone SSC model can fit well the general properties of the time-averaged low state. This fact was explained by the flux dominance of the extended jet emission at low energies against the likely more compact and energetic zones which seem to be the origin of the high-energy flux. Likewise, this multi-zone picture put forth by the optical polarimetric data was also able to explain some features of the multiwavelength SED of PKS 2155-304, in particular the fact that at least part of the gamma-ray flux must originate from external Compton emission of soft optical photons from within the jet but external to the compact zones where the energetic scattering electrons are located.

The work presented here on PKS 2155-304 was the first in a long-term project for the optical polarimetric study of VHE-emitting blazars, which is being performed jointly at the Laboratório Nacional de Astrofísica (LNA) and the South African Astronomical Observatory (SAAO). More recently, we have extended this project to study the nearby

Radio Galaxy M 87, for which optical polarimetric observations were taken in April/10 with the RINGO-II polarimeter at the Liverpool Telescope [326]. The observations were conducted during a historically high gamma-ray state, and were part of a large MWL campaign with H.E.S.S./MAGIC/VERITAS, the *Fermi* LAT instrument, RXTE and Chandra, as well as VLBI, and represents a continuation of previous MWL efforts on the study of its jet [343].

More especifically in relation to the variability at VHE, I have used the data on the extremely large flare of PKS 2155-304 in July 2006 to study extrinsic, energy-dependent variability effects on the source's light curve which allowed the best constraints to date to be put on Lorentz invariance from Blazars, disfavouring predictions of some QG models for a non-constant, energy-dependent velocity of light due to vacuum fluctuations up to $\sim 20\%\ E_{\rm Planck}$. For performing this study a new statistical method was developed for the measurement of spectral-depent delays, the Kolmogorov distance method, whose broader scope of application was illustrated by putting some constraints on the location of particle acceleration sites within the jet of PKS 2155-304, using the same dataset from July 2006.

Prospects for H.E.S.S.-II and the Cherenkov Telescope Array

The second phase of the H.E.S.S. project will consist on the installation of a fifth, 28-m telescope at the centre of the H.E.S.S. array, with the expected start of operations at the end of 2011 [121]. The main observational advantage of H.E.S.S.-II for extragalactic gamma-ray astronomy will be the expansion of the energy range of observations down to $\sim$ 30 GeV [72], which will grant the observatory a larger spectral overlap with the *Fermi* satellite, and will also allow to observe directly the peak of the IC bump in HBLs, which is a crucial parameter for determining the spectral shape of the SED and therefore constraining the mechanisms of emission and deciding between leptonic and hadronic scenarios.

Furthermore the construction of a large system of dozens of Cherenkov Telescopes organised in two arrays is planned, one in the Northern hemisphere and one in the South, to explore the sky in the energy range 10 GeV – 100 TeV [116]. This large Cherenkov Telescope Array (CTA) involves an international consortium which will combine the ex-

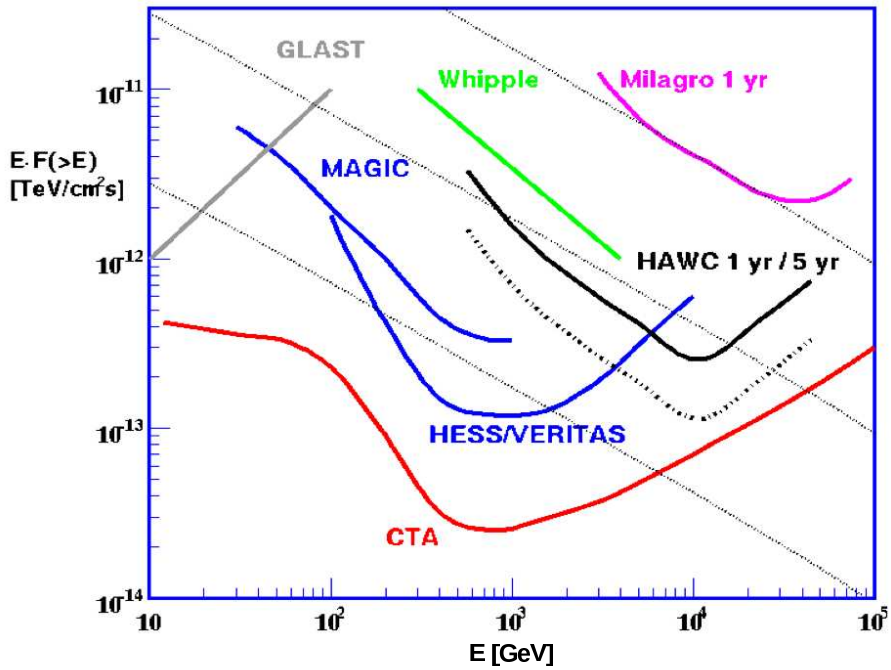

Figure 7.1: Simulated sensitivity curve for CTA, in relation to other gamma-ray observatories. Credits: CTA Consortium.

periences gained with the third generation instruments H.E.S.S., MAGIC and VERITAS to build the first major ground-based gamma-ray observatory for the international astronomical community. The main mark of this next-generation instrument is that the large $O(50)$ telescopes of the array will significantly increase the sensitivity of the observatory in relation to what exists today in the field – see Figure 7.1. Furthermore, the existence of two arrays (CTAs North and South) will allow for a complete coverage of the sky, with the Northern-hemisphere site being optimised for the study of extragalactic sources, for which the higher-energy photons suffer from EBL absorption, a lower energy threshold being thus required. CTA will allow for a sound increase in the catalogue of extragalactic objects detected in gamma-rays, with an expected $O(10^2)$ new objects being added to the current 30-odd list. The greater sensitivity will bring with it much-improved photon statistics so that timing studies of fast variability and low-magnitude effects such as LIV and Dark Matter signals, as well as ongoing particle acceleration signatures in jets, will greatly benefit.

Additionally, the large number of telescopes which will compose the array will allow for a number of different observation modes that will be able to operate simultaneously, thus making this an excellent facility for coordinated multiwavelength observations. Fi-

nally, for the case of the nearest objects such as the radio galaxies Centaurus A and M 87, the improved 1.5 – 2× angular resolution of CTA (expected to be ~ few arcmin) will allow a better (albeit restricted) mapping of the source's VHE emission, from the central areas to the outer lobes.

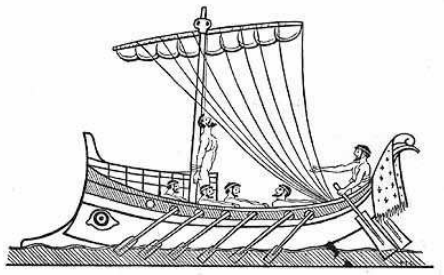

Figure 7.2:

Bibliography

[1] Z. Abraham, U. Barres de Almeida, T.P. Dominici & A. Caproni (2007), *Free-free absorption in the nucleus of Cen A: evidences from 7 mm emission variability.*, Mon. Not. R. Astron. Soc., **375**, pp. 171–176.

[2] A. Abramowski et al. [HESS Collaboration] (2010), *VHE gamma-ray emission of PKS 2155-304: spectral and temporal variability*, **arXiv1005.3702** pp 17.

[3] F. Acero et al. [HESS Collaboration] (2009), *Detection of gamma-rays from a starburst galaxy.*, Science, **326**, pp. 1080–1082.

[4] F. Acero et al. [HESS Collaboration] (2010), *Search for Lorentz invariance breaking with a likelihood fit of the PKS 2155-304 flare data taken on MJD 53944.*, **in preparation**

[5] F. Acero et al. [HESS Collaboration] (2010), *Localising the VHe gamma-ray source at the Galactic Centre*, Month. Not. R. Astron. Soc., **402**, pp. 1877-1882.

[6] F. Acciari et al. [VERITAS Collaboration] (2009), *Multiwavelength observations of a TeV-flare from W Comae*, Astrophys. Journal, **707**, pp. 612-620.

[7] R.J. Adler & D.I. Santiago (1999), *On gravity and the uncertainty principle*, **arXiv:gr-qc/9904026**

[8] O. Adriani, G.C. Barbarino, G.A. Bazilevskaya, R. Bellotti, M. Boezio et al. (2009), *An anomalous positron abundance in cosmic rays with energies 1.5-100 GeV*, Nature, **458**, pp. 607–609.

[9] F.A. Aharonian & A.K. Konopelko (1997), *Stereo imaging of VHE gamma-ray sources*, **arXiv:astro-ph/9712044**

[10] F. Aharonian et al. [HEGRA Collaboration] (1999), *The cosmic ray proton spectrum determined with the imaging atmospheric cherenkov technique*, Phys. Rev. D, **59**, id 092003.

[11] F. Aharonian, A.A. Belyanin, E.V. Derishev, V.V. Kocharovsky & Vl.V. Kocharovsky (2002), *Constraints on the extremely high-energy cosmic ray accelerators from classical electrodynamics*, Phys. Rev. D, **66**, id 023005.

[12] F. Aharonian (2004), **Very high energy cosmic gamma radiation**, World Scientific, Singapore.

[13] F. Aharonian et al. [HESS Collaboration] (2004), *Calibration of cameras of the H.E.S.S. detector*, Astrop. Phys., **22**, pp 109–125.

[14] F. Aharonian et al. [HESS Collaboration] (2004b), *High-energy particle acceleration in the shell of a supernova remnant.*, Nature, **432**, pp 75–77.

[15] F. Aharonian et al. [HESS Collaboration] (2005), *Multi-wavelength observations of PKS 2155-304 with HESS*, Astron. & Astrophys., **442**, pp 895–907.

[16] F. Aharonian et al. [HESS Collaboration] (2005b), *A new population of very high energy gamma-ray sources in the Milky Way*, Science, **307**, pp 1938–1942.

[17] F. Aharonian et al. [HESS Collaboration] (2005c), *Discovery of very high energy gamma rays associated with an X-ray binary.*, Science, **309**, pp 746–749.

[18] F. Aharonian et al. [HESS Collaboration] (2005d), *Discovery of the binary pulsar PSR B1259-63 in very-high-energy gamma-rays around periastron with H.E.S.S.*, Astron. & Astrophys., **442**, pp 1–10.

[19] F. Aharonian et al. [HESS Collaboration] (2006), *Observations of the Crab nebula with H.E.S.S.*, Astron. & Astrophys., **457**, pp 899–915.

[20] F. Aharonian et al. [HESS Collaboration] (2006b), *A low level of extragalactic background light as revealed by γ-rays from blazars*, Nature, **440**, pp 1018–1021.

[21] F. Aharonian et al. [HESS Collaboration] (2006c), *A detailed spectral and morphological study of the gamma-ray supernova remnant RX J1713.7-3946 with H.E.S.S.*, Astron. & Astrophys., **449**, pp 223–242.

[22] F. Aharonian et al. [HESS Collaboration] (2006d), *The H.E.S.S. survey of the Inner Galaxy in very-high energy gamma-rays*, Astrophys. J., **636**, pp 777–797.

[23] F. Aharonian et al. [HESS Collaboration] (2006e), *Discovery of very-high-energy gamma-rays from the Galactic Centre ridge*, Nature, **439**, pp 695–698.

[24] F. Aharonian et al. [HESS Collaboration] (2006f), *3.9 day orbital modulation in the TeV gamma-ray flux and spectrum of the X-ray binary LS 5039.*, Astron. & Astrophys., **460**, pp 743–749.

[25] F. Aharonian et al. [HESS Collaboration] (2006g), *Energy dependent gamma-ray morphology in the pulsar wind nebula HESS J1825-137*, Astron. & Astrophys., **460**, pp 365–374.

[26] F. Aharonian et al. [HESS Collaboration] (2007), *An exceptional very high energy gamma-ray flare of PKS 2155-304*, Astrophys. Journal, **664**, pp L71–L74.

[27] F. Aharonian, J. Buckley, T. Kifune & G. Sinnis (2008), *High energy astrophysics with ground-based gamma ray detectors*, Rev. Prog. Phys., **71**, 096901, pp. 56.

[28] F. Aharonian et al. [HESS Collaboration] (2008), *Limits on an energy dependence of the speed of light from a flare of the active galaxy PKS 2155-304*, Phys. Rev. Lett., **101**, 170402.

[29] F. Aharonian et al. [HESS Collaboration] (2008b), *The energy spectrum of cosmic-ray electrons at TeV energies.*, Phys. Rev. Lett., **101**, id. 261104.

[30] F. Aharonian et al. [HESS Collaboration] (2008c), *Discovery of very high energy gamma ray emission coincident with molecular clouds in the W28 (G6.4-0.1) field.*, Astron. & Astrophys., **481**, pp 401–410.

[31] F. Aharonian, D. Khangulyan & L. Costamante (2008), *Formation of hard VHE gamma-ray spectra of blazars due to internal photon-photon absorption.*, Mon. Not. R. Astron. Soc., **482**, pp 449–460.

[32] F. Aharonian et al. [HESS Collaboration] (2009), *Simultaneous multiwavelength observations of the second exceptional γ-ray flare of PKS 2155-304 in July 2006*, Astron. & Astrophys., **502**, pp 749–770.

[33] F. Aharonian et al. [HESS Collaboration] (2009b), *H.E.S.S. observations of gamma-ray bursts in 2003-2007.*, Astron. & Astrophys., **495**, pp 505–512.

[34] F. Aharonian et al. [HESS Collaboration] (2009c), *H.E.S.S. upper limit on the very-high energy gamma-ray emission from the globular cluster 47 Tucanae*, Astron. & Astrophys., **499**, pp 273–277.

[35] F. Aharonian et al. [HESS & Fermi–LAT Collaborations] (2009), *Simultaneous observations of PKS 2155-304 with HESS, Fermi, RXTE and Atom: spectral energy distributions and variability in a low state*, Astrophys. Journal, **696**, pp L150–L155.

[36] F. Aharonian et al. [HESS Collaboration] (2010), *Probing the ATIC peak in the cosmic-ray electron spectrum with H.E.S.S.*, Astron. & Astrophys., **508**, pp 561–564.

[37] F. Aharonian et al. [HESS Collaboration] (2010b), *Discovery of VHE gamma-rays from the BL Lac object PKs 0548-322.*, **arXiv1006.5289**.

[38] J. Albert et al. [MAGIC Collaborations] (2006), *Variable very high energy gamma ray emission from the microqusar LSI +61 303*, Science, **312**, pp 1771–1774.

[39] J. Albert et al. [MAGIC Collaborations] (2007), *Variable very high energy γ-ray emission from markarian 501.*, Astrophys. Journal, **669**, pp 862–883.

[40] J. Albert et al. [MAGIC Collaborations] (2007), *Discovery of very-high energy gamma-ray emission from the low-frequency peaked blazar BL Lacertae.*, Astrophys. Journal Lett., **666**, pp L17–L23.

[41] J. Albert et al. [MAGIC Collaborations] (2008), *Very-High-energy gamma rays from a distant quasar: how transparent is the universe?*, Science, **320**, pp 1752–1754.

[42] J. Albert et al. [MAGIC Collaborations] (2008), *Probing quantum-gravity using photons from a flare of the active galactic nucleus Markarian 501 observed by the MAGIC telescope*, Phys. Lett. B **668**, pp 253–257.

[43] E. Aliu et al. [MAGIC Collaboration] (2008), *Observation of pulsed γ-rays above 25 GeV from the Crab pulsar with MAGIC*, Science **322**, pp 1221–1227.

[44] H. Alfvén (1942), *Existence of electromagnetic-hydrodynamic waves*, Nature, **150**, pp 405–406.

[45] R.G. Allen, P.S. Smith, J.R.P. Angel, B.W. Miller et al. (1993), *Ultraviolet polarimetry and spectroscopy of the BL Lacertae object PKS 2155-304*, Astrophys. Journal, **403**, pp 610–620.

[46] D.R. Altschuler (1989), *Variability of extragalactic radio sources*, Fund. Cosmic Phys., **14**, pp 37–129.

[47] G. Amelino-Camelia, J. Ellis, N.E. Mavromatos, D.V. Nanopoulos & S. Sakar (1998), *Tests of quantum gravity from observations of gamma-ray bursts*, Nature, **395**, pp 525–530.

[48] G. Amelino-Camelia & L. Smolin (2009), *Prospects for constraining quantum-gravity disperion with near term observations.*, Phys. Rev. D, **80**, pp 084017.

[49] I. Andruchow, S.A. Cellone, G.E. Romero et al. (2003), *Microvariability in the optical polarization of 3C 279*, Astron. & Astrophys., **409**, pp 857–865.

[50] I. Andruchow, G.E. Romero & S.A. Cellone (2005), *Polarization microvariability of BL Lacertae objects*, Astron. & Astrophys., **442**, pp 97–107.

[51] R.R.J. Antonucci (1983), *Optical polarisation angle versus radio structure axis in Seyfert galaxies*, Nature, **303**, pp 158–159.

[52] R.R.J. Antonucci (1993), *Unified models for active galactic nuclei and quasars*, Ann. Rev. Astron. & Astrophys., **31**, pp 473–521.

[53] P. Armstrong, P.M. Chadwick, P.J. Cottle et al. (1999), *The University of Durham Mark 6 Gamma-ray telescope*, Exp. Astron., **9**, pp 51–80.

[54] W.B. Atwood & Fermi–LAT Collaboration (2009), *The Large Area Telescope on the Fermi Gamma-ray Space Telescope mission*, Astrophys. Journal, **697**, pp 1071–11102.

[55] P. Auger, P. Ehrenfest, R. Maze, J. Daudin & R.A. Fréon (1939), *Extensive cosmic-ray showers.*, Rev. Mod. Phys., **11**, pp 288–291.

[56] W. Baade & R. Minkowski (1954), *Identification of the radio sources in Cassiopeia, Cygnus A and Puppis A*, Astrophys. Journal, **119**, pp 206–214.

[57] W. Baade (1956), *Polarization in the jet of Messier 87*, Astrophys. Journal, **123**, pp 550–551.

[58] J.E. Baldwin & F.G. Smith (1956), *Radio emission from the extragalactic nebula M 87*, The Observatory, **76**, pp 141–144.

[59] K.R. Ballard, A.R.G. Mead, P.W.J.L. Brand & J.H. Hough (1990), *The optical and infrared emission of blazars*, Month. Not. Royal Astron. Soc., **243**, pp 640–665.

[60] D.L. Band & J.E. Grindlay (1985), *The synchrotron-self-Compton process in spherical geometries. I. Theoretical framework*, Astrophys. Journal, **298**, pp 128–146.

[61] D.L. Band & E. Ferrara (2009), *Fermi Gamma-ray Telescope – Cicerone: Detailed Manual for Fermi Science Tools*, NASA Goddard Space Flight Center, pp.107.

[62] U. Barres de Almeida, P.M. Chadwick, M.K. Daniel, S. Nolan & L. McComb (2008), *Event-sequence time series analysis in ground-based gamma-ray astronomy*, in High-energy gamma-ray astronomy (Gamma08), AIP Conf. Proc., **1085** pp. 775-778.

[63] U. Barres de Almeida & M.K. Daniel (2009), *An unbinned test for quantum gravity effects in high-energy light-curves.*, **arXiv:0906.5257**.

[64] U. Barres de Almeida [for the HESS Collaboration] (2010), *Results from H.E.S.S. observations of relativistic sources*, Int. J. Mod. Phys. D, **19** pp.1013–1022.

[65] U. Barres de Almeida, M.J. Ward, T.P. Dominici, Z. Abraham et al. (2010), *Particle Acceleration and Magnetic Field Structure in PKS 2155-304: Optical Polarimetric Observations*, Month. Not. Royal Astron. Soc., **408** pp. 1778–1787.

[66] U. Barres de Almeida & M.K. Daniel. (2010), *A method to test for energy-dependent dispersion in high-energy light-curves of astrophysical sources*, **submit. to Astrop. Phys.**.

[67] S.A. Baum, E.L. Zirbel & C.P. O'Dea (1995), *Toward understanding the Fanaroff-Riley dichotomy in radio source morphology and power*, Astrophys. Journal, **451**, pp 88–99.

[68] J.J. Beatty & S. Westerhoff (2009), *The Highest-energy cosmic rays*, Ann. Rev. Nucl. Part. Sci., **59**, pp 319–345.

[69] W. Bednarek & R.M. Wagner (2008), *A model for delayed emission in a very-high energy gamma-ray flare in Markarian 501*, Astron. & Astrophys, **486**, pp 679–682.

[70] R. Belmont, J. Malzac & A. Marcowith (2008), *Simulating radiation and kinetic processes in relativistic plasmas*, Astron. & Astrophys., **491**, pp 617–631.

[71] S.D. Biller, A.C. Breslin, J. Buckley, M. Catanese et al. (1999), *Limits to quantum gravity effects on energy dependence of the speed of light from observations of TeV flares in Active Galaxies.*, Phys. Rev. Lett. **83**, pp. 2108–2111

[72] Y. Becherni, A. Djannati-Atai, M. Punch, K. Bernlöhr et al. (2008), *HESS-II reconstruction strategy and performance in the low-energy (20-150 GeV) domain.*, AIPC Conf. Proc., **1085**, pp 738–741.

[73] M.C. Begelman, R.D. Blandford & M.J. Rees (1984), *Theory of extragalactic radio sources*, Rev. Mod. Phys., **56**, pp 255–359.

[74] M.C. Begelman & M. Sikora (1987), *Inverse compton scattering of ambient radiation by a cold relativistic jet - A source of beamed, polarised continuum in blazars?*, Astrophys. Journal, **322**, pp 650–661.

[75] M.C. Begelman, A.C. Fabian & M.J. Rees (2008), *Implications of very rapid TeV variability in blazars*, Mon. Not. R. Astron. Soc., **384**, pp L19–L23.

[76] A.R. Bell (1978a), *The acceleration of cosmic rays in shock fronts - I*, Mon. Not. R. Astron. Soc. , **182**, pp 147–156.

[77] A.R. Bell (1978b), *The acceleration of cosmic rays in shock fronts - II*, Mon. Not. R. Astron. Soc., **182**, pp 443–455.

[78] W. Benbow [for the HESS Collaboration] (2005), *The H.E.S.S. standard analysis technique*, in Proc. Conf. Towards a Network of Cherenkov Detectors VII, Palaiseau, France, pp 163–172.

[79] D. Berge, S. Funk & J. Hinton (2007), *Background modelling in very-high energy gamma-ray astronomy.*, Astron. & Astrophys. **466**, pp 1219–1229.

[80] K. Bernlöhr, O. Carrol, R. Cornils, S. Elfahem et al. (2003), *The optical system of the H.E.S.S. imaging atmospheric Cherenkov telescopes. Part I: layout and components of the system.*, Astrop. Phys. **20**, pp 111–128.

[81] E. Bertone, G. Tagliaferri, G. Ghisellini, A. Treves et al. (2000), *ISO observations of the BL Lacertae object PKS 2155-304*, Astron. & Astrophys. **356**, pp 1–10.

[82] D. Bettoni, R. Falomo, G. Fasano, F. Govoni (2003), *The black hole mass of low redshift radiogalaxies*, Astron. & Astrophys., **399**, pp 868–878.

[83] C.-I. Björnsson (1982), *Polarisation properties of a source in relativistic motion*, Astrophys. Journal **260**, pp 855–867.

[84] C.-I. Björnsson & Blumenthal (1982), *Spectral properties of optically thin synchrotron radiation*, Astrophys. Journal **259**, pp 805–819.

[85] C.-I. Björnsson (1985), *Frequency-dependent polarisation in blazars*, Mont. Not. Royal Astron. Soc. **216**, pp 241–253.

[86] R.D. Blandford & D.G. Payne (1982), *Hydromagnetic flows from accretion discs and the production of radio jets.*, Month. Not. R. Astron. Soc. **199**, pp 883–903.

[87] G.R. Blumenthal & R.J. Gould (1970), *Bremsstrahlung, synchrotron radiation, and Compton scattering of high-energy electrons traversing dilute gases*, Rev. Mod. Phys. **42**, pp 237–270.

[88] S.E. Boggs, C.B. Wunderer, K. Hurley & W. Coburn (2004), *Testing Lorentz invariance with GRB 021206.*, Astrophys. Journal. **611**, pp L77–L80.

[89] J. Bolmont, A. Jacholkowska, J.-L. Atteia, F.Piron & G.Pizzichini (2006), *Study of time lags in HETE-2 gamma-ray bursts with redshift:serach for astrophysical effects and a quantum gravity signature.*, Astrophys. Journ. **676**, pp 532–544.

[90] M. Böttcher (2007), *Modelling the emission processes in blazars*, Astrophys. & Space Sc. **309**, pp 95–104.

[91] C. Brindle, J.H. Hough, J.A. Bailey et al. (1986), *Simultaneous optical and infrared polarisation measurements of blazars*, Mon. Not. R. Astron. Society **221**, pp 739–768.

[92] C. Brindle (1996), *The internight variability of the optical to near-infrared flux density and polarization of the blazars 0215+015 and 0851+202 during outbursts*, Mon. Not. R. Astron. Society **282**, pp 788–796.

[93] G.R. Burbidge (1956), *On synchrotron radiation from Messier 87*, Astrophys. Journal **124**, pp 416–429.

[94] D.N. Burrows, J.E. Hill, J.A. Nousek, J.A. Kennea et al. (2005), *The Swift X-ray Telescope*, Space Science Rev. **120**, pp 165–195.

[95] A. Caproni & Z. Abraham (2004), *Precession in the inner jet of 3C 345.*, Astrophys. Journal. **602**, pp 625–634.

[96] E. Carmona, P. Majumdar, A. Moralejo et al. (2008), *Monte Carlo simulations for the MAGIC-II system.*, Proc. 30th Int. Cosmic Ray Conf. (ICRC), Mexico - Vol. 3, pp 1373–1376.

[97] J.-M. Casandjian & I.A. Grenier (2008), *A revised catalogue of EGRET γ-ray sources*, Astron. & Astrophys. **489**, pp 849–883.

[98] M.F. Cawley, J. Claer, D.J. Fegan, K.Gibbs, N.A. Potter & T.C. Weekes (1982), *The Whipple observatory camera for high energy gamma-ray astronomy*, in Proc. of Very High energy Gamma-Ray Astronomy Int. Symposium, Ootacamun, India. Eds. R. Murphy and T.C. Weekes, pp 292–293.

[99] A. Celotti, A.C. Fabian & M.J. Rees (1998), *Limits from rapid TeV variability of Mrk 421*, Mon. Not. R. Astron. Soc. **293**, pp 239–242.

[100] A. Celotti (2001), *Blazars*, in Relativistic Flows in Astrophysics – Springer Lecture Notes in Physics. **589**, pp 88–100.

[101] P.M. Chadwick, K. Lyons, T.J.L. McComb, K.J. Orford, J.L. Osborne et al. (1999), *Very high energy gamma-rays from PKS 2155-304*, Astrophys. Journal. **513**, pp 161–167.

[102] S. Chandrasekhar (1946), *On the radiative equilibrium of a stellar atmosphere: XI.*, Astrophys. Journal. **104**, pp 110–132.

[103] J. Chang, J.H. Adams Jr, H.A. Ahn, G.L. Bashindzhagyan, M. Christl et al. (2007), *An excess of cosmic ray electrons at energies of 300-800 GeV*, Nature **456**, pp 362–365.

[104] P.A. Charankov (1934), *Visible emission of clean liquids by action of γ radiation.*, Dodkl. Akad. Nauk SSSR (in Russian) **2**, pp 451–562.

[105] G. Cocconi (1959), *Proc. Int. Cosmic Ray Conference*, Moscow, Russia **2**, pp 309–312.

[106] E. Collett (2005), **Field guide to polarization**, eBook – SPIE Digital Library.

[107] A.H. Compton (1923), *A quantum theory of the scattering of X-rays by light elements*, Phys. Rev. **21**, pp 483–502.

[108] P.S. Coppi & R.D. Blandford (1990), *Reaction rates and energy distributions for elementary processes in relativistic pair plasmas*, Mon. Not. Royal Astron.Soc. **245**, pp 453–469.

[109] M. Coram (2002), **Nonparameteric Bayesian classification**, Ph.D. Thesis, Stanford University.

[110] E. Costa, R. Bellazzini, P. Soffitta, F. Muleri, M. Feroci et al. (2006), *POLARIX: a small mission of x-ray polarimetry*, Proc. of SPIE **6266**.

[111] L. Costamante & G. Ghisellini (2002), *TeV candidate BL Lac candidates*, Astron. & Astrophys. **384**, pp 56–71.

[112] L. Costamante, F. Aharonian, R. Buehler et al. (2009), *The new surprising behaviour of the two prototype blazars PKS 2155-304 and 3C 279*, Proc. of Gamma 2008 Heidelberg Symposium **arXiv0907.3966**.

[113] T.J.-L. Courvoisier, A. Blecha, P. Bouchet, P. Bratschi et al. (1995), *Multiwavelength monitoring of the BL Lacertae object PKS 2155-304. III. Ground-based observations in 1991 November.*, Astrophys. Journal. **438**, pp 108–119.

[114] R.T. Cox (1961), **The algebra of probable inference**, Johns Hopkins Press, Baltimore.

[115] L.J. Cox, J.H. Hough, A. McCall (1978), *The Hatfield near-infrared polarimeter*, Mon. Not. R. Astron. Society **185**, pp 199–205.

[116] The CTA consortium [W. Hofmann & M. Martinez et al.] (2010), *Design concepts for the Cherenkov Telescope Array*, **arXiv:1008.3703**, pp 120.

[117] H.D. Curtis (1918), *Descriptions of 762 Nebulae and Clusters Photographed with the Crossley Reflector*, Publ. Lick Obs. **13**, pp 9–42.

[118] M.K. Daniel (2002), *The attenuation of atmospheric Cherenkov photons*, **Ph.D. Thesis**, University of Durham.

[119] M.K. Daniel, H.M. Badran, I.H. Bond et al. (2002), *Spectrum of very-high energy gamma-rays from the blazar 1ES 1959+650 during flaring activity in 2002.*, Astrophys. J. **621**, pp. 181–187.

[120] J.M. Davies & E.S. Cotton (1957), , Journal of Solar Energy, **1**, pp. 16–22.

[121] C. Deil, C. van Eldik, A. Forster, G. Hermann, W. Hofmann & M. Panter (2008), *H.E.S.S. II – Telescope structure, reflector and drive system.*, AIP Conf. Proc. **1085**, pp. 693–695.

[122] M. de Naurois (2006), *Analysis methods for atmospheric cherenkov telescopes*, **arXiv:astro-ph/0607247**, pp. 12.

[123] H.J. Dickinson (2010), *Very-high energy gamma-rays from binary systems.*, **Ph.D. Thesis**, University of Durham.

[124] J.A. de Diego (2010), *Testing tests on AGN microvariability*, Astron. Journal **139**, pp. 1269–1282.

[125] T.P. Dominici, Z. Abraham & A. Galo (2006), *Optical and near-infrared simultaneous observations of the BL Lacs PKs 2005-489 and PKS 2155-304*, Astron. & Astrophys. **460**, pp. 665–672.

[126] T.P. Dominici, Z. Abraham, A. Pereyra & A.M. Magalhães (2008), *Optical Polarization variability in TeV blazars* in Workshop on Blazar Variability across the Electromagnetic Spectrum, Palaiseau, France 2008. Proc. of Science.

[127] C. Done (2010), *Observational characteristiscs of accretion onto black holes*, **arXiv:1008.2287**.

[128] A. Einstein (1905), *Zur Elektrodynamik bewegter Körper*, Ann. der Phys., **322**, pp.891–921.

[129] A. Einstein (1916), *Die Grundlage der allgemeinen Relativitätstheorie*, Ann. der Phys., **354**, pp.769–822.

[130] J. Ellis, K. Farakos, N.E. Mavromatos, V.A. Mitsou & D.V. Nanopoulos (2000), *A search in gamma-ray burst data for nonconstancy of the velocity of light*, Astroph. J., **535**, pp.139–151.

[131] J. Ellis, N.E. Mavromatos, D.N. Nanopoulos & A.S. Sakharov (2003), *Quantum-gravity analysis of gamma-ray bursts using wavelets*, Astron. & Astrophys., **402**, pp. 409–424.

[132] J. Ellis, N.E. Mavromatos, D.V. Nanopoulos, A.S. Sakharov & E.K.G. Sarkisyan (2006), *Robust limits on Lorentz violation from gamma-ray bursts.*, Astrop. Phys., **25**, pp. 402-411.

[133] J. Ellis, N. Harries, A. Meregaglia, A. Rubbia & A.S. Sakharov (2008), *Probes of Lorentz violation in neutrino propagation*, Phys. Rev. D, **78**, pp. 033013.

[134] J. Ellis, N.E. Mavromatos & D.V. Nanopoulos (2008), *Derivation of a vacuum refractive index in a stringy space-time foam model*, Phys. Lett. B, **665**, pp.412–417.

[135] C. Enrico, R. Bellazzini, G. Tagliaferri, G. Matt, A. Argan et al. (2010), *POLARIX: a pathfinder mission of X-ray polarimetry.*, Astro 2010: Springer Science + Business Media B.V. **doi. 10.1007/s10686-010-9194-1**.

[136] R. Falomo, E. Giraud, L. Maraschi, J. Melnick et al. (1991), *On the nebulosity surrounding the BL Lacertae object PKS 2155-304*, Astrophys. Journal. **380**, pp L67–L69.

[137] B.L. Fanaroff & J.M. Riley. (1974), *The morphology of extragalactic radio sources of high and low luminosity*, Mon. Not. R. Astron. Soc. **167**, pp 31–35.

[138] D.J. Fegan (1997), *Gamma/hadron separation at TeV energies*, J. Phys. G, **23**, pp 1013–1060.

[139] G.J. Feldman & R.D. Cousins (1998), *Unified approach to the classical statistical analysis of small signals*, Phys. Rev. D **57**, pp 3873–3889.

[140] E. Fermi (1949), *On the origin of the cosmic radiation*, Phys. Rev., **75**, pp 1169–1174.

[141] Fermi/LAT & GBM Collaborations, A.A. Abdo et al. (2008), *Fermi observations of high-energy gamma-ray emission from GRB 080916C.*, Science, **323**, pp 1688–1693.

[142] Fermi/LAT & GBM Collaborations, A.A. Abdo et al. (2009), *A limit on the variation of the speed of light arising from quantum gravity effects.*, Nature, **462**, pp 331–334.

[143] Fermi/LAT Collaboration, A.A. Abdo et al. (2009), *Discovery of high-energy gamma-ray emission from the globular cluster 47 Tucanae with Fermi.*, Science, **325**, pp 845–852.

[144] Fermi/LAT Collaboration, A.A. Abdo et al. (2009b), *Measurement of the cosmic ray $e^+ + e^-$ spectrum from 20 GeV to 1 TeV with the Fermi Large Area Telescope*, Phys. Rev. Lett., **102**, doi-id. 181101.

[145] Fermi/LAT Collaboration, A.A. Abdo et al. (2010), *Suzaku observations of Luminous quasars: revealing the nature of blazar emission in quiescent states*, **arXiv:1004.2857**, pp 36

[146] Fermi/LAT Collaboration, A.A. Abdo et al. (2010b), *Fermi Large Area Telescope Observations of the Crab Pulsar and Nebula*, Astrophys. J., **708**, pp 1256–1263.

[147] Fermi/LAT Collaboration, A.A. Abdo et al. (2010c), *The Fermi large area telescope view of misaligned AGN*, Astrophys. J., **720**, pp 912–933.

[148] Fermi/LAT Collaboration, A.A. Abdo et al. (2010d), *The spectral energy distribution of Fermi bright blazars.*, Astrophys. J., **716**, pp 30–93.

[149] Fermi/LAT Collaboration, A.A. Abdo et al. (2010e), *Fermi large area telescope first source catalog*, Astrophys. J. Supl., **188**, pp 405–435.

[150] Fermi/LAT Collaboration, A.A. Abdo et al. (2010f), *The first catalogue of active galactic nuclei detected by the Fermi large area telescope.*, Astrophys. J., **715**, pp 429–435.

[151] Fermi/LAT Collaboration, A.A. Abdo et al. (2010g), *Gamma-ray lightcurves and variability of bright Fermi-detected blazars.*, **arXiv:1004.0348**.

[152] Fermi/LAT Collaboration, A.A. Ackermann et al. (2010h), *Fermi-LAT observations of cosmic-ray electrons from 7 GeV to 1 TeV.*, **arXiv:1008.3999**.

[153] R.P. Feynman, R.B.Leighton & M. Sands (1963). **The Feynman Lectures on Physics - Vol. I**, Addion-Wesley Publishing Co., California.

[154] M. Forot, P. Laurent, I.A. Grenier, C. Gouifès & F. Lebrun (2008), *Polarisation of the Crab pulsar and nebula as observed by the INTEGRAL/IBIS telescope.*, Astroph. Journal **688**, pp L29–L32.

[155] L. Foschini, A. Treves, F. Tavecchio, D. Impiombato et al. (2008), *Infrared to X-ray observations of PKS 2155-304 in a low state*, Astron. & Astrophys. **484**, pp L35–L38.

[156] G. Fossati, L. Maraschi, A. Celotti, A. Comastri & G. Ghisellini (1998), *A unifying view of the spectral energy distributions of blazars*, Mon. Not. R. Astron. Soc. **299**, pp 433–448.

[157] I.M. Frank & Ig Tamm (1937), Dokl. Akad. SSSR **14**, pp 109–118.

[158] J. Frank, A. King & D. Raine (2002). **Accretion power in astrophysics**, Cambridge Univ. Press, Cambridge, UK.

[159] W.L. Freedman, B.F. Madore, B.K. Ginson, L. Ferrarese et al. (2001), *Final results of the Hubble Space Telescope key project to measure the Hubble constant*, Astrophys. Journal **553**, pp 47–72

[160] R. Fukugita, K. Shimasaku, T. Ichikawa (1995), *Galaxy colours in various photometric badn systems*, Pub. Astron. Soc. Pacific **107**, pp 945–958.

[161] S. Funk, G. Hermann, J. Hinton, D. Berge, K. Bernlöhr et al. (2004), *The trigger system of the H.E.S.S. telescope array.*, Astrop. Phys. **22**, pp 285–296.

[162] D.C. Gabuzda, E.A. Rastorgueva, P.S. Smith & S.P. O'Sullivan (2006), *Evidence for cospatial optical and radio polarized emission in active galactic nuclei*, Month. Not. Royal Astro. Society **369**, pp 1596–1602.

[163] T. K. Gaisser (1990), **Cosmic rays and particle physics**, Cambridge Univ. Press, Cambridge, UK.

[164] Y.A. Gallant (2001), *Particle acceleration at relativistic shocks*, in Relativistic Outflows in Astrophysics, Springer Lecture Notes in Physics **589**, pp 24–40.

[165] M. Georganopoulos & D. Kazanas (2003), *Decelerating flows in TeV blazars: a resolution tothe BL Lacertae-FR I unification problem*, Astrophys. Journal **594**, pp L27–L30.

[166] G. Ghisellini, L. Maraschi & A. Treves (1985), *Inhomogeneous synchrotron-self-Compton models and the problem of relativistic beaming of BL Lac objects*, Astron. & Astrophys. **146**, pp 204–212.

[167] G. Ghisellini & A. Celotti, G. Fossati, L. Maraschi & A. Comastri (1998), *A theoretical unifying scheme for gamma-ray bright blazars*, Mon. Not. Royal Astron. Soc. **301**, pp 451–468.

[168] G. Ghisellini & D. Lazzati (1999), *Polarization light curves and position angle variation of beamed gamma-ray bursts*, Mon. Not. Royal Astron. Soc. **309**, pp L7–L11.

[169] G. Ghisellini & F. Tavecchio (2008), *Rapid variability in TeV blazars: the case of PKS 2155-304*, Month. Notic. Royal Astron. Society **386**, pp L28–L32.

[170] G. Ghisellini & F. Tavecchio (2010), *The blazar sequence: a new perspective*, Month. Notic. Royal Astron. Society **387**, pp 1669–1680.

[171] G. Ghisellini, F. Tavecchio, L. Foschini, G. Ghirlanda et al. (2010), *General physical properties of bright Fermi blazars*, Month. Notic. Royal Astron. Society **402**, pp 497–518.

[172] B. Giebels, E.D. Bloom, W.Focke, G. Godfrey, G. Madejski et al. (2002), *Observation of X-ray variability in the BL Lacertae object 1ES 1959+65.*, Astroph. Journal **571**, pp 763–770.

[173] B. Giebels & B. Degrange (2009), *Lognormal variability in BL Lacertae*, Astron. & Astroph. **503**, pp 797–799.

[174] M. Gierliński, M. Middleton, M. Ward & C. Done (2008), *A peridicity of ~ 1 hour in X-ray emission from the active galaxy RE J1034+396*, Nature **455**, pp 369–371.

[175] V.L. Ginzburg & S.I. Sirovatskii (1965), *Cosmic Magnetobremsstrahlung (synchrotron radiation)*, Ann. Rev. of Astron. & Astrophys. **3**, pp 297–350.

[176] V.L. Ginzburg & S.I. Sirovatskii (1969), *Developments in the theory of synchrotron radiation and its absorption*, Ann. Rev. of Astron. & Astrophys. **7**, pp 375–420.

[177] M. Giroletti, G. Giovannini, G.B. Taylor, R. Falomo (2004), *A sample of low-redshift BL Lacertae objects. I. The radio data*, Astrophys. Journal **613**, pp 752–769.

[178] M. Giroletti, G. Giovannini, G.B. Taylor, R. Falomo (2004), *A sample oflow-redshift BL Lacertae objects. II. EVN and MERLIN data and multiwavelength analysis* , Astrophys. Journal **646**, pp 801–814.

[179] D. Gorbunov, P. Tinyakov, I. Tkachev & S. Troitsky (2008), *On the correlation of the Highest-Energy Cosmic Rays with nearby extragalactic objects reported by the Pierre Auger Collaboration.*, JETP Letters, **9**, pp 461–463.

[180] D. Grasso, S. Profumo, A.W. Strong, L. Baldini, R. Bellazzini et al. (2009), *On possible interpretations of the high energy electron-positron spectrum measured by the Fermi Large Area Telescope.*, Astrop. Phys., **32**, pp 140–151.

[181] P.J. Green (1995), *Reversible jump Markov chain Monte Carlo computation and Bayesian model determination*, Biometrika, **82**, pp 711–732.

[182] K. Greisen (1966), *End of the cosmic-ray spectrum?*, Phys. Rev. Lett., **16**, pp 748–750.

[183] P. Gregory (2005), **Bayesian logical data analysis for the physical sciences**, Cambridge Univ. Press.

[184] R.E. Griffiths, S. Tapia, U. Briel & L. Chaisson (1979), *Optical and X-ray Properties of the Newly Discovered BL Lacertae Object PKS 2155-304 (= H2155-304)*, The Astrophys. Journal **234**, pp 810–817.

[185] R.E. Griffiths, U. Briel & HEAO A-3 Group (1979), *H2155-304*, IAU Circular No. **3279** (GB).

[186] V.A. Hagen-Thorn & S.G. Marchenko (1994), *Photometry and Polarimetry of Active Galactic Nuclei*, Baltic Astron. **8**, pp 575–592.

[187] V.A. Hagen-Thorn, V.M. Larionov, S.G. Jorstad, A.A. Arkharov et al. (2008), *The outburst of the blazar AO 0235+164 in 2006 December: shock-in-jet interpretation.*, Astrophys. Journal **672**, pp 40–47.

[188] J. Hakkila & Nemiroff (2001), *Testing the gamma-ray burst pulse start conjecture*, Astroph. Journal **705**, pp 372–385.

[189] R.C. Hartman, D.L. Bertsch, S.D. Bloom, A.W. Chen, P. Deines-Jones et al. (1999), *The third EGRET catalog of high-energy gamma-ray sources*, Astrophys. Journal Supp. Ser. **123**, pp 79–202.

[190] M.G. Hauser, E. Dwek (2001), *The cosmic infrared background:measurements and implications*, Ann. Rev. Astron. & Astrophys. **39**, pp 249–307.

[191] M. Hauser, C. Möllenhoff, G. Pühlhofer, S.J. Wagner et al. (2004), *ATOM – an Automatic Telescope for Optical Monitoring*, Astron. Nach. **325**, pp 659–695.

[192] V.F. Hess (1912), *Über Beobachtungen der durchdringenden Strahlung bei sieben Freiballon fahrt.*, Phys. Zeit. **13**, pp 1084–1091.

[193] R.H. Hildebrand, J.A. Davidson, J.L. Dotson, C.D. Dowell et al. (2000), *A primer on far-infrared polarimetry*, Pub. Astron. Soc. Pacific **112**, pp 1215–1235.

[194] A.M. Hillas (1984), *The origin of ultra-high energy cosmic rays.*, Ann. Rev. Astron. & Astrophys., **22**, pp 424–444.

[195] A.M. Hillas (1985), *Cherenkov light images of EAS produced by primary gamma.*, in Proc. 19th Int. Cosmic Ray Conf. (ICRC), NASA – Goddard Space Flight Center, **3**, pp 445–448.

[196] A.M. Hillas (1996), *Differences between gamma-ray and hadronic showers*, Space Sc. Rev. **75**, pp 17–30.

[197] A.M. Hillas (2005), *Can diffusive shock acceleration in supernova remnants account for high-energy galactic cosmic rays?*, J. Phys. G. **31**, pp R95–R131.

[198] J.A. Hinton (2004), *The status of the H.E.S.S. project*, New Astron. Rev. **48**, pp 331–337.

[199] J.A. Hinton & W. Hofmann (2009), *Teraelectronvolt Astronomy*, Ann. Rev. Astron. & Astrophys. **47**, pp 523–565.

[200] W. Hofmann, I. Jung, A. Konopelko, H. Krawczynski, H. Lampeitl G. Pühlhofer (1999), *Comparison of techniques to reconstruct VHE gamma-ray showers from multiple stereoscopic Cherenkov images*, **arXiv 9904234**, pp 14.

[201] P.A. Holmes, P.W.J.L. Brand, C.D. Impey & P.M. Williams (1984), *Infrared polarimetry and photometry of BL Lac objects – III*, Mon. Not. R. Astron. Society **210**, pp 961–977.

[202] F. Hoyle & W.A. Fowler (1963), *On the nature of strong radio sources*, Mon. Not. R. Astron. Society **125**, pp 169–176

[203] P.A. Hughes, H.D. Aller & M.F. Aller (1985b), *Polarised radio outbursts in BL Lacertae. II. The flux and polarisation of a piton-driven shock*, Astrophys. Journal **298**, pp 301–315.

[204] C.D. Impey, P.W.J.L. Brand, R.D. Wolstencroft & P.M. Williams (1982), *Infrared polarimetry and photometry of BL Lac objects*, Mon. Not. R. Astron. Society **200**, pp 19–40.

[205] C.D. Impey, P.W.J.L. Brand, R.D. Wolstencroft & P.M. Williams (1984), *Infrared polarimetry and photometry of BL Lac objects – II*, Mon. Not. R. Astron. Society **209**, pp 245–269.

[206] S. Inoue & F. Takahara (1996), *Electron acceleration and gamma-ray emission from blazars*, Astrophys. Journal **463**, pp 555–564.

[207] B. Jackson, J.D. Scargle, D. Barnes, S. Arabhi, A. Alt et al. (2004), *An algorithm for optimal partitioning of data on an interval.*, **arXiv:math/0309285v2**.

[208] U. Jacob & T. Piran. (2008), *Lorentz-violation-induced arrival delays of cosmological particles.*, J. Cosm. Astrop. Phys., **031**, pp 1–4.

[209] W. Jaffe, H. Ford, L. Ferrarese, F. van den Bosch & R. O'Connel et al. (1993), *A large nuclear accretion disk in the active galaxy NGC 4261.*, Nature, **364**, pp 213–215.

[210] K. Jahoda, J.H. Swank, A.B. Giles, M.J. Stark et al. (1996), *In-orbit performance and calibration of the Rossi X-ray Timing Explorer (RXTE) Proportional Counter Array (PCA)*, Proc. SPIE – EUV, X-ray and Gamma-ray Instrumentation for Astronomy VII, **2808**, pp 59–70.

[211] R.C. Jennison & M.K. Das Gupta (1953), *Fine Structure of the extra-terrestrial radio source Cygnus I*, Nature **172**, pp 996–997.

[212] J.V. Jelley (1951). *Detection of μ-Mesons and other fast charged particles in cosmic radiation by the Chrenkov effect in distilled water*, Proc. Phys. Soc. A **64** pp. 82–87.

[213] J.V. Jelley (1958). **Cherenkov Radiation and its applications**, UK Atomic Energy Authority, Pergamon Press.

[214] J.V. Jelley (1987). *In days of yore.*, in Proc. of Very-High Energy Gamma-ray Astronomy, ed. K.E. Turver, NATO ASI Series c: Mathematical and Physical Sciences **199** pp. 27-37.

[215] T.W. Jones, S.L. O'Dell & J. Stein (1974), *Physics of compact nonthermal sources. H. Determination of physical parameters*, Astrophys.Journal **192**, pp 261–278.

[216] T.W. Jones & S.L. O'Dell (1977), *Physical conditions in polarised compact radio sources*, Astron. & Astrophys. **61**, pp 291–293.

[217] T.W. Jones, L.Rudnik, H.D. Aller, M.F. Aller et al. (1977), *Magnetic field structures in active compact radio sources*, Astrophys. Journal **290**, pp 627–636.

[218] T.W. Jones (1988), *Polarization as a probe of magnetic field and plasma properties of compact radio sources: simulation of relativistic jets*, Astrophys. Journal **332**, pp 678–695.

[219] P. Jordan & W. Pauli (1928), *Zur Quantenelektrodynamik ladungsfreier Felder*, Zeit. Phys. **47**, pp 151–173.

[220] S.G. Jorstad, A.P. Marscher, J.A. Stevens, P.S. Smith et al. (2007), *Multiwaveband Polarimetric Observations of 15 Active Galactic Nuclei at High Frequencies: Correlated Polarization Behavior*, Astron. Journal **134**, pp 799–824.

[221] T. Kamae, V. Andersson, M. Arimoto, M. Axelsson, C.B. Marini et al. (2010), *PoGOLite A high sensitivity ballon-borne soft-gamma-ray polarimter*, Astrop. Phys. **30**, pp 72–84.

[222] K. Katarzyński, J.-P. Lenain, A. Zech et al. (2008), *Modelling rapid TeV variability of PKS 2155-304*, Month. Not. Royal Astron. Society **390**, pp 371–376.

[223] M.J.L. Kesteven, A.H. Bridle & G.W. Brandie (1976), *Variability of extragalactic sources at 2.7 GHz. I - Results of a 2-yr monitoring program*, Astron. Journal **81**, pp 919–932.

[224] C.R. Kitchin (1984). **Astrophysical Techniques**, Adam Hilger Ltd, Bristol and Philadelphia.

[225] O. Klein & Y. Nishina (1928), *The scattering of light by free electrons according to Dirac's new relativistic dynamics*, Nature **122**, pp 398–399.

[226] F.R. Klinkhamer (2010), *Potential sensitivities to Lorentz violation from non-birefringent modified-Maxwell theory of Auger, HESS and CTA*, **arXiv1008.1967**, pp. 12.

[227] A. Kolmogorov (1992), *General measure theory and probability calculus* in Selected works of Andrei Kolmogorov – probability theory and mathematical statistics 2, pp 48–59.

[228] A.S. Kompaneets (1957), *Establishment of thermal equilibirum between quanta and electrons*, Sov. Phys. – JETP **4**, pp 730–743.

[229] A.A. Korchakov & S.I. Syrovat-skii (1962), *Polarization of radiation and the structure of magnetic fields in cosmic sources of synchrotron radiation*, Sov. Astron. **5**, pp 678–686.

[230] J.K. Kotilainen, R. Falomo & R. Scarpa (1998), *The host galaxies of BL Lac objects in the near-infrared*, Astron. & Astrophys. **336**, pp 479–489.

[231] H. Krawczynski, D.A. Carter-Lewis, C. Duke, J. Holder et al. (2006), *Gamma-hadron separation methods for the VERITAS array of four imaging atmospheric Cherenkov telescopes*, Astrop. Phys. **25**, pp 380–390.

[232] F. Krennrich, I.H. bond, S.M. Bradbury, J.H. Buckley et al. (2002), *Discovery of spectral variability of Markarian 421 at TeV energies*, Astrophys. Journal, **575**, pp L9–L13.

[233] J.H. Krolik (1999), **Active Galactic Nuclei**, Princeton Series in Astrophysics, Princeton Univ. Press, New Jersey.

[234] R.A. Laing (1980), *A model for the magnetic-field structure in extended radio sources*, Mon. Not. Royal Astron. Soc. **193**, pp 439–449.

[235] R.A. Laing (1981), *Magnetic fields in extragalactic radio sources*, Astrophys. Journal **248**, pp 87–104.

[236] L.D. Landau & E.M. Lifshitz (1975), **The classical theory of fields**, Pergamon Press, Oxford, England.

[237] M.P.C. Legg & K.C. Westfold (1968), *Elliptic polarisation of synchrtron radiation*, Astrophys. Journal **154**, pp 499–514.

[238] P. Léna, F. Lebrun & F. Mignard (1998). **Observational Astrophysics**, Astronomy & Astrophysics Library, Springer.

[239] J.-P. Lenain (2009). **Ph.D. Thesis**, Observatoire de Paris, Meudon.

[240] J.-P. Lenain, M. Daniel, C. Boisson, H. Sol et al. (2010). *A tour of very-high energy emitting Active Galactic Nuclei through synchrotron self-Compton modelling*, in preparation.

[241] G. Leyshon (1998). *On the reduction and presentation of data in astronomical two-channel photopolarimetry* Exper. Astron. **8** , pp 153–175.

[242] T.-P. Li & Y.-Q. Ma (1983). *Analysis methods for results in gamma-ray astronomy.*, Astroph. Journal **272**, pp 317–324.

[243] T. Li, J. Qu, H. Feng, L. Song et al. (2004). *Timescale analysis of spectral lags*, Chin. J. Astron. & Astrophys. **4**, pp 583–598.

[244] W. Liller (1969). *On the optical polarisation of three quasi-stellar objects*, Astrophys. Journal **155**, pp 1113–1115.

[245] K.R. Lind & R.D. Blandford (1985). *Semidynamical models of radio jets: relativistic beaming and source counts*, Atrophys. Journal **295**, pp 358–367.

[246] M.L. Lister & P.S. Smith (2000). *Intrinsic Differences in the Inner Jets of High and Low Optically Polarized Radio Quasars*, Atrophys. Journal **541**, pp 66–87.

[247] M.S. Longair (1994). **High Energy Astrophysics - Volumes 1 and 2**, Cambridge Univ. Press, Second Ed., Cambridge.

[248] D. Lynden-Bell (1969). *Galactic nuclei as collapsed old quasars*, Nature **223**, pp 690–694.

[249] A.M. Magalhães, E. Benedetti, E.H. Roland et al. (1984). *A photoelectric polarimeter with tilt-scan capability*, Pub. Astron. Soc.of Pacific **96**, pp 383–390.

[250] A.M. Magalhães, C.V. Rodrigues, V.E. Margonier et al. (1996). *High Precision CCD Imaging Polarimeter*, ASP Conf. Series – Polarimetry of the ISM **97**, pp 118–122.

[251] K. Mannheim (1993), *The proton blazar*, Astron. & Astrophys. **269**, pp 67–76.

[252] A.P. Marscher & W.K. Gear (1985), *Models for high-frequency radio outbursts in extragalactic sources, with application to the early 1983 millimeter-to-infrared flare of 3C 273*, Astrophys. Journal **298**, pp 114–127.

[253] A.P. Marscher (1999), *The compact jets of TeV blazars*, Astrop. Phys. **11**, pp 19–25.

[254] A.P. Marscher, S.G. Jorstad, F.D. D'Arcangelo, P.S. Smith et al. (2008), *The inner jet of active galactic nucleus as revealed by a radio-to-gamma-ray outburst*, Nature **452**, pp 966–969.

[255] M. Martinez & M. Errando (2007), *A new approach to study energy-dependent arrival delays on photons from astrophysical sources.*, Astrop. Phys. **31**, pp 226–232.

[256] A. Mastichiadis (2001), *Radiative processes in relativistic outflows*, in Relativistic Flows in Astrophysics – Springer Lecture Notes in Physics **589**, pp 1–23.

[257] G. Matt (2010), *High energy phenomena studied with x-ray polarimetry*, Int. J. Mod. Phys. D **19**, pp 723–728.

[258] D. Mattingly (2005), *Modern tests of Lorentz invariance*, **arXiv:gr-qg/0502097**.

[259] D. Mazin & M. Raue (2007), *New limits on the density of the extragalactic background light in the optical to the near infrared from the spectra of all known TeV blazars*, Astron. & Astrophys. **471**, pp 439–452.

[260] M. McConnell, M.C. Baring, R. Bellazzini, P.F. Bloser, E. Costa et. al. (2009), *X-ray and Gamma-ray polarimetry*, White paper submission **Astro2010: The Astronomy and Astrophysics DEcadal Survey**.

[261] J. McKinney (2005a), *Jet formation in black hole accretion systems I: theoretical unification model*, **arXiv:astro-ph/050638**.

[262] J. McKinney (2005b), *Jet formation in black hole accretion systems I: numerical models*, **arXiv:astro-ph/050639**

[263] J. McKinney (2006), *General relativistic magnetohydrodynamic simulations of the jet formation and large-scale propagation from black hole accretion systems.*, Mon. Not. Royal Astron. Soc. **368**, pp 1561–1582.

[264] R.J. McLure, M.J. Kukula, J.S. Dunlop, S.a. Baum, et al. (1999), *A comparative HST imaging study of the host-galaxies of radio-quiet quasars, radio-loud quasars and radio-galaxies - I*, Mon. Not. Royal Astron. Soc. **308**, pp 377–404.

[265] A.R.G. Mead, K.R. Ballard, P.W.J.L. Brand, J.H. Hough, et al. (1990), *Optical and Infrared polarimetry and photometry of blazars*, Astron. & Astrophys. Suppl. Series. **83**, pp 183–204.

[266] F. Melia & H. Falcke. (2001), *The supermassive black hole at the galactic center*, Ann. Rev. Astron. & Astrophys. **39**, pp 309–352.

[267] F. Melia (2009), **High-energy astrophysics**, Princeton Series in Astrophysics.

[268] Milagro Collaboration [A.A. abdo et al.] (2008), *A measurement of the spatial distribution of Diffuse TeV Gamma-ray emission from the Galactic plane with Milagro.*, Astrophys. J. **688**, pp 1078–1083.

[269] J.S. Miller (1978), *BL Lac objects*, Comm. Modern Physics **7**, pp 175–182.

[270] F.I. Mirabel & L.F. Rodríguez (1998), *Microquasars in our Galaxy*, Nature **338**, pp 95–103.

[271] R. Moderski, M. Sikora, M. Blażejowski (2003), *Numerical simulations of radiation from blazar jets.*, Astron. & Astrophys. **406**, pp 855–865.

[272] G. Mohanty, S. Biller, D.A. Carter-Lewis, D.J. Fegan, A.M. Hillas et al. (1998), *Measurement of TeV gamma-ray spectra with the Chernkov imaging technique*, Astrop. Phys. **9**, pp 15–43.

[273] R.L. Moore, J.T. McGraw, J.R.P. Angel, R. Duerr et al. (1982), *The noise of BL Lacertae*, Astrophys. Journal **260**, pp 415–436.

[274] P. Morrison (1957), *On the origin of cosmic rays*, Rev. Mod. Phys. **29**, id. 235–243.

[275] H. Mueller (1948), *The foundations of optics*, J. Opt. Am. Soc. **38**, pp. 661–683.

[276] R. Mukherjee, D.L. Bertsch, S.D. Bloom, B.L. Dingus, J.A. Esposito et al. (1997), *EGRET observations of high-energy gamma-ray emission from blazars: an update*, Astrophys. Journal, **490**, pp. 116–135

[277] A. Neronov & D.V. Semikoz (2009), *Sensitivity of gamma-ray telescopes for detection of magnetic fields in ntergalactic medium*, Phys. Rev. D **80**, id. 123012.

[278] S.J. Nolan (2002). **Ph.D. Thesis**, University of Durham, UK.

[279] K.H. Nordsieck (1976), *Optical polarisation models of quasi-stellar objects and BL Lacertae objects*, Astrophys. Journal **209**, pp 653–662.

[280] J.P. Norris, R.J. Nemiroff, J.T. Bonnel, J.D. Scargle et al. (1996). *Attributes of pulses in long bright gamma-ray bursts*, Astrophys. Journal **459**, pp 393–398.

[281] S. Ohm, C. van Eldik & K. Egberts (2009). *Gamma/hadron seperation in very-high-energy gamma-ray astronomy using a multivariate analysis method*, Astrop. Phys. **31**, pp 383–391.

[282] J.H. Oort & Th. Walraven (1956). *Polarisation and Composition of the Crab Nebula*, Bull. Astron. Inst. Netherl. **12**, pp 285–308.

[283] A.G. Pacholczyk (1970). **Radio Astrophysics**, W.H. Freeman and company, San Francisco.

[284] A.A. Penzias & R.w. Wilson (1965). *A measurement of excess antenna temperature at 4080 Mc/s*, Astrophys. J. **142**, pp 419–421.

[285] A. Pereyra (2008). **Ph.D. Thesis**, University of São Paulo.

[286] J.E. Pesce, C.M. Urry, L. Maraschi, A. Treves et al. (1997), *Multiwavelength monitoring of the BL Lacertae object PKS 2155-304 in 1994 May. I. The ground-based campaign*, Astrophys. Journal. **486**, pp 770–783.

[287] The Pierre Auger Collaboration [J. Abraham et al.] (2007), *Correlation of the Highest-Energy Cosmic Rays with Nearby Extragalactic Objects*, Science **318**, pp 938–943.

[288] The Pierre Auger Collaboration [J. Abraham et al.] (2008), *Observation of the suppression of the flux of cosmic rays above $4{\times}10^{19}$ eV*, Ph. Rev. Lett. **101**, doi:10.1103/PhysRevLett.101.061101, pp 6.

[289] The Pierre Auger Collaboration [J. Abraham et al.] (2008b), *Correlations of the highest-energy cosmic rays with the positions of nearby active galactic nuclei*, Astrop. Phys. **29**, pp 188–204.

[290] B.G. Piner & P.G. Edwards (2004), *The parsec-scale structure and jet motions of the TeV Blazars 1ES 1959+650, PKS 2155-304 and 1ES 2344+514.*, Astrophys. Journal. **600**, pp 115–126.

[291] B.G. Piner, N. Pant & P.G. Edwards (2008), *The parsec-scale jets of the TeV blazars H 1426+428, 1ES 1959+650 and PKS 2155-304: 2001-2204.*, Astrophys. Journal. **678**, pp 64–77.

[292] M. Planck (1901), *Über das Gesetz der Energieverteilung in Normalspectrum*, Ann. der Phys. **309**, pp 553–563.

[293] W.H. Press, S.A. Teukolsky, W.T. Vetterling & B.P. Flannery (1992), *Numerical recipes in FORTRAN. The art of scientific computing.*

[294] M. Punch, C.W. Akerlof, M.F. Cawley, M. Chantell, et al. (1992), *Detection of TeV photons from the active galaxy Markarian 421*, Nature **358**, pp 477–478.

[295] S.-J. Qian, A. Quirrenbach, A. Witzel, T.P. Krichbaum et al. (1991), *A model for the rapid radio variability in the quasar 0917+624*, Astron. & Astrophys. **241**, pp 15–21.

[296] S.-J. Qian (1993), *An interpretation for the rotation in the angle of polarization in blazars*, Chin. Astron. & Astrophys. **17**, pp 229–237.

[297] J.P. Rachen & P.L. Biermann (1993), *Extragalactic high-energy cosmic rays – Pat one – Contribution from hot spots in FR-II radio galaxies.*, Astron. & Astrophys. **272**, pp 161–172.

[298] T.A. Rector, E.S. Perlman (2003), *A search for intraday variability in the blazar PKS 2005-489*, Astron. Journal **126**, pp 47–52.

[299] M.J. Rees (1966), *Apperance of relativistically expanding radio sources*, Nature **21**, pp 468–470.

[300] M.J. Rees (1967), *Studies in radio source structure I. A relativistically expanding model for variable quasi-stellar radio sources.*, Mon. Not. Royal Astron. Soc. **135**, pp 345–360.

[301] M.J. Rees (1978), *The M87 jet - Internal shocks in a plasma beam.*, Mon. Not. R. Astron. Soc. **184**, pp 61–81.

[302] M.J. Rees, M.C. Begelman, R.D. Blandford & E.S. Phinney (1982), *Ion-supported tori and the origin of radio jets*, Nature **295**, pp 17–21.

[303] M.J. Rees (1984), *Black hole models for active galactic nuclei.*, Ann. Rev. Astron. & Astrophys. **22**, pp 471–506.

[304] W. Rindler (1991), **Introduction to special relativity**, Oxford Science Publications, Clarendon Press, Oxford.

[305] G.B. Rybicki & A.P. Lightman (2004). **Radiative processes in astrophysics**, Physics Textbooks, Wiley-VCH, Weinheim.

[306] M. Salmenkivi & H. Mannila (2005), *Using Markov chain Monte Carlo and dynmic programming for event sequence data.*, Knowl. & Inform. Syst. **7**, pp 267–288.

[307] E.E. Salpeter (1964), *Accretion of interestellar matter by massive objects*, Astrophys. Journal **140**, pp 796–800.

[308] V.N. Sazonov (1972), *The circular polarisation of sources of synchrotron radiation*, Astrophys. & Space Sc. **19**, pp 25–45.

[309] V.N. Sazonov (1972), *Determination of the properties of a synchrotron-radiation source from its spectrum*, Soviet Astron. **15**, pp 946–949.

[310] J.D. Scargle (1982), *Studies in astronomical time series analysis. II - Statistical aspects of spectral analysis of unevenly spaced data*, Astrophys. Journal **263**, pp 835–853.

[311] J.D. Scargle (1998), *Studies in astronomical time series analysis. V. Bayesian blocks, a new method to analyse structure in photon counting data*, Astrophys. Journal **504**, pp 405–408.

[312] J.D. Scargle, J.P. Norris & J.T. Bonnel (2008), *An algorithm for detecting quantum gravity photon dispersion in gamma-ray bursts: DisCan*, Astrophys. Journal **673**, pp 972–980.

[313] J.D. Scargle (2010), *Studies in astronomical time series analysis: VI. Optimum Partition of the interval: Bayesian blocks, histograms and triggers.*, **in preparation**.

[314] B.E. Schaefer (1999), *Severe limits on variations of the speed of light with frequency*, Phys. Rev. Lett., **82**, pp 4964–4966.

[315] M. Schmidt (1963), *3C 273: A star-like object with large red-shift*, Nature **197**, pp 1040–1043.

[316] J. Schwinger (1949), *On the classical radiation of accelerated electrons*, Phys. Rev. **75**, pp 1912–1925.

[317] C.K. Seyfert (1943), *Nuclear emission in spiral nebulae*, Astrophys. Journal **97**, pp 28–40.

[318] N.I. Shakura & R.A. Sunyaev (1973), *Black holes in binary systems. Observational appearance*, Astron. & Astrophys. **24**, pp 337–355.

[319] F. Shankar, P. Salucci, G.L. Granato, G. De Zotti & L. Danese (2004), *Supermassive black hole demography: the match between the local and accreted mass functions*, Mon. Not. R. Astron. Soc. **354**, pp 1020–1030.

[320] F.H. Shu (1991). **The Physics of Astrophysics - Vol. I Radiation**, University Science Books, California.

[321] M. Sikora, M.C. Begelman & M.J. Rees (1994), *Comptonization of diffuse ambient radiation by a relativistic jet: the source of gamma-rays from blazars?*, Astrophys. Journal **421**, pp 153–162.

[322] P.S. Smith & M.L. Sitko (1991), *Optical polarimetry of PKS 2155-304 and constraints on Accretion disk models for BL Lacertae objects*, Astrophys. Journal **383**, pp 580–586.

[323] P.S. Smith, B.T. Jannuzi & R. Elston (1991), *UBVRI photometry of stars in the fields of X-ray selected BL Lacertae objects*, Astrophys. Journal Suppl. Series **77**, pp 67–73.

[324] P.S. Smith, P.B. Hall, R.G. Allen & M.L. Sitko (1992), *Intensive optical monitoring of the BL Lacertae object PKS 2155-304*, Astrophys. Journal **400**, pp 115–126.

[325] L. Stawarz, M. Sikora & M. Ostrowski (2003), *High-energy gamma-rays from FR I jets*, Astrophys. Journal **597**, pp 186–201

[326] I.A. Steele, S.D. Bates, D. Carter, D. Clarke, A. Gomboc et al. (2006), *RINGO: a novel ring polarimeter for rapid GRB follow-up*, Ground-based and airborne instrumentation for Astronomy – SPIE **6269**, pp 179–196.

[327] I.A. Steele, C.G. Mundell, R.J. Smith, et al. (2009), *Ten percent polarized optical emission from GRB 090102*, Nature **462**, pp 767–769.

[328] G.G. Stokes (1852). *On the composition and resolution of streams of polarised light from different sources*, Trans. Camb. Phil. Soc. **9**, pp 399–416.

[329] F. Tavecchio & D. Mazin (2009). *Intrinsic absorption in 3C 279 at GeV-TeV energies and consequences for estimates of the extragalactic background light.*, Mon. Not. R. Astron. Soc. **392**, pp L40–L44.

[330] J. Terrell (1964). *Quasi-stellar diameters and intensity fluctuations*, Science **145**, pp 918–919.

[331] J. Terrell (1967). *Size limits on fluctuating astronomical sources*, Astrophys. Journal **213**, pp L93–L97.

[332] J. Tinbergen (2005). **Astronomical polarimetry**, Cambridge University Press.

[333] L. Tommasi, R. Díaz, E. Palazzi, E. Pian et al. (2001), *Multiband optical polarimetry of the BL Lacertae object PKS 2155-304: Intranight and long-term variability.*, Astrophys. Journal **132**, pp 73–82.

[334] D.F. Torres & L.A. Anchordoqui (2004), *Astrophysical origins of ultrahigh energy cosmic rays*, Rep. Prog. Phys. **67**, pp 1663–1730.

[335] E. Troja, S. Rosswog & N. Gehrels (2010), *Precursors of short gamma-ray bursts*, **arXiv:1009.1385**.

[336] C.M. Urry & P. Padovani (1995), *Unified Schemes for Radio-Loud Active Galactic Nuclei*, Publ. Astron. Soc. Pac. **107**, pp 803–845.

[337] C.M. Urry & A. Treves, L. Maraschi, H.L. Marshall, T. Kii et al. (1997), *Multiwavelength monitoring of the BL Lac object PKS 2155-304 in 1994 May. III. Probing the Inner jet through multiwavelength correlations.*, Astrophys. Journal **486**, pp 799–825.

[338] T.N. Ukwatta, M. Stamatikos, K.S. Dhuga, T. Sakamoto et al. (2010), *Spectral lags and the lag-luminosity relation: an investigation with Swift BAT gamma-ray bursts.*, Astrophys. Journal **711**, pp 1073–1086.

[339] L. Valtaoja, A. Sillanpaa, E. Valtaoja et al. (1991), *UBVRI photopolarimetry of BL Lac objects - The connection between frequency-dependent polarisation and growing radio shocks*, Astron. Journal **101**, pp 78–87.

[340] L. Valtaoja, E. Valtaoja, N.M. Shakhovskoy, Y.S Efimov et al. (1991), *The connection between the low polarisation quasar 3C 273 and blazars*, Astron. Journal **102**, pp 1946–1955.

[341] S. Vaughan, R. Edelson, R.S Warwick & P. Uttley (2003), *On characterising the variability properties of X-ray light curves from active galaxies*, Month. Not. R. Astron. Soc. **345**, pp 1271–1284.

[342] The VERITAS Collaboration (2009), *A connection between star formation activity and cosmic rays in the starburst galaxy M 82.*, Nature. **462**, pp 770–772.

[343] The VERITAS Collaboration, the VLBA 43 GHz Monitoring Team, H.E.S.S. collaboration & Magic Collaboration (2009), *Radio imaging of the Very-high energy gamma-ray emission region of the central engine of a radio galaxy*, Science. **24**, pp 444–448.

[344] W.T. Vestrand, J.G. Stacy & P. Sreekumar (1995), *High-energy gamma-rays from the BL Lacertae object PKS 2155-304*, Astrophys. Journal Lett. **454**, pp L93.

[345] R.M. Wagner (2008), *Synoptic studies of 17 blazars detected in very-high energy gamma-rays*, Month. Not. of Royal Astron. Soc. **385**, pp 119–135.

[346] R.M. Wagner (2009), *Exploring quantum-gravity with very-high-energy gamma-ray isntruments – prospects and limitations*, **arXiv:0901.2932**, pp .11

[347] M.J. Ward, P.R. Blanco, A.S. Wilson & M. Nishida (1991), *Infrared spectroscopy of a Cygnus A – Implications for the obscured active nucleus.*, Astrophys. Journal **382**, pp 115–120.

[348] A.A. Watson, S. Westerhoff, G. Wieczorek, L. Wiencke, B. Wilczyńska et al. (2008), *Correlation of the highest-energy cosmic rays with the positions of nearby active galactic nuclei*, Astrop. Phys. **29**, pp 188–204.

[349] T.C. Weekes (2001), *Radio pulses from cosmic ray air showers.*, AIP conf. Proc. **579**, pp 3–13.

[350] T.C. Weekes (2003). **Very-high energy gamma-ray astronomy**, IoP Publ. – Series in Astronomy and Astrophysics, Bristol.

[351] T.C. Weekes (1989), *Observation of TeV gamma-rays from the Crab Nebula using the atmospheric Cherenkov imaging technique.*, Astrophys. Journal **342**, pp 379–395.

[352] M.C. Weisskopf, E.H. Silver, H.L. Kestenbaum, K.S. Long and R. Novick (1978), *A precision measurement of the X-ray polarisation of the Crab Nebula without pulsar contamination*, Astrophys. Journal Lett. **220**, pp L117–L121.

[353] K.C. Westfold (1959), *The polarisation of synchrotron radiation*, Astrophys. Journal **130**, pp 241–258.

[354] J.A. Wheeler (1955), *Geons*, Phys. Rev. **97**, pp 511–536.

[355] R. Wiston (1970), , J. Opt. Soc. America **60**, pp 245–247.

[356] G.T. Zatsepin & V.a. Kuz'min (1966), *Upper limit of the Spectrum of cosmic rays*, Journal Exp. and Theor. Phys. Lett. **4**, pp 78.

[357] Ya.B. Zel'Dovich & I.D. Novikov (1965), *Relativistic Astrophysics, Part I*, Soviet Astrophys. – Uspekhi **7**, pp 763–788.

[358] E. L. Zirbel & S.A. Baum (1995), *On the FR I/FR II dichotomy in powerful radio sources: analysis of their emission-line and radio luminosities*, Astrophys. Journal **448**, pp 521–547.

Appendix A

R Numerical Codes

A.1 Bayesian Blocks

A.1.1 Routine InputEventSequence

```
function(...)
{
#read data into timetag array
timetag<-scan(...)
timetag<-timetag-timetag[1]
N<-length(timetag)

#plot histogram for the event sequence
event.hist<-hist(timetag,breaks=N/10,plot=F)
event.hist$breaks<-event.hist$breaks[-length(event.hist$breaks)]
plot(event.hist$breaks, event.hist$counts, type="l",
xlim=c(event.hist$breaks[1],event.hist$breaks[length(event,hist$breaks)],
main="count
histogram", xlab="time(seconds)", ylab="counts", ylim=c(-2,20))
i<-1:N
s1<-array(-2,20)
s2<-array(0,N)
barcode1<-(timetag-50)
```

```
barcode2<-(timetag-50)
segments(barcode1[i],s1[i],barcode2[i],s2[i],lwd=0.5)

return(timetag)}
```

A.1.2 Routine DataCell

```
function(timetag,...)
{
#function input is the events time tags
N<-length(timetag)

#generate waiting-time distribution for events
i<-2:N
wt.dist<-c(timetag[2]-timetag[1], timetag[i]-timetag[i-1])

#plot histogram of wt.dist
hist(wt.dist, breaks=N, main="waiting-time
dist",xlab="seconds",ylab="")

#create datacells
i<-2:(N-1)
cells<-c(wt.dist[1],
(wt.dist[i]-wt.dist[i-1])/2+(wt.dist[i+1]-wt.dist[i])/2,
wt.dist[N]-wt.dist[N-1])
f<-1-trunc(log10(signif(min(wt.dist))))
ticks<-trunc(timetag*10^f)
cells<-trunc(timetag*10^f)
cat("tick length (secs):")
print(10^f)

#print control histogram for integer-time event sequence
tick.hist<-hist(ticks, breaks=N/8, plot=F)
tick.hist$breaks[1]<-tick.hist$breaks[-length(tick.hist$breaks)]
```

```
plot(tick.hist$breaks, tick.hist$counts, type="1",
xlim=c(tick.hist$breaks[1],
tick.hist$breaks[length(tick.hist$breaks)],main="integer time unit
sequence", ylab="counts")
i<-1:N
y<-rep.int(0,N)
points(ticks[i],y,pch="+")

#create output datacell array
datacell<-data.frame(ticks,cells)

return(datacell)}
```

A.1.3 Routine InspectEventSequence

```
function(datacell, pois.seq,...)
{
#statistical inspection of the event sequence
#adjust graph parameters
par(mfrow=c(2,1))
N<-length(datacell$ticks)

#plot event sequence histogram
event.hist<-hist(datacell$ticks,breaks=N/5,plot=F)
event.hist$breaks<-event.hist$breaks[-length(event.hist$breaks)]
plot(event.hist$breaks,event.hist$counts,type="l",xlim=c(event.hist$breaks[1],
event.hist$breaks[length(event.hist$breaks)]),main="count histogram",
xlab="time(ticks)",ylab="counts",ylim=c(-2,20))
i<-1:N
s1<-array(-2,N)
s2<-array(0,N)
barcode1<-(datacell$ticks)
barcode2<-(datacell$ticks)
segments(barcode1[i],s1[i],barcode2[i],s2[i],lwd=0.5)
```

```
#plot cumulative distribution for lc and poisson events
plot(ecdf(datacell$ticks),pch=".",main="CDF(events)",xlab="time(seconds)",
ylab="Fn(time)")
i<-2:N
vals<-unique(pois.seq$ticks)
rvals<-cumsum(tabulate(match(pois.seq$ticks,vals)))/N
pts.out<-seq(0,datacell$ticks[N],by=10)
x<-approx(vals,rvals,xout=pts.out,method="linear")
points(x$x, x$y, pch=".", col=2)
print(ks.test(datacell$ticks, pois.seq$ticks,p.value=T))

return(NULL)}
```

A.1.4 Routine LikelihoodFunction

```
function(datacell, pois.seq,...)
{
#calculate likelihood function for the blocks
par(mfrow=c(1,1))
n<-dim(datacell)[1]

#plot single-block likelihood curve
i<-1:n
N<-cumsum(i)
M<-cumsum(datacell$cells)
loglikelihood<-N*log(N/M)+(M-N)*log(1-(N/M))
plot(loglikelihood, ylab="loglikelihood", xlab="cells", main="Log
Likelihood",type="l")
legend(150,5000,legend="single-block likelihood",lty=1,bty="n",
text.width=1)

#plot poisson comparison light-curve
N<-cumsum(i)
```

```
M<-cumsum(pois.seq$cells)
pois.loglikelihood<-N*log(N/M)+(M-N)*log(1-(N/M))
lines(pois.likelihood,lty=2)
legend(150,-3000,legend="const-process likelihood",lty=2, bty="n",
text.width=1)
max.dif<-max(abs(loglikelihood-pois.loglikelihood))
cat("Maximum Differenc Loglikelihood:")
print(max.dif)

return(loglikelihood)}
```

A.1.5 Routine BlockPartition

```
function(datacell, pois.seq, lngamma)
{
#calculate optimum partition for the sequence
xX11(2);X11(3);X11(4);X11(5)
N<-dim(datacell)[1]
optimum.partition<-array(0,N)
last.changepoint<-array(0,N)
fitness.function<-array(-1E6,N)

for(j in 1:length(lngamma))
{
for(tf in 1:N)
{
lastblock<-NULL
ti<-1
N<-cumsum(tabulate(1:(tf-ti+1)))[(tf-ti+1):1]
M<-cumsum(datacells$cells[(tf-ti+1):1])[(tf-ti+1):1]
lastblock<-N*log(N/M)+(M-N)*log(1-(N/M))-lngamma[j]

if(tf==N && lngamma[j]==lngamma[length(lngamma)]){
dev.set(which=2)
```

```
plot(lastblock, type="1", main="Lastblock Likelihood Function",
xlab="cells",ylab="logliklihood")}

if(lngamma[j]>lngamma[1]){
dev.set(which=2)
lines(lastblock, type="l",col=j)}

if(tf==1){
fitness.fucntion[tf]<-lastblock[tf]
optimum.partition[tf]<-lastblock[tf]}
else{
for(ti in 1:tf){
if(ti==1){fitnessfunction[ti]<-lastblock[ti]}
else{fitness.fucntion[ti]<-lastblock[ti]+optimum.partition[ti-1]}
}}

if(tf==N && lngamma[j]==lngamma[length(lngamma)]){
dev.set(which=3)
plot(fitness.function,type="l",main="Fitness
Function",xlab="cells",ylab="loglikelihood")}
if(lngamma[j]>lngamma[1]){
dev.set(which=3)
lines(fitness.function,type="l",col=j)}

optimum.partition[tf]<-max(fitness.function)
last.changepoint[tf]<-which(fitness.function==max(fitness.function),arr.ind=T)
}

if(lngamma[j]==lngamma[1]){
likelihood<-optimum.partition
cpt<-last.changepoint
partition<-data.frame(likelihood,cpt)}
else{
```

```
likelihood<-optimum.partition
cpt<-last.changepoint
partition<-cbind(partition,likelihood)
partition<-cbind(partition,cpt)}

plot.changepoint<-matrix(c(unique(last,changepoint),which(last.changepoint==
unique(last.changepoint))),nrow=length(unique(last.changepoint)),ncol=2,byrow=T)
print(plot.changepoint)

if(lngamma[j]==lngamma[1]){
dev.set(which=4)
plot(optimum.partition,type="l",main="model likelihood", xlab="cells",
ylab="loglikelihood")
dev.set(which=5)
plot(last.changepoint,type="p",pch=".", main="optimal change-point
array", xlab="data cells", ylab="changepoints")}
else{
dev.set(which=4)
lines(optimum.partition,type="l",col=j)
dev.set(which=5)
points(last.changepoint, type="p",pch".", col=j)
}

return(partition)}
```

A.1.6 Routine PartitionModel

```
function(partition, datacell, lngamma,...)
{
#calculate best-partition model for the light-curve
M<-length(datacell$ticks)
N<-length(partition[[1]])
n<-length(lngamma)
```

```
tick.hist<-hist(datacell$ticks, breaks=M/8, plot=F)
tick.hist$breaks<-tick,hist$breaks[-length(tick.hist$breaks)]
plot(tick.hist$breaks,tick.hist$counts,type="l",xlim=c(min(datacell$ticks),
max(datacell$ticks)),main="integer
time unit sequence",xlab="ticks",ylab="counts")

for(iin 1:n){
changepoint<-partition[[2*i]][N]
j<-1
m<-changepoint[1]

repeat{
j<-(j+1)
if((changepoint[j-1]-1)==0)break
changepoint<-c(changepoint,partition[[2*i]][m-1])
m<-partition[[2*i]][m-1]}
changepoint<-c(lngamma[i],changepoint[length(changepoint):1])

if(i==1){
models<-matrix(changepoint,nrow=length(changepoint),ncol=1,byrow=F)}
else{models<-cbind(models,c(changepoint,rep(1,length(models[,1]-
length(changepoint))))}
k<-2:length(changepoint)
cpt<-c(lngamma[i],datacells$ticks[changepoint[k]])

if(i==1){
cpt.models<-matrix(cpot,nrow=length(cpt),ncol=1,byrow=F)}
else{cpt.models<-cbind(cpt.models,c(cpt,rep(1,length(cpt.models[,1]-
length(cpt))))}

j<-1:M
y<-rep.int(0,M)
points(datacell$ticks[j],y,pch="+")
```

```
abline(v=cpt.models[2:length(cpt.models[,i]),i],col=i+1)}

print(models)
print(cpt.models)

return(models)}
```

A.2 Kolmogorov Distance

```
function (largeflare)
{
#programme to analyse data from large flare of PKS 2155-304.
ti<-c(208, 1309, 1828, 2492, 3111)
tf<-c(764, 1536, 2362, 3188, 3702)
Kdist<-NULL

N<-length(time)

X11(width=10, height=7)
par(mfrow=c(2,1))
ell<-0.5
ehh<-1.
el<-c(0.3, 0.3, 0.3, 0.3, 0.3)
eh<-c(1., 1., 1., 1., 1.)

par(mar=c(0.3,4,1,1), cex.axis=1.55, cex.lab=1.6)
hist<-hist(largeflare$time[which(largeflare$energy<ell,arr.ind=T)],breaks=40,plot=F)
mids<-hist$mids
counts<-hist$counts
plot(mids, counts, pch="", xlab="", ylab="counts", tck=0.02, xaxt="n", ylim=c(0,180))
i<-1:length(mids)
print(sum(counts))
y<-sqrt(counts)
```

```
x<-largeflare$time[length(largeflare$time)]/100
yy<-rep(c(-5,186,186,-5),5)
xx<-c(208,208,764,764,1309,1309,1536,1536,1828,1828,2362,2362,2492,2492,3188,3188,
3111,3111,3702,3702)
polygon(xx,yy,col=gray(0.7), border=NA)
segments(mids[i],counts[i]-y[i], mids[i],counts[i]+y[i], lty=1)
segments(mids[i]-x, counts[i], mids[i]+x, counts[i], lty=1)
legend(3500, 175, "E < 500 GeV", bty="n", cex=2.5)

par(mar=c(4,4,0.3,1), cex.axis=1.55, cex.lab=1.6)
hist<-hist(largeflare$time[which(largeflare$energy>ehh,arr.ind=T)],breaks=40,
plot=F)
mids<-hist$mids
counts<-hist$counts
plot(mids, counts, pch="", xlab="seconds", ylab="counts", tck=0.02, ylim=c(0,25))
i<-1:length(mids)
print(sum(counts))
y<-sqrt(counts)
x<-largeflare$time[length(largeflare$time)]/100
y<-rep(c(-0.5,25.5,25.5,-0.5),5)
polygon(xx,yy,col=gray(0.7), border=NA)
segments(mids[i],counts[i]-y[i], mids[i],counts[i]+y[i], lty=1)
segments(mids[i]-x, counts[i], mids[i]+x, counts[i], lty=1)
legend(3500, 23, "E > 1 TeV", bty="n", cex=2.5)

X11(width=10,height=15)
par(mfrow=c(5,2))
#X11(width=8,height=12)
par(mfrow=c(1,1))

for(j in 1:length(ti)){
tau<-seq(-(tf[j]-ti[j])/4, (tf[j]-ti[j])/4, 0.1)
Kdist<-NULL
```

```
###KOLMOGOROV DISTANCE###
for(i in 1:length(tau)){

time<-largeflare$time[which(largeflare$time > ti[j] & largeflare$time < tf[j],
arr.ind=T)]
energy<-largeflare$energy[which(largeflare$time > ti[j] & largeflare$time < tf[j],
arr.ind=T)]

time<-largeflare$time-tau[i]*largeflare$energy
energy<-largeflare$energy

time<-time-tau[i]*energy
aux<-data.frame(time,energy)
ord<-order(aux$time)
events<-aux[ord,]

time<-events$time[which(events$time > ti[j] & events$time < tf[j],arr.ind=T)]
energy<-events$energy[which(events$time > ti[j] & events$time < tf[j],arr.ind=T)]

events<-data.frame(time,energy)
print(length(events$time))
print(events$time[1:10])
print(events$energy[1:10])



low<-rep(1/length(events$energy[which(events$energy<el[j],arr.ind=T)]),
length(events$energy[which(events$energy<el[j])]))
high<-rep(1/length(events$energy[which(events$energy>eh[j],arr.ind=T)]),
length(events$energy[which(events$energy>eh[j])]))

if(i==1){
print(c("E < 500 GeV", length(events$energy[which(events$energy<el[j])])))
```

```
print(c("E > 1 TeV", length(events$energy[which(events$energy>eh[j])])))
print(c("mean E1", mean(events$energy[which(events$energy<el[j])])))
print(c("mean E2", mean(events$energy[which(events$energy>eh[j])])))
}

cdf.low<-cumsum(low)
cdf.high<-cumsum(high)

N<-length(time)

bin_step<-(max(events$time[which(events$energy<el[j] | events$energy>eh[j],
arr.ind=T)])-min(events$time[which(events$energy<el[j] | events$energy>eh[j],
arr.ind=T)]))/100
bin0<-min(events$time[which(events$energy<el[j] | events$energy>eh[j], arr.ind=T)])

l<-1:100
bin<-c(bin0,bin0+l*bin_step)

P.low<-NULL
P.high<-NULL
x0<-min(events$time)
for(k in 1:101){
P.low[k]<-max(cdf.low[which(events$time[which(events$energy<el[j],arr.ind=T)]<
bin[k],arr.ind=T)])
P.high[k]<-max(cdf.high[which(events$time[which(events$energy>eh[j],arr.ind=T)]<
bin[k],arr.ind=T)])
}

P.low[which(P.low==-Inf)]<-0
P.high[which(P.high==-Inf)]<-0
P.low[which(is.na(P.low)==T)]<-0
P.high[which(is.na(P.high)==T)]<-0
```

```
plot(bin, P.low, type="l")
lines(bin,P.high,type="l",lty=2)
text(min(bin), 0.8, tau[i])
text(min(bin), 0.7,length(low))
text(min(bin), 0.6, length(high))

if(abs(tau[i])==min(abs(tau))){
dev.set(dev.prev())
if(j > 1 & j < length(ti)){
par(mar=c(4,0,1,0), cex.axis=1.65, cex.lab=1.6)
plot(bin, P.low, type="l", xlab="seconds", ylab ="", tck=0.02)
points(bin, P.high, type="l", lty = 2)
plot(bin, abs(P.low-P.high), type="l")}
if(j==1){
par(mar=c(4,4,1,0), cex.axis=1.65, cex.lab=1.6)
plot(bin, P.low, type="l", xlab="seconds", ylab="Cumulative Distribution", tck=0.02)
points(bin, P.high, type="l", lty = 2)
plot(bin, abs(P.low-P.high), type="l")}
if(j==length(ti)){
par(mar=c(4,0,1,1), cex.axis=1.65, cex.lab=1.6)
plot(bin,P.low, type="l", lty = 1, xlab = "seconds",ylab="", tck=0.02)
points(bin, P.high, type="l", lty = 2)
plot(bin, abs(P.low-P.high), type="l")}
}

Kdist[i]<-max(abs(P.low-P.high))
}

dev.set(dev.next())

Kdist.min<-min(Kdist)
Kdist.tau<-tau[which(Kdist==min(Kdist),arr.ind=T)][1]
```

```
print(c("Kdist.min"))
print(c("tau =", Kdist.tau, "s"))

if(j == 1){
yleg<-c(0.45,0.4,0.35,0.3,0.25)
leg<-c("BF 1", "BF 2", "BF 3", "BF 4", "BF 5")
par(mar=c(4.5,4.5,1,1), cex.axis=1.55, cex.lab=1.6)
plot(tau, Kdist, type="l", xlab="hard lag (s/TeV)", ylab="Kolmogorov Distance",
tck=0.02, ylim=c(0.05,0.9), yaxp=c(0., 1.,10), lty=1, col=1, xlim=c(-500, 500),
xaxp=c(-500,500,7))
legend(300, yleg[j], leg[j], bty="n", cex=1.8, text.col= j)
}
if(j==1){
par(mar=c(4.5,4.5,1,0), cex.axis=1.55, cex.lab=1.6)
points(tau, Kdist, type="l", lty=1, col=j)
legend(300, yleg[j], leg[j], bty="n", cex=1.8, text.col= j)
axis(2, tck=0.02, labels=F)
legend(-200, 0.85, c("FLARE", j), bty="n", cex=1.8)}
if(j==length(ti)){
par(mar=c(4.5,0,1,1), cex.axis=1.55, cex.lab=1.6)
points(tau, Kdist, type="l", xlab=" hard lag(s)", ylab ="", yaxt="n",
tck=0.02, ylim=c(0.05,0.9))
axis(2, tck =0.02, labels=F)
legend(-200, 0.85, c("FLARE", j), bty="n", cex=1.8)}
}

return()}
```

Appendix B

Complete Journal of PKS 2155-304 Multi-wavelenght Campaign

B.1 LNA Optical Polarimetry Data

Table B.1: Journal of LNA Polarimetric Observations

Date	MJD (-54000)	Filter	Flux (mJy)	P (%)	P.A. (°)
2008 Sep 01	712.54	V	27.550 (.011)	6.73 (.06)	89.0 (0.2)
	712.57	R	28.748 (.011)	6.36 (.05)	88.7 (0.2)
	712.58	I	31.458 (.013)	5.96 (.03)	86.0 (0.1)
	712.61	R	27.105 (.011)	5.86 (.05)	90.1 (0.2)
	712.63	R	27.411 (.011)	5.76 (.05)	90.0 (0.2)
	712.64	R	26.313 (.014)	5.81 (.09)	90.2 (0.4)
	712.65	R	27.366 (.014)	5.76 (.08)	90.1 (0.3)
	712.66	R	27.882 (.011)	5.90 (.08)	89.9 (0.4)
	712.67	R	27.325 (.011)	5.75 (.04)	89.3 (0.1)
	712.67	V	27.736 (.011)	5.85 (.02)	91.4 (0.1)
	712.69	R	27.947 (.014)	5.65 (.02)	89.8 (0.1)
	712.69	I	30.864 (.014)	5.55 (.06)	85.6 (0.3)
	712.71	R	27.678 (.020)	5.70 (.05)	88.9 (0.2)

	712.72	R	26.723 (.081)	5.63 (.06)	88.3 (0.3)
	712.73	R	27.117 (.054)	5.58 (.07)	87.8 (0.3)
	712.74	R	26.615 (.088)	5.41 (.05)	87.7 (0.2)
	712.75	R	25.716 (.065)	5.41 (.07)	87.6 (0.4)
2008 Sep 02	713.48	V	25.017 (.013)	2.59 (.05)	95.0 (0.5)
	713.49	R	25.688 (.021)	2.64 (.04)	95.5 (0.4)
	713.50	I	29.440 (.030)	2.77 (.04)	91.0 (0.4)
	713.52	R	26.016 (.022)	2.88 (.07)	96.7 (0.7)
	713.53	R	25.448 (.137)	2.67 (.13)	94.9 (1.4)
	713.54	R	24.946 (.011)	2.60 (.08)	95.7 (0.9)
	713.55	R	25.377 (.026)	2.69 (.10)	96.0 (1.1)
	713.56	R	24.665 (.116)	2.78 (.11)	94.8 (1.1)
	713.57	R	23.993 (.010)	2.92 (.06)	96.9 (0.6)
	713.58	R	25.723 (.010)	2.67 (.05)	96.2 (0.5)
	713.59	V	25.158 (.010)	2.64 (.05)	97.5 (0.5)
	713.60	R	26.079 (.010)	2.65 (.06)	99.1 (0.6)
	713.61	I	28.203 (.015)	2.64 (.06)	93.1 (0.7)
	713.63	R	25.427 (.012)	2.59 (.03)	96.2 (0.3)
	713.64	R	25.608 (.010)	2.48 (.05)	98.3 (0.5)
	713.65	R	25.697 (.011)	2.55 (.05)	97.8 (0.5)
	713.66	R	25.247 (.010)	2.69 (.03)	98.1 (0.3)
	713.67	R	25.436 (.013)	2.70 (.05)	98.3 (0.5)
	713.67	R	25.457 (.012)	2.74 (.02)	98.9 (0.3)
	713.68	R	26.637 (.010)	2.68 (.05)	98.6 (0.5)
	713.69	R	25.567 (.011)	2.77 (.04)	99.8 (0.5)
	713.70	R	24.992 (.010)	2.81 (.03)	100.7 (0.3)
	713.71	V	24.338 (.011)	2.95 (.04)	99.5 (0.4)
	713.72	R	24.960 (.013)	2.88 (.01)	101.2 (0.1)
	713.73	I	29.701 (.012)	3.00 (.09)	98.8 (0.8)
	713.74	R	25.352 (.011)	3.02 (.03)	102.1 (0.3)
	713.75	R	25.235 (.021)	3.02 (.03)	102.2 (0.3)
2008 Sep 03	714.46	V	26.182 (.047)	4.80 (.02)	108.1 (1.5)
	714.47	R	25.648 (.015)	4.78 (.05)	107.3 (0.3)

	714.49	I	30.217 (.014)	4.25 (.02)	107.0 (1.7)
	714.51	R	25.873 (.012)	4.66 (.06)	108.3 (0.3)
	714.53	R	24.405 (.016)	4.76 (.05)	108.4 (0.3)
	714.54	R	26.439 (.012)	4.62 (.05)	109.2 (0.3)
	714.55	R	25.636 (.011)	4.65 (.02)	109.1 (0.1)
	714.56	R	26.000 (.012)	4.63 (.04)	109.0 (0.2)
	714.58	R	25.420 (.025)	4.72 (.03)	108.9 (0.2)
	714.59	R	31.513 (.030)	4.76 (.06)	109.3 (0.4)
	714.60	R	27.238 (.011)	4.83 (.04)	109.1 (0.2)
	714.61	V	25.163 (.014)	5.17 (.04)	109.9 (0.2)
	714.63	R	32.653 (.015)	5.31 (.06)	113.4 (0.3)
	714.64	I	29.723 (.016)	4.96 (.06)	109.7 (0.3)
	714.65	R	25.942 (.010)	5.24 (.05)	110.1 (0.3)
	714.66	R	26.953 (.011)	5.29 (.04)	109.5 (0.2)
	714.67	R	26.921 (.018)	5.40 (.05)	109.7 (0.2)
	714.68	R	28.521 (.022)	5.33 (.09)	109.9 (0.4)
	714.69	R	24.525 (.022)	5.46 (.05)	109.4 (0.3)
	714.70	R	25.589 (.016)	5.43 (.03)	110.3 (0.1)
	714.71	R	27.348 (.016)	5.48 (.02)	110.3 (0.1)
	714.72	R	26.461 (.018)	5.42 (.03)	110.5 (0.1)
	714.73	V	23.475 (.021)	5.71 (.10)	111.4 (0.5)
	714.75	R	24.800 (.059)	5.65 (.05)	109.9 (0.2)
	714.75	I	29.973 (.064)	5.44 (.07)	109.2 (0.3)
2008 Sep 04	715.56	R	26.323 (.073)	8.24 (.10)	114.6 (0.3)
	715.57	R	25.697 (.031)	8.26 (.06)	115.1 (0.2)
	715.58	R	26.340 (.011)	8.26 (.06)	114.7 (0.2)
	715.59	R	26.004 (.054)	8.27 (.07)	114.8 (0.2)
	715.60	R	26.566 (.019)	8.15 (.02)	115.1 (0.1)
	715.61	R	26.088 (.035)	8.45 (.06)	114.6 (0.2)
	715.62	R	25.598 (.011)	8.19 (.05)	115.0 (0.1)
	715.63	V	26.745 (.078)	8.56 (.02)	115.7 (0.1)
	715.64	R	26.366 (.011)	8.17 (.06)	114.7 (0.2)
	715.65	I	31.219 (.013)	7.60 (.08)	114.9 (0.2)

	715.66	R	26.293 (.010)	8.21 (.04)	114.6 (0.1)
	715.67	R	26.603 (.013)	8.12 (.04)	114.9 (0.1)
	715.68	R	26.427 (.010)	8.06 (.02)	114.3 (0.1)
	715.70	R	25.667 (.010)	8.04 (.03)	114.5 (0.1)
	715.71	R	26.795 (.011)	8.03 (.05)	114.8 (0.1)
	715.72	R	25.930 (.011)	7.96 (.07)	114.6 (0.2)
2008 Sep 05	716.62	R	27.500 (.011)	7.76 (.02)	116.2 (0.8)
	716.63	R	27.190 (.012)	7.79 (.14)	116.3 (0.5)
	716.65	R	23.736 (.032)	8.24 (.16)	116.3 (0.5)
	716.66	R	25.617 (.013)	7.79 (.21)	116.3 (0.7)
	716.67	R	24.193 (.018)	7.87 (.17)	116.9 (0.6)
	716.68	R	28.050 (.012)	7.81 (.21)	116.8 (0.7)
	716.68	V	26.767 (.011)	8.18 (.01)	119.9 (0.6)
	716.70	R	28.764 (.011)	7.66 (.18)	118.1 (0.6)
	716.70	I	30.864 (.012)	7.12 (.06)	119.0 (0.2)
	716.72	R	27.295 (.012)	7.92 (.17)	116.6 (0.6)
2008 Sep 06	717.62	R	30.691 (.098)	5.80 (.09)	130.6 (0.4)
	717.65	R	31.227 (.174)	5.79 (.40)	131.6 (1.9)
	717.66	R	31.331 (.168)	5.62 (.07)	131.1 (0.4)
	717.68	R	30.747 (.063)	5.55 (.05)	131.8 (0.2)
	717.69	R	31.253 (.085)	5.58 (.14)	132.0 (0.7)